

Stability and evolution of gravity-driven flow in porous media : applied to hydrological and ecological problems

Citation for published version (APA):

Pieters, G. J. M. (2004). *Stability and evolution of gravity-driven flow in porous media : applied to hydrological and ecological problems*. [Phd Thesis 1 (Research TU/e / Graduation TU/e), Mathematics and Computer Science]. Technische Universiteit Eindhoven. <https://doi.org/10.6100/IR580167>

DOI:

[10.6100/IR580167](https://doi.org/10.6100/IR580167)

Document status and date:

Published: 01/01/2004

Document Version:

Publisher's PDF, also known as Version of Record (includes final page, issue and volume numbers)

Please check the document version of this publication:

- A submitted manuscript is the version of the article upon submission and before peer-review. There can be important differences between the submitted version and the official published version of record. People interested in the research are advised to contact the author for the final version of the publication, or visit the DOI to the publisher's website.
- The final author version and the galley proof are versions of the publication after peer review.
- The final published version features the final layout of the paper including the volume, issue and page numbers.

[Link to publication](#)

General rights

Copyright and moral rights for the publications made accessible in the public portal are retained by the authors and/or other copyright owners and it is a condition of accessing publications that users recognise and abide by the legal requirements associated with these rights.

- Users may download and print one copy of any publication from the public portal for the purpose of private study or research.
- You may not further distribute the material or use it for any profit-making activity or commercial gain
- You may freely distribute the URL identifying the publication in the public portal.

If the publication is distributed under the terms of Article 25fa of the Dutch Copyright Act, indicated by the "Taverne" license above, please follow below link for the End User Agreement:

www.tue.nl/taverne

Take down policy

If you believe that this document breaches copyright please contact us at:

openaccess@tue.nl

providing details and we will investigate your claim.

Stability and Evolution of Gravity-Driven Flow in Porous Media

applied to hydrological and ecological problems

Stability and Evolution of Gravity-Driven Flow in Porous Media

applied to hydrological and ecological problems

PROEFSCHRIFT

ter verkrijging van de graad van doctor aan de
Technische Universiteit Eindhoven, op gezag van de
Rector Magnificus, prof.dr. R.A. van Santen, voor een
commissie aangewezen door het College voor
Promoties in het openbaar te verdedigen
op maandag 15 november 2004 om 16.00 uur

door

Gert-Jan Joseph Mathilde Pieters

geboren te Hulst

Dit proefschrift is goedgekeurd door de promotoren:

prof.dr.ir. C. J. van Duijn
en
prof.dr. A. Doelman

CIP-DATA LIBRARY TECHNISCHE UNIVERSITEIT EINDHOVEN

Pieters, Gert-Jan J.M.

Stability and evolution of gravity-driven flow in porous media : applied to hydrological and ecological problems / by Gert-Jan J.M. Pieters. -

Eindhoven : Technische Universiteit Eindhoven, 2004.

Proefschrift. - ISBN 90-386-0932-9

NUR 919

Subject headings: mathematical models / hydrodynamic stability / porous media ; transport phenomena / groundwater / porous media

2000 Mathematics Subject Classification: 76E06, 35K55, 76E15, 76E30, 76F25, 76M30, 76M25, 76S05

Copyright © 2004 by Gert-Jan J.M. Pieters

Gedrukt door: Universiteitsdrukkerij, Technische Universiteit Eindhoven

*'It is no longer stable situations or permanency that interest us,
but rather evolutions, crises and instabilities.'*

~ Ilya Prigogine (1917–2003),
(1977 Nobel Prize winner in Chemistry)
in "Order Out of Chaos", 1984.

Preface

This thesis is an outcome of research during my Ph.D. study at Eindhoven University of Technology from January 2001 until November 2004. During these years my work was supported, encouraged and inspired by a number of people. Therefore, I would like to express my gratitude towards them.

First of all, I would like to thank my advisor prof.dr.ir. C. J. (Hans) van Duijn, who introduced me to the challenging research topic. His dedication and hard-working attitude is definitely reflected in this thesis.

I am also indebted to prof.dr. A. (Arjen) Doelman (Universiteit van Amsterdam), prof.dr.ir. G. J. F. (GertJan) van Heijst, and prof.dr.ir. P. A. C. (Pieter) Raats (emeritus, Wageningen Universiteit) for carefully reading the first versions of this manuscript.

Furthermore, I am particularly appreciative to dr. I. S. (Sorin) Pop from TU/e, dr. C. (Kees) Rappoldt from ALTERRA Wageningen, and dr. H. M. (Henk) Schuttelaars from Universiteit Utrecht for illuminating discussions and cooperation in some of my research topics.

I am also thankful to all members of CASA, the Centre for Analysis, Scientific computing and Applications, in particular to Frans Martens and Tom ter Elst for their support in my teaching activities. Special thanks also go to Kamyar Malakpoor, Dragan Bežanović, Dave Bekers, and Yodi Gunawan for their mental coaching and encouraging discussions.

And last but not least, I am indebted to my parents for their unconditional support through these years.

Eindhoven, November 2004

Gert-Jan J.M. Pieters

Contents

Preface	i
1 Introduction	1
1.1 Gravity-driven flow in porous media	1
1.2 Model equations	4
1.2.1 Conservation of mass and thermal energy	5
1.2.2 Conservation of momentum	6
1.2.3 Flow problems considered in this thesis	7
1.3 Hydrodynamic stability analysis: concepts and methodology	10
1.4 Overview and main results of this thesis	16
References	21
I Mathematical Aspects	25
2 Qualitative properties of the perturbation equation	27
2.1 The ground state solution and its properties	27
2.2 The perturbation equations	29
2.3 The linearised perturbation equation: existence, uniqueness and regularity	29
References	34
3 Stability thresholds for the vertical boundary layer	35
3.1 Linear stability analysis and properties of the spectrum	37
3.2 Variational analysis: the energy method	42
3.2.1 Integral constraint	44
3.2.2 Differential constraint	47
3.2.3 Weighted energy method	51
3.3 Transient energy growth in a linearly stable regime	57
3.4 Comparison with laboratory experiments	59
References	61

4	Growing instabilities and pattern dynamics	63
4.1	Two-dimensional finite element simulations	67
4.2	Reduction to a Landau type amplitude equation	70
4.3	Bifurcation analysis by means of continuation of the reduced model	74
4.3.1	Validation of the reduced model	74
4.3.2	The dynamics of roll/stripe patterns	75
4.3.3	The dynamics of hexagonal patterns	80
4.4	Discussion and future directions	81
	References	81
II	Application to Other Ecological and Hydrological Flow Problems	83
5	Convection as a transport mechanism in peat moss layers	85
5.1	Problem formulation	87
5.1.1	Model equations	87
5.1.2	Groundstate solutions	90
5.2	Stability of the ground states	91
5.3	Finite Element simulations	96
5.4	Analysis of measured temperatures	98
5.5	Discussion	99
5.A	Hydraulic conductivity and temperature measurements in peat moss	102
	References	103
6	The stability of steady flows in unsaturated soils	107
6.1	Problem formulation	110
6.1.1	Classes of soils	112
6.2	Steady-state background flows	114
6.2.1	Uniqueness of steady vertical flows	114
6.2.2	Classification of steady vertical flows	117
6.3	Transient behaviour of perturbations of the matric flux potential . .	118
6.3.1	General approach	118
6.3.2	Application to specific classes of soils	121
6.4	Saturation estimates	122
6.4.1	Estimates that may involve transient growth	122
6.4.2	Sharp estimates	124
6.5	Non-equilibrium Richards equation	125
6.6	Different norms and transient growth	127
6.7	Discussion	129
6.A	The spectrum of the linearised perturbation equation	130
6.B	Saturation estimates for Gardner class soils	132
	References	135

A	A modified spectral Chebyshev–Galerkin method	139
A.1	Discretization of the initial value problem	140
A.2	Solving the discrete eigenvalue problem	143
	References	146
	Summary	149
	Samenvatting	151
	Curriculum Vitae	153

Over the years, there has been considerable interest in the migration of solutes in groundwater. Many of the current pressing problems of environmental concern involve transport issues including groundwater contamination, seawater intrusion in coastal aquifers, radioactive waste disposal, geothermal energy development, groundwater-surface water interaction, and subsurface storage of materials, fluids, and energy.

Groundwater contamination is affected by natural factors and human activities. For instance, 'natural' pollution occurs in coastal aquifers due to saltwater intrusion, and at the subsurface of salt lakes. Examples of pollution by human interference are disposal of industrial waste in natural waters, irrigation return flows containing salt, fertilizers and pesticides, and silting of man-made reservoirs. The chemical composition of groundwater, in particular near drinking water reservoirs, is continuously and intensively monitored and in the past decades many advanced and dedicated techniques have been developed to avoid or reduce contamination of soil-groundwater systems.

One of the mechanisms for solute transport is diffusion. Diffusion is a process that evolves very slowly in time. Hence, in view of the fact that environmental pollution questions usually have to be answered in short time, diffusion on that timescale has a relatively unimportant contribution to the transport of contaminants. In reality, however, the migration of solutes is dramatically enhanced with respect to time and space by *convective* motion of the fluid in which the solutes are dissolved. Convection may, for example, be induced by the action of gravity on the fluid.

1.1 Gravity-driven flow in porous media

In certain hydrogeological situations, fluid density variations occur because of changes in the solute or colloidal concentration, temperature, and pressure of the groundwater. These density gradients basically define two types of flow problems. The first type is characterized by the situation in which the density increases in the direction of the gravity. This situation occurs, for example, in salt water intrusion problems.

These flow problems are characterized by the fact that there exists an abrupt transition or interface separating the fresh and salt groundwater. The second type, and the type that is studied in this thesis, defines flow problems in which the density decreases in the direction of gravity. This is a potentially unstable configuration since the fluid with higher density will have the tendency to ‘fall’ into the direction of gravity, leading to so-called fingers. This phenomenon is called *gravity-driven convection* and can lead to additional transport of heat and solutes. In particular, the convective process enhances hydrodynamic mixing of the dense solute with the less dense ambient groundwater. This is significant for three main reasons (Simmons et al., 2001): (i) the *total quantity of solute* transport involved in the hydrodynamic mixing process is typically much larger than that of diffusive transport, (ii) the *time scales* associated with the mixing process are significantly reduced, and (iii) the *dimensions of the mixing zone* are typically larger and, therefore, enable solutes to spread over much larger domains.

In general, flow and transport in porous media can be split into two parts:

- Flows in *fully saturated* porous media.
- Flows in *unsaturated* or *partly unsaturated* porous media.

In the following subsections we discuss for both the saturated and the unsaturated case the physical mechanisms that cause hydrodynamic mixing. This will be done by means of several hydrological and ecological flow problems.

Flow in fully saturated porous media

An increasing threat to groundwater systems is contamination by salt. As mentioned above, this natural pollution occurs at the subsurface of salt lakes. Salt lakes, or playas, are formed by evaporation of groundwater containing dissolved salts at a groundwater discharge surface. There a saline buildup until saturation occurs, followed by precipitation of salt at the land surface, see Figure 1.1(B). Salt lakes occur in arid and semi-arid environments throughout the world, and they cover approximately one-third of total world land area (Figure 1.1(A)) (Gilman and Bear, 1996; Simmons and Narayan, 1997; Wooding et al., 1997a,b). They represent extensive discharge zones that occur naturally or are induced by changes of land rise. These salt lakes may be dry at the surface, or may contain standing water (ponding), perhaps varying seasonally between the two states. Besides the natural salt precipitation, there may also be a considerable amount of other pollution at the salt lake surface due to direct human interference. Salt lakes in Australia and the USA, for example, are used as disposal sites for saline groundwater and drainage waters from agricultural regions.

In salt lakes, salt diffusion/dispersion rates may balance transport of salt by evaporation (Wooding et al., 1997a,b). Consequently, a zone of high salinity is formed as a relatively thin layer adjacent to the surface, a boundary layer. The fluid density gradient is likely to be very steep and is potentially unstable in a gravitational sense. This is a situation in which convective fingering may occur. Convective fingering affects mixing processes especially by extension of interfaces. Therefore, the use of

salt lakes as evaporation basins and disposal sites raises significant questions concerning the impacts on the groundwater dynamics of salt lakes. In particular when the fingers, possibly containing other pollutants, extend to deeper layers and mix with the relatively fresh water basin under the salt lake.

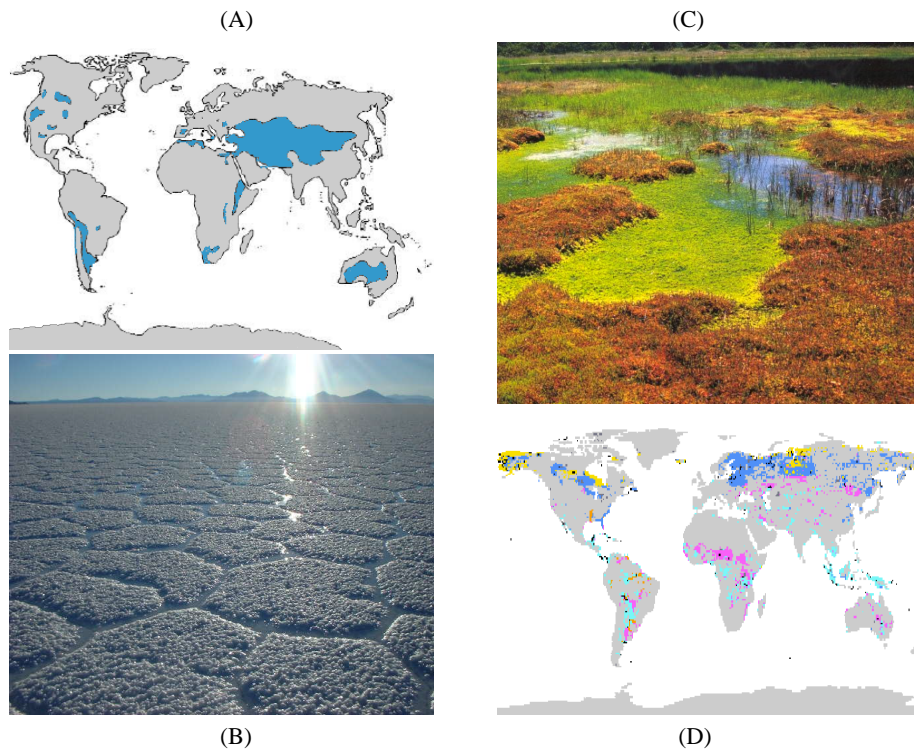


Figure 1.1. (A) Blue areas indicate the distribution of salt lakes around the world (after Williams (2002)). (B) Photograph image of the surface of a salt lake or playa. The surface is covered by precipitated salt crystals with in between little water canals. Observe that these canals divide the salt lake surface in remarkable hexagonal-like structures. (C) A mire with water-saturated green hollows and brownish hummocks. (Photograph courtesy L. Zier). (D) Colored areas indicate the global distribution of different types of wetland ecosystems (after Matthews and Fung (1987)).

In a more general context, the presence of density gradients in a fluid saturated porous medium converts gravitational potential energy into motion through the action of buoyant forces. Density differences can for example be induced by forcing concentration differences in mixtures as in the salt lake case. Density differences may also be induced by maintaining the surface at a temperature different from that of the medium and the saturating fluid. For example, an upflow of warm or hot groundwater has been postulated for some shallow geothermal areas (Wooding, 1960). As the surface is relatively cold, a thermal boundary layer of cool water is formed below the surface. A similar situation arises with *in situ* coal gasification (Homsy and Sherwood, 1975), where a hot reaction surface forms a boundary layer at the lower horizontal boundary of a cooler permeable layer.

A similar situation occurs in wetland ecosystems. A wetland ecosystem typically consists of two layers. The upper part of a mire consists of a sponge-like layer of predominantly moss species, the acrotelm (Ingram, 1978), with a porosity above 95%, see Figure 1.1(C). Below the acrotelm a denser layer, the catotelm, is present where the hydraulic conductivity is much lower than in the acrotelm (Ingram et al., 1974). During the night the surface cools leading to relatively cold water on top of warm water, and if the temperature drop is sufficiently large, the cold water sinks and the warm water rises leading to considerable mixing.

Flow in unsaturated porous media

The theory of flow of water in unsaturated porous media, i.e. when air is also present in the pores, has been developed by soil physicists and hydrologists because of its importance in soil science and in investigations of irrigation, drainage of agricultural lands, infiltration, etc. We will consider the special case of infiltration of water into a soil column. When water is applied in excess at the top of a soil column, the water will enter at a rate depending on the water content in the column and on the physical properties of the soil, like for example the permeability. In the first stages the moisture profile gradually changes, but later it maintains a fixed profile which moves downwards at constant speed. This downward movement of the water profile may be potentially unstable with respect to gravity. Indeed, laboratory observations show instabilities leading to preferential flow paths or ‘fingers’.

Fingering is one form of preferential flow resulting from instability of infiltration through the unsaturated zone. It significantly increases the vertical water and solute velocity which in turn may lead to the rapid movement of harmful chemicals and microbial organisms.

Combinations of the above described mechanisms are also possible. For example, the coexistence of both a thermal and a solutal boundary layer occurs in for example hydrothermal systems and magmatic intrusion problems, see Schoofs (1999) and Brandt and Fernando (1996) for further details and references. These types of flows are called double-diffusive or thermohaline convection problems. In this thesis we do not consider these combined processes.

1.2 Model equations

Fluid flow in the void spaces of a porous medium is described by the Navier–Stokes equations, subject to appropriate boundary and initial conditions. Solving these equations in the fluid domain is not practical because of the enormous complexity of the flow geometry. Even if one could determine a solution for an idealized domain, still the question remains how to relate measured field quantities to micro-scale modeling results. To overcome these difficulties, a continuum theory for flow in porous media has been established. In this continuum or macro-scale approach, averaged micro-scale details reappear in the form of macro-scale coefficients.

The macro-scale equations, in terms of volume averaged and measurable quantities, for salt and heat transport in porous media are based on three fundamental

principles: mass conservation of both fluid and salt, conservation of thermal energy, and momentum conservation of the fluid (Bear, 1972).

1.2.1 Conservation of mass and thermal energy

Assuming the (effective) porosity ϕ [-] to be constant, the fluid mass balance equation for a porous medium that is not fully saturated reads

$$\phi \frac{\partial(\rho\Theta)}{\partial t} + \nabla \cdot (\rho\mathbf{q}) = 0 , \quad (1.2.1)$$

where ρ [$\text{kg}\cdot\text{m}^{-3}$] denotes the fluid density, Θ [$\text{m}^3\cdot\text{m}^{-3}$] saturation, \mathbf{q} [$\text{m}^3\cdot(\text{m}^2\text{s})^{-1}$] the volumetric flux vector, and t [s] is time. The saturation Θ is defined as the fraction of the void volume of the porous medium occupied by fluid. Equation (1.2.1) is known as the continuity equation.

The salt mass balance is given by

$$\phi \frac{\partial(\rho\omega)}{\partial t} + \nabla \cdot (\rho\omega\mathbf{q} + \mathbf{J}_\omega) = 0 , \quad (1.2.2)$$

where \mathbf{J}_ω denotes the dispersive mass flux vector and ω [$\text{kg}\cdot\text{kg}^{-1}$] the salt mass fraction. The salt mass fraction ω is defined as the salt mass concentration c [$\text{kg}\cdot\text{m}^{-3}$] divided by the fluid density ρ [$\text{kg}\cdot\text{m}^{-3}$]. In analogy to diffusive mass transport, the dispersive mass flux \mathbf{J}_ω is assumed to have the form of Fick's law,

$$\mathbf{J}_\omega = -\rho\mathbb{D}_\omega\nabla\omega , \quad (1.2.3)$$

which indicates a linear proportionality between dispersive mass flux and the salt mass fraction gradient. In (1.2.3), \mathbb{D}_ω [$\text{m}^2\cdot\text{s}^{-1}$] denotes an appropriately-defined diffusivity or dispersivity which is assumed to be a scalar. We note that expression (1.2.3) can only be justified for relatively low salt concentrations.

Assuming that the fluid and porous matrix are in thermal equilibrium, the conservation of thermal energy can be expressed as

$$\phi \frac{\partial T}{\partial t} + \nabla \cdot (T\mathbf{q} + \mathbf{J}_T) = 0 , \quad (1.2.4)$$

where \mathbf{J}_T denotes the heat flux and T [K] the temperature. Again, the heat flux \mathbf{J}_T is assumed to obey Fick's law,

$$\mathbf{J}_T = -\frac{\kappa_T}{c_{\text{eff}}}\nabla T =: -\mathbb{D}_T\nabla T , \quad (1.2.5)$$

where κ_T [$\text{m}\cdot\text{kg}/(\text{s}^3\cdot\text{K})$] denotes the thermal conductivity, c_{eff} [$\text{kg}/(\text{m}\cdot\text{s}^2\cdot\text{K})$] heat capacity, and \mathbb{D}_T thermal diffusivity.

Several physical phenomena can affect the fluid volume, and thereby its density. These are: thermal expansion, pressure compressibility and volume changes due to

high salt content. This implies that the fluid density is a function of absolute temperature T , fluid pressure p , and salt mass fraction ω . The empirical relation between these variables is given by the equation of state (Bear, 1972, Section 2.3)

$$\rho = \rho(T, p, \omega) = \bar{\rho} e^{-\alpha_T(T-\bar{T}) - \alpha_p(p-\bar{p}) + \gamma\omega},$$

where $\bar{\rho}$ denotes a reference density, and where α_T and α_p respectively denote the thermal expansion and the compressibility coefficient. Under isothermal and isobaric conditions, and disregarding fluid volume changes due to small pressure variations, the equation of state reduces to

$$\rho = \bar{\rho} e^{\gamma\omega}, \quad (1.2.6)$$

where $\bar{\rho}$ denotes the density of fresh water. Under isohaline and isobaric conditions, the equation of state is given by $\rho = \bar{\rho} e^{-\alpha_T(T-\bar{T})}$. For small temperature differences, we obtain the approximate relation

$$\rho \cong \bar{\rho} - \alpha_T \bar{\rho} (T - \bar{T}). \quad (1.2.7)$$

1.2.2 Conservation of momentum

The fluid momentum balance equation in a nondeformable medium and in the absence of inertial effects, is usually taken as

$$\mathbf{q} = -\frac{\kappa}{\mu} (\nabla p - \rho g \mathbf{e}_z), \quad (1.2.8)$$

where p [$\text{N}\cdot\text{m}^{-2}$] denotes fluid pressure, κ [m^2] the intrinsic permeability tensor, μ [$\text{kg}\cdot(\text{sm})^{-1}$] the dynamic viscosity, g [$\text{m}\cdot\text{s}^{-2}$] the acceleration of gravity, and \mathbf{e}_z the unit vector in the z -direction, pointing downwards. Equation (1.2.8) expresses a balance between the driving forces due to gravity and fluid pressure gradients, i.e. $-(\nabla p - \rho \mathbf{g})$, and the drag force exerted by the solid phase upon the fluid phase, expressed by $(\mu/\kappa)\mathbf{q}$. The momentum balance equation (1.2.8) is generally referred to as Darcy's law.

Combining the continuity equation (1.2.1), (1.2.2) and (1.2.3), and assuming that the porous medium is fully saturated ($\Theta \equiv 1$), gives

$$\phi \rho \frac{\partial \omega}{\partial t} + \rho \mathbf{q} \cdot \nabla \omega - \nabla \cdot (\rho \mathbb{D}_\omega \nabla \omega) = 0,$$

and using the equation of state (1.2.6) leads to

$$\phi \frac{\partial \rho}{\partial t} + \mathbf{q} \cdot \nabla \rho - \mathbb{D}_\omega \Delta \rho = 0, \quad (1.2.9)$$

where Δ denotes the Laplacian. Substitution of (1.2.5) into (1.2.4) and using the equation of state (1.2.7) gives for the fully saturated case

$$\phi \frac{\partial T}{\partial t} + \nabla \cdot (\mathbf{q} T) - \mathbb{D}_T \Delta T = 0. \quad (1.2.10)$$

The quantities \mathbb{D}_ω , \mathbb{D}_T , κ , κ_T , c_{eff} and μ are assumed to be independent of the salt mass fraction ω , temperature T and the spatial coordinates.

Although suffering from the lack of a rigorous mathematical justification, we shall now consider the approximate salt-transport equations obtained by replacing (1.2.1) with the incompressibility condition

$$\nabla \cdot \mathbf{q} = 0 . \quad (1.2.11)$$

This approximation is usually referred to as the Oberbeck–Boussinesq approximation (Bear, 1972; Nield and Bejan, 1992; Wooding et al., 1997a). Hence the governing equations are given by (1.2.11), (1.2.8) and (1.2.9) for solute transport, or (1.2.11), (1.2.8) and (1.2.10) for the transport of thermal energy. Observe that both problems have in essence the same mathematical structure.

Flow through *unsaturated* porous media is governed by the continuity equation (1.2.1) and Darcy's law (1.2.8). Assuming the water to be incompressible, the balance of mass can be written as the volumetric balance equation

$$\frac{\partial \theta}{\partial t} = \nabla \cdot (k \nabla \Psi - k \mathbf{e}_z) , \quad (1.2.12)$$

where $\theta := \phi \Theta$ denotes the (volumetric) water content, $k = \kappa \rho g / \mu$ [$\text{m} \cdot \text{s}^{-1}$] hydraulic conductivity, and $\Psi = p / (\rho g)$ [$\text{Ns}^2 \cdot \text{kg}^{-1}$] the pressure head. In contrast to the fully saturated case, the quantities k and Ψ depend on θ making the problem nonlinear. Usually one defines the soil water diffusivity $\mathbb{D}_\theta = \mathbb{D}_\theta(\theta) = k d\Psi / d\theta$ so that (1.2.12) reduces to

$$\frac{\partial \theta}{\partial t} - \nabla \cdot (\mathbb{D}_\theta(\theta) \nabla \theta - k(\theta) \mathbf{e}_z) = 0 . \quad (1.2.13)$$

Equation (1.2.13) is known as Richards equation (Richards, 1931). Alternative formulations of this equation also exist, see Chapter 6 of this thesis.

1.2.3 Flow problems considered in this thesis

In this thesis we consider three different flow problems. For each case we consider a uniform isotropic porous medium occupying the three-dimensional subspace

$$\Omega = \{(x, y, z) : (x, y) \in \Omega_\perp \subseteq \mathbb{R}^2, 0 < z < H\} , \quad (1.2.14)$$

where $0 < H \leq \infty$ denotes the dimensional depth of the layer and where z points vertically downwards. Further, Ω_\perp may be either bounded or \mathbb{R}^2 . In the latter case it is sometimes convenient to divide the flow domain in periodicity cells:

$$\mathcal{C} = \{(x, y, z) : |x| < \pi/a_x, |y| < \pi/a_y, 0 < z < H\} , \quad (1.2.15)$$

where a_x and a_y are the, as yet unspecified, horizontal wavenumbers. We call

$$a := \sqrt{a_x^2 + a_y^2} \quad (1.2.16)$$

the horizontal wavenumber of the periodicity cell \mathcal{C} . The periodicity assumption implies that we can restrict our flow domain to the (horizontally bounded) periodicity cell \mathcal{C} .

The following flow problems are considered:

Downward migration of salt near the surface of a salt lake. The medium is saturated with a fluid of variable density ρ : i.e. water with dissolved salt. Along the upper boundary $\{z = 0\}$ we prescribe density and fluid flow corresponding to a ‘dry lake bed’, with a sufficient rate of evaporation \mathbb{E} [$\text{m}\cdot\text{s}^{-1}$] to remove all free surface water and an instantaneous buildup of salt. If ρ_r denotes the fluid density in reference circumstances, i.e. far away from the outflow boundary, and ρ_m the maximum density at the outflow boundary, we have $\rho_r \leq \rho \leq \rho_m$ throughout the flow domain Ω . Here ρ_m may represent the fluid density in an overlying pond or the density of the salt-saturated solution near the subsurface. The initial density may have any spatial distribution between ρ_r and ρ_m . The initial density is represented by the function $f^* : \Omega \mapsto [\rho_r, \rho_m]$. Equations (1.2.9), (1.2.8) and (1.2.11) are considered in Ω for $t > 0$, where $\Omega_{\perp} \equiv \mathbb{R}^2$ and $H \equiv \infty$.

Remark 1.1. *When there is no throughflow present and when $H < \infty$, the above described problem is known as the Rogers–Horton–Lapwood or Darcy convection problem (Horton and Rogers, 1945; Lapwood, 1948). It is the porous media equivalent of the well-known Rayleigh–Bénard problem for free fluids. Both problems have been extensively studied over the years, see, among others, Nield and Bejan (1992); Joseph (1976).*

We recast the problem in dimensionless form by setting

$$S = \frac{\rho - \rho_r}{\rho_m - \rho_r} \quad \text{and} \quad \mathbf{U} = \frac{\mathbf{q}}{u_c}, \quad u_c = \frac{(\rho_m - \rho_r)g\kappa}{\mu}, \quad (1.2.17)$$

and by introducing the thickness of the equilibrium boundary layer $\delta = \mathbb{D}/\mathbb{E}$ and $\phi\mathbb{D}/\mathbb{E}^2$, respectively, as scales for length and time. This yields

$$(P1) \left\{ \begin{array}{ll} \frac{\partial S}{\partial t} + \text{Ra} \nabla \cdot (\mathbf{U} S) = \Delta S & \text{in } \Omega, t > 0, \\ \nabla \cdot \mathbf{U} = 0 & \text{in } \Omega, t > 0, \\ \mathbf{U} + \nabla P - S \mathbf{e}_z = \mathbf{0} & \text{in } \Omega, t > 0, \\ \mathbf{U} \cdot \mathbf{e}_z = -\text{Ra}^{-1}, S = 1 & \text{at } z = 0, t > 0, \\ S = f & \text{in } \Omega, t = 0, \end{array} \right.$$

where $f = (f^* - \rho_r)/(\rho_m - \rho_r)$. Here $P = (p - \rho_r g \delta z)/(\rho_m - \rho_r)g\delta$ represents departures of the dimensionless pressure from hydrostatic reference conditions and Ra the system Rayleigh number

$$\text{Ra} = \frac{(\rho_m - \rho_r)g\kappa}{\mu\mathbb{E}} = \frac{u_c}{\mathbb{E}}. \quad (1.2.19)$$

Solute transport in wetland ecosystems. Again the porous medium is considered fully saturated with a fluid of variable density. This time the water is exposed to surface temperature fluctuations. Along the upper boundary $\{z = 0\}$ we prescribe the temperature according to a time-periodic surface temperature with period τ_0 and temperature difference ΔT , and along $\{z = H\}$ we prescribe no-flux and no-flow boundary conditions. We do not take into account any form of evaporation by assuming a zero vertical water flux at the surface. Equations (1.2.10), (1.2.8) and (1.2.11) are considered in Ω , where $\Omega_\perp \equiv \mathbb{R}^2$, and read in *dimensionless* form (for the definition of the scales we refer to Chapter 5)

$$(P2) \left\{ \begin{array}{ll} \frac{\partial T}{\partial t} + \text{Ra} \nabla \cdot (\mathbf{U}T) = \Delta T & \text{in } \Omega, t > 0. \\ \nabla \cdot \mathbf{U} = 0 & \text{in } \Omega, t > 0, \\ \mathbf{U} + \nabla P - T \mathbf{e}_z = \mathbf{0} & \text{in } \Omega, t > 0, \\ \mathbf{U} \cdot \mathbf{e}_z = 0, T = \Phi(t) & \text{at } z = 0, t > 0, \\ \mathbf{U} \cdot \mathbf{e}_z = \nabla T \cdot \mathbf{e}_z = 0 & \text{at } z = h, t > 0. \end{array} \right.$$

The system Rayleigh number for this case is defined by

$$\text{Ra} = \frac{\bar{\rho} g \kappa}{\mu} \alpha_T \Delta T \sqrt{\frac{\tau_0}{\mathbb{D}_T}}. \quad (1.2.21)$$

Steady infiltration in unsaturated soils. We consider equation (1.2.13) in the flow domain Ω , where Ω_\perp is now a bounded subset of \mathbb{R}^2 , for $t > 0$. We restrict ourselves to constant boundary data: along $\{z = 0\}$ we set $\theta = \theta_T$ and along $\{z = H\}$ we impose $\theta = \theta_B$. In this definition $\theta_r \leq \theta_T, \theta_B \leq \theta_o$, where θ_o is the volumetric water content at saturation and θ_r the irreducible volumetric water content. Along the vertical boundaries we have $\nabla \theta \cdot \mathbf{n} = 0$. Again, the initial condition for θ is given by some spatial distribution function $f^* : \Omega \mapsto [\theta_r, \theta_o]$. The equation in *dimensionless* form is given by (see Chapter 6 for the definition of the scales):

$$(P3) \left\{ \begin{array}{ll} \frac{\partial S}{\partial t} + \text{Ra} \nabla \cdot (k(S)\mathbf{e}_z) = \nabla \cdot (D(S)\nabla S) & \text{in } \Omega, t > 0. \\ S = S_T & \text{at } z = 0, t > 0, \\ S = S_B & \text{at } z = 1, t > 0, \\ \nabla S \cdot \mathbf{n} = 0 & \text{at } \partial\Omega_\perp \times (0, 1), t > 0, \\ S = f & \text{in } \Omega, t = 0, \end{array} \right.$$

where the system Rayleigh number is defined by

$$\text{Ra} = \frac{H}{(\theta_o - \theta_r)/c_0} \quad (c_0 \text{ is the reference volumetric water capacity}). \quad (1.2.23)$$

Concerning these three flow problems, we observe the following:

- (i) All problems involve a system parameter $Ra \in \mathbb{R}_+$. This parameter is usually referred to as the *bifurcation parameter* and will be denoted by R .
- (ii) Depending on the initial condition f , they all have a solution that corresponds to a ‘trivial’ *one-dimensional* diffusion / convection type process, see Sections 2.1, 5.1.2 and 6.2. This solution is referred to as the *ground-state solution*.
- (iii) Depending on the value of R , other ‘nontrivial’ solutions *may* exist. Some of these solutions are candidates for steady three-dimensional convective flow.

As mentioned in Section 1.1, convective flows are important in solute transport processes. Hence we are interested in the transition from the ground-state solution to a convective regime. The ground state is said to lose its stability if it bifurcates to a neighboring (convective) steady-state. It should be emphasized that this concept only makes sense when multiple steady solutions exist. However, uniqueness of a ground-state solution is not always easy to prove, see Section 6.2.1 of this thesis, and is often not even true. Then one is usually left with direct numerical simulations of the underlying mathematical model to show the non-uniqueness of the ground state.

The transition critically depends on the bifurcation parameter R . The determination of this critical value is one of the most important topics in hydrodynamic stability analysis.

1.3 Hydrodynamic stability analysis: concepts and methodology

In this section we introduce the concept *hydrodynamic stability* and we discuss in detail the role of the bifurcation parameter. To fix ideas, we first recall some concepts and techniques from dynamical systems theory. For this purpose we follow Dauchot and Manneville (1997).

The model equations described in Section 1.2.3 are all within the class described by the following general system:

$$\mathcal{M}_R \frac{\partial \mathbf{F}}{\partial t} = \mathcal{L}_R \mathbf{F} + \mathcal{N}_R(\mathbf{F}), \quad (1.3.1)$$

where $\mathbf{F} = \mathbf{F}(\mathbf{x}, \mathbf{z}, t)$ is the vector containing the unknowns in which the spatial variables are defined on a *cylindrical* domain. This means that $(\mathbf{x}, \mathbf{z}) \in \mathbb{R}^m \times \Omega_{\parallel}$, where $\Omega_{\parallel} \subset \mathbb{R}^n$ is an open domain (and $m \geq 1, n \geq 0$), so that $\mathbf{F} : \mathbb{R}^m \times \Omega_{\parallel} \times \mathbb{R}_+ \mapsto \mathbb{R}^N$. The $N \times N$ constant coefficient ‘mass’ matrix \mathcal{M}_R is assumed to be non-negative, in the sense that all its eigenvalues are real and nonnegative. Note that this implies that \mathcal{M}_R is not necessarily invertible. In the right-hand side of (1.3.1), \mathcal{L}_R and \mathcal{N}_R are differential operators essential to the dynamics of the system. The linear operator \mathcal{L}_R is assumed to be elliptic and \mathcal{N}_R is a nonlinear operator of order less than \mathcal{L}_R . Both operators may depend directly on the variable $\mathbf{z} \in \Omega_{\parallel}$.

The operators \mathcal{M}_R , \mathcal{L}_R and \mathcal{N}_R will typically contain the bulk equations, but it may also be convenient in some cases to include some of the boundary conditions in their definitions. Eventually, the remaining boundary conditions will be grouped into a set \mathcal{H} to which the vector \mathbf{F} is said to belong. Thus, a problem definition includes the statements $\mathbf{F} \in \mathcal{H}$ as well as \mathbf{F} satisfies (1.3.1). To conclude, we assume that the bifurcation parameter R is one-dimensional (thus we consider here a co-dimension 1 bifurcation). For the first flow problem from Section 1.2.3 we have $N = 5$, $m = 2$, $n = 1$, $\mathbf{F} = (S, P, \mathbf{U})^T$ and $R = \text{Ra}$.

The next essential ingredient for hydrodynamic stability analysis is the assumption that (1.3.1) has a ‘trivial’ solution that depends on the coordinates \mathbf{z} only, i.e. $\mathbf{F}(\mathbf{x}, \mathbf{z}, t) = \mathbf{F}_0(\mathbf{z})$; the ground-state solution. Thus, the ground state \mathbf{F}_0 is supposed to be only a function of the variable $\mathbf{z} \in \Omega_{\parallel}$. We recall that the stability of a given ground state \mathbf{F}_0 , controlled by parameter R , is understood as its ability to recover from perturbations. Thus we study the stability of \mathbf{F}_0 by setting

$$\mathbf{F}(\mathbf{x}, \mathbf{z}, t) = \mathbf{F}_0(\mathbf{z}) + \mathbf{f}(\mathbf{x}, \mathbf{z}, t) , \quad (1.3.2)$$

where $\mathbf{f} : \mathbb{R}^m \times \Omega_{\parallel} \times \mathbb{R}_+ \mapsto \mathbb{R}^N$ denotes a perturbation. Substitution of expansion (1.3.2) into (1.3.1) and redefining the operators \mathcal{L}_R and \mathcal{N}_R yields the perturbation equation

$$\mathcal{M}_R \frac{\partial \mathbf{f}}{\partial t} = \mathcal{L}_R \mathbf{f} + \mathcal{N}_R(\mathbf{f}) . \quad (1.3.3)$$

Equation (1.3.3) will play a crucial role in the stability analysis. Generally speaking, stability properties depend on R . With respect to this bifurcation parameter, three critical values can be identified:

- **The linear instability threshold R_L .** This threshold can be obtained from linear stability analysis, i.e. by solving the generalized eigenvalue problem $\mathcal{L}_R \mathbf{f} = \sigma \mathcal{M}_R \mathbf{f}$. Clearly the eigenvalues depend on R . Assuming the real parts to be ordered we have $\dots < \text{Re}(\sigma_n) < \dots < \text{Re}(\sigma_2) < \text{Re}(\sigma_1) =: \sigma_{\max}$. Here Re denotes the real part of the eigenvalues. The threshold R_L is determined by the solution of $\sigma_{\max}(R) = 0$. The solution of this equation is characterized by the fact that for $R > R_L$ there exists at least one (infinitesimal) perturbation against which the ground state is unstable, i.e. for $R > R_L$ we have $\sigma_{\max}(R) > 0$.

- **The energy (or monotonic) stability threshold R_E .** To assign a definite meaning to the concept ‘stability’, we introduce the functional \mathcal{E} which has the properties of a norm: it is zero when the observed state is indistinguishable from the ground state and strictly positive otherwise. The quantity \mathcal{E} is usually based on the L^2 -norm of the difference between the observed state and the ground state, i.e.

$$\mathcal{E} = \mathcal{E}(t) := \int_{\mathcal{C}} \mathbf{f}^T(\mathbf{A}\mathbf{f}) =: \langle \mathbf{f}, \mathbf{f} \rangle , \quad \text{with } \mathbf{f} = \mathbf{F} - \mathbf{F}_0 , \quad (1.3.4)$$

where $\mathbf{A} \in \mathbb{R}^{N \times N}$ denotes a positive semidefinite matrix, e.g. \mathcal{M}_R or the identity \mathcal{I} .

Remark 1.2. Working with \mathcal{E} is the essence of the energy method (Joseph, 1976; Straughan, 2004; Galdi and Padula, 1990). One must realize that the name ‘energy

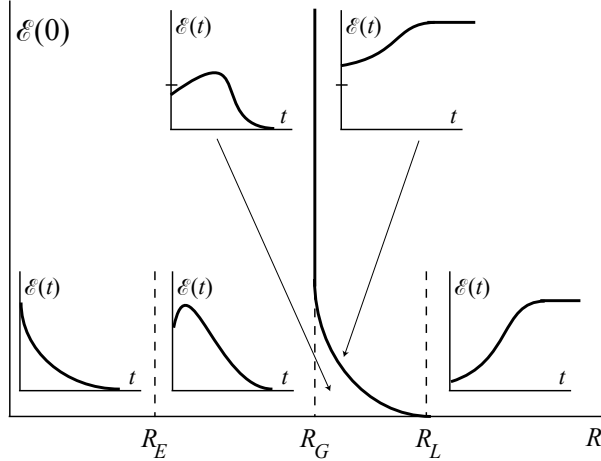


Figure 1.2. The behavior of perturbations to the ground state as a function of $\mathcal{E}(0)$ and of the value of the bifurcation parameter R . The initial amplitude $\mathcal{E}(0)$ may be taken arbitrary for Rayleigh numbers between 0 and R_G . For Rayleigh number between R_G and R_L , the behaviour of $\mathcal{E}(t)$ depends critically on the initial perturbation, and for $R > R_L$ we only consider infinitesimally small initial perturbations.

method' is misleading here in the sense that it is not related to the energy as a physical quantity, see definition (1.3.4).

Now if we can decompose the linear operator \mathcal{L}_R into $\mathcal{L} + R\mathcal{B}$ and if the non-linear part satisfies the dissipativity condition $\langle \mathcal{N}_R(\mathbf{f}), \mathbf{f} \rangle \leq 0$, then it follows from (1.3.3)

$$\frac{1}{2} \frac{d}{dt} \langle \mathbf{f}, \mathbf{f} \rangle = \langle \mathcal{L}_R \mathbf{f}, \mathbf{f} \rangle + \langle \mathcal{N}_R(\mathbf{f}), \mathbf{f} \rangle \leq \langle \mathcal{L} \mathbf{f}, \mathbf{f} \rangle + R \langle \mathcal{B} \mathbf{f}, \mathbf{f} \rangle. \quad (1.3.5)$$

If R is chosen such that the right-hand side of (1.3.5) is negative for all perturbations from an appropriately chosen class \mathbf{H} of admissible perturbations, then stability is guaranteed. This leads to the maximum problem

$$\frac{1}{R_E} = \sup_{\mathbf{f} \in \mathbf{H}} \frac{-\langle \mathcal{B} \mathbf{f}, \mathbf{f} \rangle}{\langle \mathcal{L} \mathbf{f}, \mathbf{f} \rangle}.$$

The threshold R_E is thus defined by the condition that for $R < R_E$ the functional $\mathcal{E}(t)$ decays for all positive time. For $R \geq R_E$, however, there may exist perturbations for which the norm \mathcal{E} does not monotonically decay with time, see Figure 1.2. However, such flows can still be *globally stable* in the sense that the norm \mathcal{E} may eventually decay to zero despite the fact that it exhibits (finite time) transient growth. Thus, to refine the concept of stability a third critical Rayleigh number is introduced:

- **The global stability threshold R_G .** The largest value of R for which global stability can be guaranteed is called the global stability threshold and is denoted by R_G . It is determined from the property that, for $R < R_G$, perturbations of arbitrary shapes and 'amplitudes' all decay asymptotically as time tends to infinity: the flow returns to the ground state which is therefore unconditionally stable. Clearly we must have $R_E \leq R_G \leq R_L$ but, whereas R_L and R_E can be derived from definite strategies, R_G is not easy to determine since it requires testing for all possible perturbations,

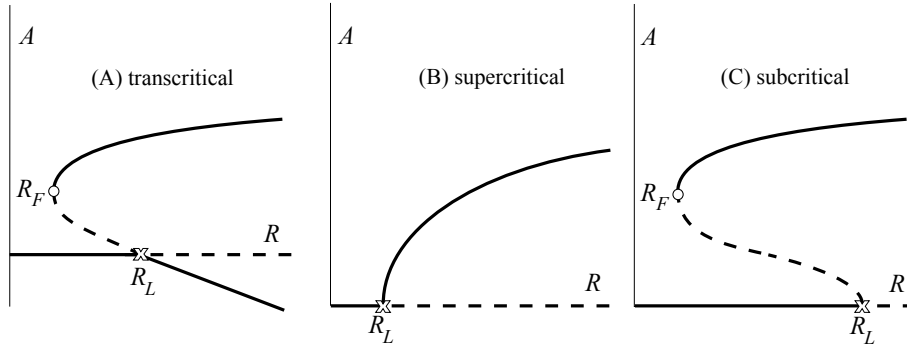


Figure 1.3. Bifurcation diagrams for the three generic cases: (A) transcritical; (B) supercritical; (C) subcritical. Dashed curves depict unstable branches, the solid curves stable branches.

and not only for infinitesimal ones whose initial dynamics are governed by a linear operator.

When $R \geq R_G$, the ground-state solution is unstable to some perturbation, though it may be (conditionally) stable to small perturbations (see Figure 1.2). More than one solution of ‘permanent’ form may be possible when $R \geq R_G$. In particular, we want to know the number of such solutions, their dependence on parameters, and their stability properties. This is in general an extremely hard problem for analysis. However, some parts of it can be managed through *bifurcation analysis*. Bifurcation analysis may be roughly divided into two different approaches.

In the first approach, although not specifically developed for determining the global stability threshold, *weakly nonlinear stability analysis* (Mielke, 2002) may be very useful to obtain information about the location of R_G . In weakly nonlinear stability analysis one usually traces nontrivial solutions in the vicinity of R_L by applying a power-series expansion in terms of $R - R_L$. This technique, however, is rather complicated and it is problem specific. Generically, at the point where the ground-state solution loses its stability to an infinitesimally small perturbation, three situations may occur:

- (i) The transcritical bifurcation (Figure 1.3(A)) for which at lowest order, prior to the threshold R_L , there coexist a stable branch and an unstable branch. The stable branch correspond to the ground-state solution and the unstable branch corresponds to a nontrivial solution. Beyond the threshold R_L , both branches ‘interchange’ stability, i.e. the stable branch becomes unstable and the unstable branch becomes stable. This case occurs for problems when no special symmetry is present, for example due to geometrical asymmetries. The system, however, can find another stable solution, but only at finite distance from the initial state and this new solution usually ‘appears’ through a fold or saddle-node bifurcation at some value R_F of the bifurcation parameter R . In principle, this bifurcated solution can be obtained by considering the perturbation expansion at higher orders.

- (ii) The supercritical case for which the new solutions appear beyond the critical point R_L and the system bifurcates continuously toward a stable state (Figure 1.3(B)).
- (iii) The subcritical case for which the new solutions already exist before the critical value is reached, see Figure 1.3(C).

The quantity A in Figure 1.3, which can, for example, be the amplitude of the most unstable eigenmode of the linear stability problem, can be obtained by an expansion at lowest non-trivial order. For the transcritical and subcritical case the global threshold R_G is then determined by the location of the fold bifurcation, i.e. by R_F . However, it should be emphasized that weakly nonlinear stability analysis is based on expansions in $R - R_L$ and therefore its validity is limited to Rayleigh numbers close to the threshold R_L . This may imply that the location of the fold bifurcation lies outside the validity range and can therefore not be determined by this method.

A second and more general method to approximate R_G is to derive amplitude equations, also called Landau equations, by using projection methods. This strategy does not involve expansions in terms of $R - R_L$ and hence it does not suffer from the problems encountered in weakly nonlinear stability analysis. A commonly used approach is to use a numerical Galerkin method for projection (Schuttelaars, 1998; Calvete et al., 1999, 2002). It allows a systematic calculation of finite-dimensional amplitude equations from the basic equations of the unknown fields in series of the *eigenfunctions* of the linear problem, i.e. the eigenfunctions of \mathcal{L}_R , followed by a projection of the equations on suitably defined testfunctions.

Both techniques for bifurcation analysis are called *locally* super/sub/transcritical to emphasize the fact that the search for a stable or unstable bifurcated solution is performed in the neighborhood of the ground state only. When there are no non-trivial solutions in the immediate vicinity of the ground state for values of the control parameter close enough to the linear threshold R_L , the search has to be performed in the full phase space. The system can be said *globally* subcritical as soon as an attractor coexists with the stable state; otherwise it is *globally* supercritical.

Implicit in expression (1.3.4) is the definition of a canonical scalar product that may serve us to determine the adjoint operator \mathcal{L}_R^\dagger of \mathcal{L}_R . In this way we can split \mathcal{L}_R in a symmetric and asymmetric part: $\mathcal{L}_R \equiv \mathcal{L}_R^s + \mathcal{L}_R^a$. When \mathcal{L}_R is *symmetric*, and hence *normal*, with respect to this scalar product, the linear instability threshold R_L and the energy stability threshold R_E coincide ($R_E \equiv R_L$) and, since $R_E \leq R_G$ and $R_G \leq R_L$, one has $R_G = R_L$ so that the (primary) bifurcation is globally supercritical (Henningson and Reddy, 1994). When \mathcal{L}_R is not normal for this scalar product, but the nonlinear term $\mathcal{N}_R(\mathbf{f})$ satisfies $\langle \mathcal{N}_R(\mathbf{f}), \mathbf{f} \rangle \leq 0$, Galdi and Padula (1990) showed that nonlinear stability analysis is reduced to the study of the spectrum of the *symmetric* part of the linear operator, i.e. \mathcal{L}_R^s .

To improve the threshold R_E , a modified method is needed (Galdi and Straughan, 1985). One method is to formulate a “generalized energy” by coupling different norms with suitable coupling parameters, see Straughan (2004). The idea is to optimize these coupling parameters to obtain a sharper stability bound R_E , and in some cases it even removes the stability gap, i.e. one obtains $R_E \equiv R_L$. Such energies are introduced on purely heuristic grounds but they give in general valuable information

about the stability of the system.

In some cases the concept of symmetrizable operators can be used. By this we mean that \mathcal{L}_R may be asymmetric with respect to some scalar product, but becomes symmetric if we replace the scalar product by a different one. A sufficient condition under which an operator \mathcal{L}_R is symmetrizable, is that there exists an invertible operator \mathcal{S} such that $\mathcal{S}^{-1}\mathcal{L}_R\mathcal{S}$ is symmetric. This procedure is called a *similarity transformation* and the resulting operator $\mathcal{S}^{-1}\mathcal{L}_R\mathcal{S}$ is called *similar* (to \mathcal{L}_R). An important property of such a similar operator is that its spectrum is a subset of the spectrum of \mathcal{L}_R , and, moreover, that it is symmetric (Lax, 1954; Istratescu, 1981). The new energy norm is then given by

$$\tilde{\mathcal{E}}(t) = \int_{\mathcal{C}} (\mathcal{S}^{-1}\mathbf{f})^\top (\mathbf{A}\mathcal{S}^{-1}\mathbf{f}) =: \langle \mathbf{f}, \mathbf{f} \rangle_{\mathcal{S}} . \quad (1.3.6)$$

Once we have identified such an operator \mathcal{S} , we can apply the above described theory as developed by Galdi and Straughan for the energy measured in the norm induced by $\langle \cdot, \cdot \rangle_{\mathcal{S}}$: due to the symmetry of the similar operator, the linear stability bound R_L coincides with the new nonlinear stability bound \tilde{R}_E provided that the nonlinear term satisfies $\langle \mathcal{N}_R(\mathbf{f}), \mathbf{f} \rangle_{\mathcal{S}} \leq 0$. In general, the nonlinear term $\mathcal{N}_R(\mathbf{f})$ is no longer dissipative for the new scalar product $\langle \cdot, \cdot \rangle_{\mathcal{S}}$ for *every* perturbation field $\mathbf{f} \in \mathbf{H}$. It may be well possible that the dissipativity condition still holds for a subclass of admissible perturbations $\tilde{\mathbf{H}} \subset \mathbf{H}$. On the other hand, for some cases it is possible to prove that the quantity $\tilde{\mathcal{E}}$ always decreases for *any* perturbation $\mathbf{f} \in \mathbf{H}$ provided it is initially sufficiently small (conditional stability), which is another way to express that the basic state is linearly stable (Joseph, 1976; Straughan, 2004). All these ‘generalized energy methods’ have in common, besides the difficulties in the physical interpretation of these measures, that the resulting energy stability threshold R_E critically depends on the class of admissible perturbations one considers. So in general we are still left with the inequalities $R_E \leq R_G \leq R_L$.

Up to now we have not paid much attention to the behaviour of $\mathcal{E}(t)$ in the region $[R_E, R_G]$. In some cases the eigenfunctions of the linearized operator \mathcal{L}_R are not orthogonal with respect to the L^2 scalar product. For instance see Chapter 2 when evaporation causes a first-order spatial derivative in the operator. Such operators are called *nonnormal* (Kato, 1976). Sometimes a different scalar product may give normality (orthogonal eigenfunctions). Clearly every nonnormal operator is asymmetric. Due to this non-orthogonality of the eigenfunctions, nonnormal operators exhibit particular transient behaviour which cannot be captured by linear stability analysis. It is well known that a linearly stable but nonnormal system may temporarily move far away from equilibrium before approaching it as $t \rightarrow \infty$ (Schmidt and Henningson, 2001). This implies that there can be considerable transient algebraic growth of the energy norm $\mathcal{E}(t)$, even when the system is linearly stable. This transient growth may be quite large: in Poiseuille flow at Reynolds number 5000, Butler and Farrell (1992) found disturbances that could grow in ‘energy’ by a factor of 4897, despite the fact that Poiseuille flow is linearly stable at this Reynolds number. The concept is that a group of eigenfunctions are nearly linearly dependent so that, in order to represent an arbitrary disturbance, it is then possible that the coefficients can be quite

large (Reddy and Henningson, 1993). All that can be said from this general, so far unspecific, standpoint is summarized in Figure 1.2.

The Ansatz that perturbations grow or decay exponentially in time is not valid when the ground state depends on time, i.e. $\mathbf{F}_0 = \mathbf{F}_0(\mathbf{z}, t)$. Therefore the method of linearised stability is not applicable in these cases. In abstract terms, linearization gives the *non-autonomous* problem

$$\mathcal{M}_R \frac{d\mathbf{f}}{dt} = \mathcal{L}_R(t)\mathbf{f} + \mathcal{N}_R(t, \mathbf{f}). \quad (1.3.7)$$

However if the growth rate of the ground state is small compared to the growth of the perturbations, time t can be used as a parameter in the system. For this case it is said that the frozen profile hypothesis holds. However, in most cases this hypothesis does not hold uniformly in time, e.g. for small times it is violated whereas for asymptotically large times it is a very good approximation.

An alternative approach to analyse the stability of the solution of (1.3.7), is to use Galerkin projections, resulting in a non-autonomous system of linear ODEs. For the special case that $\mathbf{F}_0(\cdot, t) = \mathbf{F}_0(\cdot, t + \tau_0)$, thus when \mathbf{F}_0 is periodic with period τ_0 , one can analyse stability of this system by means of classical Floquet theory (Cesari, 1963). For the non-periodic case, one would have to introduce an appropriate (in)stability criterion that has to be tested for *any* possible initial condition. However, Caltagirone (1980) showed that there is no universal method for determining such a criterion because the initial condition crucially determines the large time behaviour.

Basically, the only viable method for analysing the stability of time-dependent ground states is the energy method. For periodic ground states, Homsy (1974) proposed a method to explicitly incorporate this time-periodicity in the energy method. His approach is based on the fact that some specific flow problems (e.g. Chhuon and Caltagirone (1979), Caltagirone (1976) among many others) have periodic ground states which for the first half of the period represent a potentially unstable situation, and for the second half of the period they correspond to an unconditionally stable situation. Homsy (1974) showed that the stable half period may *stabilize* the unstable half period in such a way that the system as a whole is more stable than one would find by examining the unstable half period only. Hence this concept may result in an improved energy stability bound. Homsy's idea is from a conceptual point of view straightforward but to obtain the desired stability threshold is technically very complicated since one has to solve two optimization problems.

1.4 Overview and main results of this thesis

This thesis is devoted to the study of the stability properties of flow problems (P1), (P2), and (P3) with respect to their ground state solutions by using the techniques from Section 1.3. In particular, we investigate ground states that correspond to equilibrium solutions (problems (P1) and (P3)), and we consider ground states that depend on time as well. With respect to these time-dependent problems we consider both non-periodic (problem (P1)) and periodic ground states (problem (P2)).

The thesis is split in two parts. In Part I (Chapters 2, 3, and 4) we focus on the stability of (P1), and in Part II (Chapters 5 and 6) we treat problems (P2) and (P3)

separately.

Downward migration of salt near the surface of a salt lake: Chapters 2 (Pieters et al., 2004), 3 (van Duijn et al., 2002; Pieters and van Duijn, 2004), and 4 (Pieters and Schuttelaars, 2004). We formulate a stability problem involving a porous medium of infinite thickness ($H = \infty$) which is saturated with saline water flowing vertically upwards through a horizontal surface. The upflowing water is assumed to evaporate completely at the surface. Salt saturation is established quickly and is sustained there, with excess salt precipitated on the surface. Below the surface, a saline boundary layer grows by diffusion in the counter direction to the upflow. If this layer remains stable under gravity, an equilibrium state is reached where the salinity (or density) profile is exponential, decreasing downwards towards the ambient upflow value.

We start in Chapter 2 by introducing a ground-state solution $S_0(z, t)$ for problem (P1) that describes the above mentioned growing boundary layer and derive the nonlinear perturbation equation (NP). For the analysis of the *linearized* perturbation equation (LP), we need some special properties of the ground state solution. We apply a Fourier transform to the linearized perturbation equation to obtain a one-dimensional initial-boundary value problem in which the Fourier wavenumber a appears as a parameter. For initial conditions belonging to a particular class, we prove existence and uniqueness of solutions of (LP) by using a fixed-point argument.

In Chapter 3 we determine the stability thresholds. We start in Section 3.1 with the analysis of the spectrum of (LP). Since (LP) is not self-adjoint with respect to $L^2(\Omega)$, we cannot directly make use of variational techniques to obtain information about its spectrum. Things are even more complicated since we consider the linearized problem on a semi-infinite domain. We show that the spectrum consists of a finite number of discrete eigenvalues corresponding to a discrete point spectrum, and that there are solutions that correspond to an uncountable point spectrum. Numerical computations, however, show that this part of the spectrum is important in the linear stability analysis. In addition, using a variational principle for the largest eigenvalue we prove exchange of stability: for each wavenumber $a > 0$ we have $R(a) \leq R_L(a)$ if and only if $\sigma_{\max} = \sigma_{\max}(R, a) := \max_i \{\sigma_i\} \leq 0$, where $R_L(a)$ is determined by solving for R the equation $\sigma_{\max}(R, a) = 0$. In this way we obtain the linear stability threshold

$$R_L^* := \min_{a>0} R_L(a) = R_L(a^*) \cong 14.35 \quad \text{with } a^* \cong 0.759. \quad (1.4.1)$$

In Section 3.2 we use the energy method to obtain energy stability thresholds. In applying the energy method we follow two approaches in which the functional is based on the standard L^2 -norm. In the first approach one incorporates an integral constraint in the space of admissible perturbations, which is based on continuity and the integrated Darcy equation. The Euler–Lagrange equations with boundary conditions can be combined into a second order eigenvalue problem with time as a parameter. We demonstrate in Section 3.2.1 that at equilibrium, when the boundary layer has reached its large time profile, this eigenvalue problem can be solved in terms of Bessel functions yielding

$$R_{E_1}^* \cong 5.7832 \quad (1.4.2)$$

as a value of the Rayleigh number below which the system is definitely stable. This stability bound corresponds to the square of the first root of the Bessel function J_0 .

In a second approach, outlined in Subsection 3.2.2, we use the same functional, but we replace the integral constraint with an exact differential relation which is now based on continuity and the ‘pointwise’ Darcy equation. This yields a sixth order eigenvalue problem which we solve numerically by a modified Chebyshev–Galerkin method. With the given boundary conditions we find at equilibrium approximately

$$R_{E_2}^* := \min_{a>0} R_{E_2}(a) = R_{E_2}(a^*) \cong 8.59, \quad \text{with } a^* \cong 0.339, \quad (1.4.3)$$

as the largest Rayleigh number below which the system is definitely stable.

Given the physical parameters of the system a value for the Rayleigh number Ra results. This value may fall within one of three ranges: definitely stable for $Ra \leq R_{E_2}^*$, definitely unstable for $Ra > R_L^*$, and possibly unstable to disturbances of finite amplitude (leading to subcritical instabilities) when $R_{E_2}^* < Ra \leq R_L^*$.

Section 3.2.2 also explains the stability analysis for the growing boundary layer. Here time t appears as a parameter. In the early stages of development, the layer is sufficiently thin to be stabilised by the given boundary conditions. However, the monotonic increase in layer thickness with time will be accompanied by decreasing stability of the system as the influence of the boundary diminishes. The stability curves are obtained with the energy method based on the differential constraint and where the equilibrium boundary layer $\tilde{S}_0(z)$ is replaced by the growing boundary layer $S_0(z, t)$. For a given and fixed time $t > 0$, let $R_E(t)$ denote the minimum of the corresponding stability curve. Further, let $R_L(t)$ denote the minimum of the stability curve at time t obtained by the method of linearised stability with the frozen profile approximation. We now have the following refinement with respect to the equilibrium case. If $Ra \leq R_E(\infty) = R_{E_2}^*$, the layer will attain a stable equilibrium profile. If, however, $Ra > R_{E_2}^*$ we can determine a time t_E^* , corresponding to $Ra = R_{E_2}(t_E^*)$, and conclude the stability of the growing boundary layer for $t < t_E^*$. In particular, we show analytically that for all Ra there exists such a t_E^* , which implies that the system is always initially stable (with respect to the energy method). On the other hand, if $Ra > R_L^*$ we can nominate an elapsed time t_L^* corresponding to $Ra = R_L(t_L^*)$ and conclude the instability of the layer for $t > t_L^*$.

For the equilibrium boundary layer, the improved energy stability threshold $R_{E_2}^*$ does not coincide with the linear instability threshold R_L^* . This implies that the transition to convection may be subcritically. To obtain more information about the behaviour of the system for $R_{E_2}^* < Ra < R_L^*$, we modify in Subsection 3.2.3 the L^2 -norm. The new functional is now given by a *weighted* norm, where the weight is induced by the similarity transformations as discussed in Section 3.1. The introduction of a weight in the energy norm usually imposes some additional constraints in the space of admissible perturbations. We show for the equilibrium case necessary and sufficient conditions for stability with respect to the *weighted* energy functional and for perturbations in the restricted space of perturbations. An important conclusion is that subcritical convective solutions can never be in this restricted space of perturbations, and this is numerically shown in Chapter 4. Further, we also apply the weighted energy method to the growing boundary layer and show that the subcritical

regions are smaller compared to the ‘standard’ energy method.

The weight in the scalar product changes the ‘geometric’ structure of the eigenfunctions of problem (LP). In Section 3.3 we show that the use of a weight in the scalar product orthogonalize the eigenfunctions and this implies monotonic decay of the weighted norm. However, without this weight the eigenfunctions are not perpendicular and the L^2 -norm may exhibit transient growth in time, even when all eigenvalues of problem (LP) are in the left stable halfplane. We show that this is indeed the case by analysing the *symmetric* part of problem (LP). The eigenfunctions of this problem specify initial conditions for (LP) that initiate transient growth.

In Section 3.4 we present conclusions and discuss experimental Hele–Shaw results (Wooding et al. (1997a,b)) in terms of our theoretical findings. Theory and experiment show excellent agreement.

The shape, i.e. number of ‘salt-fingers’, of growing instabilities depends substantially upon the perturbations present during the initial stable period. This is investigated numerically in Chapter 4, where we use Finite Element simulations to validate the theoretical stability thresholds from Chapter 3. For a given set of initial perturbations, we do a time-integration of the discretized full model. We evaluate for every time step a functional $\mathcal{U}(t)$ that is based on the velocity perturbation. This global measure is then used to determine different solutions. If the initial perturbations are sufficient close to the patterns we are expected to see, we observe nontrivial convective solutions in the theoretically predicted range. As to be expected, the functional $\mathcal{U}(t)$ does not completely reveal the nonlinear dynamics of the problem. In particular, it only detects the *stable* convective solutions but it does not give information about the unstable ones. Hence, a detailed bifurcation analysis (in which one also incorporates the unstable solutions), is virtually impossible with this approach. In addition, the numerical simulations are from a computational point of view quite expensive.

Therefore we derive in Section 4.2 a lower-dimensional Landau type amplitude equation that functions as an approximation of the fully nonlinear model. In Section 4.3 we use this reduced model for bifurcation analysis. It is first validated in Subsection 4.3.1 by means of the Finite Element simulations. A careful comparison shows excellent agreement. We perform a detailed bifurcation analysis for two different patterns with respect to the horizontal plane: perturbations that correspond to stripes/rolls, and perturbations that correspond to hexagonal patterns. For the stripe/roll patterns we show that the primary bifurcation is a subcritical pitchfork. For hexagonal patterns, however, this transition is transcritical. Further, for both the roll/stripe and hexagonal patterns, bifurcation analysis reveals the existence of Hopf bifurcations. To conclude, we find from the bifurcation diagrams an upperbound for the global stability threshold:

$$R_G < 13.22 . \quad (1.4.4)$$

Solute transport in wetland ecosystems: Chapter 5 (Rappoldt et al., 2003). Transport of nutrients, CO₂, methane and oxygen plays an important ecological role at the surface of wetland ecosystems. A possibly important transport mechanism in a

water-saturated peat moss layer (usually *Sphagnum cuspidatum*) is nocturnal buoyancy flow: the downward flow of relatively cold surface water and the upward flow of warm water induced by nocturnal cooling. In Section 5.2 we show that buoyancy flow occurs in an impulsively cooled porous layer of semi-infinite extent if the system's Rayleigh number (Ra) exceeds 7. For a block-wave surface temperature, this critical Rayleigh number is given by 18 and for a harmonic wave it is given by 25. Further, it is shown numerically that the critical Rayleigh number increases with decreasing layer thickness. For a temperature difference of 10 K between day and night a typical Ra -value for a peat moss layer is 80, which leads to quickly developing buoyancy cells (see Appendix 5.A). Numerical simulation in Section 5.3 demonstrated that the fluid flow leads to a considerable mixing of the water. Temperature measurements in a cylindrical peat sample of 50 cm height and 35 cm diameter were in agreement with the theoretical results, see Section 5.4. The nocturnal flow and the associated mixing of the water represent a mechanism for solute transport in water-saturated parts of peat land and in other types of terrestrializing vegetation. This mechanism may be particularly important in continental wetlands where Ra -values in summer are often much larger than the threshold for fluid flow.

Steady infiltration in unsaturated soils: Chapter 6 (van Duijn et al., 2004). The stability of steady, vertically upward and downward flow of water in a homogeneous layer of soil is analyzed in Chapter 6. In Section 6.1 three equivalent dimensionless forms of the Richards equation are introduced, namely the pressure head, saturation, and matric flux potential forms. To illustrate general results and derive special results, use is made of several representative classes of soils. For all classes of soils with a Lipschitz continuous relationship between the hydraulic conductivity and the matric flux potential, steady flows are shown to be unique (Subsection 6.2.1). In addition, linear stability of these steady flows is proved in Section 6.3 and, in a setting as proposed by Y. Yortsos, in Appendix 6.A. To this end, use is made of the energy method, in which one considers (weighted) L^2 -norms of the perturbations of the steady flows. This gives a general restriction of the dependence of the hydraulic conductivity upon the matric flux potential, yielding linear stability and exponential decay with time of a specific weighted L^2 -norm. In Sections 6.4 and 6.6 it is shown that for other norms the ultimate decay towards the steady-solution is preceded by transient growth. An extension of the Richards equation to take into account dynamic memory effects is also considered (Section 6.5). It is shown that the stability condition for the standard Richards equation implies linear stability of the steady solution of the extended model.

A modified spectral Chebyshev–Galerkin method (Appendix A). In several parts in above mentioned chapters we complement the analytical results with numerical computations. For this purpose we make use of a modified Chebyshev–Galerkin method. The modification of the standard Chebyshev–Galerkin method is basically a combination of ideas posed by Heinrichs (1989, 1991) and Shen (1995), see also Pop (1995), and implies that the discretization matrices have excellent properties for numerical computations. In the appendix we explicitly give the coefficients of these matrices since they can be computed by hand. Spectral methods also require less discretization points and hence the method is very fast and accurate for solving the

initial-boundary-value and eigenvalue problems in Chapters 3. Further, the obtained eigenfunctions are used for the model reduction in Chapter 4.

References

- Bear, J.: 1972, *Dynamics of Fluids in Porous Media*. New York: Elsevier.
- Brandt, A. and H. J. S. Fernando: 1996, *Double-Diffusive Convection*, Vol. 94 of *Geophysical Monograph*. American Geophysical Union.
- Butler, K. M. and B. F. Farrell: 1992, 'Three dimensional optimal perturbations in viscous shear flows'. *Phys. Fluids A* **5**, 1390–1393.
- Caltagirone, J. P.: 1976, 'Stabilité d'une couche poreuse horizontale soumise à des conditions aux limites périodiques'. *Int. J. Heat Mass Transfer* **19**, 815–220.
- Caltagirone, J.-P.: 1980, 'Stability of a saturated porous media layer subject to a sudden rise in surface temperature: comparison between the linear and energy methods'. *Quart. J. Mech. Appl. Math.* **33**, 47–58.
- Calvete, D., H. E. de Swart, and A. Falqués: 2002, 'Effect of depth-dependent wave stirring on the final amplitude of shoreface-connected sand ridges'. *Cont. Shelf Res.* **22**, 2763–2776.
- Calvete, D., A. Falqués, H. E. de Swart, and N. Dodd: 1999, 'Nonlinear modelling of shoreface-connected sand ridges'. In: N. C. Kraus and W. G. McDougal (eds.): *Proceedings Coastal Sediments*, Vol. 2. Reston (VI), ASCE.
- Cesari, L.: 1963, *Asymptotic Behavior and Stability Problems in Ordinary Differential Equations*. Berlin: Springer-Verlag.
- Chhuon, B. and J. P. Caltagirone: 1979, 'Stability of a horizontal porous layer with timewise periodic boundary conditions'. *ASME Journal of Heat Transfer* **101**, 244–248.
- Dauchot, O. and P. Manneville: 1997, 'Local versus global concepts in hydrodynamic stability theory'. *J. Phys. II France* **7**, 371–389.
- Galdi, G. P. and M. Padula: 1990, 'A new approach to energy theory in the stability of fluid motion'. *Arch. Ration. Mech. Anal.* **110**(3), 187–286.
- Galdi, G. P. and B. Straughan: 1985, 'Exchange of stabilities, symmetry, and nonlinear stability'. *Arch. Rat. Mech. Anal.* **89**, 211–228.
- Gilman, A. and J. Bear: 1996, 'The influence of free convection on soil salinization in arid regions'. *Transport in Porous Media* **24**, 275–301.
- Heinrichs, W.: 1989, 'Improved condition number for spectral methods'. *Math. Comput.* **53**, 103–119.
- Heinrichs, W.: 1991, 'Stabilization techniques for spectral methods'. *J. Sci. Comp.* **6**, 1–19.
- Henningson, D. S. and S. C. Reddy: 1994, 'A note on measures of disturbance size in spatially evolving flows'. *Phys. Fluids* **6**, 2862–2864.
- Homsy, G. M.: 1974, 'Global stability of time-dependent flows. Part 2: Modulated fluid layers'. *J. Fluid Mech.* **62**, 387–403.
- Homsy, G. M. and A. E. Sherwood: 1975, 'Convective instabilities in porous media with throughflow'. Technical Report UCRL-76539, Lawrence Livermore Laboratory.

- Horton, C. W. and F. T. Rogers: 1945, 'Convection currents in a porous medium'. *J. Appl. Phys.* **16**, 367.
- Ingram, H. A. P.: 1978, 'Soil layers in mires: Function and terminology'. *J. Soil Science* **29**, 224–227.
- Ingram, H. A. P., D. W. Rycroft, and D. J. A. Williams: 1974, 'Anomalous transmission of water through certain peats'. *J. Hydrol.* **22**, 213–218.
- Istratescu, V.: 1981, *Introduction to Linear Operators*. New York: Marcel–Dekker.
- Joseph, D. D.: 1976, *Stability of Fluid Motions I,II*. Berlin: Springer–Verlag.
- Kato, T.: 1976, *Perturbation Theory for Linear Operators*. New York: Springer–Verlag.
- Lapwood, E. R.: 1948, 'Convection of a fluid in a porous medium'. *Proc. Cambridge Phil. Soc.* **44**, 508–521.
- Lax, P.: 1954, 'Symmetrizable linear transformations'. *Comm. Pure and Applied Math.* **7**, 633–647.
- Matthews, E. and I. Fung: 1987, 'Methane emission from natural wetlands: Global distribution, area, and environmental characteristics of sources'. *Glob. Biogeochem. Cycles* **1**, 61–86.
- Mielke, A.: 2002, 'The Ginzburg–Landau equation in its role as a modulation equation'. In: B. Fiedler (ed.): *Handbook for Dynamical Systems*. Holland: Elsevier, pp. 759–834.
- Nield, D. A. and A. Bejan: 1992, *Convection in Porous Media*. New York: Springer–Verlag, 2nd edition.
- Pieters, G. J. M., I. S. Pop, and C. J. van Duijn: 2004, 'On the existence and uniqueness of a coupled system arising in the linear stability analysis of gravity-driven flow in porous media'. To appear.
- Pieters, G. J. M. and H. M. Schuttelaars: 2004, 'Bifurcation analysis for the steady boundary layer formed by throughflow near the surface of a porous medium'. To appear.
- Pieters, G. J. M. and C. J. van Duijn: 2004, 'Transient growth in linearly stable gravity-driven flow in porous media'. To appear.
- Pop, I. S.: 1995, 'Numerical Approximation of Differential Equations by Spectral Methods'. Technical report, "Babes-Bolyai" University, Cluj-Napoca. (in romanian).
- Rappoldt, C., G. J. M. Pieters, E. Adema, G. J. Baaijens, and C. J. van Duijn: 2003, 'Buoyancy-driven flow in a peat moss layer as a mechanism for solute transport'. *Proc. Natl. Acad. Sci. USA* **100**, 14937–14942.
- Reddy, S. C. and D. S. Henningson: 1993, 'Energy growth in viscous channel flows'. *J. Fluid Mech.* **252**, 209–238.
- Richards, L. A.: 1931, 'Capillary conduction of liquids through porous mediums'. *Physics* **1**, 318–333.
- Schmidt, P. J. and D. S. Henningson: 2001, *Stability and Transition in Shear Flows*. Berlin: Springer.
- Schoofs, S.: 1999, 'Thermochemical Convection in Porous Media: An Application to Hydrothermal Systems and Magmatic Intrusions'. Ph.D. thesis, University of Utrecht.
- Schuttelaars, H. M.: 1998, 'Nonlinear long term equilibrium profiles in a short tidal embayment'. In: J. Donkers and M. B. A. M. Scheffers (eds.): *Physics of Estuaries*

- and Coastal Seas*. Rotterdam: Balkema.
- Shen, J.: 1995, 'Efficient spectral-Galerkin method II. Direct solvers of second and fourth order equations by using Chebyshev polynomials'. *SIAM J. Sci. Comput.* **16**, 74–87.
- Simmons, C. T., T. R. Fenstemaker, and J. M. Sharp Jr.: 2001, 'Variable-density groundwater flow and solute transport in heterogeneous porous media: Approaches, resolutions and future challenges'. *J. Contam. Hydrol.* **52**, 245–275.
- Simmons, C. T. and K. A. Narayan: 1997, 'Mixed convection processes below a saline disposal basin'. *J. Hydrol.* **194**, 263–285.
- Straughan, B.: 2004, *The Energy Method, Stability and Nonlinear Convection*, Vol. 91 of *Applied Mathematical Sciences*. New York: Springer-Verlag, 2nd edition.
- van Duijn, C. J., G. J. M. Pieters, and P. A. C. Raats: 2004, 'Steady flows in unsaturated soils are stable'. *Transport in Porous Media* **57**, 215–244.
- van Duijn, C. J., G. J. M. Pieters, R. A. Wooding, and A. van der Ploeg: 2002, 'Stability criteria for the vertical boundary layer formed by throughflow near the surface of a porous medium'. In: P. A. C. Raats, D. Smiles, and A. W. Warrick (eds.): *Environmental Mechanics - Water, Mass and Energy Transfer in the Biosphere*, Vol. 129 of *Geophysical Monographs*. American Geophysical Union, pp. 155–169.
- Williams, W. D.: 2002, 'Environmental threats to salt lakes and the likely status of inland saline ecosystems in 2025'. *Environmental Conservation* **29**(2), 154–167.
- Wooding, R. A.: 1960, 'Rayleigh instability of a thermal boundary layer in flow through a porous medium'. *J. Fluid Mech.* **9**, 183–192.
- Wooding, R. A., S. W. Tyler, and I. White: 1997a, 'Convection in groundwater below an evaporating salt lake: 1. Onset of instability'. *Water Resour. Res.* **33**, 1199–1217.
- Wooding, R. A., S. W. Tyler, I. White, and P. A. Anderson: 1997b, 'Convection in groundwater below an evaporating salt lake: 2. Evolution of fingers or plumes'. *Water Resour. Res.* **33**(6), 1219–1228.

PART I

MATHEMATICAL ASPECTS

Chapter 2

Qualitative properties of the perturbation[★] equation

This chapter is entirely devoted to the derivation and analysis of the perturbation equations. For the derivation of the perturbation equation we need to define a ground state solution. Setting $f \equiv 0$ in (P1)₄ gives a solution involving a one-dimensional saturation profile and uniform upflow. It is called the ground station solution, describing a growing boundary layer near the outflow surface of the domain.

We perturb the ground state solution to study its stability. Under certain assumptions on the perturbations, the resulting *linearized* perturbation equation is shown to depend on one spatial variable only (in z -direction) and on time t . We show existence and uniqueness of this equation by using a fixed point argument.

Throughout this chapter the flow domain is given by the halfspace $\Omega := \mathbb{R}^2 \times \mathbb{R}_+$.

2.1 The ground state solution and its properties

Starting from zero initial saturation, direct verification shows that the following triple (\mathbf{U}_0, S_0, P_0) satisfies problem (P1):

(i)

$$\mathbf{U}_0 := -\text{Ra}^{-1} \mathbf{e}_z \quad \text{in } \Omega .$$

(ii) $S_0 = S_0(z, t)$ is the unique bounded solution of

$$\left\{ \begin{array}{l} \frac{\partial S}{\partial t} = \frac{\partial^2 S}{\partial z^2} + \frac{\partial S}{\partial z} \quad \text{in } Q := \mathbb{R}_+ \times \mathbb{R}_+ , \end{array} \right. \quad (2.1.1a)$$

$$\left\{ \begin{array}{l} S = 1 , \quad z = 0, t > 0 , \end{array} \right. \quad (2.1.1b)$$

$$\left\{ \begin{array}{l} S = 0 , \quad z > 0, t = 0 . \end{array} \right. \quad (2.1.1c)$$

[★] This chapter is joint work with I.S. Pop (Eindhoven University of Technology) and parts of it will appear as a paper in *Zeitschrift für Angewandte Mathematik und Physik (ZAMP)*.

(iii) P_0 is determined (up to a constant) by integrating Darcy's law (P1)₃.

This triple is called the ground state solution. It describes uniform upflow, with a growing salt boundary layer near $z=0$. Observe that the initial condition (2.1.1c) is not compatible with boundary condition (2.1.1b). The solution of (2.1.1) is given by (van Duijn et al., 2001)

$$S_0 = S_0(z, t) = \frac{1}{2}e^{-z} \operatorname{erfc} \left[\frac{z-t}{2\sqrt{t}} \right] + \frac{1}{2} \operatorname{erfc} \left[\frac{z+t}{2\sqrt{t}} \right], \quad \text{in } Q. \quad (2.1.2a)$$

The equilibrium boundary layer for this case, which arises as $t \rightarrow \infty$, is given by a decaying exponential, i.e.

$$\bar{S}_0 = \bar{S}_0(z) = e^{-z}, \quad \text{for } z > 0. \quad (2.1.2b)$$

Below we introduce the half strip $Q_T := \mathbb{R}_+ \times (0, T]$, where $T > 0$ is arbitrary chosen. Without using the explicit form (2.1.2a) we prove

Lemma 2.1. (i) $0 < S_0(z, t) < F(z/\sqrt{t})$ for $(z, t) \in Q$, where F is the similarity solution satisfying $\frac{1}{2}\eta F' + F'' = 0$ for $0 < \eta < \infty$, with $F(0) = 1$ and $F(\infty) = 0$;

(ii) $S_0 \in H^1(Q_T)$.

This lemma will be used in several parts of this chapter.

Proof. The first assertion is a direct consequence of the fact that $\partial_z S_0 < 0$ and $\partial_t S_0 > 0$ in Q . It immediately implies

$$\int_{Q_T} S_0^2 \leq \sqrt{T} \int_{\mathbb{R}_+} F^2 d\eta.$$

Multiplying (2.1.1a) by $1 - S_0$ gives

$$\partial_t (S_0 - \frac{1}{2}S_0^2) = \partial_z ((1 - S_0)\partial_z S_0) + (\partial_z S_0)^2 + \partial_z (S_0 - \frac{1}{2}S_0^2).$$

Integrating this expression over Q_T gives

$$\int_{Q_T} (\partial_z S_0)^2 = \frac{1}{2}T + \int_{\mathbb{R}_+} (S_0 - \frac{1}{2}S_0^2) dz \leq \frac{1}{2}T + \sqrt{T} \int_{\mathbb{R}_+} (F - \frac{1}{2}F^2) d\eta.$$

■

Remark 2.2. In this thesis we only consider the initial condition $S_0(z, 0) = 0$ for $z > 0$. However, other initial conditions are possible provided that they belong to $L^2(\mathbb{R}_+) \cap L^\infty(\mathbb{R}_+)$ and that they decay sufficiently fast as $z \rightarrow \infty$. For instance, one could take $S_0(z, 0) = 1 - H(z - \zeta)$ for $z > 0$, with $\zeta \in (0, \infty)$ being fixed and H denoting the Heaviside function. Again, the corresponding solution can be determined explicitly and is given by

$$S_0^\zeta(z, t) = \frac{1}{2}e^{-z} \operatorname{erfc} \left[\frac{\zeta + z - t}{2\sqrt{t}} \right] - \frac{1}{2} \operatorname{erfc} \left[\frac{\zeta - z - t}{2\sqrt{t}} \right] + 1, \quad \text{in } Q.$$

2.2 The perturbation equations

For the purpose of the stability analysis we perturb the ground state and write the solution of (P1) as

$$S = S_0 + s, \quad \mathbf{U} = \mathbf{U}_0 + \mathbf{u} \quad \text{and} \quad P = P_0 + p, \quad (2.2.1)$$

with $\mathbf{u} = (u, v, w)$, and where S, \mathbf{U} and P satisfy (P1). We require that the perturbations vanish at both the inflow and outflow boundary:

$$s = \mathbf{u} = 0 \quad \text{at } z = 0, \infty, \quad (2.2.2)$$

expressing that $\{S, \mathbf{U}\}$ and $\{S_0, \mathbf{U}_0\}$ both satisfy (P1)₄ and behave similarly at large depth.

Substituting (2.2.1) into equations (P1)_{1,2,3} and writing R instead of Ra , yields the system (in Ω and for all $t > 0$)

$$\text{(NP)} \left\{ \begin{array}{l} \frac{\partial s}{\partial t} - \frac{\partial s}{\partial z} + R w \frac{\partial S_0}{\partial z} + R \mathbf{u} \cdot \nabla s = \Delta s. \quad (2.2.3a) \\ \nabla \cdot \mathbf{u} = 0, \quad (2.2.3b) \\ \mathbf{u} + \nabla p - s \mathbf{e}_z = \mathbf{0}, \quad (2.2.3c) \end{array} \right.$$

As in Lapwood (1948) we note that equations (2.2.3b) and (2.2.3c) can be combined to give for s and w the linear relation

$$\Delta w = \Delta_{\perp} s \quad \text{in } \Omega, \quad (2.2.4)$$

where Δ_{\perp} denotes the horizontal Laplacian $\partial_{xx} + \partial_{yy}$. This relation plays a crucial role in various parts of this thesis.

For infinitesimally small perturbations one can disregard the higher order terms in (2.2.3a) and considers the approximate *linear* problem (in Ω and for all $t > 0$)

$$\text{(LP)} \left\{ \begin{array}{l} \frac{\partial s}{\partial t} = \Delta s + \frac{\partial s}{\partial z} - R w \frac{\partial S_0}{\partial z}, \quad (2.2.5a) \\ \Delta w = \Delta_{\perp} s. \quad (2.2.5b) \end{array} \right.$$

2.3 The linearised perturbation equation: existence, uniqueness and regularity

Based on experimental observations, we assume that perturbations are periodic in the horizontal (x, y) -plane, i.e. $\{s, w\}(x, y, z, t) = \{s, w\}(z, t) e^{i(a_x x + a_y y)}$. This is consistent with the fact that the coefficients in (2.2.5a,b) do not depend on x and

y. Substitution into the perturbation equations (2.2.5) yields the one-dimensional problem

$$(P) \begin{cases} \frac{\partial s}{\partial t} = \frac{\partial^2 s}{\partial z^2} + \frac{\partial s}{\partial z} - a^2 s - R \frac{\partial S_0}{\partial z} w & \text{in } Q, & (2.3.1a) \\ -\frac{\partial^2 w}{\partial z^2} + a^2 w = a^2 s & \text{in } \mathbb{R}_+, \text{ for each } t > 0, & (2.3.1b) \\ s = w = 0 & z = 0, t > 0, & (2.3.1c) \\ s = f & z > 0, t = 0. & (2.3.1d) \end{cases}$$

We fix $t > 0$ and consider the subproblem

$$-\frac{\partial^2 w}{\partial z^2} + a^2 w = a^2 s, \quad w(0) = 0, \quad \text{in } L^2(\mathbb{R}_+). \quad (2.3.2)$$

For the solution w of problem (2.3.2) we have the following *a priori* estimates:

Lemma 2.3. *Let $s \in L^2(\mathbb{R}_+)$ and let w be a solution of (2.3.2). Then $w \in \text{BUC}([0, \infty))$, $w \rightarrow 0$ as $z \rightarrow \infty$ and we have the estimates*

$$\begin{aligned} \|w\|_2 &\leq \|s\|_2, \\ \|\partial_z w\|_2 &\leq \frac{1}{2}a \|s\|_2, \\ \|w\|_\infty &\leq \frac{1}{2}\sqrt{2} \|w\|_{H^1} \leq \sqrt{\frac{1}{2}(1 + \frac{1}{4}a^2)} \|s\|_2. \end{aligned}$$

The proof is based on the application of the Cauchy–Schwarz inequality and on a result from Burenkov (1998, Theorem 4, p. 138). To obtain an explicit form for the solution $w(z)$ we introduce

Definition 2.4. *For $a > 0$ we define the Green's function*

$$G_w(z, \zeta) = \begin{cases} \frac{a(e^{-az} - e^{a(\zeta-z)})}{e^{-a\zeta} - 2} & \text{for } z < \zeta, \\ \frac{a(e^{-a\zeta} - e^{a(z-\zeta)})}{e^{-a\zeta} - 2} & \text{for } \zeta < z. \end{cases} \quad (2.3.3)$$

Following ideas of Métivier (2004) we find

Proposition 2.5. *For $a > 0$ and $s \in L^2(\mathbb{R}_+)$ equation (2.3.2) has a unique solution $w \in H^2(\mathbb{R}_+)$ given by*

$$w(z) = a^2 \int_{\mathbb{R}_+} G_w(z, \zeta) s(\zeta) d\zeta. \quad (2.3.4)$$

2.3. The linearised perturbation equation: existence, uniqueness and regularity 31

Proof. Since $-\partial_{zz}w = a^2(s-w)$ we find via Lemma 2.3 that $\|\partial_{zz}w\|_2 = a^2\|s-w\|_2 \leq 2a^2\|s\|_2$. Thus $w \in H^2(\mathbb{R}_+)$. ■

With the integral solution (2.3.4) we associate the linear operator $B : L^2(\mathbb{R}_+) \mapsto H^2(\mathbb{R}_+)$ by setting $w = Bs$. Then B has the following properties:

Lemma 2.6. *The integral operator B is bounded in $L^2(\mathbb{R}_+)$ and in $BUC(\mathbb{R}_+)$.*

Proof. Boundedness in $L^2(\mathbb{R}_+)$ is straightforward. To demonstrate boundedness in $BUC(\mathbb{R}_+)$ we show that $\|w\|_\infty \leq \|s\|_\infty$. For this purpose we consider the weak formulation of (2.3.2):

$$\int_{\mathbb{R}_+} \frac{\partial w}{\partial z} \frac{\partial \varphi}{\partial z} + a^2 \int_{\mathbb{R}_+} w \varphi = a^2 \int_{\mathbb{R}_+} s \varphi, \quad (2.3.5)$$

for all $\varphi \in H_0^1(\mathbb{R}_+)$. Let $M_s := \|s\|_\infty$. Subtracting $a^2 \int_{\mathbb{R}_+} M_s \varphi$ from both sides of equation (2.3.5) and testing with $\varphi = [w - M_s]_+$ gives

$$\begin{aligned} 0 &\leq \int_{\{w-M_s>0\}} (\partial_z(w - M_s))^2 + a^2 \int_{\{w-M_s>0\}} (w - M_s)^2 = \\ &= a^2 \int_{\mathbb{R}_+} (s - M_s)[w - M_s]_+ \leq 0. \end{aligned}$$

This implies that $[w - M_s]_+ = 0$ almost everywhere in \mathbb{R}_+ . Since $w \in BUC(\mathbb{R}_+)$ we find $w \leq M_s$. In a similar way we get $w \geq -M_s$ in \mathbb{R}_+ giving $\|B\|_\infty \leq 1$. ■

Now we turn our attention back to problem (P), which we solve in Q_T for any $T > 0$, and prove existence and uniqueness by a contraction argument. For this purpose we take $T > 0$ arbitrary and split problem (P) into two parts. Note that (2.3.1b) involves spatial derivatives only, so time can be seen here as parameter. With $v \in L^\infty(0, T; L^2(\mathbb{R}_+)) \cap L^\infty(Q_T)$ and for arbitrary $0 < t < T$, we first solve

$$(P_w) \begin{cases} -\frac{\partial^2 w}{\partial z^2} + a^2 w = a^2 v & \text{in } \mathbb{R}_+, \\ w = 0 & z = 0. \end{cases} \quad (2.3.6a)$$

$$(2.3.6b)$$

where $v = v(t)$. Its solution $w = w(t)$ is then used in problem

$$(P_u) \begin{cases} \frac{\partial u}{\partial t} - \frac{\partial^2 u}{\partial z^2} - \frac{\partial u}{\partial z} + a^2 u = -R \frac{\partial S_0}{\partial z} w & \text{in } Q_T, \\ u = 0 & z = 0, 0 < t < T, \\ u = f & z > 0, t = 0. \end{cases} \quad (2.3.6c)$$

$$(2.3.6d)$$

$$(2.3.6e)$$

In (2.3.6c) we replace w by $B(v)$. We construct an *integral* solution $u = \mathcal{F}(v)$, with $u = u_1 + u_2$, where u_1 solves

$$(P_{u_1}) \begin{cases} \frac{\partial u}{\partial t} - \frac{\partial^2 u}{\partial z^2} - \frac{\partial u}{\partial z} + a^2 u = 0 & \text{in } Q_T, \\ u = 0 & z = 0, 0 < t < T, \\ u = f & z > 0, t = 0, \end{cases}$$

and where u_2 solves

$$(P_{u_2}) \begin{cases} \frac{\partial u}{\partial t} - \frac{\partial^2 u}{\partial z^2} - \frac{\partial u}{\partial z} + a^2 u = -R \frac{\partial S_0}{\partial z} B(v) =: \Phi_v & \text{in } Q_T, \\ u = 0 & z = 0, 0 < t < T, \\ u = 0 & z > 0, t = 0. \end{cases}$$

Lemma 2.7. For $v \in L^\infty(0, T; L^2(\mathbb{R}_+))$ we have $\Phi_v \in L^2(Q_T)$.

Proof. By Lemma 2.3, $B(v)$ is essentially bounded in Q_T . Further, by Lemma 2.1, we have $\partial_z S_0 \in L^2(Q_T)$, thus the product of these two functions is in $L^2(Q_T)$. ■

The solutions of problems (P_{u_1}) and (P_{u_2}) are given by integral solutions, i.e. they can be written in the form (Polyanin, 2002)

$$u_1(z, t) = e^{-a^2 t} \int_{\mathbb{R}_+} G_u(z, \zeta, t) f(\zeta) d\zeta, \quad (2.3.7)$$

$$u_2(z, t) = e^{-a^2 t} \int_0^t \int_{\mathbb{R}_+} G_u(z, \zeta, t - \tau) \Phi_v(\zeta, \tau) d\zeta d\tau, \quad (2.3.8)$$

where the Green's function $G_u(z, \zeta, \tau)$ is given by

$$G_u(z, \zeta, \tau) = \frac{1}{2\sqrt{\pi\tau}} e^{\frac{1}{2}(\zeta-z) + (a^2 - \frac{1}{4})\tau} \left\{ e^{-(z-\zeta)^2/4\tau} - e^{-(z+\zeta)^2/4\tau} \right\}.$$

Integral representations (2.3.7) and (2.3.8) define the operator \mathcal{F} :

$$\mathcal{F}(v) := e^{-a^2 t} \left\{ \int_{\mathbb{R}_+} G_u(z, \zeta, t) f(\zeta) d\zeta + \int_0^t \int_{\mathbb{R}_+} G_u(z, \zeta, t - \tau) \Phi_v(\zeta, \tau) d\zeta d\tau \right\}. \quad (2.3.9)$$

Since $\Phi_v \in L^2(Q_T)$, the integral solution $u = \mathcal{F}(v)$ defines a weak solution of Problem (2.3.6c) with $\partial_t u, \partial_{zz} u \in L^2(Q_T)$. To show that problem (P) has a unique solution we prove

Lemma 2.8. For given $a > 0$, $R > 0$ and $f \in L^2(\mathbb{R}_+) \cap L^\infty(\mathbb{R}_+)$, let $\delta = \frac{1}{3R^2}$ and $M_0 := \sqrt{2} \|f\|_2$. Further, define the closed and convex set

$$K_0 := \left\{ v \in L^\infty(0, \delta; L^2(\mathbb{R}_+)) : \sup_{0 \leq t \leq \delta} \|v(t)\|_2 \leq M_0 \right\}. \quad (2.3.10)$$

Then \mathcal{T} is a contraction in K_0 .

Proof. We first prove that the operator \mathcal{T} maps K_0 into itself. Since $u = \mathcal{T}(v)$ solves (P_u) with $w = B(v)$ we test the equation by u and obtain for $0 \leq t \leq \delta$ the estimate

$$\begin{aligned} \|u\|_2^2 - \|f\|_2^2 + 2 \int_0^t \|\partial_z u\|_2^2 + 2a^2 \int_0^t \|u\|_2^2 &= -2R \int_0^t \int_{\mathbb{R}_+} \frac{\partial S_0}{\partial z} B(v)u \leq \\ &\leq 2R \int_0^t \left(\|\partial_z(B(v))\|_2 \|u\|_2 + \|B(v)\|_2 \|\partial_z u\|_2 \right) dt \leq \\ &\leq a^2 \int_0^t \|u\|_2^2 + \frac{R^2}{a^2} \int_0^t \|\partial_z(B(v))\|_2 + \int_0^t \|\partial_z u\|_2^2 + R^2 \int_0^t \|B(v)\|_2^2 \leq \\ &\leq a^2 \int_0^t \|u\|_2^2 + \int_0^t \|\partial_z u\|_2^2 + \frac{3}{2} R^2 \int_0^t \|v\|_2^2. \end{aligned} \quad (2.3.11)$$

Inequality (2.3.11), Definition (2.3.10) and Lemma 2.3 imply

$$\|u(t)\|_2^2 \leq \frac{3}{2} R^2 t M_0^2 + \|f\|_2^2 \leq \frac{3}{2} R^2 \delta M_0^2 + \|f\|_2^2 \quad \text{for all } t \in [0, \delta], \quad (2.3.12)$$

and hence $\sup_{0 \leq t \leq \delta} \|u(t)\|_2 \leq M_0$ implying $u \in K_0$ for $t \in [0, \delta]$.

We continue to show that \mathcal{T} is a contraction in K_0 . For this we take $v_1, v_2 \in K_0$. This gives $u_1 := \mathcal{T}(v_1)$ and $u_2 := \mathcal{T}(v_2)$. Further, let $u = u_1 - u_2$ and $v = v_1 - v_2$. Then u satisfies (P_u) with zero initial data. Following the same procedure as in (2.3.11), (2.3.12) we obtain for all $t \in [0, \delta]$

$$\|u(t)\|_2^2 \leq \frac{3}{2} R^2 \int_0^\delta \|v\|_2^2 \leq \frac{3}{2} R^2 \delta \sup_{0 \leq t \leq \delta} \|v(t)\|_2^2 = \frac{1}{2} \sup_{0 \leq t \leq \delta} \|v(t)\|_2^2,$$

implying $\sup_{0 \leq t \leq \delta} \|\mathcal{T}(v)(t)\|_2^2 \leq \frac{1}{2} \sup_{0 \leq t \leq \delta} \|v(t)\|_2^2$ and hence \mathcal{T} is a contraction in K_0 . \blacksquare

By the Banach fixed point theorem (Zeidler, 1995) there exists a unique $v^* \in K_0$ such that $u := \mathcal{T}(v^*) = v^*$. This is an integral and by standard arguments a weak solution of (P) for $t \in [0, \delta]$. The next step is to extend the solution to the interval $\delta \leq t \leq 2\delta$. To do so we first notice that $u \in H^1(0, \delta; H^{-1}(\mathbb{R}_+)) \cap L^2(0, \delta; H^1(\mathbb{R}_+))$ and thus $u \in C([0, \delta]; L^2(\mathbb{R}_+))$ (Renardy and Rogers, 1993, Lemma 10.4). Hence we can use $u(\delta)$ as initial data in (P_u) for $\delta \leq t \leq 2\delta$. With K_1 defined by

$$K_1 := \left\{ v \in L^\infty(\delta, 2\delta; L^2(\mathbb{R}_+)) : \sup_{\delta \leq t \leq 2\delta} \|v(t)\|_2 \leq \sqrt{2} M_0 \right\},$$

we repeat the above argument to extend the solution to $\delta \leq t \leq 2\delta$, and similarly to arbitrary but finite times. In this way we obtained a unique solution for (P). This is defined in a weak sense. In fact, the solution is classical for any positive t , as we can see from below.

Let $\mu > 0$. Then $u \in C(0, T; L^2(\mathbb{R}_+))$. However, since $S_0(z, t) \in C^\infty(\mathbb{R}_+ \times [\mu, T])$, $\partial_z S_0$ bounded, and $u \in L^\infty(0, T; L^2(\mathbb{R}_+))$ we immediately find $B(u) \in L^\infty(0, T; H^2(\mathbb{R}_+))$. Thus in (P_{u_2}) we have $\Phi_v \in L^\infty([\mu, T]; H^2(\mathbb{R}_+))$. Using a bootstrap argument in combination with the integral representation (2.3.9) we finally obtain $u \in C^\infty([\mu, T] \times \mathbb{R}_+)$.

Thus we have shown

Theorem 2.9. *Problem (P) has a unique solution which is C^∞ for any positive time.*

References

- Burenkov, V. I.: 1998, *Sobolev Spaces on Domains*. Leipzig: B. G. Teubner.
- Lapwood, E. R.: 1948, 'Convection of a fluid in a porous medium'. *Proc. Cambridge Phil. Soc.* **44**, 508–521.
- Métivier, G.: 2004, *Small Viscosity and Boundary Layer Methods, Theory, Stability Analysis, and Applications*. Boston: Birkhäuser.
- Polyanin, A. D.: 2002, *Handbook of Linear Partial Differential Equations for Engineers and Scientists*. Boca Raton: Chapman & Hall / CRC.
- Renardy, M. and R. C. Rogers: 1993, *An Introduction to Partial Differential Equations*. New York: Springer-Verlag.
- van Duijn, C. J., R. A. Wooding, and A. van der Ploeg: 2001, 'Stability criteria for the boundary layer formed by throughflow at a horizontal surface of a porous medium: Extensive version'. Technical Report RANA 01-05, Eindhoven University of Technology.
- Zeidler, E.: 1995, *Applied Functional Analysis*, No. 108, 109 in Applied Mathematical Sciences. New York: Springer-Verlag.

Chapter 3

Stability thresholds for the vertical boundary* layer

Central issue in this chapter is to quantify the boundary layer stability or its gravitational instability in terms of the system parameters. First results in this direction are given by several authors. Wooding (1960) treated the case of a constant-pressure (ponded) boundary by linearised stability theory. Jones and Persichetti (1986) applied linear analysis to a permeable layer with all combinations of boundary condition and throughflow direction. Approximate stability criteria by variational means are obtained by Nield (1987). Gilman and Bear (1996) treated the linearised stability of a horizontal unsaturated layer (vadoze zone) overlying a shallow water table. Wooding et al. (1997a,b) discussed saturated groundwater movement with dry or ponded conditions at the surface, and used both experimental and numerical methods to simulate the unstable behaviour of a boundary layer growing from an initial salinity discontinuity at the surface, and including the margin, of a dry salt lake.

In this chapter we summarize these results and make some important extensions with respect to the stability thresholds. Two paths are followed to analyse stability: the method of linearised stability and the energy method. We consider the equilibrium and the growing boundary layer separately. We start with the equilibrium case; the growing boundary layer case is discussed in Subsection 3.2.3.

The method of linearised stability (Section 3.1) incorporates an analysis of the spectrum of the linearised perturbation equation. We first show that the linear operator defined by the linear part of the perturbation equation can be symmetrized by means of a similarity transformation. From the obtained symmetric operator we prove some properties of the spectrum and derive a stability threshold expressed in the system parameters. For certain problems on a semi-infinite domain, however, like the Blasius boundary layer (Grosch and Salwen, 1978; Salwen and Grosch, 1981), one can show that there is a finite number of discrete eigenvalues corresponding to a discrete point spectrum and that there are solutions that correspond to an uncountable

* Some parts of this chapter have appeared in *Environmental Mechanics - Water, Mass and Energy Transfer in the Biosphere* (van Duijn et al., 2002) and other parts will appear as a paper in *European Journal of Mechanics B/Fluids*.

point spectrum. The latter is sometimes referred to as the continuum. In this section we consider a saline boundary layer in a semi-infinite domain for which both spectra occur. In this respect it is clear that one can only determine a finite number of discrete eigenvalues and corresponding eigenfunctions.

The energy method (Section 3.2) requires constraints on saturation and velocity perturbations. The usual constraint is based on the *integrated* Darcy equation. We give a complete analytical treatment of this case and show that the corresponding stability threshold equals the square of the first root of the Bessel function J_0 (Subsection 3.2.1). This explains previous numerical investigations by Homsy and Sherwood (1975, 1976). We also present two alternative energy methods using the *pointwise* Darcy equation as constraint: one using the standard energy functional based on the L^2 -norm, and one using a spatial weighting function in the energy functional. This first alternative energy method yields a substantially higher stability threshold.

The energy stability thresholds, however, do not coincide with the linear stability threshold, i.e. there exists a – so-called – subcritical region in parameter space. The existence of such region implies that instabilities of finite amplitude are possible at Rayleigh numbers below the critical value derived using linear theory (Davis, 1971; Straughan, 2004). One of the first observations regarding the occurrence of these gaps was given by Davis (1969a,b, 1971), and, independently and in a different context, by Homsy and Sherwood (1975, 1976) and later by Galdi and Straughan (1985). These authors showed that one of the essential connections between linear and nonlinear theory is the idea of symmetry of the linear operator. Under certain conditions for the nonlinear term in the perturbation equation, Galdi and Straughan (1985) showed that nonlinear stability analysis reduces to the study of the spectrum of the symmetric part of the linearized perturbation equation. The presence of throughflow results in a first-order term in the stability equation implying that the linear operator is asymmetric. Hence its spectrum does not coincide with the spectrum of the symmetric part the linear operator, and this results in a stability gap. Hence, when the linear part of the perturbation equation is symmetric, both methods give similar stability thresholds.

To quantify this gap and to understand the behaviour of the physical system in this subcritical region, a modified energy method is needed (Galdi and Padula, 1990). This is the main topic of Subsection 3.2.3. We introduce a weighted energy norm such that the asymmetric linear operator becomes symmetric with respect to the underlying weighted inner product. We show that the spatial weighting function in the energy norm is directly induced by the similarity transformation in Section 3.1. The introduction of a weight in an energy norm basically restricts the space of admissible perturbations. Using the theory of Galdi and Straughan (1985), we prove necessary and sufficient stability conditions for perturbations from the restricted space of admissible perturbations.

For system parameter values in the subcritical region, we also show that there exist initial perturbations for which the linearly stable system exhibits transient growth of the ‘classical’ L^2 energy norm (Section 3.3). It is well known that linearly stable but nonnormal (and thus asymmetric) systems may temporarily move far away (with respect to the L^2 -norm) from equilibrium before approaching it as $t \rightarrow \infty$ (Schmidt and Henningson, 2001). The concept is that a group of eigenfunctions are nearly linearly dependent (due to the nonnormality of the linear operator) so that, in order

to represent an arbitrary disturbance, it is possible that the coefficients can be quite large. This mechanism is taken a step further by Reddy and Henningson (1993) in order to determine the *optimal* initial condition that produces the largest relative energy growth for a certain time period. Their variational optimization method relies on the fact that every initial perturbation can be decomposed by a sum of eigenfunctions, i.e. the eigenfunctions form a complete set. Such a construction is not possible for problems on semi-infinite domains (Criminale et al., 2003). However, it is still possible to find initial perturbations that *initiate* transient growth, but they are, of course, not optimal. These special perturbations can be determined by analysing the *numerical range* (Kato, 1976) of the linear perturbation operator. The numerical range is the largest eigenvalue of the symmetric part of the linear perturbation operator and this eigenvalue is equal to half of the initial slope of the energy norm (Farrell and Ioannou, 1996). Hence, the numerical range is closely related to the energy method. This understanding has led to general analysis of nonnormal systems that has since been used extensively to understand transient growth in deformation and shear flows. For further references see, for example, Schmidt and Henningson (2001), and Criminale et al. (2003). To conclude this chapter, we present in Section 3.4 experimental Hele–Shaw results (Wooding et al., 1997a,b) in terms of our theoretical findings. Theory and experiment show excellent agreement.

3.1 Linear stability analysis and properties of the spectrum

Our starting point for this section is the linearised perturbation equations (2.3.1). We first consider the stationary ground state, i.e. $S_0 = \bar{S}_0 = e^{-z}$. The growing boundary layer case will be discussed in Section 3.2.3. Thus we consider the problem

$$\left\{ \begin{array}{l} \frac{\partial s}{\partial t} = \frac{\partial^2 s}{\partial z^2} + \frac{\partial s}{\partial z} - a^2 s + a^2 R e^{-z} B(s) =: Ls \quad \text{in } \mathbb{R}_+ \times \mathbb{R}_+, \quad (3.1.1a) \\ -\frac{\partial^2 w}{\partial z^2} + a^2 w = a^2 s \quad \text{in } \mathbb{R}_+ \times \mathbb{R}_+, \quad (3.1.1b) \\ s = w = 0 \quad z = 0, t > 0, \quad (3.1.1c) \\ s = f \quad z > 0, t = 0. \quad (3.1.1d) \end{array} \right.$$

To investigate the spectrum of L , we fix $a > 0$ and $R > 0$ and seek for solutions of the problem

$$Ls = D^2 s + Ds - a^2 s + R e^{-z} B(s) = \sigma s, \quad s(0) = 0, \quad \text{in } L^2(\mathbb{R}_+), \quad (3.1.2)$$

where D denotes differentiation with respect to z . To our knowledge, no explicit solution of eigenvalue problem (3.1.2) is known. However, it can be treated by a semi-analytical technique based on a Frobenius expansion in terms of descending exponentials (Wooding, 1960). Here we solve it numerically by means of a modified Chebyshev–Galerkin method, see Appendix A for details. Let the numerical approximations of the eigenvalues $\{\sigma_i = \sigma_i(a, R)\}$ of L be ordered by

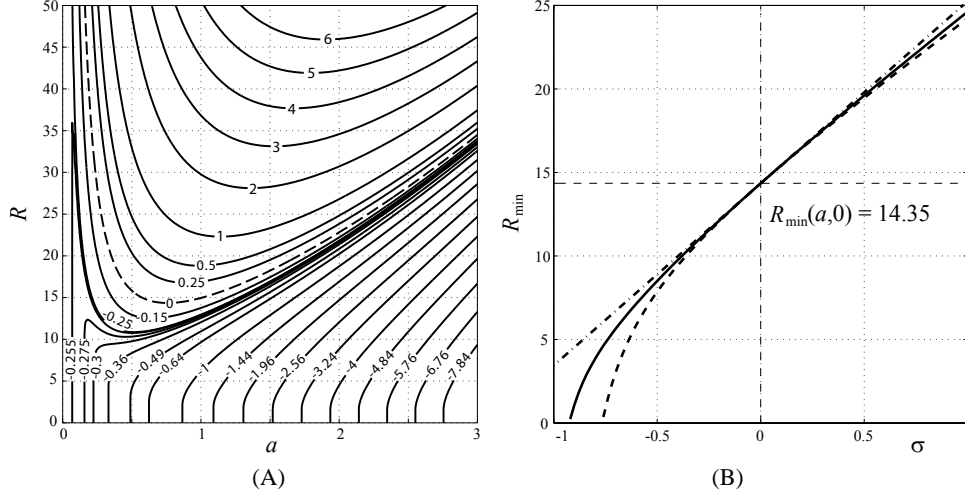


Figure 3.1. (A) Isocurves of the largest eigenvalue σ_{\max} of operator L . The dashed curve $\sigma_{\max} \equiv 0$ corresponds to the neutral stability curve $R_L(a)$ (see text for its definition). (B) Upperbound $c\sigma$ and lower bound $\sigma f(\sigma)$ for $R_{\min}(a, \sigma)$ for $a=0.759$ (cf. Theorem 3.1).

$\dots < \text{Re}(\sigma_n) < \dots < \text{Re}(\sigma_2) < \text{Re}(\sigma_1) =: \sigma_{\max}$. For a and R in relevant ranges, σ_{\max} is plotted in Figure 3.1 as isocurves. Numerical computations show that all approximate discrete eigenvalues $\{\sigma_i\}$ are real. In fact, as will be shown later, we expect the eigenvalues to be real, thus $\sigma_{\max} = \sigma_1$. Observe that the isocurves become vertical as $R \searrow 0$ indicating that $\sigma_{\max} = \sigma_{\max}(a)$. Indeed, by setting $R = 0$ in operator L , problem (3.1.2) can be solved explicitly to obtain $\sigma_{\max} = -\frac{1}{4} - a^2$.

The dashed isocurve in Figure 3.1 is usually referred to as the neutral stability curve. It is often found by solving the rewritten eigenvalue problem

$$\mathcal{L}_\sigma s := D^2 s + Ds - (a^2 + \sigma)s = -\text{Re}e^{-z} B(s) =: R\mathcal{B}s, \quad (3.1.3)$$

with $s(0) = 0$ and $s \in L^2(\mathbb{R}_+)$. In other words, the role of R and σ as eigenvalues can be interchanged. Suppose again that the set of approximate eigenvalues $\{R_i = R_i(a, \sigma)\}$ of problem (3.1.3) are ordered by $R_{\min} := R_1 < R_2 < \dots < R_n < \dots$. Then the neutral stability curve is then defined by $R_L(a) := R_{\min}(a, 0)$. The curve $R_L(a)$, $a > 0$ is depicted in Figure 3.2 as curve number 3. In the same figure point values of the Frobenius approximation $R_L^F(a)$ have been plotted as crosses, showing excellent agreement with curve 3.

In the sequel of this section we investigate the behaviour of $R_{\min}(a, \sigma)$ near $\sigma = 0$. Figure 3.1 suggests that for fixed $a > 0$, at least for σ sufficiently close to zero, we have $\sigma \geq 0$ if and only if $R \geq R_{\min}(a, \sigma = 0) = R_L(a)$. This property is crucial in linearised stability theory and its interpretation is that the conductive ground state exchanges stability with a convective flow regime. In general, exchange of instability is easy to prove when the linear operator L is symmetric with respect to $L^2(\mathbb{R}_+)$ (Galdi and Straughan, 1985). However, the operator L (and \mathcal{L}_σ) is asymmetric in

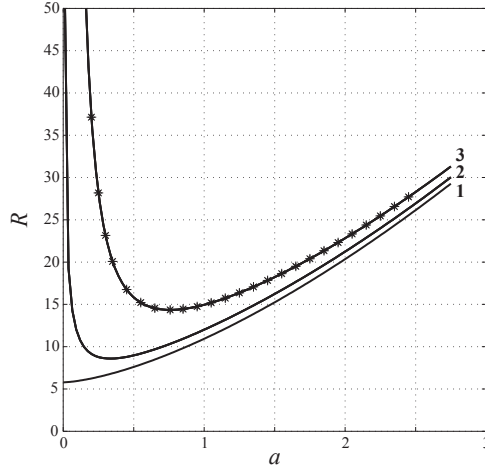


Figure 3.2. Comparison of estimates involving lowest eigenvalue R_{\min} versus wavenumber a for the equilibrium boundary layer. Curve 1: Energy method using integral constraint. Curve 2: Energy method using differential constraint. Curve 3: Linearised stability method using a Chebyshev–Galerkin (solid curve) and Frobenius expansion (crossed points).

$L^2(\mathbb{R}_+)$ due to the occurrence of the first order derivative. Therefore, to show the stability exchange, a direct analysis of L is not straightforward.

We follow a different approach in which we will make use of similarity transformations. Two operators \mathcal{A} and \mathcal{B} are called *similar* (Kato, 1976) if there exists an invertible operator \mathcal{M} such that $\mathcal{A} = \mathcal{M}\mathcal{B}\mathcal{M}^{-1}$. Let the operator \mathcal{B} act on $L^2(\mathbb{R}_+)$ and consider the problem $\mathcal{A}f = \mathcal{M}\mathcal{B}\mathcal{M}^{-1}f =: \mathcal{M}\mathcal{B}g$. Since g is in $L^2(\mathbb{R}_+)$, we must have $\mathcal{M}^{-1}f \in L^2(\mathbb{R}_+)$ as well. Hence operator \mathcal{A} acts on the space $\{f : \mathcal{M}^{-1}f \in L^2(\mathbb{R}_+)\} \subset L^2(\mathbb{R}_+)$. Without loss of generality we may assume that operator \mathcal{M}^{-1} is such that it restricts to the space $L^2(\mathbb{R}_+)$. In this particular case it is easy to show that $\Sigma(\mathcal{B}) \equiv \Sigma(\mathcal{A})$. However, when operator \mathcal{A} acts on the larger space $L^2(\mathbb{R}_+)$, then the spectra of \mathcal{A} and \mathcal{B} are related by the inclusion $\Sigma(\mathcal{B}) \subseteq \Sigma(\mathcal{A})$ (Lax, 1954). Here the spectrum Σ of the (closed) linear operator \mathcal{A} is given by the set of complex numbers λ for which $\mathcal{A} - \lambda I$ has no inverse.

We will show that operator L is similar to an operator L_1 which is symmetric with respect to the inner product defined on $L^2(\mathbb{R}_+)$. In particular, $\Sigma(L_1) \subseteq \Sigma(L)$ and L_1 has discrete and real eigenvalues. Hence it suffices here to analyse the (discrete) spectrum of the similar operator L_1 .

Inspired by Reddy and Trefethen (1994, Section 5), we define for $\alpha \in [0, 1]$ the functions $u(x, y, z, t)$ and the family of (multiplication) operators M_α by

$$s(x, y, z, t) = M_\alpha u(x, y, z, t) := e^{-\frac{1}{2}\alpha z} u(x, y, z, t). \quad (3.1.4)$$

This implies

$$\begin{aligned} Ls &= e^{-\frac{1}{2}\alpha z} [D^2 u + (1 - \alpha)Du + (\frac{1}{4}\alpha^2 - \frac{1}{2}\alpha - a^2)u + a^2 R e^{(\frac{1}{2}\alpha - 1)z} B(e^{-\frac{1}{2}\alpha z} u)] \\ &=: M_\alpha L_\alpha M_\alpha^{-1} s, \end{aligned} \quad (3.1.5)$$

where L_α is given by

$$L_\alpha = D^2 + (1 - \alpha)D + \left(\frac{1}{4}\alpha^2 - \frac{1}{2}\alpha - a^2\right) + a^2 R e^{\left(\frac{1}{2}\alpha - 1\right)z} B \left(e^{-\frac{1}{2}\alpha z} \cdot\right). \quad (3.1.6)$$

For $\alpha \equiv 0$, we regain the operator L in (3.1.1a) and for $\alpha = 1$ we obtain the symmetric eigenvalue problem (in $L^2(\mathbb{R}_+)$)

$$L_1 u = D^2 u - \left(\frac{1}{4} + a^2\right)u + a^2 R e^{-\frac{1}{2}z} B \left(e^{-\frac{1}{2}z} u\right) = \sigma u, \quad u(0) = 0. \quad (3.1.7)$$

With (3.1.6) in mind, we now consider the family of problems

$$\left\{ \begin{array}{l} \frac{\partial u}{\partial t} = D^2 u + (1 - \alpha)D u + \left(\frac{1}{4}\alpha^2 - \frac{1}{2}\alpha - a^2\right)u + \\ \quad + a^2 R e^{\left(\frac{1}{2}\alpha - 1\right)z} B \left(e^{-\frac{1}{2}\alpha z} u\right) =: L_\alpha u, \quad \text{in } \mathbb{R}_+, t > 0, \quad (3.1.8a) \\ -D^2 w + a^2 w = a^2 e^{-\frac{1}{2}\alpha z} u \quad \text{in } \mathbb{R}_+, t > 0, \quad (3.1.8b) \\ u = w = 0 \quad \text{on } \{z = 0\}, t > 0, \quad (3.1.8c) \\ u = e^{\frac{1}{2}\alpha z} f =: g \quad \text{in } \mathbb{R}_+, t = 0. \quad (3.1.8d) \end{array} \right.$$

Since operator L_1 is symmetric and since the spectrum of L_1 is contained in the spectrum of L , we are now in the position to prove exchange of instability quite easily by using L_1 instead of L . For this purpose we again rewrite the eigenvalue problem $L_1 u = \sigma u$ in the form

$$\mathcal{L}_\sigma u := D^2 u - \left(a^2 + \frac{1}{4} + \sigma\right)u = R \mathcal{B} u, \quad (3.1.9)$$

with $\mathcal{B} u := -e^{-\frac{1}{2}z} B \left(e^{-\frac{1}{2}z} u\right)$. We prove

Theorem 3.1. *Suppose that the smallest eigenvalue $R_{\min}(a, \sigma)$ of (3.1.9) depends smoothly on $a > 0$ and $\sigma \in \mathbb{R}$. Then there exist a constant $c > 0$ and a smooth function $f : \mathbb{R} \mapsto \mathbb{R}$, satisfying $f(0) = 0$, $f(\sigma) \geq 0$ if $\sigma \geq 0$ and $\sigma f(\sigma) \leq c\sigma$ for all $\sigma \in \mathbb{R}$, such that*

$$\sigma f(\sigma) \leq R_{\min}(a, \sigma) - R_L(a) \leq c\sigma. \quad (3.1.10)$$

Moreover, $f''(0) < 0$.

Proof. First observe that

$$\langle \mathcal{B} u, u \rangle = - \left\langle B \left(e^{-\frac{1}{2}z} u\right), e^{-\frac{1}{2}z} u \right\rangle = - \langle w, s \rangle$$

and $\langle w, s \rangle = a^{-2} \|Dw\|_2^2 + \|w\|_2^2 \geq 0$. Hence $\langle \mathcal{B} u, u \rangle \leq 0$. Further, $\mathcal{L}_\sigma = \mathcal{L}_0 - \sigma I$ where I denotes the identity operator. Since \mathcal{L}_σ and \mathcal{B} are self-adjoint, we have the following variational characterization of $R_{\min}(a, \sigma)$:

$$0 < R_{\min}(a, \sigma) = \inf_{0 \neq \bar{u} \in H_0^1(\mathbb{R}_+)} \frac{\langle \mathcal{L}_\sigma \bar{u}, \bar{u} \rangle}{\langle \mathcal{B} \bar{u}, \bar{u} \rangle} = \frac{\langle \mathcal{L}_\sigma u_\sigma, u_\sigma \rangle}{\langle \mathcal{B} u_\sigma, u_\sigma \rangle}. \quad (3.1.11)$$

In particular, for $\sigma = 0$ we have

$$\begin{aligned} 0 < R_{\min}(a, 0) &= \inf_{\bar{u} \in H_0^1(\mathbb{R}_+)} \frac{\langle \mathcal{L}_0 \bar{u}, \bar{u} \rangle}{\langle \mathcal{B} \bar{u}, \bar{u} \rangle} \leq \frac{\langle \mathcal{L}_0 u_\sigma, u_\sigma \rangle}{\langle \mathcal{B} u_\sigma, u_\sigma \rangle} = \\ &= \frac{\langle \mathcal{L}_\sigma u_\sigma, u_\sigma \rangle}{\langle \mathcal{B} u_\sigma, u_\sigma \rangle} + \sigma \frac{\langle u_\sigma, u_\sigma \rangle}{\langle \mathcal{B} u_\sigma, u_\sigma \rangle} = R_{\min}(a, \sigma) + \sigma \frac{\|u_\sigma\|_2^2}{\langle \mathcal{B} u_\sigma, u_\sigma \rangle}. \end{aligned}$$

This implies

$$R_{\min}(a, \sigma) - R_L(a) \geq \sigma \frac{\|u_\sigma\|_2^2}{-\langle \mathcal{B} u_\sigma, u_\sigma \rangle} =: \sigma f(\sigma). \quad (3.1.12)$$

In a similar way we find the upper bound

$$R_{\min}(a, \sigma) - R_L(a) \leq \sigma \frac{\|u_\sigma\|_2^2}{-\langle \mathcal{B} u_\sigma, u_\sigma \rangle} =: \sigma c. \quad (3.1.13)$$

The upper and lower bounds (3.1.12) and (3.1.13) imply $R_{\min}(a, \sigma) \geq R_L(a)$ for $\sigma \geq 0$, which proves (3.1.10).

Note that inequalities (3.1.12), (3.1.13) and since $\langle \mathcal{B} u_1, u_1 \rangle \leq 0$ also imply

$$0 < \frac{\|u_\sigma\|_2^2}{-\langle \mathcal{B} u_\sigma, u_\sigma \rangle} = \left. \frac{\partial R_{\min}(a, \sigma)}{\partial \sigma} \right|_{\sigma=0}, \quad (3.1.14)$$

Differentiating $\mathcal{L}_\sigma u_\sigma = R_{\min}(a, \sigma) \mathcal{B} u_\sigma$ with respect to σ and setting $v_\sigma = du_\sigma/d\sigma$ gives

$$\mathcal{L}_\sigma v_\sigma - u_\sigma = R_{\min}(a, \sigma) \mathcal{B} v_\sigma + \frac{\partial R_{\min}(a, \sigma)}{\partial \sigma} \mathcal{B} u_\sigma,$$

implying

$$\langle \mathcal{L}_\sigma v_\sigma - R_{\min}(a, \sigma) \mathcal{B} v_\sigma, v_\sigma \rangle - \langle u_\sigma, v_\sigma \rangle = \frac{\partial R_{\min}(a, \sigma)}{\partial \sigma} \langle \mathcal{B} u_\sigma, v_\sigma \rangle.$$

Since

$$\langle u_\sigma, v_\sigma \rangle = \frac{1}{2} \frac{d}{d\sigma} \|u_\sigma\|_2^2, \quad \langle \mathcal{B} u_\sigma, v_\sigma \rangle = \frac{1}{2} \frac{d}{d\sigma} \langle \mathcal{B} u_\sigma, u_\sigma \rangle,$$

$$\langle \mathcal{L}_\sigma v_\sigma - R_{\min}(a, \sigma) \mathcal{B} v_\sigma, v_\sigma \rangle < 0,$$

we find

$$\frac{d}{d\sigma} \|u_\sigma\|_2^2 < - \frac{\partial R_{\min}(a, \sigma)}{\partial \sigma} \frac{d}{d\sigma} \langle \mathcal{B} u_\sigma, u_\sigma \rangle. \quad (3.1.15)$$

Differentiating the function $f(\sigma)$ in (3.1.12), and using (3.1.14), (3.1.15) results in

$$-\langle \mathcal{B}u_o, u_o \rangle \frac{d}{d\sigma} \|u_\sigma\|_2^2 \Big|_{\sigma=0} + \|u_o\|_2^2 \frac{d}{d\sigma} \langle \mathcal{B}u_\sigma, u_\sigma \rangle \Big|_{\sigma=0} < 0 ,$$

which immediately implies $\frac{df}{d\sigma} \Big|_{\sigma=0} < 0$. Since $\frac{d^2}{d\sigma^2}(\sigma f(\sigma)) = 2 \frac{df}{d\sigma} + \sigma \frac{d^2 f}{d\sigma^2}$, we find

$$\frac{d^2 f}{d\sigma^2}(\sigma f(\sigma)) \Big|_{\sigma=0} < 0 ,$$

which proves the concavity of (3.1.12). Note that the upper bound (3.1.13) is a straight line through the point $(0, R_{\min}(a, 0))$. This proves the second assertion of the theorem. The upper and lower bounds for $R_{\min}(a, \sigma)$ for $a = 0.759$ are depicted in Figure 3.1(A). ■

Theorem 3.1 implies the following. Let the system Rayleigh number Ra be sufficiently close to $R_L(a)$. If $Ra > R_L(a)$, then there exists a $\sigma > 0$ such that $Ra = R_{\min}(a, \sigma)$. In other words, if $Ra > R_L(a)$, there exists a infinitesimal perturbation which implies that the boundary layer is unstable. If $Ra < R_L(a)$ no definite statement about stability can be made. Only certain infinitesimal perturbations now decay. Others, and in particular large perturbations, may still grow in time. From Figure 3.2 we find

$$R_L^* := \min_{a>0} R_L(a) = R_L(a^*) = 14.35 \quad \text{with} \quad a^* = 0.759 \quad (3.1.16)$$

approximately. These numbers, in good agreement with the numerical results of Homsy and Sherwood (1976), are characteristic of the linearised stability method.

3.2 Variational analysis: the energy method

For the energy method we reconsider the nonlinear problem

$$\left\{ \begin{array}{l} \frac{\partial s}{\partial t} = \Delta s + \frac{\partial s}{\partial z} - R \frac{\partial S_0}{\partial z} w - R \mathbf{u} \cdot \nabla s \quad \text{in } \mathbb{R}^2 \times \mathbb{R}_+, t > 0 , \end{array} \right. \quad (3.2.1a)$$

$$\left\{ \begin{array}{l} \nabla \cdot \mathbf{u} = 0 \quad \text{in } \mathbb{R}^2 \times \mathbb{R}_+, t > 0 , \end{array} \right. \quad (3.2.1b)$$

$$\left\{ \begin{array}{l} \mathbf{u} + \nabla p - s \mathbf{e}_z = \mathbf{0} \quad \text{in } \mathbb{R}^2 \times \mathbb{R}_+, t > 0 \end{array} \right. \quad (3.2.1c)$$

$$\left\{ \begin{array}{l} s = w = 0 \quad \text{on } \{z = 0\} \times \mathbb{R}_+, t > 0 , \end{array} \right. \quad (3.2.1d)$$

where $S_0 = S_0(z, t)$ denotes the ground state solution given by (2.1.2a). In the energy method one estimates the time derivative of the L^2 -norm of the saturation perturbation. In particular, the aim is to find the largest R -interval for which

$$\frac{d}{dt} \int_{\mathcal{C}} s^2(t) < 0 . \quad (3.2.2)$$

Here and in integrals below we disregard the infinitesimal volume elements in the notation. The related maximum R -value clearly will depend on the wavenumber a and, because $S_0 = S_0(z, t)$, on time t . Once (3.2.2) is established, it follows that the L^2 -norm of the velocity perturbation is bounded as well. This is a direct consequence of (3.2.1c) and (3.2.1b). Multiplying (3.2.1c) by \mathbf{u} , integrating the result over \mathcal{C} and using (3.2.1b) yields $\int_{\mathcal{C}} s w - \int_{\mathcal{C}} |\mathbf{u}|^2 = 0$. Using the inequality $s w \leq \frac{1}{2} s^2 + \frac{1}{2} w^2$ we find

$$\int_{\mathcal{C}} |\mathbf{u}|^2 \leq \frac{1}{2} \int_{\mathcal{C}} s^2 + \frac{1}{2} \int_{\mathcal{C}} w^2 \leq \frac{1}{2} \int_{\mathcal{C}} s^2 + \frac{1}{2} \int_{\mathcal{C}} |\mathbf{u}|^2$$

and hence

$$\int_{\mathcal{C}} |\mathbf{u}|^2 \leq \int_{\mathcal{C}} s^2 . \quad (3.2.3)$$

To investigate (3.2.2), we multiply (3.2.1a) by s and integrate over \mathcal{C} . Using (3.2.1b) we find the identity

$$\frac{1}{2} \frac{d}{dt} \int_{\mathcal{C}} s^2 = - \int_{\mathcal{C}} |\nabla s|^2 - R \int_{\mathcal{C}} s w \frac{\partial S_0}{\partial z} . \quad (3.2.4)$$

Thus if R is chosen such that the right-hand side of (3.2.4) is negative for all perturbations satisfying a given constraint, then stability is guaranteed.

It is our aim to investigate the consequences of two different constraints. In the first we consider perturbations satisfying (3.2.1b) and the integrated Darcy equation:

$$\nabla \cdot \mathbf{u} = 0 , \quad \int_{\mathcal{C}} |\mathbf{u}|^2 - \int_{\mathcal{C}} s w = 0 . \quad (3.2.5)$$

This approach is a modification of that used by Homay and Sherwood (1976). While they considered a stationary ground state only and solved the corresponding eigenvalue problem numerically, we are in the position to deal with time evolution of the ground state as well. However, we shall not pursue the time dependence for this constraint. Instead we give a complete analytical treatment of the case where the ground state is given by the equilibrium case: $\bar{S}_0(z) = e^{-z}$. This analysis explains quite elegantly some of the previously obtained numerical results.

In the second constraint, we consider perturbations satisfying the differential expression

$$\Delta w = \Delta_{\perp} s . \quad (3.2.6)$$

We shall treat the time dependent ground state and show that this differential constraint significantly improves the integral constraint (3.2.5), but the obtained stability threshold does not coincide with the linear stability threshold.

The energy stability threshold can be improved up to the linear stability threshold by further restricting the class of admissible perturbations. This can be done by using the similarity transformation as discussed in Section 3.1. In particular, we show that the similarity transformations M_{α} induce a *weighted* energy norm, and this in turn gives additional constraints for the class of admissible perturbations. As a result, we show that the stability threshold based on this weighted energy method coincides with the linear stability threshold.

3.2.1 Integral constraint

Identity (3.2.4) and constraints (3.2.5) lead to the maximum problem

$$\frac{1}{R} = \sup_{(s, \mathbf{u}) \in \mathbf{H}} \frac{-\int_{\mathcal{C}} \frac{\partial S_0}{\partial z} s w}{\int_{\mathcal{C}} |\nabla s|^2} \quad (3.2.7)$$

with

$$\mathbf{H} = \mathbf{H}_1 := \left\{ (s, \mathbf{u}) : x, y\text{-periodic with respect to } \mathcal{C}, s = \mathbf{u} = 0 \text{ at } z = 0, \infty, \right. \\ \left. \nabla \cdot \mathbf{u} = 0 \text{ and } \int_{\mathcal{C}} |\mathbf{u}|^2 = \int_{\mathcal{C}} s w \right\}.$$

The Euler–Lagrange equations follow from the first variation of the functional

$$J(s, \mathbf{u}) = \int_{\mathcal{C}} |\nabla s|^2 + R \int_{\mathcal{C}} \frac{\partial S_0}{\partial z} s w + \mu \int_{\mathcal{C}} (|\mathbf{u}|^2 - s w) + \int_{\mathcal{C}} \pi \nabla \cdot \mathbf{u},$$

where μ (constant in space) and π are Lagrange multipliers. As a result we find

$$\begin{cases} -2\Delta s + R \frac{\partial S_0}{\partial z} w - \mu w = 0, \\ 2\mu \mathbf{u} - \nabla \pi + R \frac{\partial S_0}{\partial z} s \mathbf{e}_z - \mu s \mathbf{e}_z = \mathbf{0}, \\ \nabla \cdot \mathbf{u} = 0 \quad \text{and} \quad \int_{\mathcal{C}} |\mathbf{u}|^2 = \int_{\mathcal{C}} s w, \end{cases}$$

where μ (constant in space) and π are Lagrange multipliers. Applying the scaling

$$\mathbf{u} := \frac{\lambda}{\sqrt{R}} \mathbf{u}, \quad \mu = \frac{R}{\lambda^2} \quad \text{and} \quad p = -\frac{1}{2} \frac{\lambda}{\sqrt{R}} \pi,$$

one finds

$$\begin{cases} \frac{\sqrt{R}}{2} \left(\frac{1}{\lambda} - \lambda \frac{\partial S_0}{\partial z} \right) w + \Delta s = 0, & (3.2.8a) \\ \frac{\sqrt{R}}{2} \left(\frac{1}{\lambda} - \lambda \frac{\partial S_0}{\partial z} \right) s \mathbf{e}_z - \mathbf{u} - \nabla p = \mathbf{0}, & (3.2.8b) \\ \nabla \cdot \mathbf{u} = 0, & (3.2.8c) \\ \int_{\mathcal{C}} |\mathbf{u}|^2 = \frac{\sqrt{R}}{\lambda} \int_{\mathcal{C}} s w. & (3.2.8d) \end{cases}$$

These equations were also found by Homsy & Sherwood with a slightly different interpretation of the parameter λ . Note that (3.2.8b) has a structure similar to Darcy's law.

As before, (3.2.8b) and (3.2.8c) can be combined to give

$$\Delta w = \frac{\sqrt{R}}{2} \left(\frac{1}{\lambda} - \lambda \frac{\partial S_0}{\partial z} \right) \Delta_{\perp} s . \quad (3.2.9)$$

Further, multiplying (3.2.8b) by \mathbf{u} , integrating the result over \mathcal{C} , and using (3.2.8d) yields the useful identity

$$\lambda^2 = \frac{\int_{\mathcal{C}} s w}{-\int_{\mathcal{C}} \frac{\partial S_0}{\partial z} s w} . \quad (3.2.10)$$

Finally, multiplying (3.2.8a) by s , integrating the result over \mathcal{C} , and using (3.2.10) gives

$$\int_{\mathcal{C}} |\nabla s|^2 = \frac{\sqrt{R}}{\lambda} \int_{\mathcal{C}} s w . \quad (3.2.11)$$

Next we introduce the periodicity. Setting $s := a s$, with a given by (1.2.16), we find from (3.2.8a) and (3.2.9) the equations (with D signifying d/dz)

$$(D^2 - a^2) s + \frac{a\sqrt{R}}{2} \left(\frac{1}{\lambda} - \lambda \frac{\partial S_0}{\partial z} \right) w = 0 , \quad (3.2.12)$$

$$(D^2 - a^2) w + \frac{a\sqrt{R}}{2} \left(\frac{1}{\lambda} - \lambda \frac{\partial S_0}{\partial z} \right) s = 0 , \quad (3.2.13)$$

for $0 < z < \infty$. Note that in these equations t appears as a parameter through the ground state. We seek non-trivial solutions subject to the homogeneous conditions (2.2.2) and the constraint (3.2.10).

As a first observation we note that (3.2.12), (3.2.13) and the boundary conditions imply $s = w$. Hence we are left with the second order boundary value problem (for $0 < z < \infty$)

$$\begin{cases} (D^2 - a^2) s + \frac{a\sqrt{R}}{2} \left(\frac{1}{\lambda} - \lambda \frac{\partial S_0}{\partial z} \right) s = 0 , & (3.2.14a) \\ s(0) = s(\infty) = 0 , & (3.2.14b) \end{cases}$$

subject to the constraint (replacing w by s in (3.2.10))

$$\lambda^2 = \frac{\int_0^{\infty} s^2}{-\int_0^{\infty} \frac{\partial S_0}{\partial z} s^2} . \quad (3.2.15)$$

Identity (3.2.11) is rewritten as

$$\int_0^\infty (Ds)^2 = \left(\frac{a\sqrt{R}}{\lambda} - a^2 \right) \int_0^\infty s^2. \quad (3.2.16)$$

This expression and equation (3.2.14a), using $\partial S_0/\partial z \rightarrow 0$ as $z \rightarrow \infty$, imply that nontrivial solutions only exist in the parameter range

$$1 < \frac{\sqrt{R}}{a\lambda} < 2.$$

So far we have not used the explicit form of S_0 . In the analysis below we confine ourselves to the equilibrium case where S_0 is a simple decaying exponential. Introducing the new parameters

$$\delta = \frac{\sqrt{R}}{a\lambda} \quad (\text{with } 1 < \delta < 2), \quad \alpha = \sqrt{\frac{2R}{\delta}}, \quad \beta = \beta(a, \delta) = 2a\sqrt{1 - \frac{\delta}{2}}, \quad (3.2.17)$$

and the transformation

$$\xi = \alpha e^{-\frac{1}{2}z}, \quad f(\xi) = s(z), \quad (3.2.18)$$

we find for f a boundary value problem involving the Bessel equation

$$\xi^2 f'' + \xi f' + (\xi^2 - \beta^2)f = 0 \quad \text{on } 0 < \xi < \alpha, \quad (3.2.19)$$

with

$$f(0) = f(\alpha) = 0. \quad (3.2.20)$$

Here primes denote differentiation with respect to ξ . A solution of (3.2.19) satisfying the first condition in (3.2.20) is

$$f(\xi) = J_\beta(\xi), \quad (3.2.21)$$

with J_β denoting the Bessel function of the first kind, order β . Next we fix $a > 0$ and consider

$$J_{\beta(a, \delta)}(\xi_1) = 0 \quad \text{for } 1 < \delta < 2, \quad (3.2.22)$$

where $\xi_1 = \xi_1(a, \delta)$ is the first positive zero of J_β . Then setting $\alpha = \xi_1$ in the third equation of (3.2.17), we obtain the first eigenvalue R_1 for the given values of a and δ :

$$R_1 = R_1(a, \delta) = \frac{1}{2}\delta(\xi_1(a, \delta))^2 \quad \text{for } 1 < \delta < 2. \quad (3.2.23)$$

Keeping a fixed, we now turn to the integral constraint (3.2.15). In the transformed variables it reads

$$\frac{1}{\delta} = 2a^2 \frac{\int_0^{\xi_1} \frac{1}{\xi} J_\beta^2(\xi) d\xi}{\int_0^{\xi_1} \xi J_\beta^2(\xi) d\xi}. \quad (3.2.24)$$

The question now arises whether there exists a unique number $\delta_a \in (1, 2)$ such that $\delta = \delta_a$ satisfies (3.2.24). This would result in the first eigenvalue

$$R_1(a) := R_1(a, \delta_a) \quad \text{for } a > 0. \quad (3.2.25)$$

The proof involves some technical details which are given in van Duijn et al. (2001). The energy stability curve in the (a, R) -plane is plotted as curve 1 in Figure 3.2. If perturbations are x, y -periodic with wavenumber a and if $Ra < R_1(a)$, then the ground state (at equilibrium) is stable in the L^2 -sense. The construction implies

$$R_{E_1}^* := \lim_{a \downarrow 0} R_1(a) = 5.78318 \dots \quad (\text{first zero of } J_0)^2. \quad (3.2.26)$$

Homsy and Sherwood used a numerical shooting method to solve the eigenvalue problem. They found (3.2.26) approximately as a stability threshold.

3.2.2 Differential constraint

In a second approach we want to achieve (3.2.4) for perturbations satisfying the differential constraint (3.2.6). This leads to a maximum problem in which (3.2.7) is considered for the space of perturbations

$$\mathbf{H} = \mathbf{H}_2 := \left\{ (s, w) : x, y\text{-periodic with respect to } \mathcal{C} ; s = w = 0 \text{ at } z = 0, \infty ; \right. \\ \left. \text{and } \Delta w = \Delta_\perp s \text{ in } \mathcal{C} \right\}.$$

This maximum problem results in an eigenvalue problem which has a much higher complexity than the eigenvalue problem related to (3.2.5). In fact it leads to a sixth order differential equation in terms of w , for which no explicit solution is known. However, one expects to have a more accurate description, yielding larger Rayleigh numbers, in particular since (3.2.6) is based on the pointwise Darcy equation.

Theorem 3.2. *The maximum problem (3.2.7) subject to \mathbf{H}_2 yields a larger energy stability threshold than the one obtained by solving the maximum problem subject to \mathbf{H}_1 .*

Proof. We compare the maximum problem (3.2.7) for the admissible perturbations \mathbf{H}_1 and \mathbf{H}_2 . In particular we show that \mathbf{H}_2 can be identified with a proper subspace of \mathbf{H}_1 .

Let $(s, w) \in \mathbf{H}_2$. For this given s we have the unique decomposition (Temam, 1984)

$$s\mathbf{e}_z = \mathbf{v} + \nabla\varphi \quad (\mathbf{v}, \varphi \text{ are } x, y\text{-periodic}), \quad (3.2.27)$$

where $\nabla \cdot \mathbf{v} = 0$ and $\mathbf{v} \cdot \mathbf{n} = 0$ on $\partial\mathcal{C}$. Here \mathbf{n} denotes the unit normal at the boundary $\partial\mathcal{C}$. As in (2.2.4) we find

$$\Delta v_3 = \Delta_{\perp} s \quad \text{in } \mathcal{C},$$

where v_3 is the vertical component of \mathbf{v} . This implies

$$\Delta(v_3 - w) = 0 \quad \text{in } \mathcal{C},$$

and the boundary conditions on $\partial\mathcal{C}$ give $v_3 = w$ in \mathcal{C} . Thus given $(s, w) \in \mathbf{H}_3$ we have obtained the pair (s, \mathbf{v}) with $\nabla \cdot \mathbf{v} = 0$ and $v_3 = w$ in \mathcal{C} . Multiplying (3.2.27) by \mathbf{v} and integrating the result over \mathcal{C} gives

$$\int_{\mathcal{C}} |\mathbf{v}|^2 = \int_{\mathcal{C}} s w,$$

in other words, $(s, \mathbf{v}) \in \mathbf{H}_1$.

The converse is not true. Given $(s, \mathbf{u}) \in \mathbf{H}_1$ and using (3.2.27) we obtain the vector field \mathbf{v} satisfying $\Delta v_3 = \Delta_{\perp} s$ in \mathcal{C} . So $(s, v_3) \in \mathbf{H}_2$, but in general $\mathbf{v} = \mathbf{u} + \nabla \times \Phi$ for a smooth vector field Φ which vanishes on $\partial\mathcal{C}$. ■

Proceeding as usual we consider the functional

$$J(s, w) = \int_{\mathcal{C}} |\nabla s|^2 + R \int_{\mathcal{C}} \frac{\partial S_0}{\partial z} s w + \int_{\mathcal{C}} \pi (\Delta w - \Delta_{\perp} s),$$

where π is again a Lagrange multiplier. The Euler–Lagrange equations read

$$\left\{ \begin{array}{l} -2\Delta s + R \frac{\partial S_0}{\partial z} w - \Delta_{\perp} \pi = 0, \end{array} \right. \quad (3.2.28a)$$

$$\left\{ \begin{array}{l} \Delta \pi + R \frac{\partial S_0}{\partial z} s = 0, \end{array} \right. \quad (3.2.28b)$$

$$\left\{ \begin{array}{l} \Delta w = \Delta_{\perp} s. \end{array} \right. \quad (3.2.28c)$$

Here $\pi(x, y, 0) = 0$ appears as a natural boundary condition. Eliminating π from equations (3.2.28a) and (3.2.28b) yields a fourth order equation in s and w , and the further elimination of s using (3.2.28c) and explicitly using the periodicity leads to the sixth order w equation

$$(D^2 - a^2)^3 w + \frac{a^2 R}{2} \left\{ (D^2 - a^2) \left(\frac{\partial S_0}{\partial z} w \right) + \frac{\partial S_0}{\partial z} (D^2 - a^2) w \right\} = 0. \quad (3.2.29)$$

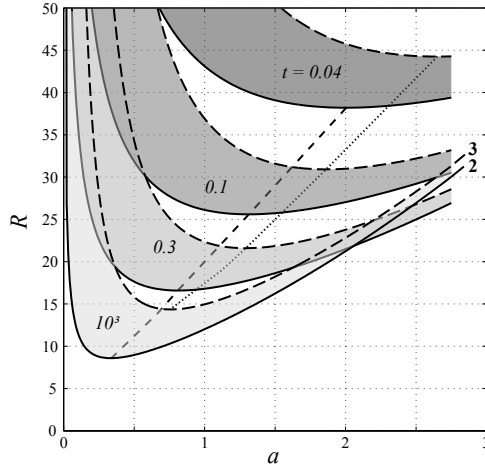


Figure 3.3. Stability curves for the boundary layer according to the energy method with differential constraint (solid curves) and linearised stability method (dashed curves). The curves show lowest eigenvalue $R_{E_1}(a, t)$ and $R_L(a, t)$ versus wavenumber a prior to equilibrium, treating time as parameter. Numerical values are calculated by a Chebyshev–Galerkin method. Curves 2 and 3 are taken from Figure 3.2 (equilibrium case).

Equation (3.2.29) need to be solved in \mathbb{R}_+ and it contains time t (through $S_0 = S_0(z, t)$) as parameter. The corresponding boundary conditions for this equation are

$$w(\infty) = 0, \quad (3.2.30)$$

implying that all higher order derivatives vanish as well at $z = \infty$, and

$$w(0) = D^2w(0) = D^4w(0) = 0. \quad (3.2.31)$$

The first two conditions are obvious. The third one is a consequence of $\pi(0) = 0$; this condition implies $D^2s(0) = 0$ from (3.2.28a), which is then used in (3.2.28c). The eigenvalue problem (3.2.29), (3.2.30) and (3.2.31) was solved numerically for R by a Chebyshev–Galerkin method, see Appendix A.

For a given wavenumber $a > 0$ and time $t > 0$, let $R_{E_2}(a, t)$ denote the smallest positive eigenvalue. The solid curves in Figure 3.3 show the numerical approximations of the curves $\{(a, R) : a > 0, R = R_{E_2}(a, t)\}$ for increasing values of t . Note that these curves essentially move downwards, except for large a and t . At large times they converge to the equilibrium curve $R_{E_2}(a) := R_{E_2}(a, \infty)$, corresponding to a simple decaying exponential. The equilibrium boundary case is also shown in Figure 3.2 (curve 2). The results obtained with the differential constraint are superior to the results obtained with the integral constraint:

$$R_{E_2}^* := \min_{a>0} R_{E_2}(a) = R_{E_2}(a^*) = 8.59 \quad \text{with } a^* = 0.339 \quad (3.2.32)$$

approximately and this threshold is significantly higher than the threshold $R_{E_1}^* = 5.78$, conform Theorem 3.4.

To interpret the results of the time dependent case, we set

$$R_{E_2}(t) := \min_{a>0} R_{E_2}(a, t) \quad \text{for } 0 < t < \infty \quad (3.2.33)$$

and we recall the Rayleigh number of the physical system Ra , given by (1.2.19). If $Ra < R_{E_2}(\infty) = R_{E_2}^*$, the boundary layer is definitely stable for all $t > 0$. However, if $Ra > R_{E_2}^*$, we can only conclude that the boundary layer is stable for $0 < t < t_E^*$, where t_E^* is determined by $Ra = R_{E_2}(t_E^*)$. When $t > t_E^*$ no direct conclusions can be drawn.

The behaviour of $R_{E_2}(a, t)$ in Figure 3.3 suggests that the system is *always* stable for small times. This is confirmed by

Theorem 3.3. *Let (s, \mathbf{u}, p) be a (classical) solution of problem (3.2.1). Then, for any $R > 0$, there exists a $t^* > 0$ such that*

$$\frac{d}{dt} \int_{\mathcal{C}} s^2(t) < 0 \quad \text{for } t \in (0, t^*].$$

Proof. First observe that

$$s \leq |s| = \left| \int_0^z \frac{\partial s}{\partial z} dz \right| \leq \sqrt{z} \left(\int_{\mathbb{R}_+} \left(\frac{\partial s}{\partial z} \right)^2 dz \right)^{\frac{1}{2}}. \quad (3.2.34)$$

A similar estimate is obtained for w . Further, from (2.2.5b) and using the Cauchy–Schwarz inequality we derive the estimate

$$\int_{\mathcal{C}} |\nabla w|^2 = - \int_{\mathcal{C}} \nabla(\mathbf{A}\nabla s) \cdot w \leq \int_{\mathcal{C}} \mathbf{A}\nabla s \cdot \nabla w \leq \left(\int_{\mathcal{C}} |\nabla s|^2 \right)^{\frac{1}{2}} \left(\int_{\mathcal{C}} |\nabla w|^2 \right)^{\frac{1}{2}}, \quad (3.2.35)$$

where $\mathbf{A} = \text{diag}(1, 1, 0)$. We multiply (3.2.1a) by s , integrate over \mathcal{C} , and use (3.2.34), (3.2.35) to obtain

$$\begin{aligned} \frac{1}{2} \frac{d}{dt} \int_{\mathcal{C}} s^2 &= - \int_{\mathcal{C}} |\nabla s|^2 - R \int_{\mathcal{C}} s w \frac{\partial S_0}{\partial z} \leq \\ &\leq - \int_{\mathcal{C}} |\nabla s|^2 + R \left\{ \int_{\mathcal{C}} s^2 \left(-\frac{\partial S_0}{\partial z} \right) \right\}^{\frac{1}{2}} \left\{ \int_{\mathcal{C}} w^2 \left(-\frac{\partial S_0}{\partial z} \right) \right\}^{\frac{1}{2}} \leq \\ &\leq - \int_{\mathcal{C}} |\nabla s|^2 + R \int_{\mathbb{R}_+} z \left(-\frac{\partial S_0}{\partial z} \right) \int_{\mathcal{C}} |\nabla s|^2 = \\ &= \int_{\Omega} |\nabla s|^2 \left\{ -1 + R \int_{\mathbb{R}_+} S_0(z, t) dz \right\}. \end{aligned} \quad (3.2.36)$$

Let $M(t) := \int_{\mathbb{R}_+} S_0(z, t) dz$ having the properties $M(0) = 0$, $M'(t) > 0$, and $M(\infty) = 1$. Let t^* be defined by

$$\begin{cases} M(t^*) = R^{-1} & \text{for } R > 1, \\ t^* = \infty & \text{for } R \leq 1. \end{cases}$$

Then $\int_{\mathcal{C}} s^2(t)$ decays for $t \in (0, t^*]$. ■

Re-examination of Figure 3.3 reveals that the energy stability curve $R_{E_2}(a)$ (curve 2) does not coincide with the linearised stability curve $R_L(a)$ (curve 3), i.e. there exists a subcritical region (light-shaded region). For parameter values in this subcritical region, the appearance and form of the instabilities critically depends on the choice of initial perturbations. This is further investigated in the next subsection.

3.2.3 Weighted energy method

It is obvious that the energy stability thresholds depend critically on the choice of the space of admissible perturbations. They also depend on the energy functional itself. The main topic of this subsection is to find a norm that gives a sharper stability threshold. Our quest for such norm starts with an observation by Galdi and Straughan (1985). In general, evolution problems like problem (3.2.1) can be formally written as

$$\frac{\partial s}{\partial t} = \mathcal{L}s + \mathcal{N}(s) \quad \text{in } \mathcal{H} \text{ and } s(0) = f, \quad (3.2.37)$$

where \mathcal{L} represents a linear and \mathcal{N} a nonlinear operator, and with \mathcal{H} defined as in Section 1.3. Galdi and Padula (1990) showed that one of the essential connections between linear and nonlinear stability theory is the idea of *symmetry* of the linear operator \mathcal{L} . Therefore we split this operator in $\mathcal{L} = \mathcal{L}^s + \mathcal{L}^a$, where \mathcal{L}^s denotes the symmetric and \mathcal{L}^a the asymmetric part of \mathcal{L} with respect to some (not necessarily L^2) scalar product $\langle \cdot, \cdot \rangle$. Then we have the following stability result (Galdi and Straughan, 1985):

Theorem 3.4. *Let the nonlinear operator satisfy $\langle \mathcal{N}(s), s \rangle \leq 0$, and let $\sigma_1 < 0$ denote the largest eigenvalue of \mathcal{L}^s . Then the ground state is unconditionally nonlinearly stable with respect to the norm induced by the scalar product $\langle \cdot, \cdot \rangle$ and*

$$\|s(t)\| \leq e^{\sigma_1 t} \|s(0)\|. \quad (3.2.38)$$

The proof is straightforward. Multiplying (3.2.37) by s and integrating the result gives

$$\begin{aligned} \frac{1}{2} \frac{d}{dt} \|s\|^2 &= \langle \mathcal{L}s, s \rangle + \langle \mathcal{N}(s), s \rangle \leq \langle \mathcal{L}^s s, s \rangle \leq \\ &\leq \sup_{s \in \text{Dom}(\mathcal{L}^s)} \frac{\langle \mathcal{L}^s s, s \rangle}{\|s\|^2} \|s\|^2 = \sigma_1 \|s\|^2. \end{aligned} \quad (3.2.39)$$

Applying Gronwall's lemma to (3.2.39) results in (3.2.38). Note that if \mathcal{L} is symmetric, then the decay rate of the norm of the perturbation s is given by the largest negative eigenvalue of \mathcal{L} .

We first show that Theorem 3.4 is applicable for the equilibrium boundary layer case since then the linear operator can be rendered symmetric by means of a similarity transformation. We show that this similarity transformation modifies the norm and we apply once more the energy method to the growing boundary layer case with respect to the new (weighted) norm.

The equilibrium boundary layer

We identify the linear operator L in (3.1.1a) to operator \mathcal{L} and the nonlinear term $-R\mathbf{u} \cdot \nabla s$ in (3.2.1a) to operator \mathcal{N} in (3.2.37). In Section 3.1 we showed that L can be symmetrized into L_1 by the similarity transformation (3.1.4) with $\alpha = 1$. If σ_{\max} denotes the largest negative eigenvalue of $L_1 = M_1^{-1}LM_1$ we have its characterization

$$\sigma_{\max} = \sup_{u \neq 0} \frac{\langle M_1^{-1}LM_1u, u \rangle}{\|u\|_2^2} = \sup_{u \neq 0} \frac{\langle M_1^{-1}LM_1u, M_1^{-1}M_1u \rangle}{\|u\|_2^2} = \sup_{s \neq 0} \frac{\langle Ls, s \rangle_1}{\|s\|_{2,1}^2},$$

where $s = M_1u$ and where $\langle \cdot, \cdot \rangle_1$ and $\|\cdot\|_{2,1}$ denote the L^2 scalar product and corresponding norm with respect to the weight e^z .

For the nonlinear term we obtain

$$\langle \mathcal{N}(s), s \rangle_1 = -R \int_{\mathcal{C}} (\mathbf{u} \cdot \nabla s) s e^z = -\frac{1}{2}R \int_{\mathcal{C}} w u^2. \quad (3.2.40)$$

Since we are not able to determine the sign of the right-hand side of (3.2.40) for arbitrary w and u , we do not meet the conditions of Theorem 3.4. However, there are two possibilities to resolve this:

(i) Consider only perturbations u, w of the form

$$\{u, w\}(x, y, z) = \{u, w\}(z) e^{i(a_x x + a_y y)}, \quad (3.2.41)$$

i.e. a single Fourier mode in which $a = \sqrt{a_x^2 + a_y^2}$ denotes the wavenumber of the periodicity cell \mathcal{C} . Substitution of (3.2.41) in (3.2.40) immediately implies $\langle \mathcal{N}(s), s \rangle_1 \equiv 0$.

(ii) Impose additional growth conditions for the nonlinear term $\langle \mathcal{N}(s), s \rangle_1$. The addition of a weight has, in general, the effect of weakening the decay of perturbations in the sense that only conditional nonlinear stability can be obtained (Joseph, 1976). For further ideas on how to deal with terms of the type given by (3.2.40), we refer to Galdi and Straughan (1985). They applied this technique to a bio-convection stability problem. In this section, however, we will not discuss conditional (nonlinear) stability.

We follow the approach as outlined in (i). Then Theorem 3.4 states that we have unconditional nonlinear stability if $\sigma_{\max} < 0$. The nonlinear stability threshold for this case is found by solving for R the equality $\sigma_{\max}(a, R) = 0$. Since σ_{\max} is the largest eigenvalue of L_1 (and hence L), we obtain $R_{E_3}(a) = R_L(a)$ for all $a > 0$, i.e. the best possible energy stability threshold possible.

Observe that the use of this weighted energy method to the problem formulated in the s and \mathbf{u} variables is equivalent to applying the L^2 energy method directly to the problem formulated in the variables $u = e^{\frac{1}{2}z}s$ and \mathbf{u} . Therefore we can generalize this method to the more general weight $M_\alpha = e^{-\frac{1}{2}\alpha z}$ by transforming problem (3.2.1) in

terms of u and \mathbf{u} by using (3.1.4). Substitution of (3.1.4) in (3.2.1a) and combining (3.2.1b) and (3.2.1c) to (3.2.6) gives

$$\frac{\partial u}{\partial t} = \Delta u + (1 - \alpha) \frac{\partial u}{\partial z} + (\frac{1}{4}\alpha^2 - \frac{1}{2}\alpha)u + R e^{(\frac{1}{2}\alpha-1)z} w - \frac{1}{2}\alpha R w u + R \mathbf{u} \cdot \nabla u, \quad (3.2.42a)$$

$$\Delta w = e^{-\frac{1}{2}\alpha z} \Delta_{\perp} u. \quad (3.2.42b)$$

To apply the energy method with respect to the L^2 scalar product we multiply (3.2.42a) by u and integrate over the periodicity cell \mathcal{C} :

$$\frac{1}{2} \frac{d}{dt} \int_{\mathcal{C}} u^2 = - \int_{\mathcal{C}} |\nabla u|^2 + (\frac{1}{4}\alpha^2 - \frac{1}{2}\alpha) \int_{\mathcal{C}} u^2 + R \int_{\mathcal{C}} e^{(\frac{1}{2}\alpha-1)z} w u - \frac{1}{2}\alpha R \int_{\mathcal{C}} w u^2. \quad (3.2.43)$$

Here the second nonlinear term in (3.2.43) again disappears. From this point we restrict the class of admissible perturbations to

$$\mathbf{H}_3 := \{(u, w) : \{u, w\} = \{u, w\}(z) e^{ia_x x + ia_y y} \text{ in } \mathcal{C}; \\ u = w = 0 \text{ at } z = 0, \infty; \text{ and } \Delta w = e^{-\frac{1}{2}\alpha z} \Delta_{\perp} u \text{ in } \mathcal{C}\} \subset \mathbf{H}_2.$$

This leads to maximum problem

$$\frac{1}{R} = \sup_{(u, w) \in \mathbf{H}_3} \frac{\int_{\mathcal{C}} e^{(\frac{1}{2}\alpha-1)z} w u}{\int_{\mathcal{C}} |\nabla u|^2 - (\frac{1}{4}\alpha^2 - \frac{1}{2}\alpha) \int_{\mathcal{C}} u^2}. \quad (3.2.44)$$

The functional for (3.2.44) is given by

$$J(u, w) = \int_{\mathcal{C}} |\nabla u|^2 - (\frac{1}{4}\alpha^2 - \frac{1}{2}\alpha) \int_{\mathcal{C}} u^2 - R \int_{\mathcal{C}} e^{(\frac{1}{2}\alpha-1)z} w u + \\ + \int_{\mathcal{C}} \pi (\Delta w - e^{-\frac{1}{2}\alpha z} \Delta_{\perp} u),$$

where π is a Lagrange multiplier. The Euler–Lagrange equations read

$$\begin{cases} -2\Delta u - (\frac{1}{2}\alpha^2 - \alpha)u - R e^{(\frac{1}{2}\alpha-1)z} w - e^{-\frac{1}{2}\alpha z} \Delta_{\perp} \pi = 0, & (3.2.45a) \\ \Delta \pi - R e^{(\frac{1}{2}\alpha-1)z} u = 0, & (3.2.45b) \\ \Delta w = e^{-\frac{1}{2}\alpha z} \Delta_{\perp} u. & (3.2.45c) \end{cases}$$

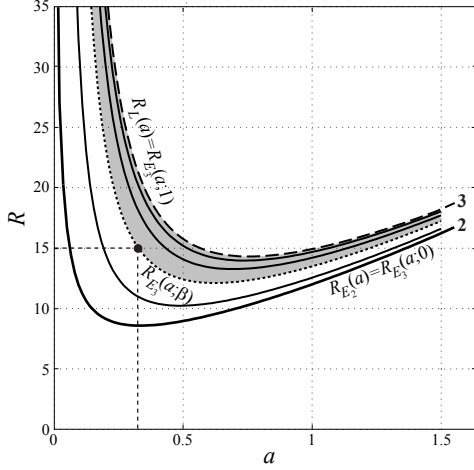


Figure 3.4. Estimates involving the lowest eigenvalue R_{E_3} versus wavenumber a for the equilibrium boundary layer, for various $\alpha \in [0, 1]$ (cf. Theorem 3.6). Fat solid curve ($\alpha \equiv 0$) corresponds to the energy method based on the L^2 -norm of the s perturbation. Dashed curve ($\alpha \equiv 1$) corresponds to linear stability analysis. Grey region depicts SC_α for $\alpha = 0.4$.

Eliminating π and w , and explicitly using the periodicity of s gives the eigenvalue problem

$$D^2u + \left(\frac{1}{4}\alpha^2 - \frac{1}{2}\alpha - a^2\right)u + \frac{1}{2}a^2R \left\{ e^{\left(\frac{1}{2}\alpha-1\right)z} B(e^{-\frac{1}{2}\alpha z}u) + e^{-\frac{1}{2}\alpha z} B(e^{\left(\frac{1}{2}\alpha-1\right)z}u) \right\} = 0. \quad (3.2.46)$$

Observe that for $\alpha = 0$ and further elimination of operator B we regain eigenvalue problem (3.2.29). For a given $a > 0$ and $\alpha \in [0, 1]$ fixed, let $R_{E_3}(a; \alpha)$ be the smallest positive eigenvalue of (3.2.46). These stability curves are depicted in Figure 3.4 for various values of α . In particular, for $\alpha = 0$ we obtain $R_{E_3}(a; 0) = R_{E_2}(a)$ and for $\alpha = 1$ we obtain $R_{E_3}(a; 1) = R_L(a)$, for all $a > 0$.

Remark 3.5. Observe that the left-hand side of (3.2.46) is exactly the symmetric part of L_α (see (3.1.8a)), i.e. $\frac{1}{2}(L_\alpha + L_\alpha^\dagger)$. In particular, for $\alpha \equiv 1$ it is equal to L_α itself.

For every $a > 0$, the curves $R_L(a)$ and $R_{E_3}(a; \alpha)$ are ordered by

Theorem 3.6. For every $\alpha \in [0, 1]$ and for every $a > 0$ fixed, we have $R_{E_3}(a; \alpha) \leq R_L(a)$.

Proof. Let $a > 0$ be fixed and let $(s_1, w_1, R_L(a))$ be the first eigensolution of the problem (in \mathbb{R}_+)

$$D^2s_1 + Ds_1 - a^2s_1 = -R_L(a)e^{-z}w_1, \quad (3.2.47a)$$

$$-D^2w_1 + a^2w_1 = a^2s_1. \quad (3.2.47b)$$

Next set $s_1 = e^{-\frac{1}{2}\alpha z}u_1$. Substitution in (3.2.47) yields

$$D^2u_1 + (1 - \alpha)Du_1 + \left(\frac{1}{4}\alpha^2 - \frac{1}{2}\alpha - a^2\right)u_1 = -R_L(a)e^{\left(\frac{1}{2}\alpha-1\right)z}w_1, \quad (3.2.48a)$$

$$-D^2w_1 + a^2w_1 = a^2u_1e^{-\frac{1}{2}\alpha z}. \quad (3.2.48b)$$

Multiplying (3.2.48a) by u_1 and integrating over \mathbb{R}_+ gives for $\alpha \in [0, 1]$

$$\frac{1}{R_L(a)} = \frac{\left\langle e^{(\frac{1}{2}\alpha-1)z} w_1, u_1 \right\rangle}{\|Du_1\|_2^2 - (\frac{1}{4}\alpha^2 - \frac{1}{2}\alpha - a^2) \|u_1\|_2^2}.$$

From (3.2.44) and explicitly using the periodicity of the perturbations, we immediately derive

$$\frac{1}{R_{E_3}(a; \alpha)} \geq \frac{1}{R_L(a)}$$

which proves the assertion. ■

The energy stability curves $R_{E_3}(a; \alpha)$, $a > 0$, in Figure 3.4 have the following interpretation. Let R_a be such that for fixed $a > 0$ it satisfies $R_{E_2}(a) < R_a < R_L(a)$. This defines a unique $\beta \in (0, 1)$ such that $R_{E_3}(a, \beta) = R_a$, see Figure 3.4 dotted curve. Then the described construction implies that for each $\alpha \in (\beta, 1)$ we have

$$\frac{d}{dt} \int_{\mathbb{R}_+} e^{\alpha z} s^2(t) < 0 \quad \text{provided} \quad \int_{\mathbb{R}_+} e^{\alpha z} s^2(0) < \infty.$$

Let $R_{E_\beta}^* := \min_{a>0} R_{E_3}(a, \beta)$. Then for any $R_a \leq R_{E_\beta}^*$ we have decay of the weighted L^2 norm for the weighting functions $e^{\alpha z}$, $\alpha \in (\beta, 1)$.

In Section 3.3 we will show that for each $\alpha \in (0, \beta)$ there exists an initial condition \bar{f} such that $\int_{\mathbb{R}_+} e^{\alpha z} s^2(t)$ exhibits transient growth.

The growing boundary layer

We generalize the use of a spatial weight in the energy method to the growing boundary layer $S_0(z, t)$ given by (2.1.2a). We consider here $\alpha \equiv 1$ since then $R_{E_3}(a; 1) \equiv R_L(a)$ for the equilibrium boundary layer. This yields the following eigenvalue problem:

$$D^2 s + (-\frac{1}{4} - a^2)s = \frac{1}{2}R \left\{ e^{-\frac{1}{2}z} B \left(e^{\frac{1}{2}z} \frac{\partial S_0}{\partial z} s \right) + e^{\frac{1}{2}z} \frac{\partial S_0}{\partial z} B(e^{-\frac{1}{2}z} s) \right\}. \quad (3.2.49)$$

For a given wavenumber $a > 0$ and $t > 0$, let $R_{E_3}(a, t)$ denote the smallest positive eigenvalue of problem (3.2.49). The solid curves in Figure 3.5 show the numerical approximation of the curves $\{(a, R) : a > 0, R = R_{E_3}(a, t)\}$ for increasing values of t .

Also depicted in Figures 3.3 and 3.5 (dashed curves), are the stability curves corresponding to the linear stability analysis of the growing boundary layer. Since for this case the ground state depends on time as well, such a construction is only possible under the assumption that the rate of change of the ground state is small compared with

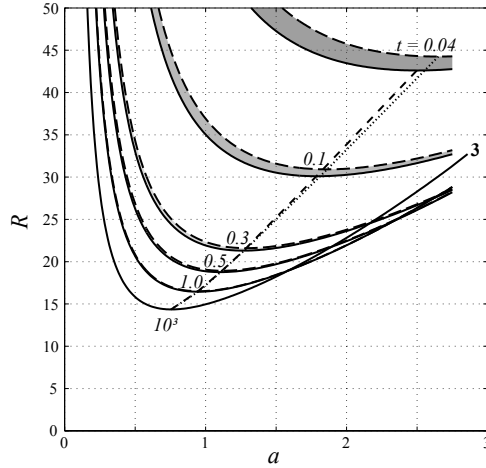


Figure 3.5. Stability curves for the growing boundary layer according to the weighted energy method with differential constraint (solid curves) and linearised stability method with the frozen profile approximation (dashed curves). The curves show lowest eigenvalue $R_{E_3}(a, t)$ and $R_L(a, t)$ versus wavenumber a prior to equilibrium, treating time as parameter. Numerical values are calculated by a Chebyshev–Galerkin method. Curve 3 is taken from Figure 3.2 (equilibrium case).

the growth rate of infinitesimal perturbations (the frozen profile approach). Hence, for given $t > 0$, we consider the approximate equation

$$\frac{\partial s}{\partial \tau} - \frac{\partial s}{\partial z} + R w \frac{\partial S_0}{\partial z}(z, t) = \Delta s \quad \text{in } \mathbb{R}_+, \quad (3.2.50)$$

for $\tau > 0$ and sufficiently small. In fact we have two time scales: a large time scale for the evolving ground state and a small time scale for the perturbation. Now again t appears as a parameter in the equation, as in the case of the energy methods.

To study the instability of the growing boundary layer we need to consider the eigenvalue problem for each finite $t > 0$. Let $R_L(a, t)$ denote the smallest positive eigenvalue. Again we used a Chebyshev–Galerkin method to find accurate numerical approximations. These results are shown in Figures 3.3 and 3.5 where the dashed curves indicate $R_L(a, t)$ for increasing values of t . Note again that these curves essentially move downwards, except for large a and t . As $t \rightarrow \infty$ convergence towards the equilibrium curve $R_L(a)$ is attained.

As before, we set

$$R_L(t) := \min_{a>0} R_L(a, t). \quad (3.2.51)$$

If $Ra > R_L(\infty) =: R_L^*$, an estimate for the onset time of instability is found by the crossover time t_L^* determined by $Ra = R_L(t_L^*)$. In other words, the boundary layer becomes unstable for $t > t_L^*$. If $Ra \searrow R_L^*$, the boundary layer becomes unstable when it is close to its equilibrium profile.

Now we compare Figures 3.3 and 3.5 once more. According to Figure 3.3, we have subcritical regions (shaded regions) for all times. In Figure 3.5 these subcritical regions are considerably smaller than the ones in Figure 3.3. However, the small time behaviour of the curves illustrate that the frozen profile approach in the linear stability analysis is not a good approximation.

3.3 Transient energy growth in a linearly stable regime

In the energy method one seeks for conditions in terms of the system parameters for monotonic decay of the energy norm. This immediately gives conditions for linear stability. We show in this section that the converse is not true for systems with a stability gap. Recall that for parameter values in this gap the system is linearly stable. However, we will show that there exist initial perturbations for which the *linearised* problem exhibits transient growth of the energy norm, such that the nonlinear energy stability criterion is violated.

Let $u(z, t)$ be a solution of problem (3.1.8) (or equivalently, let $s(z, t)$ be a solution of problem (3.1.1)). We define for $\alpha \in [0, 1]$ the functional

$$\mathcal{F}_\alpha(t) := \int_{\mathbb{R}_+} u^2(t) = \int_{\mathbb{R}_+} e^{\alpha z} s^2(t) =: \|s\|_{2,\alpha}^2. \quad (3.3.1)$$

From this point it is convenient to introduce some notation.

Definition 3.7. (i) *The spectral bound of operator L_α is defined by*

$$\sigma(L_\alpha) = \sup_{\lambda \in \Sigma(L_\alpha)} \operatorname{Re} \lambda.$$

Observe that, due to the similarity, $\sigma(L_\alpha)$ does not depend on α .

(ii) *The numerical range of operator L_α is the set*

$$W(L_\alpha) = \{\langle L_\alpha u, u \rangle : \|u\|_2 = 1\} = \{\langle Ls, s \rangle_\alpha : \|s\|_{2,\alpha} = 1\}, \quad \alpha \in [0, 1].$$

(iii) *A related quantity is the numerical bound of L_α , defined by*

$$\omega(L_\alpha) = \sup_{\lambda \in W(L_\alpha)} \operatorname{Re} \lambda. \quad (3.3.2)$$

(iv) *For $a > 0$, $R > 0$ and $\alpha \in [0, 1]$, let $\mathbf{SC}_\alpha = \{(a, R) : \omega(L) > 0, \sigma(L) < 0\}$ and $\mathbf{SC} := \mathbf{SC}_0$.*

An important property of the numerical range is that the spectrum of operator L_α is contained in the closure of its numerical range, i.e. $\Sigma(L_\alpha) \subset \overline{W(L_\alpha)}$ (Istratescu, 1981). This implies that $\omega(L_\alpha) \geq \sigma(L_\alpha)$, where equality holds for $\alpha \equiv 1$.

From (3.1.8a), using Definition 3.7, we find the relation

$$\frac{1}{2} \frac{d}{dt} \mathcal{F}_\alpha(t) = \frac{\langle L_\alpha u, u \rangle}{\|u\|_2^2} \mathcal{F}_\alpha(t) = \frac{\langle Ls, s \rangle_\alpha}{\|s\|_{2,\alpha}^2} \mathcal{F}_\alpha(t) \leq \omega(L_\alpha) \mathcal{F}_\alpha(t). \quad (3.3.3)$$

The linear problem is stable with respect to $\|\cdot\|_{2,\alpha}$ provided $\omega(L_\alpha) < 0$ and neutral stable when $\omega(L_\alpha) \equiv 0$. The Euler–Lagrange equation for maximum problem (3.3.2) is given

$$D^2 u + \left(\frac{1}{4}\alpha^2 - \frac{1}{2}\alpha - a^2\right)u + \frac{1}{2}a^2 R \left\{ e^{(\frac{1}{2}\alpha-1)z} B(e^{-\frac{1}{2}\alpha z} u) + e^{-\frac{1}{2}\alpha z} B(e^{(\frac{1}{2}\alpha-1)z} u) \right\} = \omega u. \quad (3.3.4)$$

Let ω_{\max} be the largest real eigenvalue of (3.3.4). Then $\omega(L_\alpha) = \omega_{\max}$. Figure 3.6(A) shows the isocurves of ω_{\max} for $\alpha = 0$. When (a, R) are such that $\omega_{\max} \equiv 0$, then (3.3.4) reduces to (3.2.46), i.e. the zero-level curve corresponds to $R_{E_2}(a)$.

A formal Taylor expansion of $\mathcal{F}_\alpha(t)$ around $t=0$ reveals

$$\mathcal{F}_\alpha(t) = \mathcal{F}_\alpha(0) + \mathcal{F}'_\alpha(0)t + \mathcal{O}(t^2) .$$

Now using (3.3.3), we have $\mathcal{F}'_\alpha(0)/\mathcal{F}_\alpha(0) = 2\langle Lf, f \rangle_\alpha / \|f\|_{2,\alpha}^2$, where f is the initial condition given by (3.1.1d). Let $\lambda(\alpha)$ denote the maximal initial slope of $\mathcal{F}_\alpha(t)/\mathcal{F}_\alpha(0)$, i.e.

$$\frac{1}{2}\lambda(\alpha) = \sup_{f \in \text{Dom}(L)} \frac{\langle Lf, f \rangle_\alpha}{\|f\|_{2,\alpha}^2} = \omega(L_\alpha) \quad \text{by definition 3.7 (ii)} .$$

The initial condition \bar{f} that maximizes the initial slope is found by solving the eigenvalue problem (see Remark 3.5)

$$\frac{1}{2}(L_\alpha + L_\alpha^\dagger)\bar{f} = \frac{1}{2}\lambda(\alpha)\bar{f} , \quad (3.3.5)$$

where \dagger denotes the adjoint operator. For fixed $(a, R) \in \mathbf{SC}$ we solved (3.1.8) with initial condition the eigenfunction \bar{f} corresponding to the maximum eigenvalue of (3.3.5) for several values of α . The behaviour of $\mathcal{F}_\alpha(t)/\mathcal{F}_\alpha(0)$ is depicted in Figure 3.6(B). The maximal initial growth of $\mathcal{F}_\alpha(t)/\mathcal{F}_\alpha(0)$ is obtained for $\alpha = 0$. For increasing α , the initial slope decreases and becomes negative. This is also to be expected since for increasing α the set \mathbf{SC}_α becomes smaller and for some $\beta \in (0, 1)$ the pair (a, R) lies under the stability curve $R_{E_3}(a, \beta)$, i.e. the numerical bound becomes negative, see Figure 3.4.

Remark 3.8. *The similarity transformations M_α , $\alpha \in [0, 1]$, changes the spatial structure of the eigenfunctions $\{s_j\}$ of L . From the definition of the similarity operators M_α , we find the relation*

$$\langle L_\alpha u, u \rangle = \langle M_\alpha^{-1} L M_\alpha u, u \rangle = \langle M_\alpha^{-1} L s, M_\alpha^{-1} s \rangle = \langle L s, s \rangle_\alpha . \quad (3.3.6)$$

Hence, by adjusting α in the scalar product, we can control the orthogonality of $\{s_j\}$: Let $\{u_j\}$ denote the set of orthonormal eigenfunctions of the symmetric operator L_1 . Then we find from (3.3.6)

$$\langle s_i, s_j \rangle_1 = \langle u_i, u_j \rangle = \delta_{ij} , \quad (3.3.7)$$

where δ_{ij} denotes the Kronecker symbol. This non-orthogonality of the eigenfunctions $\{s_j\}$ may give large projection coefficients in eigenfunctions expansions, and this results in the transient growth behaviour of $\mathcal{F}_\alpha(t)$.

The transient growth of $\mathcal{F}_\alpha(t)$ is not unbounded. This can be shown by two a priori estimates. From (3.3.3) we find for $\alpha = 1$ the estimate

$$\|s(t)\|_{2,1}^2 \leq e^{2\sigma(L)t} \|f\|_{2,1}^2 . \quad (3.3.8)$$

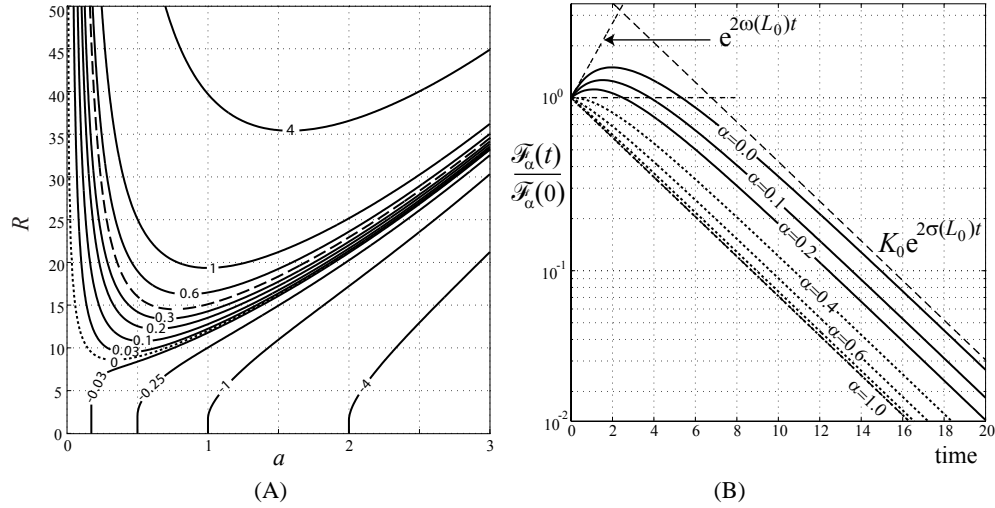


Figure 3.6. (A) Isocurves of the largest eigenvalue ω_{\max} of (3.3.4) for $\alpha=0$. Dashed curve corresponds to $R_L(a)$ and dotted curve to $R_{E_2}(a)$ (= zero level curve). (B) Actual computation for $a = 0.38$ and $R = 15$ (in SC, see also Figure 3.4), with \bar{f} given by the eigenfunction corresponding to the largest eigenvalue of (3.3.5). The upper bound (3.3.9) is depicted as dashed curves. The initial slope of $\mathcal{F}_\alpha(t)$ is given by $2\omega(L_\alpha)$.

From (3.3.8) it follows that for $\alpha \in [0, 1]$

$$\|s(t)\|_{2,\alpha}^2 \leq \|s(t)\|_{2,1}^2 \leq K_\alpha e^{2\sigma(L)t} \|f\|_{2,\alpha}^2,$$

where $K_\alpha = \|f\|_{2,1}^2 / \|f\|_{2,\alpha}^2$. Observe that K_α is a finite number ≥ 1 and this coefficient is maximal for $\alpha=0$. Further, we have the estimate

$$\|s(t)\|_{2,\alpha}^2 \leq e^{2\omega(L_\alpha)t} \|f\|_{2,\alpha}^2,$$

which follows directly from Definition 3.7. Combining these two estimates results in the upper bound

$$\frac{\mathcal{F}_\alpha(t)}{\mathcal{F}_\alpha(0)} \leq \min_{t \geq 0} \left\{ e^{2\omega(L_\alpha)t}, K_\alpha e^{2\sigma(L)t} \right\} =: B_\alpha(t), \quad (3.3.9)$$

see also the dashed curves in Figure 3.6. Obviously, $B_\alpha(t) \rightarrow e^{2\sigma(L_1)t}$ as $\alpha \rightarrow 1$.

We may conclude that there exist initial conditions \bar{f} , (or to put it in dynamical systems terminology, *directions*), that initiate growth and therefore violate the stability criterion that states that the norm $\mathcal{F}_\alpha(t)$ must decrease monotonically in time. This observation fits perfectly in the picture shown in Figure 1.2.

3.4 Comparison with laboratory experiments

Figure 3.7 repeats the equilibrium stability curves of Figure 3.2 and includes experimental measurements obtained using a tilted Hele–Shaw cell to simulate two-

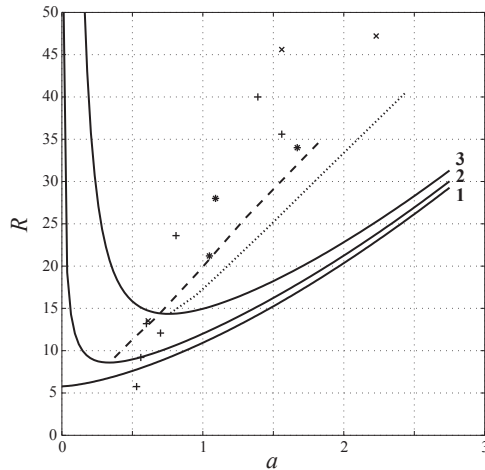


Figure 3.7. Comparison of theory with experimental results (Wooding et al., 1997a,b). Solid curves 1–3 give eigenvalues R versus wavenumber a for the equilibrium boundary layer (Figure 3.2). Curves of minima of R with respect to a for $t > 0$ increasing to equilibrium: by energy method (Figure 3.3, dashes), by linearised theory (Figure 3.3, short dashes). Symbols for experimental results are identified in the text.

dimensional flow in a porous medium, with inflow of a saline solution and evaporation along part of the upper edge (Wooding et al., 1997a,b; Simmons et al., 1999). Experimental points are represented in Figure 3.7 by the symbols $+$, \times and $*$. In the experiments, the large scale Rayleigh number Ra based on finite “aquifer” depth was greater than 10^2 times the boundary layer R -value. Although the large scale flow in the experimental work differed from a simple vertical upflow, a uniform evaporation rate was modelled and a saline boundary layer of uniform thickness was observed to develop. Wavenumbers of initial instabilities, scaled to the equilibrium boundary layer thickness, were measured for a wide range of R -values. Previously, these observations were plotted by Wooding et al. (1997a, Figure 7) using wavenumbers scaled to the diffusion thickness and therefore equivalent to a/R in the present case.

From the published experimental data, stable boundary layers were observed for R -values of 5.8, 5.6 (two experiments), and smaller R . Unstable boundary layers resulted for R -values of 5.6 (one experiment), 8.9 (two experiments), and larger R . Except for the unexplained appearance of instability in one experiment performed at $R = 5.6$, there was a clear separation of stable and unstable layers into two ranges. If the single unstable result at $R = 5.6$ is not included, the theoretical lower bound of 8.59 obtained using the alternative energy method is in agreement with the results of the experimental studies.

The dashed curves in Figure 3.7 provide traces of the minima of the stability curves defined by the energy method in Figure 3.3 and by linearised stability analysis in the same figure. For the data obtained by experimental simulation, either curve might be considered as an upper bound to the wavenumber of an instability which first appears. This is on the assumption that growth rate is zero at a critical point for stability, and a growing perturbation becomes significant when the boundary layer thickness scale has increased significantly. Clearly, however, the instabilities plotted in Figure 3.7 have been initiated by perturbations of small but finite amplitude, and the energy method with differential constraint provides the appropriate estimate. Three experimental points at the low- R end appear to be exceptional. These occur in a range where accurate observation becomes more difficult, and an inadvertent

change of background conditions could have altered the wavenumber.

References

- Criminale, W. O., T. L. Jackson, and R. D. Joslin: 2003, *Theory and Computation of Hydrodynamic Stability*. Cambridge: Cambridge University Press.
- Davis, S. H.: 1969a, 'Buoyancy, surface tension in stability by the method of energy'. *J. Fluid Mech.* **39**, 347.
- Davis, S. H.: 1969b, 'On the principle of exchange of instabilities'. *Proc. Roy. Soc. Ser. A* **310**, 341–358.
- Davis, S. H.: 1971, 'On the possibility of supercritical instabilities'. In: *Instability of Continuous Systems*. Berlin, pp. 222–227, Springer–Verlag.
- Farrell, B. F. and P. J. Ioannou: 1996, 'Generalized stability theory. Part I: Autonomous operators'. *J. Atmos. Sci.* **53**(14), 2025–2040.
- Galdi, G. P. and M. Padula: 1990, 'A new approach to energy theory in the stability of fluid motion'. *Arch. Ration. Mech. Anal.* **110**(3), 187–286.
- Galdi, G. P. and B. Straughan: 1985, 'Exchange of stabilities, symmetry, and nonlinear stability'. *Arch. Rat. Mech. Anal.* **89**, 211–228.
- Gilman, A. and J. Bear: 1996, 'The influence of free convection on soil salinization in arid regions'. *Transport in Porous Media* **24**, 275–301.
- Grosch, C. E. and H. Salwen: 1978, 'The continuous spectrum of the Orr–Sommerfeld equation. Part 1. The spectrum and the eigenfunctions'. *J. Fluid Mech.* **87**, 33–54.
- Homsy, G. M. and A. E. Sherwood: 1975, 'Convective instabilities in porous media with throughflow'. Technical Report UCRL-76539, Lawrence Livermore Laboratory.
- Homsy, G. M. and A. E. Sherwood: 1976, 'Convective instabilities in porous media with throughflow'. *Amer. Inst. Chem. Engrs. J.* **22**, 168–174.
- Istratescu, V.: 1981, *Introduction to Linear Operators*. New York: Marcel–Dekker.
- Jones, M. C. and J. M. Persichetti: 1986, 'Convective instability in packed beds with throughflow'. *Amer. Inst. Chem. Engrs. J.* **32**, 1555–1557.
- Joseph, D. D.: 1976, *Stability of Fluid Motions I,II*. Berlin: Springer–Verlag.
- Kato, T.: 1976, *Perturbation Theory for Linear Operators*. New York: Springer–Verlag.
- Lax, P.: 1954, 'Symmetrizable linear transformations'. *Comm. Pure and Applied Math.* **7**, 633–647.
- Nield, D. A.: 1987, 'Convective instability in porous media with throughflow'. *Amer. Inst. Chem. Engrs. J.* **33**, 1222–1224.
- Reddy, S. C. and D. S. Henningson: 1993, 'Energy growth in viscous channel flows'. *J. Fluid Mech.* **252**, 209–238.
- Reddy, S. C. and L. N. Trefethen: 1994, 'Pseudospectra of the convection-diffusion operator'. *SIAM J. Appl. Math.* **54**, 1634–1649.
- Salwen, H. and C. E. Grosch: 1981, 'The continuous spectrum of the Orr–Sommerfeld equation. Part 2. Eigenfunction expansions'. *J. Fluid Mech.* **104**, 445–465.

- Schmidt, P. J. and D. S. Henningson: 2001, *Stability and Transition in Shear Flows*. Berlin: Springer.
- Simmons, C. T., K. A. Narayan, and R. A. Wooding: 1999, 'On a test case for density-dependent groundwater flow and solute transport models: The salt lake problem'. *Water Resources Res.*
- Straughan, B.: 2004, *The Energy Method, Stability and Nonlinear Convection*, Vol. 91 of *Applied Mathematical Sciences*. New York: Springer-Verlag, 2nd edition.
- Temam, R.: 1984, *Navier–Stokes Equations, Theory and Numerical Analysis*, Vol. 2 of *Studies in Mathematics and its Applications*. Amsterdam, The Netherlands: Elsevier Science Publishers, 3rd edition.
- van Duijn, C. J., G. J. M. Pieters, R. A. Wooding, and A. van der Ploeg: 2002, 'Stability criteria for the vertical boundary layer formed by throughflow near the surface of a porous medium'. In: P. A. C. Raats, D. Smiles, and A. W. Warrick (eds.): *Environmental Mechanics - Water, Mass and Energy Transfer in the Biosphere*, Vol. 129 of *Geophysical Monographs*. American Geophysical Union, pp. 155–169.
- van Duijn, C. J., R. A. Wooding, and A. van der Ploeg: 2001, 'Stability criteria for the boundary layer formed by throughflow at a horizontal surface of a porous medium: extensive version'. Technical Report RANA Report 01-05, Eindhoven University of Technology.
- Wooding, R. A.: 1960, 'Rayleigh instability of a thermal boundary layer in flow through a porous medium'. *J. Fluid Mech.* **9**, 183–192.
- Wooding, R. A., S. W. Tyler, and I. White: 1997a, 'Convection in groundwater below an evaporating salt lake: 1. Onset of instability'. *Water Resour. Res.* **33**, 1199–1217.
- Wooding, R. A., S. W. Tyler, I. White, and P. A. Anderson: 1997b, 'Convection in groundwater below an evaporating salt lake: 2. Evolution of fingers or plumes'. *Water Resour. Res.* **33**(6), 1219–1228.

Chapter 4

Growing instabilities and pattern dynamics[★]

The theoretical thresholds in Chapter 3 predict how the system will respond to perturbations of the ground state. In this chapter we analyse the temporal behaviour of these growing instabilities by means of numerical simulations of the full model equations. Further, we investigate the large-time (equilibrium) nonlinear behaviour of the system for Rayleigh numbers in the vicinity and far beyond the linear stability threshold R_L^* . In particular, we are interested in the number of different convective solutions, their stability, their spatial structure, and how they evolve when the bifurcation parameter R is further increased. This kind of information, however, is not provided by the method of linearised stability and hence we have to consider the full set of model equations.

We discretize the full set of equations by means of the finite element method and for specific initial conditions (i.e. perturbations) we use time-integrations to compute steady-state convective solutions. For this purpose a *truncated* flow domain has to be chosen. We consider the model equations (P1) in $\Omega = \Omega_\perp \times (0, h)$ where the horizontal domain has the particular form

$$\Omega_\perp := \{(x, y) : 0 < x < \ell, 0 < y < \frac{2}{3}\sqrt{3}\ell\}. \quad (4.0.1)$$

In these definitions ℓ and h are the scaled length and depth of the flow domain, see Subsection 1.2.3. The aspect ratio of Ω_\perp is given by $1 : \frac{2}{3}\sqrt{3}$. This particular choice of the aspect ratio will become clear in the course of this chapter. The domain truncation requires additional boundary conditions at the lateral boundaries and at $\{z = h\}$, see Section 4.1. Using the techniques from Chapter 3, we determine for the truncated flow domain the thresholds R_L^* and $R_{E_2}^*$.

To analyse the response of the system to different initial perturbations, we compute for every step in the time-integration a functional $\mathcal{U}(t)$ similar to the one as discussed in Section 1.3. The numerical simulations are carried out for three different system Rayleigh numbers, each one corresponding to the possible states of the system: stable, subcritical and unstable. When $\mathcal{U}(t) \rightarrow \text{constant} > 0$ for t large

[★] This chapter is joint work with H.M. Schuttelaars (University of Utrecht) and parts of it will appear as a paper in *Computational Geosciences*.

enough and for Rayleigh numbers between $R_{E_2}^*$ and R_L^* , then we say that the system has converged to a nontrivial steady-state and the transition is referred to as a global subcritical bifurcation. For Rayleigh numbers beyond the linear threshold R_L^* , the transition is called globally supercritical. If $\mathcal{U}(t) \rightarrow 0$ for t sufficiently large, then we say that the system is globally stable. This approach has a severe disadvantage: to obtain a detailed picture of the dynamics of the system, one has in essence to check for *any* arbitrary initial conditions the behaviour of $\mathcal{U}(t)$, which is impossible. Hence this approach is unsuitable for a detailed bifurcation analysis.

A more natural way to carry out a detailed bifurcation analysis is to solve directly the *equilibrium* nonlinear model equations for system Rayleigh numbers in a relevant range. Johannsen (2003), for example, considers the time evolution process of the Elder problem (Elder, 1967a,b) to form a dynamical system and investigate its behaviour with respect to the Rayleigh number. His approach is to discretize the full set of nonlinear equations by means of the Finite Volume method to obtain a finite-dimensional differential algebraic system. Then the so-called pseudo-arclength continuation method with secant prediction is used to calculate some solution branches connecting the different steady solutions. The found solution branches are then visualized by means of a suitably chosen L^2 -functional. This method has the disadvantage that it is expensive from a computational point of view and in addition it still does not scan the whole parameter space in a very efficient way.

The time-integrations of the discretized system (by e.g. finite elements, finite volumes, etc.), though, gives an extremely useful first impression of the different kinds of steady solutions that may exist within the model. In particular, they provide specific information about the spatial structure of the different steady solutions. Each of these steady convective solutions represent a different salt distribution in the box. With respect to the vertical plane, these salt distributions appear as typical finger like structures, whereas in the horizontal plane they may represent roll/stripe, hexagonal, square, or combinations of these structures. In particular, we are interested in the *spatiotemporal* behaviour of the perturbations prior to equilibrium. For this purpose we apply 2D finite element simulations to a specific set of initial perturbations. These initial conditions are chosen in such a way that they are relatively close to the convective steady-state solutions that are expected to appear during the computations. More specifically, the number of fingers that will eventually appear in the steady-state solution is dictated by the perturbation of the initial condition. This approach dramatically increases the convergence of the time-integration compared to other initial conditions (e.g. a random distribution), without losing the basic mechanisms that are essential for the temporal pattern formation.

Since solving the full set of equations is very time-consuming and since we want to scan the parameter space in more detail, we construct a lower-order model by means of a Galerkin projection of the full model equations onto carefully chosen eigenmodes of the linear problem. Here we use the 2D finite element simulations to validate the results of the reduced model. The modes for projection, in this chapter referred to as the dynamically active eigenmodes, are found by a careful analysis of the results from linear stability theory. The constructed lower-order system of coupled nonlinear ODEs is usually called the Landau or, for obvious reasons, system of amplitude equations. These equations captures the local dynamics of the full model,

at least near criticality. We determine the steady-state solutions by solving the steady lower-order model by a Newton-like iteration process. The reduced model will be our primary tool to investigate the nonlinear stability of the equilibrium boundary layer.

Several authors have recognized the usefulness of the Galerkin projection method for bifurcation analysis. For example, Vadasz and Olek (1999, 2000) used a truncated Galerkin representation to investigate the route to chaos for convection in a porous layer heated from below, i.e. the Lapwood problem (Lapwood, 1948). In fact, they use only three dynamically active eigenmodes for projection and after proper rescaling they obtain the familiar Lorenz system. However, their rigorous truncation implies that their lower-order model is very limited because of its local domain of validity, which is just in the neighbourhood of the steady-state convective solution. Therefore, their method may be better classified under the *weakly nonlinear stability analysis*. For the Rayleigh–Bénard problem (which is the free fluid equivalent of the Lapwood problem), weakly nonlinear analysis is discussed in a fairly rigorous mathematical context by Mielke (2002). Although weakly nonlinear stability analysis still provides significant insight to the underlying problem, this mathematical method only gives information close to critical conditions. In different contexts, van der Vaart et al. (2002) use Galerkin projections for the nonlinear analysis of time-dependent wind-driven ocean gyres, while Schuttelaars (1998), Calvete et al. (1999, 2002) (among others) use this method for studying nonlinear problems arising in morphodynamics.

At first sight, the projection method is a very powerful tool, but one of the difficulties with this concept is the determination of the dynamically active eigenmodes that have to be chosen for the projection basis. The most natural way is to select the eigenmodes that are close to criticality since they are expected to represent the convective steady-state solution which appears just beyond threshold. This approach works fine for normal systems (Schramkowski et al., 2004). However, as in the ocean gyre problem (van der Vaart et al., 2002), the salt lake problem with evaporation is a non-normal problem, see Chapter 3. This implies that the eigenmodes do not form an orthogonal set. This lack of orthogonality may seriously complicate the choice of an appropriate projection basis. The non-orthogonality of the eigenfunctions may imply that the set of parameters in which the method is a valid approximation is very small. To be more precisely, nonlinear interactions between the non-orthogonal modes may not be necessarily restricted to the dynamically active eigenmodes close to criticality, but other interactions involving eigenmodes which are relatively far away in the spectrum may be well possible. As a consequence, convergence tests by successively increasing the number of eigenmodes are very misleading (van der Vaart et al., 2002, Table II shows that the accuracy of the approximation can decrease when one incorporates additional eigenmodes). Therefore it should be emphasized to check the results from the reduced model with numerical simulations of the full set of equations.

Keeping these pitfalls in mind, order-reduction is still valuable from a numerical viewpoint. Reduced models are preferred above the full model equations with respect to time-integrations and bifurcation analysis, in particular when the models are considered in 3D. Furthermore, the resulting patterns and bifurcation structures are more easily interpreted in the reduced model (see e.g. van der Vaart et al. (2002)).

In this chapter we consider both the 2D and 3D cases. For the 2D case we com-

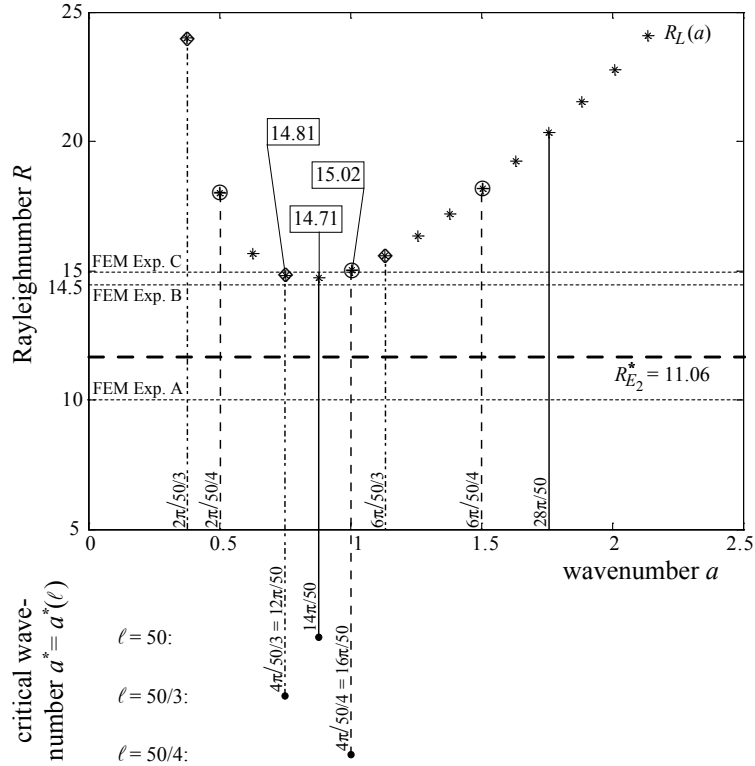


Figure 4.1. Stability thresholds corresponding to linearised stability (stars) and energy method (dashed horizontal line) for $h = 5$. The Fourier modes with wavenumber a have to fit in the laterally bounded box, and this gives a discrete set of wavenumbers. The dash-dotted vertical lines correspond to wavenumbers that fit in a box with $\ell = \frac{1}{3}50$, the vertical dashed lines to wavenumbers that fit in a box with $\ell = \frac{1}{4}50$ and solid lines to wavenumbers that fit in a box with $\ell = 50$.

pare the results of the reduced model with finite element simulations. After choosing and validating an appropriate projection basis, we construct a reduced model and show that the transition of roll patterns is indeed subcritical, as suggested in Section 3.2.2. For the 3D case we only consider hexagonal structures and we show that these structures bifurcate transcritically. Based on the bifurcation diagrams for both the roll and hexagonal patterns, we give a numerical upperbound for the *global* stability threshold R_G as discussed in Chapter 1.

In this chapter we consider several flow domains of decreasing length: $\ell = 50$, $\frac{1}{3}50$ and $\frac{1}{4}50$. For all these flow domains the thickness of the layer is fixed and is given by $h = 5$. The equilibrium boundary layer for this setting reads

$$\bar{S}_0(z) = \frac{e^{5-z} - 1}{e^5 - 1} \quad z \in (0, 5) . \quad (4.0.2)$$

With respect to the equilibrium boundary layer (4.0.2), the linear stability ‘curve’ as

well as the energy stability threshold are depicted in Figure 4.1. The linear instability threshold, i.e. the minimum of the stability ‘curve’ with respect to the modes that fit in the box, clearly depends on ℓ . For $\ell = 50$ it is given by $R_L^* = 14.71$, for $\ell = \frac{1}{3}50$ it is given by $R_L^* = 14.81$, and finally for $\ell = \frac{1}{4}50$ it is given by $R_L^* = 15.02$. The energy stability threshold is given by $R_{E_2}^* = 11.06$. Comparing Figure 4.1 with Figure 3.3 (corresponding to the case $h = \infty$), we observe that the linear instability threshold R_L^* increases with decreasing depth. The curves for the growing boundary behave similarly to Figure 3.3.

Remark 4.1. *All perturbations, and their corresponding salt distributions, computed in this chapter are depicted for the flow domain in which $\ell = 50$. This means that for $\ell = \frac{1}{3}50$ we glue three of such domains to one, and for $\ell = \frac{1}{4}50$ we glue four of these domains to one. It should be emphasized that this is only possible when we impose periodic boundary conditions at the lateral boundaries of the flow domain. Thus, when talking about the x -finger solution, the number x is counted with respect to the flow domain in which $\ell = 50$!*

4.1 Two-dimensional finite element simulations

In this section we verify the stability thresholds as derived in Chapter 3 by means of two-dimensional simulations. For this purpose we use the finite element package SEPRAN (Segal, 1993). In particular we introduce the energy functional $\mathcal{U}(t)$, which is based on the L^2 -norm of the velocity perturbation \mathbf{u} , and we track its transient behaviour during the time-integration. We first introduce the numerical method, then we present some numerical simulations which lead to different steady-state solutions.

Since we consider here two-dimensional finite element simulations, we redefine the flow domain:

$$\Omega := \{(x, z) : 0 < x < 50, 0 < z < 5\}.$$

In Ω we solve problem (P1) in terms of the saturation S and the stream function Ψ , where

$$\mathbf{U} = \left(-\frac{\partial \Psi}{\partial z}, \frac{\partial \Psi}{\partial x} \right). \quad (4.1.1)$$

Following De Josselin de Jong (1960) we obtain the system

$$\begin{cases} \frac{\partial S}{\partial t} + \text{Ra} \left(\frac{\partial \Psi}{\partial x} \frac{\partial S}{\partial z} - \frac{\partial \Psi}{\partial z} \frac{\partial S}{\partial x} \right) = \Delta S & \text{in } \Omega, t > 0, & (4.1.2a) \\ \Delta \Psi = \frac{\partial S}{\partial x} & \text{in } \Omega, t > 0. & (4.1.2b) \end{cases}$$

The corresponding boundary conditions result directly from the imposed saturation and flow behaviour, see also the boundary condition in (P1). Hence we impose at $\{z = h\}$ a zero Dirichlet condition. To mimic a flow domain of infinite horizontal

extent, we impose for the saturation S periodic boundary conditions at the lateral boundaries.

Now let $t^k = k\Delta t$, $k = 0, 1, \dots, N$, N sufficiently large, and let S^k denote the saturation at $t = t^k$. The corresponding stream function is found from

$$\Delta \Psi = \frac{\partial S^k}{\partial x} \quad \text{in } \Omega . \quad (4.1.3)$$

This problem is discretised by the finite (linear) element method. The corresponding matrix equation is iteratively solved using the conjugate gradient method. The numerical approximation of (4.1.3) is denoted by Ψ_n^k .

Next we consider

$$\frac{\partial S}{\partial t} + \text{Ra} \left(\frac{\partial \Psi_n^k}{\partial x} \frac{\partial S}{\partial z} - \frac{\partial \Psi_n^k}{\partial z} \frac{\partial S}{\partial x} \right) = \Delta S , \quad (4.1.4)$$

in Ω and for $t > t^k$. Again we use a finite element discretisation, together with an upwind discretisation for the convective part. The corresponding linear system is now iteratively solved with the bi-conjugate gradient stabilized method. For the time integration we use a predictor-corrector implicit Euler scheme. Let the preliminary numerical solution (predictor) of (4.1.4) at $t = t^{k+1}$ be denoted by $S_n^{k+1,*}$. Replacing S^k by $S_n^{k+1,*}$ in equation (4.1.3), we obtain $\Psi_n^{k+1,*}$. This solution is then plugged in (4.1.4) to obtain at time-level $t = t^{k+1}$ a *corrected* solution which will be again denoted by $S_n^{k+1,*}$. This process is iterated until convergence is reached. In this way we obtain $S_n^{k+1} = S_n^{k+1,*}$. The above cycle is repeated for subsequent time steps until S^k does not change anymore with increasing k .

The numerical method does not involve automatic time-step adaptation nor does it include algorithms for local mesh refinement. This implies that the time-step and mesh are fixed during the computations. Motivated by the convergence behaviour of the scheme, we use a time-step of $\Delta t = 0.004$ and 16,000 square elements.

The energy method involves the definition of an energy functional. We adopt this concept for the numerical simulations and hence we introduce the functional

$$\mathcal{U}(t^k) = \int_{\Omega} |\mathbf{u}_n^k|^2 \, dx \, dz , \quad \mathbf{u}_n^k = \mathbf{U}_n^k - \mathbf{U}_0 , \quad (4.1.5)$$

where $\mathbf{U}_0 = -\text{Ra}^{-1} \mathbf{e}_z$ (the ground state uniform upflow) and where \mathbf{U}_n^k follows from (4.1.1).

Our main goal is to verify the stability thresholds R_L^* and $R_{E_2}^*$ by using the functional $\mathcal{U}(t)$. In addition, we discuss the interpretation of the global measure $\mathcal{U}(t)$ in relation to the stability of the fully nonlinear model. For this purpose we investigate the response of the full model with zero initial condition to specific initial perturbations.

Implicit in the finite element simulation is the coexistence of three time-scales: a fast time-scale at which the boundary layer grows faster than the perturbations, a slow time-scale at which the boundary has nearly reached its equilibrium form, and

an intermediate time-scale at which the growth of the boundary layer balances with the growth of the perturbations. The time-scale at which the boundary grows fast is, as shown in Section 3.2.2, an unconditionally *stable* situation in the sense that the functional $\mathcal{U}(t)$ will always decrease initially. At later stages of the simulation, there is a slow time scale at which the background state can be considered to be constant and linear stability analysis predicts the behaviour of the growing instabilities. Generally speaking, at the intermediate time-scale there is less that can be said about the nonlinear behaviour of the system, but one should realize that the dynamics in this regime may significantly influence the behaviour of the system on the slow time scale, i.e. when the boundary layer is close to equilibrium. Therefore care must be taken with respect to the finite element simulations that are presented in this section.

We compute the solution of (4.1.2) and the corresponding global measure $\mathcal{U}(t)$ for the initial conditions summarized in Table 4.1. In this table we also give predictions of the behaviour of $\mathcal{U}(t)$ which are based on the results from Chapter 3.

Table 4.1. A, B and C are initial perturbations far from the equilibrium $\bar{S}_0(z)$. All initial perturbations are given by a single Fourier mode with a dominant wavenumber.

	Rayleigh number	Initial perturbation $f(x, z)$	Prediction
A	Ra = 10 (stable)	$\cos(12\pi x/50) \sin(\pi z/5)$	Decay of $\mathcal{U}(t)$ for all times
B1	Ra = 14.5 (subcritical)	$0.1 \cos(6\pi x/50) \sin(\pi z/5)$	Initial decay of $\mathcal{U}(t)$ up to $t = t^*$; <i>possible transition</i> at large times
2		$0.25 \cos(6\pi x/50) \sin(\pi z/5)$	<i>id.</i>
3		$0.1 \cos(8\pi x/50) \sin(\pi z/5)$	<i>id.</i>
4		$0.25 \cos(8\pi x/50) \sin(\pi z/5)$	<i>id.</i>
5		$0.1 \cos(12\pi x/50) \sin(\pi z/5)$	<i>id.</i>
6		$0.25 \cos(12\pi x/50) \sin(\pi z/5)$	<i>id.</i>
C1	Ra = 15 (unstable)	$0.1 \cos(12\pi x/50) \sin(\pi z/5)$	Initial decay of $\mathcal{U}(t)$ up to $t = t^*$ and <i>transition</i> to a nontrivial solution
2		$0.25 \cos(12\pi x/50) \sin(\pi z/5)$	<i>id.</i>

The numerically computed energy functionals $\mathcal{U}(t)$ are depicted in Figure 4.2. We will discuss each of the cases in Table 4.1 separately.

Experiment A

According to Figure 4.1 we expect decay of $\mathcal{U}(t)$. This is indeed the case and the relatively large perturbation eventually decays to zero.

Experiment B

The situation in the subcritical region is more interesting. We first observe that for small times all perturbations decay, conform Theorem 3.3 and using inequality (3.2.3). As already mentioned in Chapter 3, there may exist subcritical transition depending on amplitude and shape of the initial perturbation. When the perturbation is sufficiently small (B1, B3, B5) then $\mathcal{U}(t)$ decreases to zero indicating that the perturbed system returns to the ground-state solution. However, when the initial perturbation is sufficiently large (B2, B4, B6), then the system bifurcates to a nontrivial solution, and the resulting pattern depends on the form of the initial perturbation: the number of fingers correspond to the dominant wavenumber of the initial perturbation. Observe that the energy $\mathcal{U}(t \rightarrow \infty)$ increases with increasing number of fingers.

Experiment C

Now the parameters are in the unstable region, implying that the ground state has exchanged stability with a convective regime. Hence, *independent of the amplitude* of the initial perturbation, the system will always bifurcate to some convective state. The number of fingers, however, still depends on the shape of the initial perturbation. Prior to this transition, the system is stable, just as in experiment B.

The existence of non-trivial finite-amplitude steady solutions in the subcritical region does not contradict the energy stability bound $R_{E_3}(a)$ obtained in Subsection 3.2.3. Suppose that the eventual equilibrium pattern would consist of one Fourier mode of wavenumber a only, then this perturbation would be in the set \mathbf{H}_3 . This gives a contradiction since no perturbations from this class can exist in the subcritical region. Therefore the eventual equilibrium pattern *must* consist of a series of Fourier modes since these perturbations are definitely not in the set \mathbf{H}_3 . This statement will be made more precisely in Subsection 4.3.1.

4.2 Reduction to a Landau type amplitude equation

The disadvantage of solving the initial-value problem by finite element simulations is that no information is obtained about unstable convection states. In addition, a structured search for possibly other stable solutions is not possible with this approach. The picture of stable states alone is incomplete, especially in the regimes where multiple stable states are likely to exist. Although unstable states are not accessible to experiments, knowledge of these states is often necessary to understand transitions, as well as the dynamical mechanics underlying the physics of transition. Therefore, the approach followed in this section is to construct a lower-dimensional model using numerical Galerkin projection of the full model onto the dynamically active eigenmodes. Once obtained, the lower-dimensional model is then used to determine the different (both stable *and* unstable) steady-state solutions for Rayleigh numbers within a relevant range.

Let us consider the nonlinear perturbation equations (2.2.3). Relation (2.2.4) can be used to reduce the number of unknowns in (2.2.3): Using (2.2.3c) in (2.2.3a),

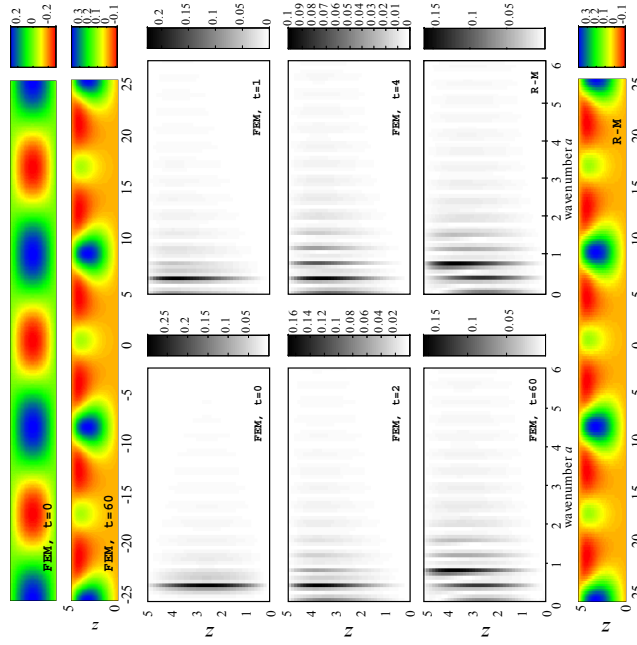


Figure 4.3. Top: saturation perturbation $s(x, z)$ computed with finite elements. Left middle: spectral density plot of the perturbation pattern. Middle right and bottom: results computed by means of a reduced model showing excellent agreement with the fully nonlinear FEM simulations.

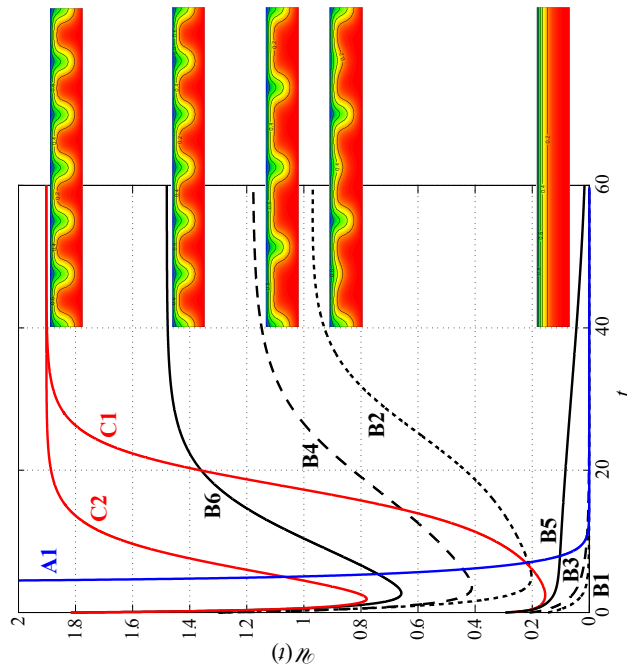


Figure 4.2. Functional $\mathcal{Z}(t)$ computed by FEM simulations versus time for the settings from Table 4.1. Blue curve: $R = 10$, black curves $R = 14.5$ and red curves $R = 15$.

and taking the divergence of (2.2.3c) and again using (2.2.3b) gives the perturbation equation in terms of s , w and the pressure perturbation p

$$\left\{ \begin{array}{l} \frac{\partial s}{\partial t} = \Delta s + \frac{\partial s}{\partial z} + R w \frac{\partial S_0}{\partial z} + R \nabla p \cdot \nabla s - R s \frac{\partial s}{\partial z} \quad \text{in } \Omega, t > 0, \quad (4.2.1a) \\ \Delta w = \Delta_{\perp} s \quad \text{in } \Omega, t > 0, \quad (4.2.1b) \\ \Delta p = \frac{\partial s}{\partial z} \quad \text{in } \Omega, t > 0, \quad (4.2.1c) \\ s = w = \frac{\partial p}{\partial z} = 0 \quad \text{at } \{z=0\} \cup \{z=h\}, t > 0, \quad (4.2.1d) \\ \mathbf{n} \cdot \nabla s = \mathbf{n} \cdot \nabla w = \mathbf{n} \cdot \nabla p = 0 \quad \text{at } \partial\Omega_{\perp} \times (0, h), t > 0, \quad (4.2.1e) \\ s = f \quad \text{in } \Omega, t = 0, \quad (4.2.1f) \end{array} \right.$$

where $\Omega = \Omega_{\perp} \times (0, h)$ and where Ω_{\perp} is given by (4.0.1). The Neumann boundary condition for w in (4.2.1e) follows from the no-flow condition along $\partial\Omega_{\perp} \times (0, h)$, i.e. $\mathbf{n} \cdot \mathbf{u} = 0$, and the relation $\nabla \times \mathbf{u} = \nabla \times (s \mathbf{e}_z)$. The boundary conditions for the pressure perturbation p follow directly from Darcy's law.

We choose a basis for projection that is spanned by selected modes from the eigenspectrum of problem (3.1.1). These modes are chosen in such a way that they build the perturbation pattern. The finite set of these wavenumbers is referred to as the dynamically active wavenumbers and is denoted by $\mathcal{A}_n = \mathcal{A}_n[a_{\text{dom}}]$, where a_{dom} denotes the *dominant* wavenumber and n refers to the number of modes taken into account. These modes are explicitly available from the analysis of the full model, see Section 3.1. Whereas in Section 3.1 we used single Fourier modes, here we make the following generalization concerning the shape of the perturbations in the *horizontal plane*:

$$\{s_j, w_j, p_j\}(x, y, z) = \{s_j, w_j, p_j\}(z) H_j(x, y),$$

where the planform function $H_j(x, y)$ satisfies $\Delta_{\perp} H_j(x, y) = -a_j^2 H_j(x, y)$ and $a_j \in \mathcal{A}_n$. Then the functions $s_j(z)$ satisfies $L s_j = \sigma_j s_j$ ($j = 1, \dots, n$) with L given by (3.1.1a). The s_j , w_j and p_j are related by

$$\left\{ \begin{array}{l} D^2 w_j - a_j^2 w_j = -a_j^2 s_j \\ w_j(0) = w_j(h) = 0 \end{array} \right. \quad \text{and} \quad \left\{ \begin{array}{l} D^2 p_j - a_j^2 p_j = D s_j \\ D p_j(0) = D p_j(h) = 0 \end{array} \right. ,$$

conform equations (4.2.1a) and (4.2.1b). Observe that $p_j(z)$ is uniquely determined up to a constant. This constant of integration is found from relations $D^2 p_j = D s_j - D w_j$ (Darcy's law) and $D^2 p_j - a^2 p_j = D s_j$, and it is determined by the condition $p_j(0) = -D w_j(0)/a^2$, $a > 0$.

Next we project the set of equations (4.2.1) onto the eigenfunctions $\{s_j, w_j, p_j\}$. We write

$$\{s, w, p\}(x, y, z, t) = \sum_{j=1}^n \sum_{i=1}^m A_j^i(t) \{s_j^i, w_j^i, p_j^i\}(z) H_j^i(x, y)$$

where m denotes the number of eigenfunctions in the z -direction. To simplify notation, we introduce the indexing convention $k := m \times (j - 1) + i$, where $j = 1, \dots, n$ and $i = 1, \dots, m$. Substitution of this decomposition into (4.2.1) yields the system

$$\begin{aligned} \sum_{k=1}^{mn} \frac{dA_k(t)}{dt} s_k(z) H_k(x, y) &= \sum_{k=1}^{mn} A_k(t) \left((D^2 + D - a_k^2) s_k(z) + \text{Re} e^{-z} w_k(z) \right) H_k(x, y) + \\ &+ R \sum_{k=1}^{mn} \sum_{l=1}^{mn} A_k(t) A_l(t) \left\{ D p_k(z) D s_l(z) - D s_k(z) s_l(z) \right\} H_k(x, y) H_l(x, y) + \\ &+ R \sum_{k=1}^{mn} \sum_{l=1}^{mn} A_k(t) A_l(t) \left\{ p_k(z) s_l(z) \right\} \left\{ H_{k,x}(x, y) H_{l,x}(x, y) + H_{k,y}(x, y) H_{l,y}(x, y) \right\}, \end{aligned} \quad (4.2.2)$$

where $H_{k,x} \equiv \partial H_k / \partial x$ and $H_{k,y} \equiv \partial H_k / \partial y$.

Now observe that $\langle s_k, s_j \rangle_1 = C_j \delta_{kj}$, where $C_j > 0$ denotes some constant, see Remark 3.8. Hence, multiplying (4.2.2) by $s_j(z) e^z H_j(x, y)$ and integrating over the flow domain Ω gives

$$\alpha_j \frac{dA_j(t)}{dt} = \sum_{k=1}^{mn} \beta_{jk} A_k(t) + R \sum_{k=1}^{mn} \sum_{l=1}^{mn} \gamma_{jkl} A_k(t) A_l(t), \quad (4.2.3)$$

where the coefficients in the projected system are defined as

$$\alpha_j = \int_{\Omega} s_k s_j e^z H_k H_j, \quad (4.2.4a)$$

$$\beta_{jk} = \int_{\Omega} \left[D^2 s_k + D s_k - a_k^2 s_k + \text{Re} e^{-z} w_k \right] s_j e^z H_k H_j, \quad (4.2.4b)$$

$$\begin{aligned} \gamma_{jkl} &= \int_{\Omega} \left[D p_k D s_l - D s_k s_l \right] s_j e^z H_k H_l H_j + \\ &+ \int_{\Omega} \left[p_k s_l \right] s_j e^z (H_{k,x} H_{l,x} + H_{k,y} H_{l,y}) H_j. \end{aligned} \quad (4.2.4c)$$

The functions $s_j, D s_j, D^2 s_j, w_j, p_j, D p_j$ are computed by an efficient modified Chebyshev–Galerkin method, see Appendix A. The coefficients α_j, β_{jk} and γ_{jkl} in (4.2.4) are computed by a Gauss quadrature rule.

4.3 Bifurcation analysis by means of continuation of the reduced model

We are now in the position to analyse the nonlinear behaviour of the system by means of continuation of the Landau equation (4.2.3) with respect to the bifurcation parameter R . Thus for Rayleigh numbers in the range $[0, 65]$ we compute possible nontrivial steady-state solutions of this equation and we determine their stability by evaluating the eigenvalues of the Jacobian, obtained after linearizing (4.2.3) around these nontrivial steady-state solutions.

In the bifurcation diagrams we use the following color codes: black denote stable solutions, red denote unstable solutions where just one eigenvalue has positive real part, green are unstable solutions where two eigenvalues have real parts, and magenta are unstable solutions where three eigenvalues have positive real parts.

4.3.1 Validation of the reduced model

We start with the validation of the reduced model by comparing its results with the finite element simulations from Section 4.1. We construct a lower-order model for the case of parallel rolls in the y -direction:

$$H_j(x, y) = \cos(a_j x) . \quad (4.3.1)$$

This is in fact a 2D flow problem since the roll (or stripe) patterns in the three-dimensional space correspond to two-dimensional fingers, making a comparison with the finite element simulations meaningful.

The strategy to choose the projection basis is as follows. We use the results from the linear stability analysis to obtain information about the stability of the modes (and thus the least stable mode) that fit in the finite box, see Figure 4.1. Subsequently, we choose a fixed dominant wave number (for example the least stable one $a^* = a^*(\ell)$, see Figure 4.1), and determine the wavenumbers that nonlinearly interact with the dominant wavenumber. To complete the set $\mathcal{A}_n[a_{\text{dom}}]$, we first observe that the equations for the coefficients, (4.2.4a) and (4.2.4c), involve quadratic and cubic terms with respect to the planform function H_j . Based on this observation, it is natural to take the modes $\mathcal{A}_n[a_{\text{dom}}] = \{(j-1) \times a_{\text{dom}}, j = 1, \dots, n\}$ as basis for projection. One should realize that, in order to get sufficient cubic interaction terms, the number n must be taken sufficiently large. The number of modes in the z -direction, denoted by m , cannot easily be determined *a priori*, since they do not form an orthogonal set. Hence both n and m are determined by means of convergence tests.

Next we compare the finite element steady-state solution from experiment B2 (see Section 4.1) with the one obtained by the reduced model. To build up the reduced model, we use the other parameters from experiment B2. We fix the flow domain at $\ell = \frac{1}{3}50$ and set $a_{\text{dom}} = 2\pi/\frac{1}{3}50 = 6\pi/50$. Based on convergence results, we take $m = 15$ and $n = 9$, i.e. we approximate the infinite dimensional problem with a $15 \times 9 = 135$ -dimensional one. The dimension of the projection basis is fixed for all computations in this section. Both the finite element (FEM) perturbation and the reduced model (R-M) perturbation are depicted in Figure 4.3(top and

bottom). In the same figure we constructed for the finite element simulation spectral density plots of the perturbation patterns at various instances of time. The perturbation pattern is found by subtracting the ground state $S_0(z, t)$ from the numerically obtained saturation S . We also computed a spectral density plot for the equilibrium perturbation as obtained from the reduced model (R-M). For each slice $0 < z < 5$ we applied the Fourier transform in the x -direction to obtain information about the horizontal wave numbers that build the pattern. For each wavenumber we computed the amplitude in the Fourier expansion. As to be expected, the spectral density plot at $t = 0$ only shows one mode, namely $6\pi/50$. As time increases, the number of interacting wavenumbers increases as well and for large time an equilibrium number of active modes is reached. Clearly visible in the spectral density plot at $t = 60$ are three vertical black ‘bands’ indicating the most relevant wavenumbers in the pattern: $a = 0$, $0.375 \approx 6\pi/50$ (corresponding to 3 fingers, as in the initial perturbation), $0.754 \approx 12\pi/50$, and minor higher-order multiples of $6\pi/50$. This is in agreement with our choice of the projection basis. The validity of this projection basis is even further confirmed in the spectral density plot corresponding to the perturbation pattern obtained by the reduced model. The dominant wavenumbers are exactly the wavenumbers that are in the set $\mathcal{A}_9[2\pi/\frac{1}{3}50]$. In fact, taking the difference between both patterns and analysing the absolute error, we found that both patterns are nearly the same, indicating that the reduced model captures the infinite-dimensional nonlinear model extremely well.

4.3.2 The dynamics of roll/stripe patterns

For the roll/stripe patterns we constructed a reduced model and computed bifurcation diagrams which are depicted in Figure 4.4. We considered the following sets of dynamically active wavenumbers: $\mathcal{A}_9[2\pi/\frac{1}{3}50]$ (diagrams (A) and (B); the dominant wavenumber is subharmonic, i.e. it does not correspond to the least unstable mode), $\mathcal{A}_9[4\pi/\frac{1}{3}50]$ (diagrams (C) and (D)). These dynamically active eigenmodes are considered in the flow domain in which $\ell = \frac{1}{3}50$. Further we consider the set $\mathcal{A}_9[2\pi/\frac{1}{4}50]$ (E) and (F)). For this experiment we use a smaller flow domain in which ℓ is given by $\ell = \frac{1}{4}50$. From these bifurcation diagrams we observe the following.

As a first observation, the bifurcation diagrams look already very complicated in the vicinity of the threshold Rayleigh number. Many other branches exist, in particular for larger Rayleigh numbers, but the analysis of these branches is beyond the scope of this section. We only focus on the branches depicted in Figure 4.4.

In the set $\mathcal{A}_9[2\pi/\frac{1}{3}50]$, the least stable eigenmode has wavenumber $a = 12\pi/50$, see Figure 4.1. Thus the ground-state solution loses its stability at $R = 14.81$ by a subcritical pitchfork bifurcation, see diagram (A). This subcritical bifurcation is now referred to as the primary bifurcation. Further, the primary bifurcation diagram in (A) is asymmetric with respect to its positive and negative branch. The negative (unstable) branch, starting from the pitchfork in $R = 14.81$, corresponds to solutions in which the convection is shallower. These solution disappear via a fold bifurcation at $R \cong 14.02$ and returns as a stable branch. On the other hand, the positive (unstable) branch has another bifurcation at $R \cong 14.38$, a pitchfork. From this pitchfork a sub-branch pops up that corresponds to the 3-finger solutions, thereby destabilizing the

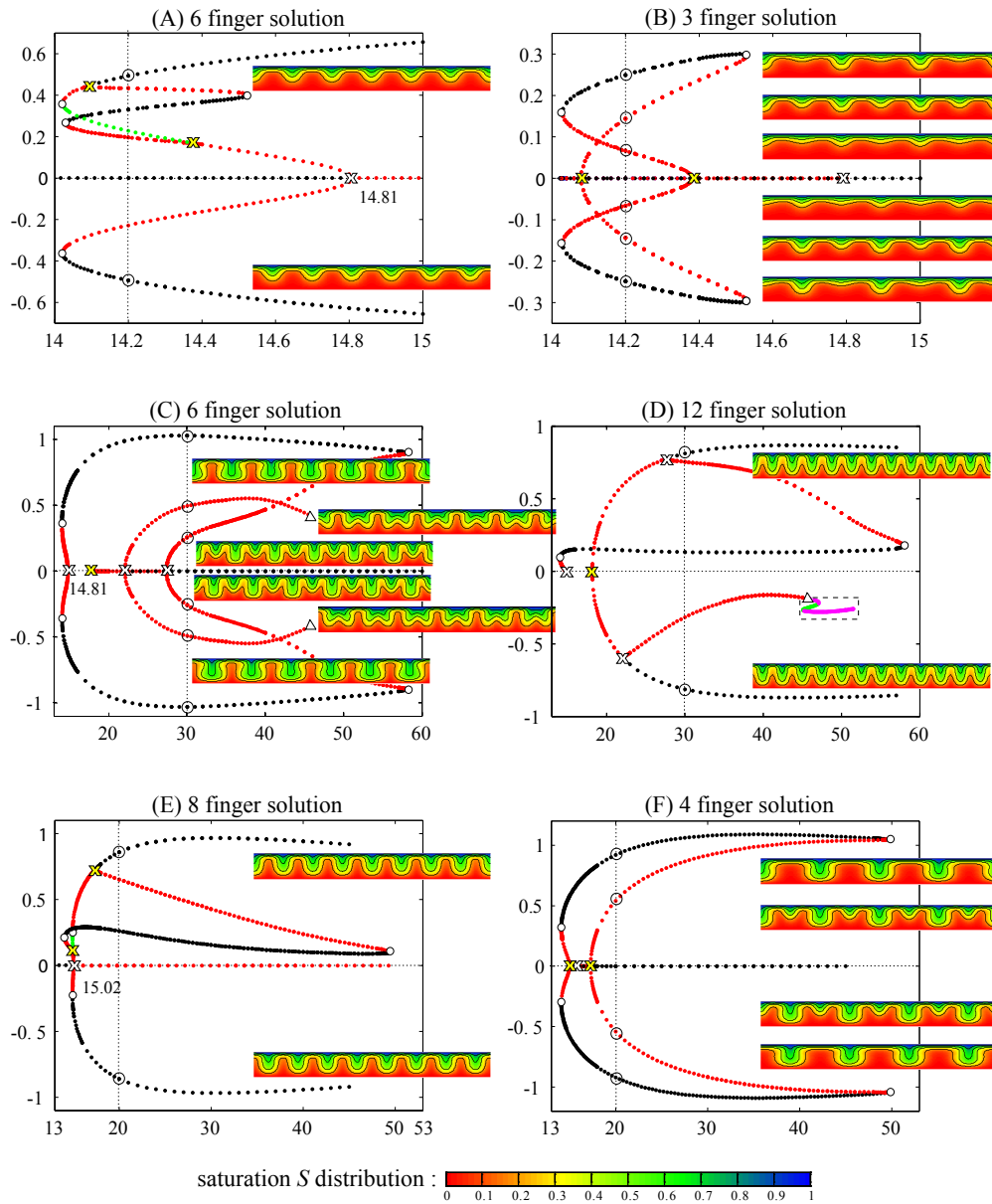


Figure 4.4. Bifurcation diagrams for roll patterns computed by the reduced model. See text for the color convention. For Rayleigh numbers indicated by the open circles we computed the corresponding saturation S distributions. White crosses correspond to pitchfork bifurcations in the primary bifurcation diagram, yellow crosses to pitchforks in the secondary bifurcation diagram. White circles correspond to fold bifurcations, and triangles to Hopf bifurcations.

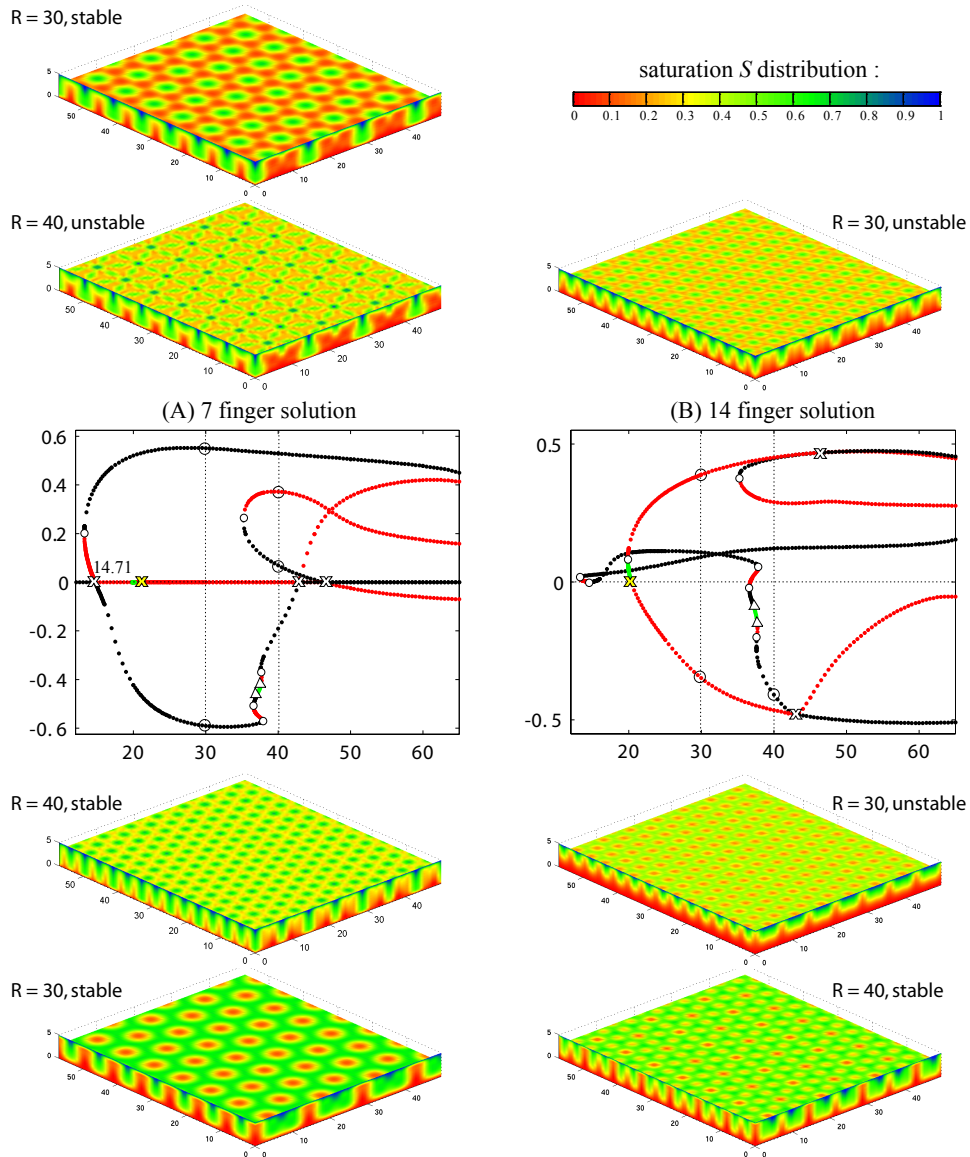


Figure 4.5. Bifurcation diagrams for hexagonal patterns computed by the reduced model. See text for the color convention. For Rayleigh numbers indicated by the open circles we computed the corresponding saturation S distributions. White crosses correspond to transcritical bifurcations in the primary bifurcation diagram, yellow crosses to transcritical bifurcations in the secondary bifurcation diagram. White circles correspond to fold bifurcations, and triangles to Hopf bifurcations.

(unstable) 6-finger solutions, viz. the green unstable primary branch that continues after the bifurcation. This green branch disappears via a fold bifurcation at $R \cong 14.02$ to a less unstable solution branch until $R \cong 14.085$. There the 6-finger solution branch bifurcates and regains its stability.

The sub-branch corresponding to the 3-finger solutions is ‘unfolded’ in diagram (B). Observe that this branch is symmetric with respect to its positive and negative parts. It turns out that the bifurcation at $R \cong 14.38$ is subcritical. One should realize that this is a bifurcation with respect to the 6-finger solution, and *not* with respect to the ground-state solution \bar{S}_0 . Therefore, Figure 4.1 does not predict the critical Rayleigh number at which this bifurcation occurs. However, the critical bifurcation point can be determined via linear stability analysis in which the 6-finger solution functions as ground state, i.e. when one linearizes around the 6-finger solution. The unstable branch starting from the subcritical bifurcation disappears again via a fold bifurcation at $R \cong 14.025$ and continues with stable 3-finger solutions until the next fold bifurcation at $R \cong 14.53$, to eventually return as an unstable branch at $R \cong 14.085$.

Now we consider the set $\mathcal{A}_9[4\pi/\frac{1}{3}50]$. This case is similar to the first experiment (diagrams (A) and (B)), except that now the 3-finger solutions are not included. In fact, bifurcation diagram (C) is a continuation of diagram (A) for larger Rayleigh numbers, but without the 3-finger solutions sub-branch that destabilizes the 6-finger solution branch. However, the situation in diagrams (C) and (D) is different. The least stable wavenumber is the dominant wavenumber $a_{\text{dom}} = 4\pi/\frac{1}{3}50 = 12\pi/50$. Hence the ground state solution again loses its stability at $R = 14.81$, thus the primary bifurcation diagram is depicted in diagram (C). Observe that this bifurcation diagram is symmetric, i.e. there are no sub-branches that destabilize the 6-finger solutions.

Starting from the subcritical pitchfork bifurcation at $R = 14.81$ in diagram (C), there exist two (positive and negative amplitude) unstable branches which disappear via a fold bifurcation at $R \cong 14.02$ to a stable 6-finger solution branch, as in diagram (A). At $R \cong 57.9$ these stable branches disappear via a fold bifurcation to unstable branches that terminate in a pitchfork bifurcation at $R \cong 27.4$. These two primary branches in diagram (C) reappear in the positive part of diagram (D). For Rayleigh numbers beyond the pitchfork value $R = 27.4$, see diagram (D), there exists a stable 12-finger solution branch. For Rayleigh numbers below this pitchfork value, there exists an unstable 12-finger solution branch that does not interact with the 6-finger solution branch since for these Rayleigh values the amplitudes of the 6-finger solutions are zero (see diagram (C)). Further decreasing the Rayleigh number in (C) brings us to the next bifurcation point at $R \cong 18.1$. This pitchfork bifurcation marks the point at which the ground-state solution becomes unstable with respect to the 12-finger solution, see diagram (D). For Rayleigh numbers beyond this point there exists an unstable 12-finger solution branch in the negative part of diagram (D) that again does not interact with the 6-finger solution branch. The unstable branch exists up to $R \cong 22.04$, again a pitchfork bifurcation. At this bifurcation point two unstable 6-finger solutions branches appear (diagram (C)). These branches ‘terminate’ with a Hopf bifurcation at $R \cong 46$. In (D) we continued this branch for larger Rayleigh numbers, see the branch in the dashed box, to show the complex dynamics of the system that occur after the Hopf bifurcation. In this thesis we do not investigate Hopf

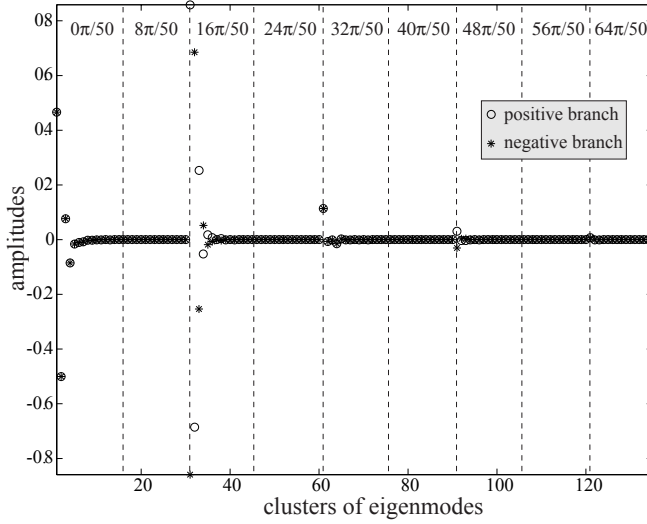


Figure 4.6. Amplitudes $\mathcal{A}_9[2\pi/\frac{1}{4}50]$ plotted in 9 dynamically active wavenumber clusters, each consisting of 15 eigenfunctions with respect to depth. Amplitudes correspond to the stable 8-finger solutions in Figure 4.4 (E).

bifurcations in detail.

To conclude the experiments for the roll patterns, we decrease the flow domain by setting $\ell = \frac{1}{4}50$ and consider the set $\mathcal{A}_9[2\pi/\frac{1}{4}50]$ and . The least stable mode in the set $\mathcal{A}_9[2\pi/\frac{1}{4}50]$ is now given by $4\pi/\frac{1}{4}50 = 16\pi/50$, see again Figure 4.1, and therefore the ground state solution loses its stability at $R = 15.02$ by a subcritical bifurcation. For the explanation of the behaviour of the branches in diagrams (E) and (F) we refer to diagrams A and (B). The fold bifurcation at which the unstable 8-finger solutions disappears in favour of stable 8-finger solutions is given by $R \cong 14.92$. The (subcritical) bifurcation point at which the 4-finger solutions enters the positive branch of diagram (D) is given by $R \cong 14.99$ and the point where it leaves this branch is given by $R \cong 17.3$, see also diagram (C). For the 4-finger solutions we find the fold bifurcations $R \cong 14.093$ and $R \cong 49.44$.

In diagrams (A) and (E) it is striking that there exist sub-branches in the positive branch of the primary bifurcations only. The negative branches in these subfigures suggest that these 6 and 8 finger patterns differ only from solutions of the positive branches by a phase-shift. However, it turns out that this is not the case. The asymmetry in diagram (E) is reflected by the amplitudes $\mathcal{A}_9[2\pi/\frac{1}{4}50]$, see Figure 4.6. In this figure we plotted the amplitudes of the 9 eigenmodes in clusters of 15 (the number of modes with respect to the depth). Observe that the clusters corresponding to the wavenumbers $8\pi/50$, $24\pi/50$, $40\pi/50$ and $56\pi/50$ are not activated in this regime. Further, the clusters of the wavenumbers 0, $32\pi/50$ and $64\pi/50$ are invariant with respect to the sign change $A_k = -A_k$, but the clusters corresponding to the wavenumbers $4\pi/\frac{1}{4}50 = 16\pi/50$ (primary bifurcation) and $48\pi/50$ are not invariant under the sign change.

From the bifurcation diagrams we conclude that the stable 3-, 4-, and 6-finger solutions only exist in finite R -intervals: stable 3-finger solutions exist for $14.025 < R < 14.53$; stable 4-finger solutions exist for $14.093 < R < 49.44$; and stable 6-finger solutions exist for $14.02 < R < 57.9$ This typical phenomenon is related to Busse

stability balloons (Manneville, 1990).

4.3.3 The dynamics of hexagonal patterns

So far we have only considered 2D and quasi-3D (i.e. rolls/stripes) pattern formation. One of the benefits of the reduced model is that it can be easily extended to the bifurcation analysis of genuine 3D patterns. In this subsection we consider structures that have a hexagonal shape with respect to the horizontal plane, i.e. we consider the planform function

$$H_j(x, y) = 2 \cos(\frac{1}{2}a_j x) \cos(\frac{1}{2}a_j \sqrt{3}y) + \cos(a_j x) \quad (4.3.2)$$

satisfying $\Delta_{\perp} H_j = -a_j^2 H_j$. These hexagonal structures have aspect ratio $1 : \frac{2}{3}\sqrt{3}$. In order to let them fit in the truncated flow domain, the aspect ratio of Ω_{\perp} has to be chosen $1 : \frac{2}{3}\sqrt{3}$ as well. This explains the particular flow domain (4.0.1). The asymmetric geometry makes the problem asymmetric as a whole and based on this observation we may expect transcritical bifurcations, see Section 1.3.

The model reduction with respect to (4.3.2) is considered for the set $\mathcal{A}_9[14\pi/50]$ only. For the flow domain we set $\ell = 50$ in (4.0.1). The dominant wavenumber $14\pi/50$ is the least stable eigenmode and corresponds to 7-finger solutions. The bifurcation diagrams are depicted in Figure 4.5. The least stable eigenmode $a = 14\pi/50$ bifurcates transcritically at $R = 14.71$. The stable ground-state solution branch continues in the negative part of diagram (A) until it disappears via a fold bifurcation at $R \cong 37.98$ to an unstable branch. This unstable branch disappears again via a fold bifurcation to a stable branch at $R \cong 36.63$ which terminates with a Hopf bifurcation at $R \cong 37.19$. Further continuation of this branch reveals a second Hopf bifurcation at $R \cong 37.72$. After the second Hopf bifurcation, the 7-finger solution branch becomes less unstable and even stable via a fold at $R \cong 37.58$. Further continuation shows that this stable 7-finger solution branch intersects the R -axis again at $R \cong 42.75$. This intersection demarcates a transcritical bifurcation point in the negative part of the 14-finger solution branch, see Figure 4.5(B).

The 14-finger solution branch in diagram (B) bifurcates transcritically at $R \cong 20.25$. The behaviour of this diagram is more or less similar to Figure 4.4(D). The unstable 14-finger solution branch regains its stability at $R \cong 46.25$ via a transcritical bifurcation. This bifurcation is basically initiated by the interaction of the 7-finger solution branch in diagram (A).

At the primary bifurcation point $R = 14.71$, there also exist in the positive part of the diagram an unstable subcritical branch that vanishes via a fold bifurcation at $R \cong 13.22$ to a stable branch corresponding to the 7-finger solutions. Its definite fate is not clear since for $R > 65$ we have to dramatically increase the set $\mathcal{A}_9[14\pi/50]$ to obtain a valid representation of the nonlinear system.

Considering again the bifurcation diagrams in this section, we may conclude that the bifurcation structure of the dynamical system is extremely complex. For Rayleigh numbers in the range $[13.22, 65]$ there exist, depending on the horizontal planform function one considers, many stable and unstable patterns, i.e. spatial distributions of salt. Therefore, an upperbound for the global stability threshold is given by $R_G < 13.22$.

4.4 Discussion and future directions

Although the method is very powerful, it also has its limitations. For large Rayleigh numbers, one has to incorporate many modes to get a reliable convergence. This is also to be expected: the modes for projection are based on the one-dimensional ground state $\bar{S}_0(z)$, and the patterns that may pop up in this large Rayleigh number regime do not have very much in common with the modes that form the projection basis. Therefore it would be better to change the projection basis when one continues a specific branch for large Rayleigh numbers. The most natural way is to linearize around the solutions of the followed branch, and then to determine the new eigenfunctions that can be used for the projection basis. Clearly, these convective solutions do not longer have a one-dimensional structure, thus one has to solve a two-dimensional eigenvalue problem. On the other hand, the number of projection modes can be drastically reduced to obtain convergence for large Rayleigh numbers.

Reconsidering the bifurcation diagrams (C) and (B) in Figure 4.6, predictions of the length scale of the observed patterns that are based on the least stable wavenumber, can be misleading. Indeed, from these diagrams we deduce for $R > 27.4$ four stable solutions. Two of them are entirely build up by the 12-finger solution, i.e. they do not interact with the 6-finger solutions, which are for this case the least stable solutions. Hence it is not clear which of these patterns will eventually show up when doing (numerical) experiments. To answer this question, one has to determine for each of these solutions their domain of attraction. These attraction domains can be determined numerically by means of stochastic methods, see Gardiner (2004, Chapter 9).

Although not considered in this thesis, all these roll/hexagonal/square etc. patterns interact with each other in a very complicated way. Therefore, the bifurcation analysis presented in this section cannot predict what kind of pattern the system will eventually select since we considered the different planform distributions independently. What we do know is that this pattern selection problem will be a hard and challenging future research topic.

References

- Calvete, D., H. E. de Swart, and A. Falqués: 2002, 'Effect of depth-dependent wave stirring on the final amplitude of shoreface-connected sand ridges'. *Cont. Shelf Res.* **22**, 2763–2776.
- Calvete, D., A. Falqués, H. E. de Swart, and N. Dodd: 1999, 'Nonlinear modelling of shoreface-connected sand ridges'. In: N. C. Kraus and W. G. McDougal (eds.): *Proceedings Coastal Sediments*, Vol. 2. Reston (VI), ASCE.
- De Josselin de Jong, G.: 1960, 'Singularity distributions for the analysis of multiple fluid flow in porous media'. *J. Geothermal Res.* **65**, 3739–3758.
- Elder, J. W.: 1967a, 'Steady free convection in a porous medium heated from below'. *J. Fluid Mech.* **27**, 29–48.
- Elder, J. W.: 1967b, 'Transient convection in a porous medium'. *J. Fluid Mech.* **27**, 609–623.

- Gardiner, C. W.: 2004, *Handbook of Stochastic Methods: For Physics, Chemistry and the Natural Sciences*. Berlin: Springer Verlag, 2nd edition.
- Johannsen, K.: 2003, 'On the validity of the Boussinesq approximation for the Elder problem'. *Comput. Geosci.* **7**, 169–182.
- Lapwood, E. R.: 1948, 'Convection of a fluid in a porous medium'. *Proc. Cambridge Phil. Soc.* **44**, 508–521.
- Manneville, P.: 1990, *Dissipative Structures and Weak Turbulence*. San Diego: Academic Press, Inc.
- Mielke, A.: 2002, 'The Ginzburg–Landau equation in its role as a modulation equation'. In: B. Fiedler (ed.): *Handbook for Dynamical Systems*. Holland: Elsevier, pp. 759–834.
- Schramkowski, G. P., H. M. Schuttelaars, and H. E. de Swart: 2004, 'Non-linear channel-shoal dynamics in long tidal embayments'. *Ocean Dynamics* **54**, 309–407. DOI: 10.1007/s10236-003-0052-9.
- Schuttelaars, H. M.: 1998, 'Nonlinear long term equilibrium profiles in a short tidal embayment'. In: J. Donkers and M. B. A. M. Scheffers (eds.): *Physics of Estuaries and Coastal Seas*. Rotterdam: Balkema.
- Segal, A.: 1993, 'SEPRAN Finite Element Package'. Ingenieursbureau SEPRA, Leidschendam.
- Vadasz, P. and S. Olek: 1999, 'Weak turbulence and chaos for low Prandtl number gravity driven convection in porous media'. *Transport in Porous Media* **37**, 69–91.
- Vadasz, P. and S. Olek: 2000, 'Route to chaos for moderate Prandtl number convection in a porous layer heated from below'. *Transport in Porous Media* **41**, 211–239.
- van der Vaart, P. C. F., H. M. Schuttelaars, D. Calvete, and H. A. Dijkstra: 2002, 'Instability of time-dependent wind-driven ocean gyres'. *Phys. Fluids* **14**, 3601–3615.

PART II

**APPLICATION TO OTHER
ECOLOGICAL AND
HYDROLOGICAL FLOW
PROBLEMS**

Chapter 5

Convection as a transport mechanism in peat* moss layers

The upper part of a living mire consists of a sponge-like layer of predominantly moss species, the acrotelm, with a porosity above 95% (Ingram, 1978). The green and brownish plants near the surface (Figure 1.1(C)) intercept light and fix CO_2 . Further down, the older plants turn yellow and start to decay. Aerobic decay in the acrotelm takes place relatively rapidly and makes nutrients available for recycling. Below the acrotelm a denser layer, the catotelm, is present where the hydraulic conductivity is much lower than in the acrotelm (Ingram et al., 1974) and where the decay rate is several orders of magnitude smaller due to the anoxic conditions (Clymo, 1984). It is the peat formation in the slowly growing catotelm that represents a sink of atmospheric CO_2 (Gorham, 1991; Van Breemen, 1995; Clymo et al., 1998).

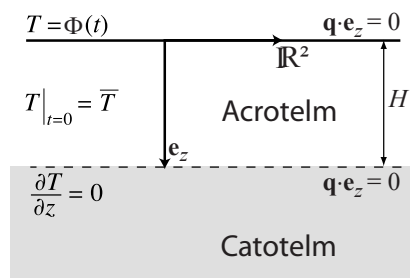


Figure 5.1. Schematized picture of a mire. The surface temperature $\Phi(t)$ is given in Table 5.1.

The production of organic matter at the surface largely depends on the recycling of nutrients originating from decomposing plant material. Since decomposition and photosynthesis take place at different depths, the transport of oxygen, carbon compounds and nutrients is an important process in the functioning of the mire ecosystem. This transport takes place both inside the plants (Rydin and Clymo, 1989) and outside

* This chapter is an extended version of a paper that has appeared in the *Proceedings of the National Academy of Sciences, USA* (PNAS) (Rappoldt et al., 2003).

the plants by diffusion and fluid flow.

In this chapter we investigate a mechanism for fluid flow in a water-saturated peat moss layer, which does not depend on capillarity or an external hydraulic pressure. During the night the surface cools, leading to relatively cold water on top of warm water, and if the temperature drop is sufficiently large, the cold water sinks and the warm water rises. This type of flow is called buoyancy flow and it implies convective transport of the heat and solutes carried with the water. Buoyancy flow often occurs as “cells” consisting of adjacent regions with upward and downward flow.

To obtain a better understanding of this phenomenon, we consider various types of both static and time-periodic surface temperatures. We first consider the case where the surface temperature impulsively drops from maximum daytime temperature $\bar{T} + \Delta T$ to minimum night temperature \bar{T} . Then we consider the case where the impulsive temperature drops and rises between $\bar{T} + \Delta T$ and \bar{T} are periodic. To mimic day and night cycles, we also consider the case in which the surface temperature varies harmonically.

Considerable theoretical work has been done on the stability of flows in fluid layers and fluid-saturated porous layers subject to static and time periodic boundary conditions, see Nield and Bejan (1992) and Homsy (1973, 1974) for an overview.

The case of the impulsive temperature drop is treated by Caltagirone (1980) for a finite fluid-saturated porous layer. In this chapter both linear stability analysis based on Galerkin projections and the energy method are discussed and compared to 2D numerical computations. Basically, the Galerkin projection method results in a *non-autonomous* system of ordinary differential equations for the amplitudes. Two difficulties arise in this approach. Firstly, for non-autonomous systems a stability analysis in terms of the eigenvalues of the system has no meaning, except for asymptotically large times since then the coefficients are constant (steady ground state), and hence an appropriate stability criterion has to be introduced. However, as indicated by Caltagirone (1980), there are no universal guidelines for determining such criterion. The second difficulty with this class of methods is the effect the choice of initial conditions has on the computed amplitudes (Foster, 1965, 1968). This is in conflict with the physical intuition that initial conditions should be relatively unimportant. In contrast to the Galerkin projection method, energy methods do not suffer from these problems.

Gresho and Sani (1971) also examined this problem in a fluid layer using two different approaches. The first approach is again based on Galerkin projections, while the second employs the “frozen profile” hypothesis in which time is treated as a parameter. Their stability criterion for the Galerkin projection method is arbitrarily chosen and is based on the z -component of the velocity perturbation. They pointed out that the frozen profile hypothesis is violated for small times, since then the growth rate of the perturbations is small compared to the rate of change of the ground state. However, the frozen profile approximation gets progressively better for large times.

The case in which the surface temperature varies harmonically is considered by Chhuon and Caltagirone (1979) and Caltagirone (1976) for a finite fluid-saturated porous medium. Their analyses are based on the Galerkin projection method, giving a system of ordinary differential equations with *time-periodic* coefficients. The sta-

bility of such problems is then determined by straightforward application of classical Floquet theory (Cesari, 1963), see also Rosenblat and Tanaka (1971).

Here we study the stability of the ground states by means of the energy method in both semi-infinite and finite peat moss layers. In addition, we apply the method of linearised stability and compare both results. We determine the critical system Rayleigh number at which instability occurs and estimate the time delays to instability. We show for the case of a square wave surface temperature in a semi-infinite domain and for a fixed system Rayleigh number that the time delays to instability, as predicted by the energy method and the method of linearised stability with the frozen profile approximation, are close together. Buoyancy flow is shown to occur in a cooling porous layer if the system Rayleigh number Ra exceeds 25. This bound is in agreement with 2D numerical simulations and laboratory experiments.

The chapter is organized as follows. In Section 5.1 we introduce the dimensionless model equations and give explicit formulas for the ground states. Then we discuss in Section 5.2 the stability of the ground states by using the methods as discussed in Chapter 3. These theoretical stability bounds are confirmed by 2D numerical simulations in Section 5.3. To conclude this chapter we compare the stability results with laboratory experiments.

5.1 Problem formulation

We model the peat moss layer as a fully saturated, uniform, isotropic porous medium occupying the three-dimensional strip $\Omega = \{(x, y, z) : -\infty < x, y < \infty, 0 < z < H\}$, where z points vertically downwards, see Figure 5.1 for further details. The boundary $\{z = H\}$, which separates the acrotelm from the catotelm, is considered to be thermally isolated. Since the catotelm is almost impermeable, we impose in addition a no-flow boundary condition. Along the upper boundary $\{z = 0\}$ we apply a time-dependent Dirichlet boundary condition that ranges between \bar{T} , the minimum temperature during the night, and $\bar{T} + \Delta T$, the maximum temperature during the day. Here the temperature difference ΔT is defined accordingly. We do not incorporate evaporation in the model.

5.1.1 Model equations

We suppose that Darcy's law is valid, and that the Oberbeck–Boussinesq approximation is applicable. We also make the other standard assumptions as discussed in Section 1.4. The equation for heat transport is given by

$$\phi \frac{\partial T}{\partial t} + \nabla \cdot (\mathbf{q} T - \mathbb{D}_{\text{eff}} \nabla T) = 0, \quad (5.1.1)$$

where $T = T(x, y, z, t)$ [K] denotes the temperature in the layer, $\mathbf{q} = \mathbf{q}(x, y, z, t)$ [$\text{m} \cdot \text{s}^{-1}$] velocity, ϕ [–] porosity, and $\mathbb{D}_{\text{eff}} := \kappa_T / c_{\text{eff}}$ [$\text{m}^2 \cdot \text{s}^{-1}$] the effective thermal diffusivity. Here c_{eff} [$\text{kg} / (\text{m} \cdot \text{s}^2 \cdot \text{K})$] and κ_T [$\text{m} \cdot \text{kg} / (\text{s}^3 \cdot \text{K})$] are, respectively, the effective heat capacity and the (overall) thermal conductivity.

For the velocity \mathbf{q} we have Darcy's law

$$\mathbf{q} = -\frac{\kappa}{\mu} \left(\nabla p - \rho(T) g \mathbf{e}_z \right), \quad (5.1.2)$$

where $p = p(x, y, z, t)$ [kg/(m·s²)] denotes the pressure, μ [kg/(s·m)] viscosity, κ [m²] permeability and $\rho(T)$ [kg·m⁻³] the temperature dependent density, g [m·s⁻²] the gravity constant. The properties ϕ , \mathbb{D}_{eff} , κ , κ_T , c_{eff} and μ in (5.1.1) and (5.1.2) are assumed to be independent of the temperature T and the spatial coordinates $\{x, y, z\}$. We disregard inertial effects in the Darcy law, i.e. it is assumed that flow velocities are small and that frictional loss, pressure gradient and gravity are instantaneously balanced.

Further, we have the incompressibility condition

$$\nabla \cdot \mathbf{q} = 0 \quad (5.1.3)$$

and the equation of state

$$\rho(T) = \bar{\rho} - \alpha \bar{\rho} (T - \bar{T}), \quad (5.1.4)$$

where α [K⁻¹] is the relative density change per unit temperature and $\bar{\rho}$ the mean density of water.

Equations (5.1.1–5.1.4) are considered in Ω and for all $t > 0$ subject to the boundary conditions

$$\begin{aligned} T &= \Phi(t) \quad \text{and} \quad \mathbf{q} \cdot \mathbf{e}_z = 0 \quad \text{at } z=0, \\ \nabla T \cdot \mathbf{e}_z &= 0 \quad \text{and} \quad \mathbf{q} \cdot \mathbf{e}_z = 0 \quad \text{at } z=H, \end{aligned} \quad (5.1.5a)$$

with $\Phi(t)$ given in Table 5.1, and initial condition

$$T|_{t=0} = \bar{T} + \Delta T \quad \text{in } \Omega. \quad (5.1.5b)$$

When the layer thickness $H \geq \sqrt{\mathbb{D}_{\text{eff}} \tau_0}$, where τ_0 is the duration of the cooling phase, we can recast the flow problem in dimensionless form by introducing the cooling front thickness $\sqrt{\mathbb{D}_{\text{eff}} \tau_0}$ and $\phi \tau_0$, respectively, as scales for length and time and redefining the variables as follows:

$$(RV) \begin{cases} \{x, y, z\} := \frac{\{x, y, z\}}{\sqrt{\mathbb{D}_{\text{eff}} \tau_0}}, & t := \frac{t}{\phi \tau_0}, \\ T := \frac{T - \bar{T}}{\Delta T}, & \mathbf{q} := \frac{\mathbf{q}}{K \alpha \Delta T}, \quad p := \frac{p - \bar{\rho} g z}{\alpha \bar{\rho} g \Delta T \sqrt{\mathbb{D}_{\text{eff}} \tau_0}}, \end{cases}$$

with $K := \bar{\rho} g \kappa / \mu$. The dimensionless thickness h of the layer becomes

$$h = \frac{H}{\sqrt{\mathbb{D}_{\text{eff}} \tau_0}} \geq 1. \quad (5.1.6)$$

Table 5.1. Three different types of the boundary condition $\Phi(t)$ along the upper boundary $\{z=0\}$. The index k is given by $k = 0, 1, 2, \dots$. Note that $t=0$ corresponds to the maximum negative temperature gradient.

	Non-dimensionless form	Dimensionless form
(i)	$\begin{cases} \bar{T} + \Delta T & t=0, \\ \bar{T} & t>0. \end{cases}$	$\begin{cases} 1 & t=0, \\ 0 & t>0. \end{cases}$
(ii)	$\begin{cases} \bar{T} + \Delta T & (2k+1) < \frac{t}{\tau_0} < (2k+2), \\ \bar{T} & 2k < \frac{t}{\tau_0} < (2k+1). \end{cases}$	$\begin{cases} 1 & (2k+1) < t < (2k+2), \\ 0 & 2k < t < (2k+1). \end{cases}$
(iii)	$\bar{T} + \frac{1}{2}\Delta T \left\{ 1 - \sin\left(\frac{\pi t}{\tau_0}\right) \right\} \quad t > 0.$	$\frac{1}{2} \{ 1 - \sin(\pi t) \} \quad t > 0.$

Remark 5.1. The length scale $\sqrt{\mathbb{D}_{\text{eff}}\tau_0}$ characterizes the distance over which a daily “temperature wave” penetrates by conductive heat transport. Note that when $H < \sqrt{\mathbb{D}_{\text{eff}}\tau_0}$, then H and $\phi H^2/\mathbb{D}_{\text{eff}}$ may be used as scales for length and time, respectively.

The reduced variables (RV) allow us to increase the layer thickness h to infinity, leaving the time-scale invariant. This in turn makes comparison of times much easier. Substitution of (RV) in (5.1.1–5.1.3) and (5.1.5) yields

$$\begin{cases} \nabla \cdot \mathbf{q} = 0, & (5.1.7a) \end{cases}$$

$$\begin{cases} \mathbf{q} + \nabla p + T \mathbf{e}_z = \mathbf{0}, & (5.1.7b) \end{cases}$$

$$\begin{cases} \frac{\partial T}{\partial t} + \nabla \cdot (\text{Ra } \mathbf{q} T - \nabla T) = 0, & (5.1.7c) \end{cases}$$

in $\Omega := \{(x, y, z) : -\infty < x, y < \infty, 0 < z < h\}$, and for all $t > 0$, subject to

$$\begin{aligned} T = \Phi(t) \quad \text{and} \quad \mathbf{q} \cdot \mathbf{e}_z = 0 \quad \text{at } z=0, \\ \nabla T \cdot \mathbf{e}_z = 0 \quad \text{and} \quad \mathbf{q} \cdot \mathbf{e}_z = 0 \quad \text{at } z=h, \end{aligned} \quad (5.1.8a)$$

and

$$T|_{t=0} = 1 \quad \text{in } \Omega. \quad (5.1.8b)$$

Here Ra represents the Rayleigh number, which is defined by

$$\text{Ra} = K\alpha\Delta T \sqrt{\frac{\tau_0}{\mathbb{D}_{\text{eff}}}}. \quad (5.1.9)$$

This dimensionless group of model parameters plays a crucial role in the presence or absence of buoyancy flow. Note that the velocity scale can also be written as $\text{Ra} \sqrt{\mathbb{D}_{\text{eff}}/\tau_0}$.

5.1.2 Groundstate solutions

A ground state solution of (5.1.7) is defined as a solution without fluid flow ($\mathbf{q} \equiv \mathbf{0}$) and which satisfies (5.1.8a,b). Since we only consider *steady* periodic flows, initial condition (5.1.8b) is superfluous for boundary conditions that vary in time. A ground-state solution is characterized by a one-dimensional temperature profile $T_0(z, t)$, i.e. there are no horizontal temperature differences and heat transport takes place by conduction only. Depending on $\Phi(t)$, the ground-state solution may be periodic with period 2. We consider the ground-state solutions that correspond to the $\Phi(t)$ in Table 5.1. Boundary conditions (I) and (II) are considered in both a semi-finite and a finite layer, and condition (III) is considered in a semi-infinite domain only. For the derivation of these explicit solutions we refer to Carslaw and Jaeger (1959).

- (I) An impulsive temperature drop at the surface of a semi-infinite layer $[0, \infty)$

$$T_0(z, t) = \text{erf}\left(\frac{z}{2\sqrt{t}}\right), \quad (5.1.10)$$

and a finite layer $[0, h]$

$$T_0(z, t) = 2 \sum_{n=0}^{\infty} \frac{(-1)^n}{\lambda_n^+} e^{-(\lambda_n^+)^2 t/h^2} \cos(\lambda_n^+(h-z)/h), \quad (5.1.11)$$

where $\lambda_n^+ = \frac{1}{2}(2n+1)\pi$.

- (II) A ‘square wave’ at the surface of a semi-infinite layer $[0, \infty)$

$$T_0(z, t) = \frac{1}{2} - \sum_{n=1}^{\infty} \frac{1}{\lambda_n^-} e^{-z\sqrt{\lambda_n^-}} \sin(2\lambda_n^- t - z\sqrt{\lambda_n^-}), \quad (5.1.12)$$

with $\lambda_n^- = \frac{1}{2}(2n-1)\pi$, and a finite layer $[0, h]$

$$T_0(z, t) = \begin{cases} 2 \sum_{n=0}^{\infty} \frac{(-1)^n}{\lambda_n^+} \frac{e^{-(\lambda_n^+)^2 t/h^2}}{1 + e^{-(\lambda_n^+)^2/h^2}} \cos(\lambda_n^+(h-z)/h) & 2k \leq t \leq 2k+1, \\ 1 - 2 \sum_{n=0}^{\infty} \frac{(-1)^n}{\lambda_n^+} \frac{e^{-(\lambda_n^+)^2(t-1)/h^2}}{1 + e^{-(\lambda_n^+)^2/h^2}} \cos(\lambda_n^+(h-z)/h) & 2k+1 \leq t \leq 2k+2. \end{cases} \quad (5.1.13)$$

(III) A harmonic wave at the surface of a semi-infinite layer $[0, \infty)$

$$T_0(z, t) = \frac{1}{2} - \frac{1}{2}e^{-z}\sqrt{\frac{1}{2}\pi} \sin\left(\pi t - z\sqrt{\frac{1}{2}\pi}\right). \quad (5.1.14)$$

Figure 5.2, for example, shows the ground-state solution for $\Phi(t)$ given by (II) in Table 5.1 for a thick layer ($h = \infty$). Since there is no fluid flow, there is a perfect symmetry between diurnal heating and nocturnal cooling.

Remark 5.2. *During the cooling phase, the ground-state solutions are in some sense closely related to each other. For instance, for small times, ground state (5.1.10) resembles (5.1.11) for finite domains. Further, for thin layers (h small) ground state (5.1.13) resembles ground state (5.1.11), and for small times also (5.1.10).*

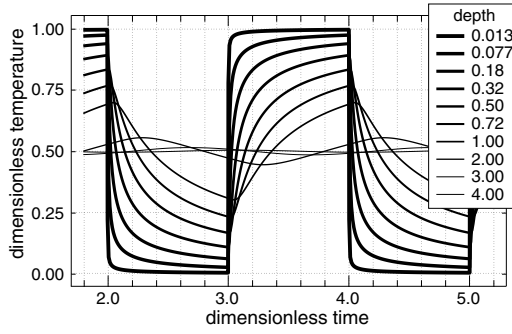


Figure 5.2. Temperature cycles at various dimensionless depths calculated for a thick layer ($H \gg \sqrt{\mathbb{D}_{\text{eff}}\tau_0}$) with heat transport by conduction only. The nocturnal cooling takes place in precisely the same way as the diurnal heating. Only the direction of the heat flow has reversed.

5.2 Stability of the ground states

During the cooling phase a ground state is not necessarily stable, however. Cold surface water may start to fall and warm water from below may start to rise. If the Rayleigh number of the system is sufficiently large, this process amplifies itself and leads to the formation of convection cells.

To analyse the stability of the ground states, we write (as in Section 2.2)

$$T = T_0 + \theta, \quad \mathbf{q} = \mathbf{0} + \mathbf{u}, \quad p = p_0 + \varrho, \quad (5.2.1)$$

with $\mathbf{u} = (u, v, w)^T$, and where T_0 denotes the ground-state solution. Again we require that the perturbations vanish at $\{z = 0\}$ and $\{z = h\}$. Substitution of (5.2.1) in (5.1.7) yields the system (in Ω and for $0 < t < 1$)

$$\left\{ \begin{array}{l} \nabla \cdot \mathbf{u} = 0, \end{array} \right. \quad (5.2.2a)$$

$$\left\{ \begin{array}{l} \mathbf{u} + \nabla \varrho + \theta \mathbf{e}_z = \mathbf{0}, \end{array} \right. \quad (5.2.2b)$$

$$\left\{ \begin{array}{l} \frac{\partial \theta}{\partial t} + R w \frac{\partial T_0}{\partial z} + R \mathbf{u} \cdot \nabla \theta = \Delta \theta. \end{array} \right. \quad (5.2.2c)$$

Equations (5.2.2a) and (5.2.2b) can again be combined to give for θ and w the linear relation

$$\Delta w = -\Delta_{\perp}\theta \quad \text{in } \Omega, \quad (5.2.2d)$$

where Δ_{\perp} denotes the horizontal Laplacian $\partial_{xx} + \partial_{yy}$.

For the stability analysis of the perturbation equations (5.2.2) we follow the same techniques as discussed in Chapter 3. We restrict the stability analysis to the cooling phase only, i.e. we consider the ground-state solutions for $t \in [0, 1]$. Hence, all flow problems considered in this section can be seen as variations of the Lapwood problem (Lapwood, 1948).

We apply the energy method with differential constraint to the perturbation equations (5.2.2) with the techniques from Section 3.2. This leads to the sixth order w equation

$$(D^2 - a^2)^3 w - \frac{a^2 R}{2} \left\{ (D^2 - a^2) \left(\frac{\partial T_0}{\partial z} w \right) + \frac{\partial T_0}{\partial z} (D^2 - a^2) w \right\} = 0, \quad (5.2.3)$$

where a denotes the wavenumber of the perturbation, R the Rayleigh number and where t appears as parameter since $T_0 = T_0(z, t)$. Depending on the problem to be considered, equation (5.2.3) needs to be solved in \mathbb{R}_+ or $(0, h)$. The corresponding boundary conditions are for layers of semi-infinite extent (*thick layers*) given by

$$w(\infty) = w(0) = D^2 w(0) = D^4 w(0) = 0,$$

and for layers of finite thickness they are given by

$$w(0) = D^2 w(0) = w(h) = D^2 w(h) = 0.$$

For a given wavenumber $a > 0$ and time $t > 0$, let $R_E(a, t)$ denote the smallest possible eigenvalue of problem (5.2.3). Further, let

$$R_E(t) := \min_{a>0} R_E(a, t) \quad \text{for } t \in (0, 1).$$

This quantities are depicted in Figure 5.3 for the ground states (5.1.10), (5.1.11), (5.1.12) and (5.1.13) for various h . We discuss the semi-infinite (thick) layer and finite layers separately.

Thick layer

The curve $R_E(t)$ for this case is depicted in Figure 5.3 as a fat dashed line, and this curve functions here as a reference. It can be easily shown that $R_E(t) = R_E^*/\sqrt{t}$ and $a_E(t) = a_E^*/\sqrt{t}$, where $R_E^* := \min_{a>0} R_E(a, 1) \equiv R_E(a_E^*, 1)$. The behaviour of $R_E(t)$ can be understood from the penetration of a cooling front into the layer. After a sudden temperature drop, the depth of the top layer affected by the cooling increases as \sqrt{t} . Initially, a thin cold layer is easily stabilized by conduction and requires a large Rayleigh number to decrease the time delay to instability. In the case

of a smaller Rayleigh number, the time delay to instability is considerably longer. In fact, for Rayleigh numbers below the threshold $R_E(1) = R_E^* \approx 7$ we obtain a time delay that spans the whole night, i.e. the cooling front reaches the bottom of the layer and cooling continuous without fluid flow. It turns out that the threshold of 7 is the minimum bound for stability.

For the square wave surface temperature, we computed the fat solid curve in Figure 5.3. The behaviour of this curve can be understood from the curve corresponding to the impulsive temperature drop. As already indicated in Remark 5.2, initially, the square wave ground state behaves like \sqrt{t} , giving a close resemblance to the fat dashed curve. As time increases, we see that the dashed fat curve deviates from the solid one. During the day, the layer warms up by a (stable) heating front. However, it is impossible to heat up the entire semi-infinite layer during the day, and this implies that there exists a certain depth at which the temperature is at equilibrium. This equilibrium temperature is given by $\bar{T} + \frac{1}{2}\Delta T$ and is entirely due to the periodic behaviour of the ground state, see also Figure 5.2. During the cooling phase, a cooling front penetrates the layer and after a short time it meets the equilibrium temperature. Since the mean temperature is lower than the maximum daytime temperature, the temperature gradient is much smaller resulting in a more stable ground state compared to ground state (5.1.10). This results in a longer time delay to instability. This immediately explains why we find for this case a threshold of approximately $R_E(1) = 17$, which is higher than the one corresponding to an impulsive temperature drop.

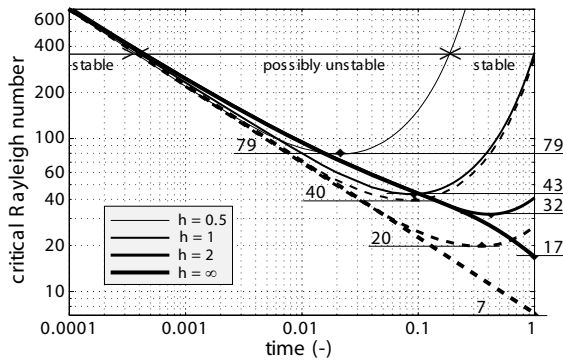


Figure 5.3. The relation between the system Rayleigh number Ra and the time delay to the onset of buoyancy flow for a square wave ground state (solid curves) and an impulsive surface temperature drop (dashed curves). Curves are computed by means of the energy method. Graphs are given for a thick layer ($h = \infty$), $h = 2$ (≈ 16 cm), $h = 1$ (≈ 8 cm) and for a thin layer $h = 0.5$ (≈ 4 cm). For $h = 0.5$ dashed and solid curves coincide.

Layers of intermediate thickness

The stability curves $R_E(t)$ for finite layers are depicted in Figure 5.3 as solid and dashed curves. We first discuss the case with an impulsive temperature drop. For small times ground state (5.1.11) is close to ground state (5.1.10). This explains why all dashed curves coincide with the fat dashed curve. At a later stage, however, the influence of the lower boundary becomes more important. Since on this boundary we have a no-flux condition, the system will stabilize and this results in stability curves that go up in time. For $h = 2$ the threshold is 20 (see Figure 5.3), for $h = 1$ the threshold is 40 and for $h = 0.5$ we find 79. Hence, the thinner the layer, the more stable the system is.

Similar observations can be made for the square wave surface temperature case. For $h = 2$ the threshold is 32 (see Figure 5.3), for $h = 1$ the threshold is 43 and for $h = 0.5$ we find 79. For thin layers (i.e. h small) we observed in Remark 5.2 that (5.1.13) for $0 \leq t \leq 1$ is close to (5.1.11). This explains why for $h = 0.5$ the solid curve coincides with the dashed curve. For Rayleigh numbers below these thresholds, the cooling front reaches the bottom of the layer before the flow sets in, and cooling continues without fluid flow.

Table 5.2. Parameter values for the water-saturated peat moss layer used in the experiment. The corresponding Rayleigh number Ra (cf. (5.1.9)) is 83. Note that α is expressed as a *relative* density change per unit temperature.

Parameter	Value	Unit	Remark
ΔT	10	K	surface temperature difference between day and night, see Section 5.5
τ_0	43200	s	half a day
H	0.15	m	typical acrotelm thickness is 0.1-0.4 m (Van Breemen, 1995)
α	15×10^{-5}	K^{-1}	for water between $10^\circ C$ and $20^\circ C$ (Gebhart et al., 1988)
\mathbb{D}_{eff}	1.4×10^{-7}	$m^2 \cdot s^{-1}$	quotient between thermal conductivity and thermal capacity of water at $10^\circ C$
K	0.1	$m \cdot s^{-1}$	based on measured values, see Appendix 5.A

Remark 5.3. For parameter values in Table 5.2, the length scale is given by 0.078 m.

Comparison with linear stability analysis

For the sake of completeness, we also consider the method of linearised stability analysis, see also Section 3.2. Since here the ground state T_0 depends on time t , such a construction is only possible under the assumption that the rate of change of the ground state is small compared with the growth rate of infinitesimal perturbations. This frozen profile approach leads to a fourth order equation for the perturbation w :

$$(D^2 - a^2)^2 w - a^2 R \frac{\partial T_0}{\partial z} w = 0, \quad (5.2.4)$$

subject to $w(0) = D^2 w(0) = w(\infty) = 0$ for thick layers, and $w(0) = D^2 w(0) = w(h) = D^2 w(h) = 0$ for layers of finite thickness. For a given wavenumber $a > 0$ and time $t > 0$, let $R_L(a, t)$ denote the smallest possible eigenvalue of problem (5.2.4). Further, let

$$R_L(t) := \min_{a>0} R_L(a, t) \equiv R_L(a_L, t) \quad \text{and} \quad a_L = a_L(t) \quad \text{for } t \in (0, 1).$$

These quantities are depicted in Figure 5.4 for the ground states (5.1.10), (5.1.11), (5.1.12) and (5.1.13) for various h .

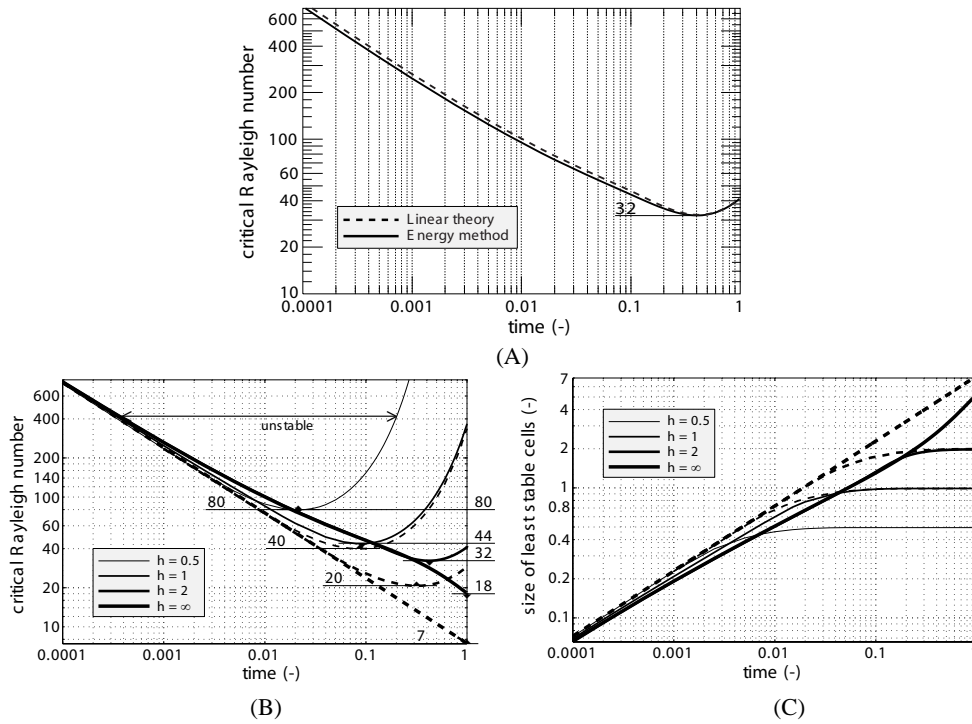


Figure 5.4. (A) Comparison of the energy method and linear stability analysis for $h=2$ and for a square wave surface temperature. (B) The relation between the system Rayleigh number and the time delay to the onset of buoyancy flow for a square wave ground state (solid curves) and an impulsive temperature drop ground state (dashed curves). Note that for $h=0.5$ these curves coincide. Curves are computed by means of the method of linearised stability with the frozen profile approach. (C) The curves in this figure give the size of the least stable perturbations, which is the expected size of appearing cells, as function of time.

The difference between the energy method and the method of linearised stability is depicted in Figure 5.4(A) for the case of a square wave surface temperature in a finite layer ($h=2$). As explained in the introduction, the two stability bounds do not coincide. However, for a fixed Rayleigh number the difference in the time delay to instability is small. Compare also Figure 5.4(B) with Figure 5.3. This means that we find nearly necessary and sufficient conditions for instability.

Let us now consider the square wave surface temperature. For a thick layer ($h=\infty$), the Rayleigh number must exceed 18 to get fluid flow before the end of the night. Fluid flow in a finite layer requires a lower Rayleigh number. For $h=2$ the threshold for *instability* is given by 32, for $h=1$ it is given by 44, and for $h=0.5$ the threshold is 80, see Figure 5.4(B).

For the parameter values in Table 5.2, i.e. for $h=2$, we find $R \approx 83$, which is sufficiently large. For this Rayleigh number Figure 5.4(B) predicts a time delay to the onset of flow of 0.015 which is about 11 minutes ($0.015 \times 43200 = 648$ s). The expected size of the buoyancy cells that become first unstable is found from

Figure 5.4(C), and is approximately 0.5.

Remark 5.4. *The stability analyses in this section does not explicitly make use of the periodicity of the ground-state solutions. In particular, after the unstable period there is a stable period in which the system can recover from instabilities triggered by perturbations during the cooling phase. Taking this ‘restabilizing’ effect into account, the system is less unstable for the period $t \in (0, 2)$ than it would be for $t \in (0, 1)$. This implies that the critical Rayleigh number (7) found in this section is just a lower-bound for instability. To analyse the stability of the system for $t \in (0, 2)$, i.e. for a complete cooling and heating cycle, one should use Floquet theory to find the proper instability threshold.*

5.3 Finite Element simulations

The stability analyses in the previous section provides us with conditions for convective flow, but it does not predict the further development of the convection cells nor their final fate. Therefore we carried out numerical experiments in the two-dimensional truncated flow domain

$$\Omega := \{(x, z) : -h < x < h, 0 < z < h\}.$$

The truncated flow domain needs additional boundary conditions: we impose no-flow and no heat transport along the lateral boundaries. At the surface we prescribe the temperature according to a square wave, i.e. we apply the Dirichlet condition (II) in Table 5.1. To trigger instabilities, we perturb this boundary condition:

$$\Phi(t) = \Phi(t) + \varepsilon \cos(2\pi x) \quad \text{with } \varepsilon = 0.01.$$

Since we only consider steady periodic flows, the initial condition can be taken arbitrarily. The steady periodic flow is then reached after several day and night cycles. For further details concerning the numerical method we refer to Section 4.1. The particle tracking in Figure 5.5 involved spatial interpolation of the finite element flow field $\mathbf{q}(x, z, t)$ (using Renka, 1999) and second order integration of the particle positions along the streamlines with time step 0.001.

The *arrows* in Figure 5.5 show a simulated flow field $\mathbf{q}(x, z, t)$ at several stages of its development. These arrows are just local velocities, however, and in order to follow the moving water we tracked the position of notional “colored dust particles” carried around by the fluid and with initial positions indicated in Figure 5.5(A). A movie of the simulation is available as supporting Movie1 on the PNAS website[★].

Using $\text{Ra} \sqrt{\mathbb{D}_{\text{eff}}/\tau_0}$ as velocity scale (with \mathbb{D}_{eff} and τ_0 from Table 5.2), we can describe the results as follows. Figure 5.5(A) shows a “daytime” situation without flow at about 8 hours before the temperature drop. Buoyancy flow started within a few minutes after the temperature drop, which is in accordance with Figure 5.4(B) for $\text{Ra} = 100$. The cells rapidly grew in height and after about two hours they almost reached the bottom of the layer. After 4.4 hours (Figure 5.5(B)) the fluid velocity

[★] <http://www.pnas.org/cgi/doi/10.1073/pnas.1936122100>

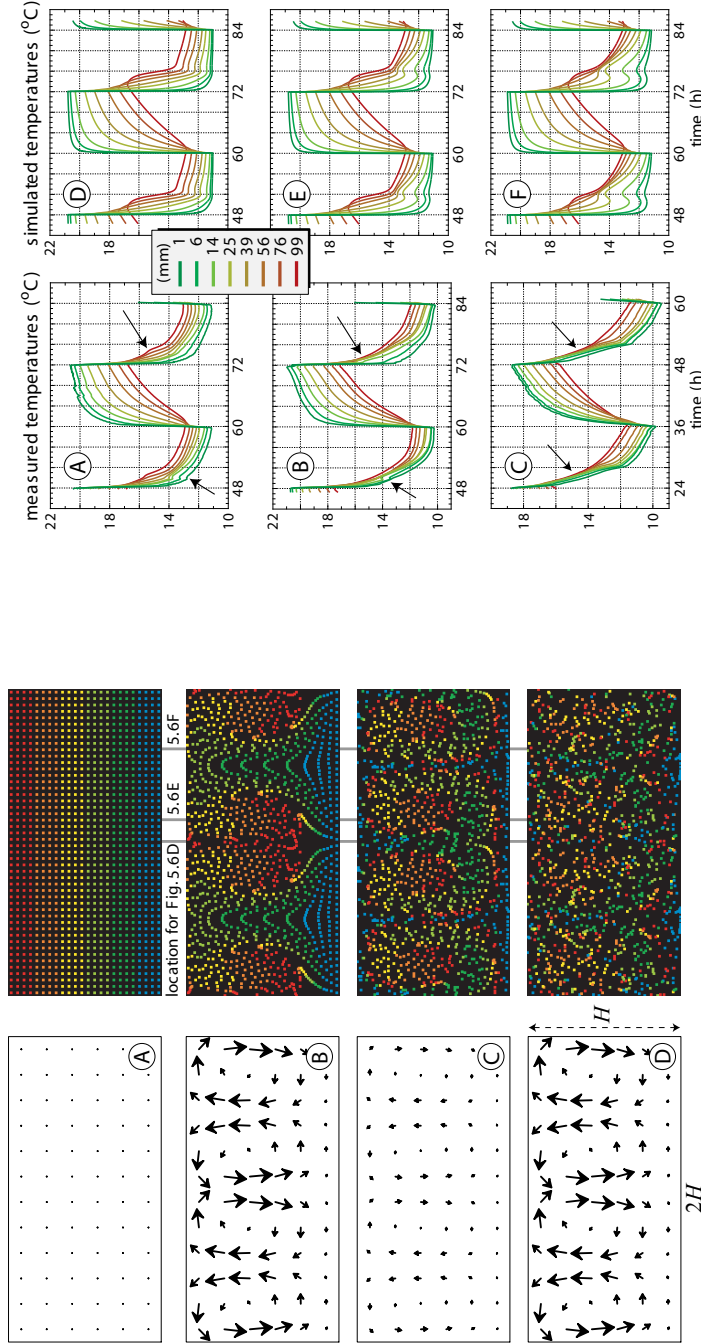


Figure 5.5. Fluid velocity simulated for $Ra = 100$ and $h = 1.92$ (≈ 15 cm). The colored points are notional “dust particles” carried around by the moving water. (A) Daytime situation at 0.7 (8.4 h) before a sudden temperature drop. The tracked particles are at their initial positions. (B) Moment of largest buoyancy flow at 0.363 (4.4 h) after the temperature drop. (C) Situation at the end of the night at 0.93 (11 h) after the temperature drop. (D) The situation of particles traveled over an average distance of $2.93 \times \sqrt{D_{\text{eff}} \tau_0} \approx 23$ cm per day. The three vertical lines show the positions of the daily temperature cycles in Figure 5.6(D-F).

Figure 5.6. Temperature cycles at eight different depths (see legend) in a layer of 15 cm of saturated peat moss. (A), (B), (C) Measurements with a vertical array of eight thermocouples inserted in a cylindrical sample with a diameter of 35 cm. The three figures show consecutive results obtained at three different horizontal positions of the thermocouples. The arrows point to signs of fluid flow during nocturnal cooling. The curves in (C) have been measured for a more slowly changing climate chamber temperature. (D), (E), (F) Temperature cycles simulated for $Ra = 100$ at the locations indicated in Figure 5.5.

reached a maximum of $2.5 \text{ mm}\cdot\text{s}^{-1}$ in the middle of the regions with downward flow. Then the flow gradually slowed down and towards the end of the night the buoyancy cells almost disappeared (Figure 5.5(C)).

The decay of the cells is caused by the absence of a heat source at the bottom of the layer. When the entire layer has cooled down, then the temperature difference is too small to keep the flow going.

The visual impression given by the simulation is that the buoyancy cells turn around once every night. The continuously changing flow field also leads to mixing, however. This is illustrated by Figure 5.5(D), showing the system at precisely 4 days after the situation of Figure 5.5(B). Flow field and temperatures are the same, but a considerable mixing of the dust particles has taken place.

5.4 Analysis of measured temperatures

Laboratory measurements have been carried out in a climate chamber using a cylindrical sample of 50 cm height and 35 cm diameter. During the sampling in the field, the spongy top layer inevitably got disturbed, but after a few weeks in a growth chamber the peat moss had restored itself. Radial heat transport was minimized by 10 cm of insulating foam around the cylinder.

We applied a temperature difference of 10 K between “days” and “nights” of 12 hours. Temperatures were measured with a vertical array of thermocouples installed at eight depths between 1 mm and 99 mm. Details are provided in Appendix 5.A.

Figures 5.6(A), 5.6(B) and 5.6(C) show daily temperature cycles measured at three consecutive horizontal positions of the thermocouple array. At each position, temperature recording was started one or two days after the installation of the thermocouples.

The temperatures in Figures 5.6(D), 5.6(E) and 5.6(F) have been calculated with the above mentioned two-dimensional model for the three locations indicated in Figure 5.5. The convective flow in the simulated system indeed caused the expected asymmetry between diurnal heating and nocturnal cooling (cf. Figure 5.2). The differences between the cooling patterns in Figures 5.6(D), 5.6(E) and 5.6(F) are caused by the differences in direction and size of the nocturnal flow in the model system.

The asymmetry between heating and cooling is also visible in the measured cycles in Figures 5.6(A), 5.6(B) and 5.6(C). The cooling curves lie much closer together than the heating ones and there are also signs of fluid flow, marked by arrows. In Figures 5.6(B) and 5.6(C), for instance, the temperatures between 25 and 99 mm practically coincide between 1 and 3 hours after the temperature drop. This suggests upward flow of relatively warm water similar to the simulated upward flow causing the temperatures of Figure 5.6(F).

In the simulated system the buoyancy cells gradually decay after about 4 hours (cf. Figure 5.5). Both in the measured and simulated temperature profiles we indeed see that the cooling curves “normalize” towards the end of the night. They describe again a normal temperature gradient, without the bumps and coinciding temperatures of the first half of the night.

A consequence of the fluid flow is that nocturnal cooling takes place more effi-

ciently than diurnal heating. Hence, starting at the same temperature everywhere, the *nocturnal heat loss* from the layer will be larger than the *diurnal heat gain*, which means that we have a heat pump. The average temperature of the layer will decrease until nocturnal loss and diurnal gain balance each other.

We indeed find this decrease. For each of the measured curves in Figure 5.6(A), 5.6(B) and 5.6(C) a 24 hour average temperature has been calculated. Figure 5.7 shows the deviation of these averages from the average surface temperature, together with curves for the simulated system. The points for Figure 5.6(A) and 5.6(B) clearly show a decrease with depth, which is somewhat larger than the decrease in the simulated system. The points for Figure 5.6(C) (the open circles) reach a plateau at about -0.7 K. The reason is probably that daily averages were still decreasing in the lower part of the layer.

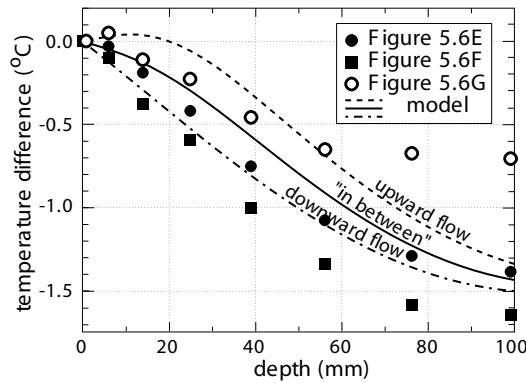


Figure 5.7. Difference between the daily average temperature and the average surface temperature. The points refer to the measurements in Figure 5.6 (using the signal at 1 mm as surface temperature). The curves have been obtained from two dimensional model calculations using $Ra = 100$.

We finally mention a noticeable small effect for upward flow locations. The predicted average temperature just below the surface slightly exceeds the surface average (cf. the curve for upward flow in Figure 5.7).

5.5 Discussion

A simplification made in the model is the use of an insulated lower boundary. Below a real peat moss layer, there is a denser zone (the catotelm) in which conductive heat flow will occur. This dense zone will not have much effect on the onset of flow, however, which is caused by the instability of a cooling top layer. Furthermore, conductive heat flow from below cannot keep the buoyancy cells going for a prolonged period of time, which implies that the decay of the cells is inevitable. Hence, the difference in the lower boundary condition is unlikely to have important consequences.

Quantitative deviations between observed and calculated temperatures in Figure 5.6 may be caused by the absence of dispersion in the model, by heterogeneity of the peat moss layer, by the more gradual surface temperature changes in the experiment and by the limitations of Darcy's law. There is a good qualitative agreement between the measured and calculated temperature patterns, however, and the decrease of the average temperature with depth fits surprisingly well (Figure 5.7).

From the consistency between the mathematical stability analysis, the numerical calculations and the cooling patterns observed, we conclude that buoyancy flow in a peat moss layer will occur provided the Rayleigh number of the system is sufficiently large.

The layer thickness H is of little importance for the stability of the system as long as the dimensionless thickness h exceeds a value of about 2 (cf. Figure 5.4(B)). The reason is the fast decrease of the amplitude of temperature waves with depth (Figure 5.2). There is little difference between a layer with $h = 2$ (≈ 16 cm) and a semi-infinite system.

Temperature changes in the field will usually be more gradual than the sudden transitions in Figures 5.3 and 5.4. A linear stability analysis for a harmonic (sinusoidal) temperature wave is shown in Figure 5.8. The Rayleigh number required for

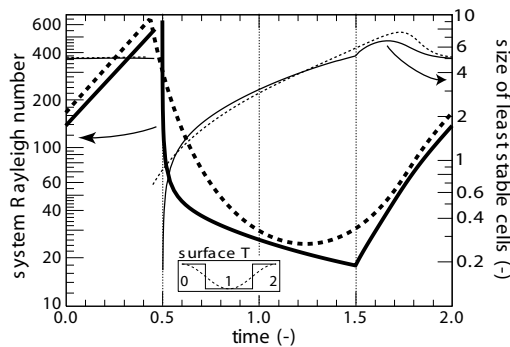


Figure 5.8. The stability of a harmonic wave (dashed curves) and square wave (solid curves) ground states for $h = \infty$ according to linear stability analysis. A small graph (inset) shows the temperature patterns relative to the time axis. The results for the square wave for $0.5 < t < 1.5$ are shown in Figure 5.4(B) at a logarithmic time scale.

fluid flow is 25, which is somewhat higher than the threshold of 18 for a square wave. Numerical simulation for $h = 1.92$ again shows significant mixing for $Ra = 100$ (with an average fluid displacement 14 cm per day, cf. Figure 5.5). For a Rayleigh number of 50, however, the displacement is less than 1 cm per day and there will be little mixing. Movies of these simulations are available as supporting Movie2 and Movie3^{*} at the PNAS website.

Significant mixing apparently requires Rayleigh numbers well above the threshold for instability. Rayleigh numbers in the field will vary with the values of three parameters: the hydraulic conductivity K of the layer, the thermal expansion coefficient α , which increases almost linearly with the (average) temperature in degrees Celsius (Gebhart et al., 1988, Appendix F), and the temperature drop ΔT .

The hydraulic conductivity of $0.1 \text{ m}\cdot\text{s}^{-1}$ in Table 5.2 is a conservative estimate for the peat moss layer in our experiment (see Appendix 5.A). We have used this value, which is also typical for coarse grained materials like gravel (Klute and Dirksen, 1986) to calculate Rayleigh numbers from the minimum temperature T_{\min} and the maximum daily temperature T_{\max} which are available (in Fahrenheit!) from the NATIONAL OCEANIC AND ATMOSPHERIC ADMINISTRATION (NOAA)^{*}. For the average of these two, the value of the thermal expansion coefficient of water has been

^{*} <http://www.pnas.org/cgi/doi/10.1073/pnas.1936122100>

^{*} <ftp.ncdc.noaa.gov/pub/data/global sod>

calculated using

$$\alpha(T) = -\frac{1}{\rho(T)} \frac{d\rho(T)}{dT} \quad (5.5.1)$$

where α is the relative density change per unit temperature in K^{-1} and $\rho(T)$ is the equation of the density of water given in Gebhart et al. (1988, Appendix F). A Rayleigh number is then found from (5.1.9) with the calculated value of α , $\Delta T = T_{\max} - T_{\min}$ and the other parameters taken from Table 5.1.

For about 5625 weather stations for altitudes below 1000 m we calculated the fraction of days in summer with a Rayleigh number above 100. A graph of this probability as function of station latitude is depicted in Figure 5.9.

For coastal stations in Europe and Alaska the probability is below 10%, which implies that buoyancy flow will be rare. For many continental weather stations in Alaska, Canada and Russia, however, summer Rayleigh numbers are above 100 at 30-60% of the days and above 140 at 20-40% of the days.

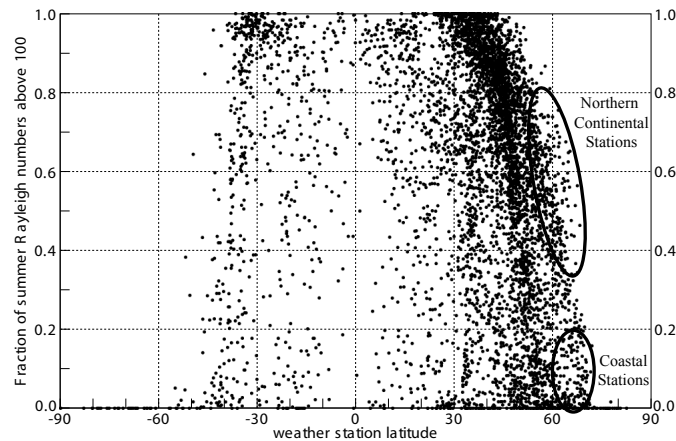


Figure 5.9. Fraction of days in summer with a Rayleigh number above 100, based on NOAA data for 5625 weather stations with altitude below 1000 m and with at least 1 year of data between 1994 and 2002. For stations at the northern hemisphere, June and July have been used as summer, for the southern hemisphere this is December and January.

The relation between a difference in air temperature and a difference in water surface temperature is not straightforward due to effects of radiation, both by day and at night. The daily temperature differences in huge continental areas, however, seem large enough to cause frequent nocturnal buoyancy flow.

The main ecological consequence of this flow is solute transport and mixing of the water. This mixing will be enhanced by dispersion and diffusion and at the time scale of a few days the peat moss layer can be considered as well mixed.

Reeve et al. (2000, 2001) describe the “shallow-flow” and “ground-water” flow hypotheses of peatland hydrology. Clearly, the dominant transport process at a landscape scale is the flow of water which is driven by rainfall and evaporation. The buoyancy flow described in this chapter operates at the much smaller scale of a water-saturated acrotelm, but there it may play an important role. Besides nutrients and

oxygen, also dissolved organic compounds and CO₂ formed by aerobic decay and by methane oxidation (Frenzel and Karofeld, 2000; Dedysh et al., 1998; Smolders et al., 2001) will be carried by the water.

Since buoyancy flow takes place only at night, the solute concentrations involved will show periodic behavior. Periodic behavior of the pH has indeed been observed in the hollows of a mire (Wehrle, 1927; Redinger, 1934), but resolving the roles of fluid flow and peat moss physiology will probably require new field measurements.

We studied nocturnal buoyancy flow in saturated peat moss having in mind the hollows of a mire. In the vast continental wetland areas of the world many other types of terrestrializing vegetation occur in which nocturnal buoyancy flow may play a significant ecological role, either as a mixing mechanism or perhaps even as a heat pump.

Appendix 5.A

Hydraulic conductivity and temperature measurements in peat moss

We measured the hydraulic conductivity using the constant head method (Klute and Dirksen, 1986). We carefully packed green peat moss into a transparent column with a length of 100 cm and a diameter of 9 cm. The hydraulic head over a distance of 61 cm was measured by means of open piezometer tubes. We plotted the measured flux density as function of the hydraulic head and fitted a parabolic curve ($y = ax - bx^2$) to the data. The slope of this curve at the origin (the fitted a value) has been taken as the hydraulic conductivity. For the maximum velocity of $0.25 \text{ cm}\cdot\text{s}^{-1}$ occurring in the simulated buoyancy cells (Figure 5.5), the observed non-linearity corresponds to a decrease in apparent conductivity of about 10%, which seems unlikely to cause important effects.

We measured conductivities of $25.6 \pm 1.8 \text{ cm}\cdot\text{s}^{-1}$ (after packing), $17.3 \pm 1.5 \text{ cm}\cdot\text{s}^{-1}$ (three days later) and $16.6 \pm 3.5 \text{ cm}\cdot\text{s}^{-1}$ (after another 11 days). The dry matter content of the column (determined afterwards) of $5.2 \text{ g}\cdot\text{liter}^{-1}$ is within the range of 3-10 $\text{g}\cdot\text{liter}^{-1}$ reported by Clymo (1970, page 39) for a green and growing peat moss layer. The measurements are depicted in Figure 5.5.

Since *the* conductivity of a peat moss layer obviously does not exist we have put the order of magnitude of $10 \text{ cm}\cdot\text{s}^{-1}$ in Table 5.2. Note that Poiseuille flow through the tube is more than 4 orders of magnitude larger than the flow rates observed, which implies that the peat moss represented a considerable resistance.

The temperatures in a cylindrical peat moss sample of 50 cm were measured in a climate chamber using eight full Copper-Constantan-Copper thermocouples with two junctions, junction 1 and junction 2, say. The wires were supported by a vertical rod and the eight junctions 1 pointed a horizontal distance of 1 cm away from the rod at the vertical positions listed in the legend of Figure 5.6. This reduces effects of the supporting rod and of heat conduction through the thermocouple wires. The eight junctions 2 were collected at the lower tip of the rod, at about 18 cm depth where also a thermistor was installed.

Each thermocouple measured the temperature difference between its first junc-

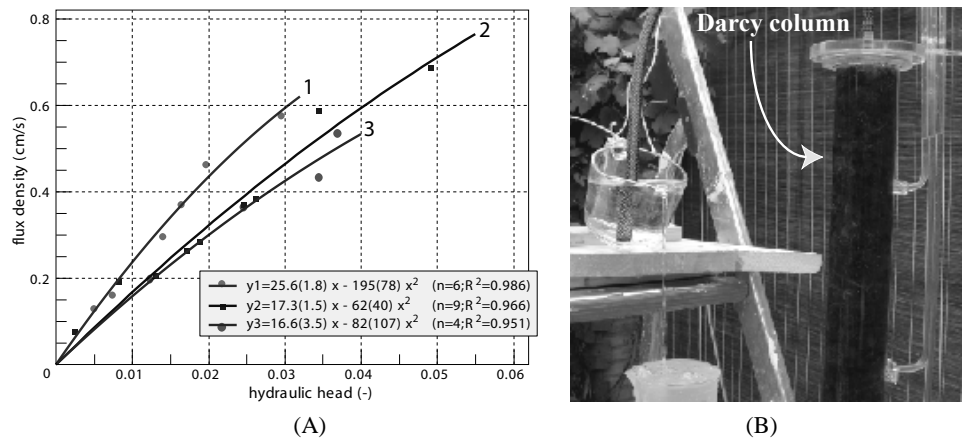


Figure 5.10. (A) Flux density versus hydraulic conductivity. (B) A transparent Darcy column packed with peat moss. The conductivity primarily depends on the packing of the peat moss. Slowly raising the water level while packing prevents unrealistic compaction of the moss.

tion, installed at a specific depth, and its second junction, installed at 18 cm together with the thermistor. Hence, all thermocouples shared the same offset temperature (the slowly changing temperature at thermistor depth) and temperature differences could be easily measured with an accuracy of 0.1 K. The thermocouple signals reverse sign if the system changes from heating to cooling.

References

- Caltagirone, J. P.: 1976, 'Stabilite d'une couche poreuse horizontale soumise a des conditions aux limites periodiques'. *Int. J. Heat Mass Transfer* **19**, 815–220.
- Caltagirone, J.-P.: 1980, 'Stability of a saturated porous media layer subject to a sudden rise in surface temperature: comparison between the linear and energy methods'. *Quart. J. Mech. Appl. Math.* **33**, 47–58.
- Carslaw, H. S. and J. C. Jaeger: 1959, *Conduction of Heat in Solids*. New York: Oxford University Press, 2nd edition.
- Cesari, L.: 1963, *Asymptotic Behavior and Stability Problems in Ordinary Differential Equations*. Berlin: Springer-Verlag.
- Chhuon, B. and J. P. Caltagirone: 1979, 'Stability of a horizontal porous layer with timewise periodic boundary conditions'. *ASME Journal of Heat Transfer* **101**, 244–248.
- Clymo, R. S.: 1970, 'The growth of *Sphagnum*: Methods of measurement'. *J. Ecology* **58**, 13–49.
- Clymo, R. S.: 1984, 'The limits to peat moss growth'. *Phil. Trans. R. Soc. B* **303**, 605–654.
- Clymo, R. S., J. Turunen, and K. Tolonen: 1998, 'Carbon accumulation in peatland'. *Oikos* **81**, 368–388.

- Dedysh, S. N., N. S. Panikov, W. Liesack, R. Großkopf, J. Zhou, and J. M. Tiedje: 1998, 'Isolation of acidophilic methane-oxidizing bacteria from northern peat wetlands'. *Science* **282**, 281–284.
- Foster, T. D.: 1965, 'Stability of a homogeneous fluid cooled uniformly from above'. *Phys. Fluids* **8**, 1249–1257.
- Foster, T. D.: 1968, 'Effect of boundary conditions on the onset of convection'. *Phys. Fluids* **11**, 1257–1262.
- Frenzel, P. and E. Karofeld: 2000, 'CH₄ emission from a hollow-ridge complex in a raised bog: The role of CH₄ production and oxidation'. *Biogeochemistry* **51**, 91–112.
- Gebhart, B., Y. Jaluria, R. L. Mahajan, and B. Sammakia: 1988, *Buoyancy-induced Flows and Transport*. New York: Hemisphere Publishing Corporation.
- Gorham, E.: 1991, 'Northern peatlands: Role in the carbon cycle and probable responses to climatic warming'. *Ecol. Appl.* **1**, 182–195.
- Gresho, P. M. and R. L. Sani: 1971, 'The stability of a fluid layer subjected to a step change in temperature: Transient vs. frozen time analyses'. *Int. J. Heat Mass Transfer* **14**, 207–221.
- Homsy, G. M.: 1973, 'Global stability of time-dependent flows: Impulsively heated or cooled fluid layers'. *J. Fluid Mech.* **60**, 129–139.
- Homsy, G. M.: 1974, 'Global stability of time-dependent flows. Part 2: Modulated fluid layers'. *J. Fluid Mech.* **62**, 387–403.
- Ingram, H. A. P.: 1978, 'Soil layers in mires: Function and terminology'. *J. Soil Science* **29**, 224–227.
- Ingram, H. A. P., D. W. Rycroft, and D. J. A. Williams: 1974, 'Anomalous transmission of water through certain peats'. *J. Hydrol.* **22**, 213–218.
- Klute, A. and C. Dirksen: 1986, 'Hydraulic conductivity and diffusivity: Laboratory methods'. In: A. Klute (ed.): *Methods of Soil Analysis, Part 1, Physical and Mineralogical Methods.*, Agronomy 9. Madison, Wisconsin USA: American Society of Agronomy, pp. 687–734.
- Lapwood, E. R.: 1948, 'Convection of a fluid in a porous medium'. *Proc. Cambridge Phil. Soc.* **44**, 508–521.
- Nield, D. A. and A. Bejan: 1992, *Convection in Porous Media*. New York: Springer-Verlag, second edition.
- Rappoldt, C., G. J. M. Pieters, E. Adema, G. J. Baaijens, and C. J. van Duijn: 2003, 'Buoyancy-driven flow in a peat moss layer as a mechanism for solute transport'. *Proc. Natl. Acad. Sci. USA* **100**, 14937–14942.
- Redinger, K.: 1934, 'Studien zur Ökologie der Moorschlenken'. *Beiheft zum Botanischen Centralblatt* **52, Abt. B**, 232–309.
- Reeve, A. S., D. I. Siegel, and P. H. Glaser: 2000, 'Simulating vertical flow in large peatlands'. *J. Hydrol.* **227**, 207–217.
- Reeve, A. S., D. I. Siegel, and P. H. Glaser: 2001, 'Simulating dispersive mixing in large peatlands'. *J. Hydrol.* **242**, 103–114.
- Renka, R. J.: 1999, 'Algorithm 790: CSHEP2D: Cubic Shepard method for bivariate interpolation of scattered data'. *ACM Transactions on Mathematical Software* **25**, 70–73.
- Rosenblat, S. and G. Tanaka: 1971, 'Modulation of thermal convection instability'. *Phys. Fluids* **14**, 1319–1322.

- Rydin, H. and R. S. Clymo: 1989, 'Transport of carbon and phosphorus-compounds about *Sphagnum*'. *Proc. R. Soc. London Ser. B* **237**, 63–84.
- Smolders, A. J. P., H. B. M. Tomassen, H. W. Pijnappel, L. P. M. Lamers, and J. G. M. Roelofs: 2001, 'Substrate-derived CO₂ is important in the development of *Sphagnum* Spp.'. *New Phytologist* **152**, 325–332.
- Van Breemen, N.: 1995, 'How *Sphagnum* bogs down other plants'. *Trends Ecol. Evol.* **7**, 270–275.
- Wehrle, E.: 1927, 'Studien über Wasserstoffionenkonzentrationsverhältnisse und Besiedelung an Algenstandorten in der Umgebung von Freiburg im Breisgau.'. *Zeitschrift für Botanik* **19**, 209–287.

Chapter 6

The stability of steady flows in unsaturated* soils

About 70 years ago, Lorenzo A. Richards consolidated the efforts of previous generations of soil physicists by formulating a general, macroscopic theory for movement of water in rigid, unsaturated soils (Richards, 1931). The theory of Richards can be formulated within the framework of the modern continuum theory of mixtures, provided that one recognizes from the outset the existence of the separate solid, liquid, and gaseous phases (Raats, 1984). It can also be justified on the basis of the principles of surface tension and viscous flow at the pore scale (Miller and Miller, 1956; Whitaker, 1986). Richards theory combines the balance of mass, expressed in the equation of continuity, and of momentum, expressed in Darcy's law. The Richards equation describes movement of water in unsaturated, isothermal, rigid soils, with the air pressure everywhere and always at atmospheric pressure.

Complications beyond the standard theory may arise from thermal gradients, chemical influences (density variations, limited wettability, electrical charges on solid phase balanced by a diffuse double layer in the fluid phase), mechanical aspects associated with swelling and shrinkage, finite permeability for the gaseous phase, spatial heterogeneity, and temporal changes of the soil. But even in the realm of the standard theory, nonlinearity and the hysteretic nature of the process of water retention remain challenging. In particular, observations of seemingly unstable flows raise the question whether these can be explained in the context of the standard theory or suggest that the theory be extended.

The first studies of unstable flow in porous media dealt with the displacement of oil by water in connection with water-drive processes in oil reservoirs (Engelberts and Klinkenberg, 1951) and the displacement of sugar liquors by water from columns of granular bone charcoal in the process of refining raw sugar (Hill, 1952). Numerous studies soon followed, including studies using displacement of one fluid by another in a Hele-Shaw cell, i.e. two closely spaced parallel glass sheets serving as a model of an oil reservoir (Saffman and Taylor, 1958) and in columns of layered glass parti-

* This chapter is a slightly adapted version of a paper that has appeared in *Transport in Porous Media* (van Duijn et al., 2004)

cles serving as a model for the displacement of air by water in layered soils (Tabuchi, 1961). The earliest studies focussed on the stability of the interface between two fluids, using either simple physical reasoning (Hill, 1952; Tabuchi, 1961) or formal linear stability analysis (Saffman and Taylor, 1958; Chuoke et al., 1959). The latter used the surface tension of the interface between the two fluids as the damping mechanism. In the 1960s and 1970s there was a steadily growing awareness and interest in the stability of movement of water in unsaturated soils. Systematic study of the stability of the displacement of air by water during infiltration and redistribution in soils started in the early 1970s (Hill and Parlange, 1972; Raats, 1973b; Parlange and Hill, 1976; Philip, 1975a,b) and has been pursued ever since, theoretically as well as experimentally (see recent reviews of some aspects by de Rooij (2000), Parlange et al. (2002), and Hendrickx and Flury (2001)).

Raats (1973b) reviewed early observations and presented some tentative explanations. He focussed on the infiltration process and extended the Green–Ampt approach pioneered by Tabuchi (1961) to discuss effects of soil crusts, vertical heterogeneity of hydraulic conductivity, air pressure build-up ahead of wetting front, hysteresis, and wettability. Generally unstable displacement of air by water arises if the pressure gradient is such that it opposes the advance of the wetting front, but less so as the front advances. Theoretical studies and observations in the laboratory and the field have shown that this may occur for infiltration at a rate less than the hydraulic conductivity at saturation, either due to limited supply of water or due to the presence of a surface crust, infiltration of ponded water with compression of air ahead of the wetting front, infiltration in soils with a fine textured layer overlying a coarse textured layer, infiltration in water repellent soils, and during redistribution of water following infiltration (Raats, 1973b; de Rooij, 2000; Hendrickx and Flury, 2001; Parlange et al., 2002).

Philip (1975a,b) analyzed the stability of the Green–Ampt model for vertical infiltration, using linear stability analysis with a macroscopic surface tension of the wetting front as a damping mechanism, thus essentially following Saffman and Taylor (1958) and Chuoke et al. (1959). Rather than applying linear stability analysis to the equation of motion of a Green–Ampt sharp interface, Diment and Watson (1982, 1983, 1985) applied it directly to the Richards equation. Their numerical solution indicated infiltration to be stable (Diment and Watson, 1983). Egorov et al. (2002) confirmed this analytically for the long time, diffuse front travelling wave solution for infiltration into initially wet soil. However, for infiltration into an initially dry soil, they found the long time, sharp front travelling wave solution to be unstable for any perturbation mode. Without the surface tension damping mechanism, Saffman and Taylor (1958), Chuoke et al. (1959), and Philip (1975a,b) would have reached the same conclusion for the motion of the sharp interfaces. Egorov et al. (2002) demonstrated that the extension of the Richards equation by Hassanizadeh and Gray (1990, 1993), to take into account dynamic memory effects, may provide a damping mechanism. This critically depends on the relaxation parameter involved.

Kapoor (1996) derived stability criteria for the various types of steady, vertical upward and downward flows in homogeneous, unsaturated porous media. Using the energy method, he showed that purely gravitational flows are stable. For the other types of steady, vertical flows he derived criteria for stability/instability. Based on experimental evidence that observed fingers often are long and narrow, he assumed

that the vertical length scale of the perturbations is large compared to the horizontal length scale and on that basis simplified the perturbation equation. However, linear stability analysis concerns the process of initiation of the fingers and in that stage the vertical length scale of the perturbations is still small. The observed long and narrow fingers are always connected with infiltration and redistribution processes reviewed briefly above. Therefore in this chapter we reconsider the problem studied by Kapoor, without ignoring the vertical gradients. Like Kapoor, we ignore possible effects of hysteresis. Our analysis will show that the vertical gradients play an essential role in the analysis. In Section 6.7 we will state the conclusions of Kapoor and compare them with our results.

In Section 6.1, we start with three equivalent formulations of the model for flow of water in unsaturated soils, namely the pressure head, water content, and matric flux potential formulations. Making the equations dimensionless by using the limiting saturated reference state and the layer thickness, we introduce the dimensionless Rayleigh number as the ratio of the layer thickness and the capillary length scale of the soil. To illustrate general results and derive special results, use is made of several representative classes of soils defined by specific water retention and hydraulic conductivity characteristics, i.e. the Broadbridge–White, Burgers, and Gardner classes of soils.

In Section 6.2 the steady background flows are analyzed. In Subsection 6.2.1 we prove uniqueness of steady flows for all classes of soils with a Lipschitz continuous relationship between the hydraulic conductivity and the matric flux potential and show that among these are the Broadbridge–White, Burgers, and Gardner classes of soils. In Subsection 6.2.2 we identify the various types of steady vertical flows.

Since the uniqueness theorem suggests stability of steady vertical flows, we concentrate in this chapter on deriving estimates of the rate of decay of perturbations of these steady flows. In Subsection 6.3.1 we prove, again subject to certain requirements concerning the relationship between the hydraulic conductivity and the matric flux potential, the stability of steady vertical flows, and, moreover, show that the squared of the weighted L^2 -norm of the perturbation of the matric flux potential decays exponentially with time. In Subsection 6.3.2, we show that the requirements for this stability theorem are fulfilled by the Broadbridge–White, Burgers, and Gardner classes of soils and the corresponding estimates of the decay rates are derived.

In Section 6.4 we consider estimates of the decay rate in terms of the squared of the L^2 -norm of the perturbation of the saturation. First we derive such an estimate directly from the estimate in terms of the perturbation of the matric flux potential. The resulting saturation based estimate shows that transient growth may occur, except for the Burgers class of soils. However, in Subsection 6.4.2 it is also indicated that in some cases a direct and sharp saturation based estimate can be obtained from the linearized equation for the perturbation of the saturation. In Appendix 6.B this is worked out in detail for the Gardner class of soils. At the end of Subsection 6.4.2 it is shown that the steady solutions for the Burgers class of soils are nonlinearly stable with respect to arbitrary finite-amplitude perturbations.

In Section 6.5 we consider an extension of the Richards equation to take into account dynamic memory effects, in a form suggested by Hassanizadeh and Gray (1990, 1993). Using the saturation formulation, we show that linear stability of the

steady solutions corresponding to the standard Richards equation implies linear stability of the steady solutions of the extended equation.

Finally in Section 6.6, again for the Burgers class of soils, transient growth is studied in more detail, using a norm based on the pressure head.

6.1 Problem formulation

In this chapter we use the convention that a prime (') denotes differentiation with respect to the argument. We restrict ourselves to a flow domain Ω which is bounded in the horizontal plane and which has vertical boundaries between $z = 0$ and $z = H$, i.e.

$$\Omega = \{(x, y, z) : (x, y) \in \Omega_{\perp}, 0 < z < H\},$$

with z being the vertical coordinate taken positive downward and where Ω_{\perp} is a bounded set in \mathbb{R}^2 with a piecewise smooth boundary $\partial\Omega_{\perp}$.

Assuming the water to be incompressible, the balance of mass can be written as a volumetric balance equation

$$\frac{\partial\theta}{\partial t} = -\nabla \cdot \mathbf{F}, \quad (6.1.1)$$

where t is the time, ∇ is the vector differential operator, θ is the volumetric water content, $\mathbf{F} = \theta \mathbf{v}$ is the volumetric flux of the water, with \mathbf{v} being the velocity of the water.

The pressure head Ψ of the water is defined by

$$\Psi = \frac{(p_w - p_g)}{\gamma g} = -\frac{p^c}{\gamma g}, \quad (6.1.2)$$

where p_w and p_g are the pressures of the aqueous and gaseous phases, p^c is the capillary pressure, γ is the density of water, and g is the gravitational constant. In the theory of Richards, it is assumed that the pressure of the gaseous phase is spatially uniform and constant. Furthermore, it is assumed that the pressure head Ψ is a monotonically increasing function of the volumetric water content θ . In this chapter we ignore the generally hysteretic nature of the $\Psi(\theta)$ relationship. The volumetric water capacity c is defined as

$$c = \frac{d\theta}{d\Psi}. \quad (6.1.3)$$

Darcy's law for the volumetric flux \mathbf{F} of the water has three alternative forms:

$$\mathbf{F} = -k\nabla\Psi + k\mathbf{e}_z = -D\nabla\theta + k\mathbf{e}_z = -\nabla\Phi + k\mathbf{e}_z. \quad (6.1.4)$$

Here, k is the hydraulic conductivity, $\mathbf{e}_z = \nabla_z$ is the unit vector field in the z -direction, $D = k d\Psi/d\theta$ is the soil water diffusivity, and Φ is the matric flux potential or Kirchhoff potential defined by

$$\Phi = \int_{-\infty}^{\Psi} k \, d\Psi = \int_0^{\theta} D \, d\theta . \quad (6.1.5)$$

The volumetric flux \mathbf{F} is the sum of a matric component $-k\nabla\Psi = -D\nabla\theta = -\nabla\Phi$ and a gravitational component $k\mathbf{e}_z$. The matric component of the volumetric flux is given by the gradient of Φ and therefore it is appropriate to call Φ the matric flux potential. A transformation of the type (6.1.5) was given around 1880 by Kirchhoff in his lectures on heat conduction (Kirchhoff, 1894). For this reason, Φ is often called the Kirchhoff potential and the transformation from Ψ and θ to Φ is then referred to as the Kirchhoff transform.

The hydraulic conductivity k is a monotonically increasing function of the volumetric water content θ . Based on this $k(\theta)$ relationship, we introduce

$$v = \frac{dk}{d\theta} \quad (6.1.6)$$

as the kinematic wave speed of the water.

Let θ_0 be the volumetric water content at saturation and θ_r the irreducible volumetric water content. Using the saturated state as the reference state, the (apparent) saturation S is defined as

$$S = \frac{\theta - \theta_r}{\theta_0 - \theta_r} , \quad (6.1.7)$$

so that $S(\theta_r) = 0 \leq S \leq S(\theta_0) = 1$. Using the layer thickness H and the saturated reference state, we redefine the variables as follows:

$$(RV1) \left\{ \begin{array}{l} \{x, y, z\} := \frac{\{x, y, z\}}{H} , \\ \nabla := H\nabla , \\ t := \frac{t}{t_{\text{ref}}} = \frac{t}{H^2/D_0} , \\ \mathbf{F} := \frac{\mathbf{F}}{|\mathbf{F}_{\text{ref}}|} = \frac{\mathbf{F}}{k_0} , \\ \Psi := \frac{\Psi}{\Psi_{\text{ref}}} = \frac{\Psi}{(\theta_0 - \theta_r)/c_0} , \\ \Phi := \frac{\Phi}{\Phi_{\text{ref}}} = \frac{\Phi}{D_0(\theta_0 - \theta_r)} , \end{array} \right. \quad (RV2) \left\{ \begin{array}{l} c := \frac{c}{c_0} , \\ k := \frac{k}{k_0} , \\ D = \frac{k}{c} := \frac{D}{D_0} = \frac{k/k_0}{c/c_0} , \\ v := \frac{v}{v_0} . \end{array} \right.$$

Since $\Psi \rightarrow 0$ as $S \rightarrow 1$, the scaling of Ψ cannot be based on its value in the reference state. Instead $(\theta_0 - \theta_r)/c_0$ serves as the capillary length scale. The redefinitions (RV2) of c , k , D , and v imply $c = k = D = v = 1$ when $S = 1$.

In terms of these reduced variables, the volumetric mass balance and the three forms of Darcy's law become

$$\frac{\partial S}{\partial t} = -\nabla \cdot (R \mathbf{F}) , \quad (6.1.8)$$

and

$$R \mathbf{F} = -k \nabla \Psi + R k \mathbf{e}_z = -D \nabla S + R k \mathbf{e}_z = -\nabla \Phi + R k \mathbf{e}_z , \quad (6.1.9)$$

in $\Omega := \{(x, y, z) : (x, y) \in \Omega_{\perp}, 0 < z < 1\}$. Here R denotes the dimensionless Rayleigh number defined as

$$R = \frac{k_0 H}{(\theta_0 - \theta_r) D_0} = \frac{H}{(\theta_0 - \theta_r) / c_0} . \quad (6.1.10)$$

Note that the Rayleigh number R is the ratio of the layer thickness and the capillary length scale $(\theta_0 - \theta_r) / c_0$.

Substituting Equations (6.1.9) into Equation (6.1.8) gives three alternative forms of the Richards equation, namely the pressure head, saturation, and matric flux potential forms, respectively

$$(RE) \left\{ \begin{array}{l} \frac{\partial S(\Psi)}{\partial t} = c(\Psi) \frac{\partial \Psi}{\partial t} = \nabla \cdot (k(\Psi) \nabla \Psi - R k(\Psi) \mathbf{e}_z) , \\ \frac{\partial S}{\partial t} = \nabla \cdot (D(S) \nabla S - R k(S) \mathbf{e}_z) , \\ \frac{\partial S(\Phi)}{\partial t} = \frac{1}{D(\Phi)} \frac{\partial \Phi}{\partial t} = \nabla \cdot (\nabla \Phi - R k(\Phi) \mathbf{e}_z) . \end{array} \right.$$

Remark 6.1. Sometimes, alternative forms of these equations are used. For instance, Kapoor (1996) writes instead of (RE)₁, after redefining our pressure head to his suction head $\Psi := -\Psi$,

$$c(-\Psi) \frac{\partial \Psi}{\partial t} = k(-\Psi) \Delta \Psi + \frac{dk(-\Psi)}{d\Psi} \nabla \Psi \cdot (\nabla \Psi + R \mathbf{e}_z) .$$

Introducing $\bar{c}(\Psi) := c(-\Psi)$, $\bar{k}(\Psi) := k(-\Psi)$, and $\bar{b}(\Psi) := -\frac{dk(-\Psi)}{d\Psi}$, we find exactly Kapoor's formulation (3a-b):

$$\bar{c}(\Psi) \frac{\partial \Psi}{\partial t} + \bar{b}(\Psi) \nabla \Psi \cdot (\nabla \Psi + R \mathbf{e}_z) - \bar{k}(\Psi) \Delta \Psi = 0 . \quad (6.1.11)$$

6.1.1 Classes of soils

In the context of the Richards equation, the relationships among the saturation S , pressure head Ψ , and hydraulic conductivity k define the hydraulic properties of a

soil. Different classes of soils have been identified with different functions approximating the physical properties. In this chapter we restrict ourselves to three typical classes.

One soil class is defined by Broadbridge and White (1988),

$$(I) \left\{ \begin{array}{l} k(S) = \frac{C-1}{C-S} S^2, \\ D(S) = \frac{(C-1)C}{(C-S)^2}, \\ \Psi(S) = 1 - \frac{1}{S} - \frac{1}{C} \ln \frac{C-S}{(C-1)S}, \\ \Phi(S) = \frac{(C-1)S}{C-S}, \end{array} \right.$$

where $1 < C < \infty$. This soil class is usually referred to as the versatile nonlinear model. Note that $\Psi(S)$ has an inflection point at $S = \frac{2C}{3}$, for $1 < C \leq \frac{3}{2}$.

We also consider the soil class defined by Clothier et al. (1981),

$$(II) \left\{ \begin{array}{l} k(S) = S^2, \\ D(S) = 1, \\ \Psi(S) = 1 - \frac{1}{S}, \\ \Phi(S) = S, \end{array} \right.$$

Note that with (II)_{1,2} Equation (RE)₂ is Burgers equation for inviscid flows. Therefore we refer to (II) as the Burgers class of soils. For this class of soils the saturation and matric flux potential coincide. Note that the Burgers class of soils corresponds to the limiting case $C \rightarrow \infty$ of the versatile nonlinear model.

Finally we consider the Gardner class of soils, where

$$(III) \left\{ \begin{array}{l} k(S) = \frac{S^2}{(1-S)^2 + S^2}, \\ D(S) = \frac{1}{(1-S)^2 + S^2}, \\ \Psi(S) = 1 - \frac{1}{S}, \\ \Phi(S) = \arctan(2S-1) + \frac{\pi}{4}, \end{array} \right.$$

Originally only the $k(\Psi)$ relationship given by (III)₁ was introduced to study steady upward and downward flow for this class of soils (Gardner, 1958; Raats, 1973a). Note that $k(S)$ has an inflection point at $S = \frac{1}{2}$.

6.2 Steady-state background flows

Problem (RE) is a nonlinear evolution equation. It is well known that certain nonlinear evolution equations may have multiple steady solutions and each of these solutions has its own stability property. Once a steady-state is qualified and quantified as being unstable, the system bifurcates from this solution to a neighboring steady solution, which is completely different from the first one. Note that this concept of instability only makes sense when multiple steady solutions exist.

Hence, the first question that needs to be answered is: has Richards' equation (RE) subject to given boundary data multiple steady solutions?

In the following subsections we show for Broadbridge–White, Burgers, and Gardner soils uniqueness and some important properties of the steady solutions of (RE). In this chapter we restrict ourselves to constant boundary data, which we give in terms of the saturation:

$$(BC) \begin{cases} S|_{z=0} = S_T \\ S|_{z=1} = S_B \end{cases} \quad \text{for all } x, y \in \Omega_{\perp}, t > 0,$$

and along the vertical boundary we impose $\frac{\partial S}{\partial \mathbf{n}} = \nabla S \cdot \mathbf{n} = 0$ for all $t > 0$.

6.2.1 Uniqueness of steady vertical flows

We first note that the different formulations in (RE) are equivalent. For instance, (RE)₂ and (RE)₃ are equivalent since

$$\Phi = f(S) = \int_0^S D(S) \, dS \quad (D(S) > 0) \quad (6.2.1)$$

is strictly increasing. Hence $S = f^{-1}(\Phi)$ exists and uniqueness of solutions of (RE)₃ implies uniqueness of solutions of (RE)₂. We show here uniqueness for (RE)₃ because for steady flow in the Φ -formulation only the gravity term is nonlinear. Thus we consider the problem

$$(P1) \begin{cases} \nabla \cdot (\nabla \Phi - R \kappa(\Phi) \mathbf{e}_z) = 0 & \text{in } \Omega =: \Omega_{\perp} \times (0, 1), \\ \frac{\partial \Phi}{\partial \mathbf{n}} = 0 & \text{on } \partial \Omega_{\perp} \times (0, 1), \\ \Phi = \Phi_{BC} = f(S_{BC}) & \text{on } \Omega_{\perp} \times (\{0\} \cup \{1\}), \end{cases}$$

where $\kappa(\Phi) := k(S(\Phi))$, $\frac{\partial \Phi}{\partial \mathbf{n}} = \nabla \Phi \cdot \mathbf{n}$, with \mathbf{n} the outward normal at $\partial \Omega_{\perp} \times (0, 1)$, and where S_{BC} denotes boundary conditions (BC). We prove the following general statement:

Theorem 6.2. Let $M := f(1)$ and let $\kappa(\Phi) : [0, M] \rightarrow [0, \infty)$ be Lipschitz continuous: i.e. there exists a constant $L > 0$ such that

$$|\kappa(\Phi_1) - \kappa(\Phi_2)| \leq L|\Phi_1 - \Phi_2| ,$$

for all $0 \leq \Phi_1, \Phi_2 \leq M$. Then problem (P1) has a unique solution for each $R > 0$. It is given by the one-dimensional profile $\Phi_0 = \Phi_0(z)$ satisfying

$$(P2) \begin{cases} \frac{d}{dz} \left(\frac{d\Phi_0}{dz} - R\kappa(\Phi_0) \right) = 0 & \text{for } 0 < z < 1 , \\ \Phi_0(0) = f(S_T) =: \Phi_T , \\ \Phi_0(1) = f(S_B) =: \Phi_B . \end{cases}$$

Proof. Since (P1)₁ is in divergence form, we follow Gilbarg and Trudinger (1977) to prove a comparison result and uniqueness. For technical reasons we extend the domain of definition of κ . Let

$$\widehat{\kappa}(\Phi) = \begin{cases} 0 & \text{for } \Phi < 0 , \\ \kappa(\Phi) & \text{for } 0 \leq \Phi \leq M , \\ \kappa(M) = 1 & \text{for } \Phi \geq M . \end{cases}$$

The function $\widehat{\kappa}$ is clearly uniformly Lipschitz continuous on \mathbb{R} . Now suppose Φ_1 and Φ_2 are two solutions of Problem (P1), with ordered boundary data: i.e.

$$\Phi_1 \geq \Phi_2 \quad \text{at } \Omega_{\perp} \times (\{0\} \cup \{1\}) .$$

We show below that

$$\Phi_1 \geq \Phi_2 \quad \text{in } \bar{\Omega} .$$

Let $\delta > 0$ (fixed) and set

$$\varphi = \frac{w}{\delta + w} , \quad w = (\Phi_1 - \Phi_2 - \delta)_+ \geq 0 ,$$

where $(u)_+ = \max\{u, 0\}$. We test (P1)₁ for the difference $\Phi_1 - \Phi_2$ with φ :

$$\int_{\Omega} \left\{ \nabla(\Phi_1 - \Phi_2) - R(\widehat{\kappa}(\Phi_1) - \widehat{\kappa}(\Phi_2))\mathbf{e}_z \right\} \cdot \nabla\varphi = 0 .$$

This gives

$$\delta \int_{\{\Phi_1 - \Phi_2 > \delta\}} \frac{|\nabla w|^2}{(\delta + w)^2} - \delta R \int_{\{\Phi_1 - \Phi_2 > \delta\}} \frac{\partial_z w}{(\delta + w)^2} (\widehat{\kappa}(\Phi_1) - \widehat{\kappa}(\Phi_2)) = 0 .$$

Since

$$\begin{aligned} R \int_{\{\Phi_1 - \Phi_2 > \delta\}} \frac{\partial_z w}{(\delta + w)^2} (\widehat{\kappa}(\Phi_1) - \widehat{\kappa}(\Phi_2)) &\leq \\ &\leq \frac{1}{2} \int_{\{\Phi_1 - \Phi_2 > \delta\}} \frac{|\nabla w|^2}{(\delta + w)^2} + \frac{R^2}{2} \int_{\{\Phi_1 - \Phi_2 > \delta\}} \frac{(\widehat{\kappa}(\Phi_1) - \widehat{\kappa}(\Phi_2))^2}{(\delta + w)^2}, \end{aligned}$$

and $\delta + w = \Phi_1 - \Phi_2$ on $\{\Phi_1 - \Phi_2 - \delta > 0\}$, we find

$$\int_{\{\Phi_1 - \Phi_2 > \delta\}} \frac{|\nabla w|^2}{(\delta + w)^2} \leq R^2 \int_{\{\Phi_1 - \Phi_2 > \delta\}} \frac{(\widehat{\kappa}(\Phi_1) - \widehat{\kappa}(\Phi_2))^2}{(\Phi_1 - \Phi_2)^2}.$$

Since $\widehat{\kappa}$ is Lipschitz-continuous with constant L , we have

$$\int_{\{\Phi_1 - \Phi_2 > \delta\}} \frac{|\nabla w|^2}{(\delta + w)^2} \leq R^2 L^2 \text{meas}(\Omega).$$

Next we apply the Poincaré inequality to

$$\left| \ln \left(1 + \frac{w}{\delta} \right) \right| = |\ln(\delta + w) - \ln(\delta)|$$

and obtain that there exists $K > 0$ such that

$$\int_{\Omega} \left| \ln \left(1 + \frac{w}{\delta} \right) \right|^2 \leq K \quad (\text{for all } \delta > 0).$$

Letting $\delta \rightarrow 0$, we see that w must vanish in Ω , that is $\Phi_1 \leq \Phi_2$. Since

$$0 = f(0) \leq \Phi \leq f(1) = M,$$

and since constants satisfy the equation, we immediately deduce for any solution of (P1)

$$0 \leq \Phi \leq M \quad \text{in } \bar{\Omega}.$$

As a consequence we can replace $\widehat{\kappa}$ by κ . Now suppose Φ_1 and Φ_2 are two solutions of (P1) for the same boundary data. The above comparison argument then implies both $\Phi_1 \leq \Phi_2$ and $\Phi_1 \geq \Phi_2$ in $\bar{\Omega}$. Hence $\Phi_1 = \Phi_2$ in $\bar{\Omega}$. ■

For Broadbridge–White soils the matric flux potential is given by (I)₄. Hence $S = f^{-1}(\Phi) = \frac{C\Phi}{\Phi + C - 1}$ implying $\kappa(\Phi) = \frac{C\Phi^2}{\Phi + C - 1}$ with $0 \leq \Phi \leq M = 1$. This function is Lipschitz continuous since

$$\begin{aligned} |\kappa(\Phi_1) - \kappa(\Phi_2)| &= \left| \frac{C(\Phi_1\Phi_2 + (\Phi_1 + \Phi_2)(C - 1))(\Phi_1 - \Phi_2)}{(\Phi_1 + C - 1)(\Phi_2 + C - 1)} \right| \leq \\ &\leq \frac{C(2C - 1)}{(C - 1)^2} |\Phi_1 - \Phi_2| =: L(C) |\Phi_1 - \Phi_2|, \end{aligned}$$

for all $0 \leq \Phi_1, \Phi_2 \leq 1$. For $1 < C < \infty$ we have $2 < L(C) < \infty$. Hence the steady solutions for the Broadbridge–White class of soils, including the Burgers class of soils as a limiting special case, are unique.

For Gardner class soils the matric flux potential is given by (II)₄. Hence $S = f^{-1}(\Phi) = \frac{1}{1+\cot(\Phi)}$, implying $\kappa(\Phi) = \sin^2(\Phi)$ for $0 \leq \Phi \leq M = \frac{\pi}{2}$. Hence

$$|\kappa(\Phi_1) - \kappa(\Phi_2)| = \frac{1}{2} |\cos(2\Phi_1) - \cos(2\Phi_2)| \leq |\Phi_1 - \Phi_2| ,$$

for all $0 \leq \Phi_1, \Phi_2 \leq \frac{\pi}{2}$. We conclude that the steady solutions for the Gardner class of soils are also unique.

The theorem rules out any other stationary solution satisfying the boundary conditions. In particular finger-like solutions, describing steady convection cells, do not exist. The theorem also suggests that problem (P2) describes the large time behaviour of transient solutions for any $R > 0$. With the exception of chaotic or temporally periodic behaviour, what else could be possible large time behaviour? In the next section we show that indeed problem (P2) describes the large time behaviour and we give rates of convergence.

6.2.2 Classification of steady vertical flows

To obtain the steady solution, we integrate (P2)₁ with respect to z , i.e.

$$\frac{d\Phi_0}{dz} = R \{ \kappa(\Phi_0) - F \} , \quad (6.2.2)$$

where RF denotes the flux. The solutions of (6.2.2) subject to (P2)₂ and (P2)₃, can be classified as follows (see also Figure 6.1):

The case $\Phi_T > \Phi_B$, or equivalently $S_T > S_B$.

- (1) Downward flow aided by capillarity: for this case $\Phi'_0(z) < 0$. From (6.2.2), using the fact that $\kappa(\Phi_0)$ is a monotonically increasing function, and since $R > 0$ we find $F > \kappa(\Phi_T) \geq \kappa(\Phi_0)$.

The case $\Phi_T \equiv \Phi_B$, or equivalently $S_T \equiv S_B$.

- (2) Purely gravitational downward flow: for this case we have $\Phi'_0(z) \equiv 0$. From (6.2.2) it then follows that $F = \kappa(\Phi_T) = \kappa(\Phi_B)$.

The case $\Phi_T < \Phi_B$, or equivalently $S_T < S_B$.

- (3) Downward flow opposed by capillarity: we now have $\Phi'_0(z) > 0$. By again using (6.2.2), the monotonicity of $\kappa(\Phi_0)$, and since we still deal with a downward flow, we obtain $0 < F < \kappa(\Phi_T) \leq \kappa(\Phi_0)$. These flows only exist when $\Phi_T > 0$.
- (4) Equilibrium: for this case $F \equiv 0$. Note that this case is only possible when $S_T < S_B$. From (6.2.2) we derive $\Phi'_0(z) = R \kappa(\Phi_0)$.

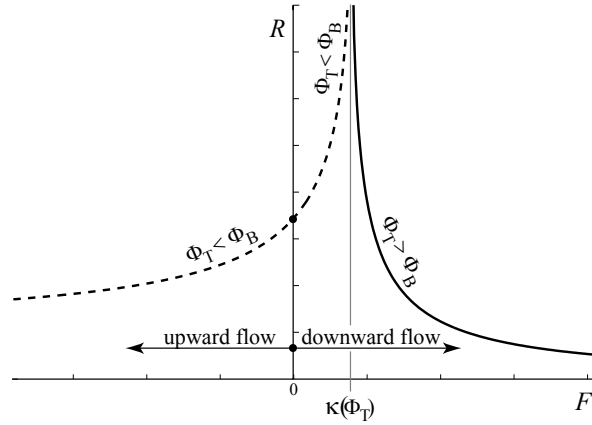


Figure 6.1. The Rayleigh number R as function of F .

(5) Upward flow: now we have $F < 0$ and $\Phi'_0(z) > R \kappa(\Phi_0) > 0$.

Separation of variables in (6.2.2) yields

$$Rz = \int_{\Phi_T}^{\Phi_0(z)} \frac{1}{\kappa(\Phi_0) - F} d\Phi_0. \quad (6.2.3)$$

The solution strategy is as follows. For given boundary condition Φ_T and Rayleigh number $R > 0$, we solve (6.2.3). Here F is still unknown. It has to be chosen such that the second boundary condition $\Phi = \Phi_B$ is satisfied. Again using (6.2.3), such a F can be found by inverting

$$R = R(F) = \int_{\Phi_T}^{\Phi_B} \frac{1}{\kappa(\Phi_0) - F} d\Phi_0. \quad (6.2.4)$$

A typical $R(F)$ relation is depicted in Figure 6.1. Note that $R(F)$ is a strictly monotonic decreasing (when $\Phi_T > \Phi_B$) or increasing (when $\Phi_T < \Phi_B$) function and for every $R > 0$ we find a unique F and hence a steady state.

6.3 Transient behaviour of perturbations of the matric flux potential

6.3.1 General approach

In this section we consider transient solutions $\Phi = \Phi(x, y, z, t)$ of (RE)₃ in Ω that satisfy the boundary conditions Φ_T at $\{z = 0\}$, Φ_B at $\{z = 1\}$, $\nabla \Phi \cdot \mathbf{n} = 0$ along the vertical boundaries, and some initial condition $\Phi|_{t=0} = \Phi(x, y, z)$. In particular, we investigate the stability of the steady solution Φ_0 . For this purpose we write

$$\Phi = \Phi_0(z) + \varphi, \quad (6.3.1)$$

where the perturbation $\varphi = \varphi(x, y, z, t)$ vanishes at the top ($z=0$) and bottom ($z=1$) of the flow domain and satisfies $\nabla\varphi \cdot \mathbf{n} = 0$ along $\partial\Omega_{\perp} \times (0, 1)$.

We substitute (6.3.1) into $(\text{RE})_3$ and disregard nonlinear terms in φ . Thus we investigate linearized stability. A common way, e.g. see Egorov et al. (2003), is to investigate the spectrum of the linearized operator. This is outlined in Appendix 6.A, where we make use of an observation communicated to us by Prof. Y. C. Yortsos (Yortsos, 2004). However, in this section we follow a different route. We are going to estimate the weighted L^2 -norm of the perturbation φ . We prove that this norm is decreasing in time and we give an estimate of the rate of convergence.

We assume here that $\kappa : [0, M] \rightarrow [0, \infty)$ is a smooth function satisfying $\kappa(0) = 0$, $\kappa(M) = 1$, and $\kappa'(\Phi) \geq 0$ for $0 \leq \Phi \leq M$. Further, κ is possible convex-concave: i.e. there exists $0 < \widehat{M} \leq M$ such that

$$\kappa''(\Phi) = \begin{cases} \geq 0 & \text{for } 0 \leq \Phi < \widehat{M}, \\ < 0 & \text{for } \widehat{M} < \Phi \leq M. \end{cases} \quad (6.3.2)$$

With respect to $S(\Phi)$ we assume

$$0 < K_1 \leq S'(\Phi) = \frac{1}{D(\Phi)} \leq K_2 < \infty \quad \text{for } 0 \leq \Phi \leq M. \quad (6.3.3)$$

Then we prove the following stability result:

Theorem 6.3. *Let $m_* := \min\{\Phi_T, \widehat{M}\}$, $m^* := \max\{\Phi_T, \widehat{M}\}$, and let*

$$\lambda := \begin{cases} \frac{1}{2} \int_0^{m_*} \frac{\kappa'(m_*) - \kappa'(\phi)}{\kappa(m_*) - \kappa(\phi)} d\phi & \text{for } S_T > S_B \text{ (or } \Phi_T > \Phi_B), \\ -\frac{1}{2} \int_{m^*}^M \frac{\kappa'(m^*) - \kappa'(\phi)}{\kappa(m^*) - \kappa(\phi)} d\phi & \text{for } S_T < S_B \text{ (or } \Phi_T < \Phi_B). \end{cases} \quad (6.3.4)$$

Further we consider the weighted L^2 -norm

$$\|\varphi(t)\|^2 := \int_{\Omega} S'(\Phi_0(x, y, z)) \varphi^2(x, y, z, t) dx dy dz \quad \text{for } t \geq 0.$$

If $\lambda < 1$, then

$$(A) \quad \|\varphi(t)\|^2 \text{ is strictly decreasing for } t > 0,$$

and in particular

$$(B) \quad \|\varphi(t)\|^2 \leq e^{-2(1-\lambda)t/K_2} \|\varphi(0)\|^2 \quad \text{for all } t > 0.$$

Hence if $\lambda < 1$, the steady solution Φ_0 is linearly exponentially stable.

Proof. Substitution of (6.3.1) in $(\text{RE})_3$ and linearizing the resulting equation gives for the perturbation φ

$$S'(\Phi_0) \frac{\partial \varphi}{\partial t} = \Delta \varphi - R \frac{\partial}{\partial z} (\kappa'(\Phi_0) \varphi) . \quad (6.3.5)$$

To obtain estimates from (6.3.5) we use the energy method (Straughan, 2004). Multiplying (6.3.5) by φ and integrating the equation over Ω gives

$$\frac{1}{2} \frac{d}{dt} \|\varphi(t)\|^2 = - \int_{\Omega} |\nabla \varphi|^2 - R \int_{\Omega} \frac{\partial}{\partial z} (\kappa'(\Phi_0) \varphi) \varphi , \quad (6.3.6)$$

Integration by parts of the last term in (6.3.6) and using the condition that φ vanishes along the horizontal boundaries gives

$$\begin{aligned} \frac{1}{2} \frac{d}{dt} \|\varphi(t)\|^2 &= - \int_{\Omega} |\nabla \varphi|^2 + \frac{R}{2} \int_{\Omega} \kappa'(\Phi_0) \frac{\partial \varphi^2}{\partial z} = \\ &= - \int_{\Omega} |\nabla \varphi|^2 - \frac{R}{2} \int_{\Omega} \left(\kappa''(\Phi_0) \frac{d\Phi_0}{dz} \right) \varphi^2 . \end{aligned}$$

Let $S_T > S_B$. Then $\frac{d\Phi_0}{dz} < 0$. Using this monotonicity and (6.3.2) gives

$$\frac{1}{2} \frac{d}{dt} \|\varphi(t)\|^2 \leq - \int_{\Omega} |\nabla \varphi|^2 - \frac{R}{2} \int_{\Omega_*} \left(\kappa''(\Phi_0) \frac{d\Phi_0}{dz} \right) \varphi^2 , \quad (6.3.7)$$

where $\Omega_* := \{(x, y, z) : (x, y) \in \Omega_{\perp}, z_* < z < 1\}$ and $\Phi_0(z_*) = m_*$. To estimate the sign of the second term on the right-hand side of (6.3.7) we use the following argument. For any fixed $(x, y) \in \Omega_{\perp}$ and $t > 0$ we write $\varphi(z) := \varphi(x, y, z, t)$ and estimate with Cauchy–Schwarz

$$\begin{aligned} \varphi(z) &\leq |-\varphi(z)| = \left| \int_z^1 \varphi'(\zeta) d\zeta \right| \leq \left(\int_z^1 1^2 d\zeta \right)^{1/2} \left(\int_z^1 (\varphi'(\zeta))^2 d\zeta \right)^{1/2} \leq \\ &\leq \sqrt{1-z} \left(\int_0^1 (\varphi'(\zeta))^2 d\zeta \right)^{1/2} . \end{aligned} \quad (6.3.8)$$

Then, using Fubini's Theorem and inequality (6.3.8) in (6.3.7), we have

$$\begin{aligned} \frac{1}{2} \frac{d}{dt} \|\varphi(t)\|^2 &\leq - \int_{\Omega} |\nabla \varphi|^2 - \frac{R}{2} \left\{ \int_{z_*}^1 (1-z) \frac{d}{dz} \kappa'(\Phi_0) dz \right\} \int_{\Omega} |\nabla \varphi|^2 =: \\ &=: -(1-\lambda) \int_{\Omega} |\nabla \varphi|^2 . \end{aligned} \quad (6.3.9)$$

For the factor λ in (6.3.9) we obtain, using (6.3.4) and the fact that $m_* \leq \Phi_T$,

$$\begin{aligned} \lambda &= -\frac{R}{2}(1-z)\kappa'(\Phi_0)\Big|_{z_*}^1 - \frac{R}{2} \int_{z_*}^1 \kappa'(\Phi_0) \, dz = \\ &= \frac{R}{2} \int_{z_*}^1 \{\kappa'(m_*) - \kappa'(\Phi_0)\} \, dz = \frac{1}{2} \int_{\Phi_B}^{m_*} \frac{\kappa'(m_*) - \kappa'(\Phi_0)}{\kappa(\Phi_T) - \kappa(\Phi_0)} \, d\Phi_0 \leq \\ &\leq \frac{1}{2} \int_0^{m_*} \frac{\kappa'(m_*) - \kappa'(\Phi_0)}{\kappa(m_*) - \kappa(\Phi_0)} \, d\Phi_0 < 1 \end{aligned}$$

by assumption. Hence, with the Poincaré inequality $\int_{\Omega} \varphi^2 \leq \int_{\Omega} |\nabla \varphi|^2$ (Zeidler, 1995) and using (6.3.3), we obtain from (6.3.9) the estimate

$$\frac{1}{2} \frac{d}{dt} \|\varphi(t)\|^2 \leq -(1-\lambda) \int_{\Omega} \varphi^2 \leq -((1-\lambda)/K_2) \|\varphi(t)\|^2 \leq 0, \quad (6.3.10)$$

which proves (A). Integrating (6.3.10) with respect to time t gives

$$\|\varphi(t)\|^2 \leq e^{-2(1-\lambda)t/K_2} \|\varphi(0)\|^2, \quad (6.3.11)$$

which proves (B).

The case $S_T < S_B$ follows in a similar fashion. Its proof is therefore omitted. ■

6.3.2 Application to specific classes of soils

Broadbridge–White and Burgers classes

First observe that $\kappa(\Phi)$ has no inflection points for $0 \leq \Phi \leq M = 1$. Hence $\widehat{M} \equiv M = 1$ and $m^* \equiv 1$. This immediately implies that $\lambda \equiv 0 < 1$ for the case $S_T < S_B$, and, hence, that in terms of the classification of the steady vertical flows in Subsection 3.2, downward flows opposed by capillarity, equilibrium, and upward flows are linearly stable.

For the case $S_T > S_B$, i.e. for downward flows aided by capillarity, we estimate λ . Since $0 \leq m_* \leq \widehat{M} = 1$ we have

$$\begin{aligned} \lambda &= \frac{1}{2} \int_0^{m_*} \frac{\kappa'(m_*) - \kappa'(\phi)}{\kappa(m_*) - \kappa(\phi)} \, d\phi = \\ &= \frac{1}{2} \left[\ln \left(\frac{2C - 2 + m_*}{C - 1 + m_*} \right) + \left(\frac{C - 1}{C - 1 + m_*} \right)^2 \ln \left(\frac{2C - 2 + m_*}{C - 1} \right) \right] \leq \ln 2 \end{aligned}$$

for all $C > 1$. Hence $\lambda \leq \ln 2 < 1$ and this implies that Φ_0 is linearly stable.

Gardner class

Observe that for this case $\kappa(\Phi)$ has an inflection point at $\Phi = \frac{\pi}{4}$. This implies $\widehat{M} = \frac{\pi}{4}$. We first consider the case $S_T > S_B$. Since $0 \leq \phi \leq m_* \leq \frac{\pi}{4}$ we have

$$\begin{aligned} \lambda &= \frac{1}{2} \int_0^{m_*} \frac{\kappa'(m_*) - \kappa'(\phi)}{\kappa(m_*) - \kappa(\phi)} d\phi = \\ &= \frac{1}{2} \int_0^{m_*} \frac{(\sin(2m_*) - \sin(2\phi))(\phi + m_*)}{\sin^2(m_*) - \sin^2(\phi)} \frac{1}{\phi + m_*} d\phi \leq \\ &\leq \frac{2m_* \cos^2(m_*) - m_*}{\sin(m_*) \cos(m_*)} \int_0^{m_*} \frac{1}{\phi + m_*} d\phi \leq \ln 2 < 1, \end{aligned}$$

implying that the steady solution Φ_0 is linearly stable.

For the case $S_T < S_B$ we again obtain $\lambda \leq \ln 2$, and hence, as to be expected, these steady states are also linearly stable.

6.4 Saturation estimates**6.4.1 Estimates that may involve transient growth**

Up to now we have estimates in terms of the matric flux potential perturbation φ . In this subsection we show that estimates for the saturation formulation can be obtained directly from the estimates derived in the previous section.

As for the matric flux potential Φ , we write $S = S(x, y, z, t)$ in the form

$$S = S_0(z) + s,$$

where $s = s(x, y, z, t)$ vanishes at the top ($z = 0$) and bottom ($z = 1$) of the flow domain, and satisfies $\nabla s \cdot \mathbf{n} = 0$ along $\partial\Omega_{\perp} \times (0, 1)$, and where $S_0 = f^{-1}(\Phi_0)$. The relation between the saturation perturbation s and matric flux potential perturbation φ follows from the expansion

$$S = S_0(z) + s = S(\Phi_0 + \varphi) = S(\Phi_0) + S'(\Phi_0)\varphi + \mathcal{O}(\varphi^2),$$

which implies $s = S'(\Phi_0)\varphi = \varphi/D(\Phi_0)$ in the linearized sense. Next we use (6.3.11) and (6.3.3) to obtain

$$\begin{aligned} \frac{1}{K_2} \int_{\Omega} s^2(t) &\leq \int_{\Omega} \frac{s^2(t)}{S'(\Phi_0)} \leq e^{-2(1-\lambda)t/K_2} \int_{\Omega} \frac{s^2(0)}{S'(\Phi_0)} \leq \\ &\leq \frac{1}{K_1} e^{-2(1-\lambda)t/K_2} \int_{\Omega} s^2(0), \end{aligned}$$

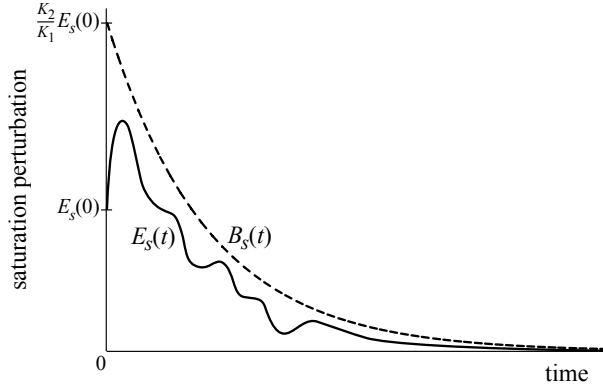


Figure 6.2. The norm gap may imply transient growth of $E_s(t)$, but $E_s(t)$ is nevertheless bounded by $B_s(t)$.

or

$$E_s(t) := \int_{\Omega} s^2(t) \leq \frac{K_2}{K_1} e^{-2(1-\lambda)t/K_2} \int_{\Omega} s^2(0) =: B_s(t). \quad (6.4.1)$$

Note that this estimate does *not* imply $\frac{dE_s(t)}{dt} \leq 0$. In fact, since $B_s(0) = \frac{K_2}{K_1} E_s(0) \geq E_s(0)$, transient growth of $E_s(t)$ may occur as sketched in Figure 6.2. We discuss this in more detail in Section 6.6.

Remark 6.4. For Broadbridge–White soils we derive from (I)₄ that

$$K_1 = \frac{C-1}{C} \leq S'(\Phi_0) \leq \frac{C}{C-1} = K_2.$$

Using these estimates in (6.4.1) gives

$$\int_{\Omega} s^2(t) \leq \frac{C^2}{(C-1)^2} e^{-\frac{2(C-1)}{C}(1-\lambda)t} \int_{\Omega} s^2(0). \quad (6.4.2)$$

Note that for the limit $C \rightarrow \infty$ (Burgers soils), we obtain the sharp estimate

$$\int_{\Omega} s^2(t) \leq e^{-2(1-\lambda)t} \int_{\Omega} s^2(0). \quad (6.4.3)$$

This means that for Burgers soils $E_s(t)$ decreases monotonically in time and is bounded by an exponential decaying function.

For Gardner soils we obtain from (III)₄ the estimates

$$K_1 = \frac{1}{2} \leq S'(\Phi_0) \leq 1 = K_2.$$

Substitution in (6.4.1) gives

$$\int_{\Omega} s^2(t) \leq 2 e^{-2(1-\lambda)t} \int_{\Omega} s^2(0).$$

Since $B_s(0) = 2$, this is again not a sharp bound, and transient growth of $E_s(t)$ may occur.

6.4.2 Sharp estimates

In some cases a sharp estimate of the saturation perturbation can be obtained directly from (6.3.5). Substituting the relation $s = S'(\Phi_0)\varphi$ gives the linearised perturbation equation

$$\frac{\partial s}{\partial t} = \nabla \cdot (D(S_0)\nabla s) + \frac{\partial}{\partial z} \left\{ D'(S_0) \frac{dS_0}{dz} s - R k'(S_0) s \right\}. \quad (6.4.4)$$

Note that this equation is more complex than Equation (6.3.5) for φ . This is the main reason why we choose the matric flux potential to study stability.

Multiplying (6.4.4) by s and integrating over Ω gives

$$\begin{aligned} \frac{1}{2} \frac{d}{dt} \int_{\Omega} s^2 &= - \int_{\Omega} D(S_0) |\nabla s|^2 + \frac{1}{2} \int_{\Omega} \left(\frac{d^2}{dz^2} D(S_0) - R \frac{d}{dz} k'(S_0) \right) s^2 \\ &=: - \int_{\Omega} D(S_0) |\nabla s|^2 + I. \end{aligned} \quad (6.4.5)$$

The expression for I can also be written as:

$$I = \frac{1}{2} \int_{\Omega} \frac{d}{dS_0} \left(\frac{dD(S_0)}{dz} - R k'(S_0) \right) \frac{dS_0}{dz} s^2.$$

Observe further that $\frac{dD(S_0)}{dz} = D'(S_0) \frac{dS_0}{dz} = \frac{D'(S_0)}{D(S_0)} R(k(S_0) - F)$, where we have used (6.2.2). Hence

$$I = \frac{R}{2} \int_{\Omega} \left\{ \frac{d}{dS_0} \left(\frac{D'(S_0)}{D(S_0)} (k(S_0) - F) - k'(S_0) \right) \right\} \frac{dS_0}{dz} s^2 =: \frac{R}{2} \int_{\Omega} \gamma(S_0) \frac{dS_0}{dz} s^2. \quad (6.4.6)$$

Expanding $\gamma(S_0)$ in (6.4.6) and splitting the result into parts gives

$$\gamma(S_0) = \gamma_1(S_0) + \gamma_2(S_0),$$

with

$$\gamma_1(S_0) = \frac{D'(S_0)}{D(S_0)} k'(S_0) - k''(S_0) = -D(S_0) \left(\frac{k'(S_0)}{D(S_0)} \right)', \quad (6.4.7a)$$

$$\gamma_2(S_0) = \left(\frac{D'(S_0)}{D(S_0)} \right)' (k(S_0) - F). \quad (6.4.7b)$$

For sharp estimates we want to have

$$I \leq \mu \int_{\Omega} |\nabla s|^2 \quad \text{with } \mu < \beta \quad \text{and } \beta := \min_{S_0} D(S_0), \quad (6.4.8)$$

since then, using the Poincaré inequality $-(\beta - \mu) \int_{\Omega} |\nabla s|^2 \leq -(\beta - \mu) \int_{\Omega} s^2$ in (6.4.5), $\frac{d}{dt} \int_{\Omega} s^2 < 0$ and in particular

$$\int_{\Omega} s^2(t) \leq e^{-2(\beta-\mu)t} \int_{\Omega} s^2(0) \leq \int_{\Omega} s^2(0) . \quad (6.4.9)$$

This would rule out transient growth as in Figure 6.2.

In Appendix 6.B we show that for the Gardner class of soils $\mu \approx 0.9296$ and $\beta = 1$. For the Broadbridge–White class of soils, however, we are not able to prove (6.4.8) for the range $1 < C < 2.5$. For the case $C \rightarrow \infty$, which corresponds to the Burgers class of soils, one can show, using techniques from Appendix 6.B, that $\mu \equiv 0$ and $\beta \equiv 1$.

For the Burgers class of soils we obtain even more than linear stability alone. For this particular case the *nonlinear* perturbation equation for s is given by

$$\frac{\partial s}{\partial t} = \Delta s - 2R \frac{\partial}{\partial z} (S_0 s) - R \frac{\partial s^2}{\partial z} . \quad (6.4.10)$$

Disregarding the quadratic term in (6.4.10) gives Equation (6.4.4). However, multiplying this quadratic term by s and integration over Ω yields

$$\int_{\Omega} \frac{\partial s^2}{\partial z} s = 2 \int_{\Omega} s^2 \frac{\partial s}{\partial z} = \frac{2}{3} \int_{\Omega} \frac{\partial s^3}{\partial z} = 0 ,$$

implying that the steady solutions of the Burgers class of soils are *nonlinearly* (unconditionally) stable with respect to arbitrary finite-amplitude perturbations.

6.5 Non-equilibrium Richards equation

An extension of the Richards equation to take into account dynamic memory effects was suggested by Hassanizadeh and Gray (1990, 1993). The key point in their model is the rejection of the equilibrium pressure-saturation relation. Instead they proposed:

$$(RE') \begin{cases} \frac{\partial S}{\partial t} = \nabla \cdot (k(S) \nabla \widehat{\Psi} - Rk(S) \mathbf{e}_z) , \\ \tau \frac{\partial S}{\partial t} = \widehat{\Psi} - \Psi(S) , \end{cases}$$

where $\widehat{\Psi}$ is the water pressure head and where τ is a dimensionless relaxation coefficient (taken as a positive constant). Combining the two equations in (RE') gives

$$\frac{\partial S}{\partial t} = \nabla \cdot (D(S) \nabla S) + \tau \nabla \cdot \left(k(S) \nabla \frac{\partial S}{\partial t} \right) + R \frac{\partial}{\partial z} k(S) = 0 . \quad (6.5.1)$$

This equation will be referred to as the extended model.

Remark 6.5. *The steady solutions of (6.5.1) do not depend on τ . In fact, the steady equations are the same for both the standard Richards equation $(RE)_2$ and the extended model (6.5.1). So is the uniqueness result from Section 6.2.1.*

In line with the general approach in Subsection 6.3.1, the normal procedure would be to rewrite (6.5.1) in terms of the matric flux potential Φ and consider the associated linearized perturbation equation. Rewriting (6.5.1) gives

$$\frac{\partial S(\Phi)}{\partial t} = \Delta \Phi + \tau \nabla \cdot \left(\kappa(\Phi) \nabla \frac{\partial S(\Phi)}{\partial t} \right) + R \frac{\partial}{\partial z} \kappa(\Phi) = 0. \quad (6.5.2)$$

Using the decomposition $\Phi = \Phi_0 + \varphi$ in (6.5.2) and linearizing the resulting equation gives

$$S'(\Phi_0) \frac{\partial \varphi}{\partial t} = \Delta \varphi + \tau \nabla \cdot \left(\kappa(\Phi_0) \nabla \left\{ S'(\Phi_0) \frac{\partial \varphi}{\partial t} \right\} \right) + R \frac{\partial}{\partial z} (\kappa'(\Phi_0) \varphi). \quad (6.5.3)$$

Following the variational approach, the τ -term in (6.5.3) gives an expression of which the sign is not fixed. Therefore the matric flux potential (Φ) formulation is unsuitable for analyzing the stability of the (RE') steady states.

To circumvent this problem, we consider the saturation perturbation equation related to (RE') . In the linearized sense we find

$$\frac{\partial s}{\partial t} = \nabla \cdot (D(S_0) \nabla s) + \tau \nabla \cdot \left(k(S_0) \nabla \frac{\partial s}{\partial t} \right) + \frac{\partial}{\partial z} \left\{ D'(S_0) \frac{dS_0}{dz} s - R k'(S_0) s \right\}. \quad (6.5.4)$$

Multiplying (6.5.4) by s , integrating over Ω , and collecting terms with a time derivative gives for any $\tau > 0$

$$\frac{1}{2} \frac{d}{dt} \left\{ \int_{\Omega} s^2 + \tau \int_{\Omega} k(S_0) |\nabla s|^2 \right\} = - \int_{\Omega} D(S_0) |\nabla s|^2 + I,$$

where I is given by (6.4.6). Now suppose that (6.4.8) holds. Then, with $\int_{\Omega} s^2 \leq \int_{\Omega} |\nabla s|^2$,

$$\begin{aligned} \frac{1}{2} \frac{d}{dt} \left\{ \int_{\Omega} s^2 + \tau \int_{\Omega} k(S_0) |\nabla s|^2 \right\} &\leq - \int_{\Omega} D(S_0) |\nabla s|^2 + \mu \int_{\Omega} |\nabla s|^2 \leq \\ &\leq -(\beta - \mu) \int_{\Omega} |\nabla s|^2 \leq -\frac{(\beta - \mu)}{2\tau} \tau \int_{\Omega} k(S_0) |\nabla s|^2 - \frac{(\beta - \mu)}{2} \int_{\Omega} s^2 \leq \\ &\leq \mu^* \left\{ \int_{\Omega} s^2 + \tau \int_{\Omega} k(S_0) |\nabla s|^2 \right\}, \end{aligned} \quad (6.5.5)$$

where we have used that $k(S_0) \leq 1$ and where, since $\tau > 0$,

$$\mu^* = \max \left\{ -\frac{\beta - \mu}{2\tau}, -\frac{\beta - \mu}{2} \right\} < 0.$$

Integrating (6.5.5) gives

$$\int_{\Omega} s^2(t) \leq \int_{\Omega} s^2(t) + \tau \int_{\Omega} k(S_0) |\nabla s(t)|^2 \leq e^{\mu^* t} \left\{ \int_{\Omega} s^2(0) + \tau \int_{\Omega} k(S_0) |\nabla s(0)|^2 \right\}.$$

Since $\mu^* < 0$, we obtain

$$\int_{\Omega} s^2(t) \rightarrow 0 \quad \text{as } t \rightarrow \infty.$$

We conclude that once (6.4.8) is satisfied, linear stability of the steady solutions of both the standard and extended Richards equation is guaranteed. Estimates for I were listed already in Section 6.4 following (6.4.8).

6.6 Different norms and transient growth

In Sections 6.3 and 6.4 we considered linearized stability in terms of the (weighted) L^2 -norms of the perturbations φ of the matric flux potential and of the perturbations s of the saturation. Independent of the chosen variable we obtained stability, but not necessarily time-monotonicity of the chosen norm. In this section we give an example of *transient growth*: initial growth of the norm of a perturbation which decays towards zero as $t \rightarrow \infty$, see sketch in Figure 6.2. We consider Burgers soil for which the steady solution is unconditionally stable and for which the norms in terms of φ and s decay monotonically in time. We show below that in terms of the pressure head transient growth may occur.

For Burgers soils the relation between $S = \Phi$ and Ψ is explicitly given by $\Psi(S) = 1 - S^{-1}$, or $S(\Psi) = \frac{1}{1-\Psi}$. We write $\Psi_0 = \Psi(S_0)$ and redefine $k(\Psi_0) := k(S(\Psi_0))$, $D(\Psi_0) := D(S(\Psi_0))$ and $c(\Psi_0) := c(S(\Psi_0))$. As in Section 6.3, we write $\Psi = \Psi_0(z) + \psi$, where $\psi = \psi(x, y, z, t)$ vanishes along the top and bottom of the flow domain. Linearizing $S(\Psi)$ gives the relation $s = S'(\Psi_0)\psi = \frac{1}{(1-\Psi_0)^2}\psi = S_0^2\psi$.

We consider the case $0 < S_B < S_T \leq 1$. Using the relation between s en ψ in the saturation estimate (6.4.3) gives

$$S_B^4 \int_{\Omega} \psi^2(t) \leq \int_{\Omega} s^2(t) \leq e^{-2(1-\lambda)t} \int_{\Omega} s^2(0) \leq S_T^4 e^{-2(1-\lambda)t} \int_{\Omega} \psi^2(0),$$

or

$$E_{\psi}(t) := \int_{\Omega} \psi^2(t) \leq \left(\frac{S_T}{S_B} \right)^4 e^{-2(1-\lambda)t} \int_{\Omega} \psi^2(0) =: B_{\psi}(t), \quad (6.6.1)$$

with $\lambda \leq \ln 2$, see Section 6.2.1 and Remark 6.4. From (6.6.1) we observe that $B_{\psi}(0) \rightarrow E_{\psi}(0)$ as $S_T/S_B \rightarrow 1$ and therefore transient growth of $E_{\psi}(t)$ cannot occur for purely gravitational flows. However, for $S_T > S_B$ we can select a perturbation for which transient growth does occur.

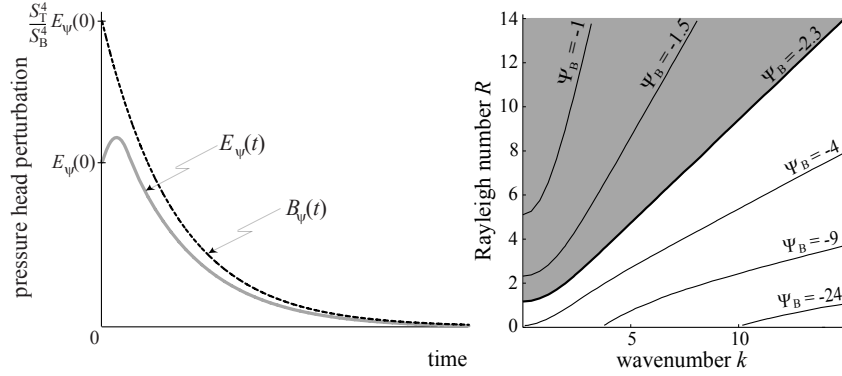


Figure 6.3. Left: a typical picture of the norm $E_\psi(t)$. Note that $E'_\psi(0) = \sigma_{\max} > 0$. Right: neutral curves (i.e. $\sigma \equiv 0$) corresponding to eigenvalue problem (6.6.6). The shaded region corresponds to the case $\Psi_T = 0$, $\Psi_B = -2.3$ ($S_T = 1$, $S_B = 0.3$) and depicts the region where $\sigma_{\max} > 0$. The white region corresponds to $\sigma_{\max} < 0$.

To show this we consider the linearized perturbation equation for ψ . Using the relation between s and ψ in (6.4.4) and using the fact that $D(\Psi_0) = k(\Psi_0)/c(\Psi_0)$ gives

$$\begin{aligned} \frac{\partial \psi}{\partial t} = \frac{k'(\Psi_0)}{c(\Psi_0)} \left[2 \frac{d\Psi_0}{dz} - R \right] \frac{\partial \psi}{\partial z} + \frac{k(\Psi_0)}{c(\Psi_0)} \Delta \psi - \\ - \left[\frac{(k'(\Psi_0))^2}{k(\Psi_0)c(\Psi_0)} - \frac{k''(\Psi_0)}{c(\Psi_0)} \right] \left[\left(\frac{d\Psi_0}{dz} \right)^2 - R \frac{d\Psi_0}{dz} \right] \psi . \end{aligned} \quad (6.6.2)$$

We restrict ourselves to x, y -periodic solutions $\psi = \psi(z, t)e^{i\mathbf{k}\cdot\mathbf{x}}$, where $\mathbf{k} = (k_x, k_y)^\top$ denotes the wave vector and $\mathbf{x} = (x, y)^\top$. Using $k(\Psi)$ and $c(\Psi)$ in (6.6.2) gives for the amplitude $\psi = \psi(z, t)$

$$\frac{\partial \psi}{\partial t} = \frac{\partial^2 \psi}{\partial z^2} - k^2 \psi + \mathcal{A}_1(\Psi_0) \frac{\partial \psi}{\partial z} + \mathcal{A}_2(\Psi_0) \psi =: \mathcal{A}(\Psi_0) \psi , \quad (6.6.3)$$

where $k = |\mathbf{k}|$ and

$$\mathcal{A}_1(\Psi_0) = \frac{4\Psi'_0(z) - 2R}{1 - \Psi_0} \quad \text{and} \quad \mathcal{A}_2(\Psi_0) = \frac{2(\Psi'_0(z))^2 - 2R\Psi'_0(z)}{(1 - \Psi_0)^2} .$$

Multiplying Equation (6.6.3) by ψ and integrating the result gives

$$\frac{1}{2} \frac{dE_\psi(t)}{dt} := \frac{1}{2} \frac{d}{dt} \int_0^1 \psi^2(t) dz = \int_0^1 (\mathcal{A}(\Psi_0)\psi(t))\psi(t) dz . \quad (6.6.4)$$

Transient growth is said to occur if $E_\psi(t) > E_\psi(0)$ for some $t > 0$. This happens, for instance, if $\left. \frac{1}{E_\psi(0)} \frac{dE_\psi(t)}{dt} \right|_{t=0} > 0$, see Figure 6.3 (left). To find the maximal initial growth we use (6.6.4) and consider

$$\frac{1}{2} \frac{1}{E_\psi(0)} \left. \frac{dE_\psi(t)}{dt} \right|_{t=0} = \int_0^1 (\mathcal{A}(\Psi_0) \psi(0)) \psi(0) dz \Big/ \int_0^1 \psi^2(0) dz .$$

This leads to the maximum problem

$$\sigma_{\max} = \sup_{\psi(0) \neq 0} \left\{ \int_0^1 (\mathcal{A}(\Psi_0) \psi(0)) \psi(0) dz \Big/ \int_0^1 \psi^2(0) dz \right\} . \quad (6.6.5)$$

Farrell and Ioannou (1996), among others, showed that the normalized maximal initial slope σ_{\max} and the initial perturbation $\psi(0)$ producing this initial growth are found from the eigenanalysis of the symmetric part of operator $\mathcal{A}(\Psi_0)$, i.e.

$$\frac{1}{2} (\mathcal{A}(\Psi_0) + \mathcal{A}^*(\Psi_0)) \psi(0) = \sigma \psi(0) , \quad (6.6.6)$$

where $*$ denotes the adjoint operator with respect to the L^2 -norm. In particular, the maximal positive eigenvalue and its associated eigenfunction provide the initial slope of $E_\psi(t)$ and the initial perturbation.

Remark 6.6. *The estimates obtained in Sections 6.3 and 6.4 imply that the eigenvalues of $\mathcal{A}(\Psi_0)$ all have negative real parts. Hence if $\mathcal{A}(\Psi_0)$ were a self-adjoint operator, then all (real) eigenvalues of (6.6.6) would have been negative as well and no transient growth would occur, see also Reddy and Henningson (1993).*

We solved (6.6.6) numerically for fixed $\Psi_T \equiv 0$ and various $-\infty < \Psi_B < 0$, and for Rayleigh numbers R and wavenumbers k in relevant ranges. The result is shown in Figure 6.3 (right). Given the boundary conditions Ψ_T , Ψ_B , and the Rayleigh number R , we can distinguish grey regions where $\sigma_{\max} > 0$, indicating initial transient growth, and white regions where $\sigma_{\max} < 0$. We do note here that since $E_\psi(t)$ is bounded by $B_\psi(t)$, the growth of the norm is only a transient phenomenon because $B_\psi(t) \rightarrow 0$ as $t \rightarrow \infty$.

6.7 Discussion

Kapoor (1996) derived stability criteria for the various types of steady vertical upward and downward flows in homogeneous, unsaturated soils. These criteria are summarized in Figure 6.4. Based on experimental evidence that observed fingers often are long and narrow, he assumed that the vertical length scale of the perturbations is large compared to the horizontal length scale and on that basis he simplified the linearized equation for the perturbation of the suction head. Allowing for the sign changes in going from the suction head to the pressure head, Kapoor (1996) in effect ignored in the right hand side of equation (6.6.2) the entire first term and z -dependent part of the

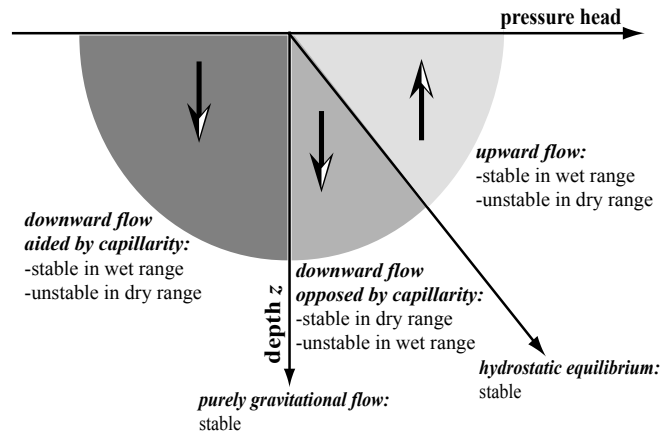


Figure 6.4. Overview of Kapoor's stability results.

second term. The results shown in Figure 6.4 then follow from considering the sign of the coefficient of ψ in the last term.

Linear stability analysis concerns the process of initiation of the fingers and in that stage the vertical length scale of the perturbations is still small. Therefore we reconsidered the stability of steady vertical flows, without ignoring the vertical gradients. First, we proved the uniqueness of the solutions for steady vertical flows. Subsequently we used the so-called energy method to prove the stability of the steady flows for various classes of soils and derived estimates of the rate of decay of perturbations. The decay of the perturbation is proportional to $\exp(-2(1-\lambda)D_{\min}t)$, where D_{\min} is an appropriate minimum value of the diffusivity. As is to be expected, using (RV1) to return to dimensional variables shows that an increase of D_{\min} or a decrease of H speeds up the decay. The analysis is complicated by the fact that, depending on the norm used in the analysis, the ultimate decay may be preceded by transient growth. Contrary to Kapoor's hypothesis, our analysis shows that the vertical gradients play an essential stabilizing role. In the analysis we considered several classes of soils, spanning a wide range of soil properties. For the Burgers class of soils, we were able to show that the steady solutions are nonlinearly stable with respect to arbitrary finite-amplitude perturbations. Finally, we showed that for the Richards equation extended with a term accounting for dynamic memory effects steady flows also remain stable.

Appendix 6.A

The spectrum of the linearised perturbation equation

In this appendix we show that the spectrum of the linearized perturbation operator (6.3.5) is real and that it is located in the left stable halfplane.

For this purpose we make use of an argument by Prof. Y. C. Yortsos. Consider

again the linearised perturbation equation (6.3.5) and write

$$\varphi(x, y, z, t) = e^{\sigma t} \varphi(x, y, z) .$$

Substitution in (6.3.5) yields

$$S'(\Phi_0) \sigma \varphi = \Delta \varphi - R \frac{\partial}{\partial z} (\kappa'(\Phi_0) \varphi) . \quad (6.7.1)$$

Introducing the transformation

$$\varphi = \frac{d\Phi_0}{dz} \tilde{\varphi} \quad (6.7.2)$$

in (6.7.1) gives the equation

$$\begin{aligned} \sigma S'(\Phi_0) \frac{d\Phi_0}{dz} \tilde{\varphi} &= \frac{\partial}{\partial z} \left(\frac{d\Phi_0}{dz} \frac{\partial \tilde{\varphi}}{\partial z} \right) + \frac{d\Phi_0}{dz} \Delta_{\perp} \tilde{\varphi} + \frac{\partial}{\partial z} \left(\frac{d^2\Phi_0}{dz^2} \tilde{\varphi} - R \kappa'(\Phi_0) \frac{d\Phi_0}{dz} \tilde{\varphi} \right) \\ &= \frac{\partial}{\partial z} \left(\frac{d\Phi_0}{dz} \frac{\partial \tilde{\varphi}}{\partial z} \right) + \frac{d\Phi_0}{dz} \Delta_{\perp} \tilde{\varphi} , \end{aligned} \quad (6.7.3)$$

where we have used equation (P2)₁ for the steady solution Φ_0 and where Δ_{\perp} denotes the horizontal Laplacian. Yortsos suggested the use of transformation (6.7.2) in combination with the use of Φ_0 as coordinate in the z direction. Therefore we introduce the ‘flow domain’

$$\Omega_{\Phi} := \{ (x, y, \Phi) : (x, y) \in \Omega_{\perp} , \Phi \text{ between } \Phi_B \text{ and } \Phi_T \} ,$$

and consider (6.7.3) in Ω_{Φ} , i.e. we write $\tilde{\varphi} = \tilde{\varphi}(x, y, z(\Phi_0)) =: \tilde{\varphi}(x, y, \Phi_0)$. This gives the following second-order (generalized) eigenvalue problem (in Ω_{Φ}):

$$(EVP) \begin{cases} \sigma S'(\Phi_0) \tilde{\varphi} = \frac{\partial}{\partial \Phi_0} \left(\left(\frac{d\Phi_0}{dz} \right)^2 \frac{\partial \tilde{\varphi}}{\partial \Phi_0} \right) + \Delta_{\perp} \tilde{\varphi} =: \nabla \cdot (\mathbf{A} \nabla \tilde{\varphi}) , \\ \tilde{\varphi} = 0 & \text{on } \Omega_{\perp} \times (\{\Phi_B\} \cup \{\Phi_T\}) , \\ \nabla \tilde{\varphi} \cdot \mathbf{n} = 0 & \text{on } \partial \Omega_{\perp} \times (\Phi_B, \Phi_T) , \end{cases}$$

with \mathbf{n} the outward normal at $\partial \Omega_{\perp} \times (\Phi_B, \Phi_T)$, and where $\nabla := (\partial_x, \partial_y, \partial_{\Phi_0})^T$ and

$$\mathbf{A} = \begin{pmatrix} 1 & 0 & 0 \\ 0 & 1 & 0 \\ 0 & 0 & \left(\frac{d\Phi_0}{dz} \right)^2 \end{pmatrix} .$$

The homogeneous boundary conditions (EVP)_{2,3} follow directly from φ via (6.7.2), see also Section 6.4.1. Now observe that problem (EVP) is self-adjoint, and hence its eigenvalues are all real.

Multiplying (EVP)₁ by $\tilde{\varphi}$ and integrating the result over Ω_Φ yields

$$0 \geq -\min\left\{1, \left(\frac{d\Phi_0}{dz}\right)^2\right\} \int_{\Omega_\Phi} |\nabla\tilde{\varphi}|^2 \geq - \int_{\Omega_\Phi} (\mathbf{A}\nabla\tilde{\varphi}) \cdot (\nabla\tilde{\varphi}) = \sigma \int_{\Omega_\Phi} S'(\Phi_0)\tilde{\varphi}^2, \quad (6.7.4)$$

and since $S'(\Phi_0) > 0$ this implies that $\sigma < 0$. This confirms again the uniqueness statement as discussed in Section 6.3.1.

In line with this chapter, we prefer not to work with the assumption of separation of variables, but consider the general case

$$S'(\Phi_0) \frac{\partial\tilde{\varphi}}{\partial t} = \nabla \cdot (\mathbf{A}\nabla\tilde{\varphi}) \quad \text{in } \Omega_\Phi.$$

Multiplying this equation by $\tilde{\varphi}$ and integrating over Ω_Φ gives the relation (using the estimate in (6.7.4) and the Poincaré inequality)

$$\begin{aligned} \frac{1}{2} \frac{d}{dt} \int_{\Omega_\Phi} S'(\Phi_0)\tilde{\varphi}^2 &= - \int_{\Omega_\Phi} (\mathbf{A}\nabla\tilde{\varphi}) \cdot \nabla\tilde{\varphi} \leq \\ &\leq -C(\Phi_B, \Phi_T) \min\left\{1, \left(\frac{d\Phi_0}{dz}\right)^2\right\} \int_{\Omega_\Phi} \tilde{\varphi}^2 \leq 0, \end{aligned}$$

implying exponential decay of the $L^2(\Omega_\Phi)$ -norm of $\tilde{\varphi}$.

Appendix 6.B

Saturation estimates for Gardner class soils

First we evaluate the components $\gamma_1(S_0)$ and $\gamma_2(S_0)$ of $\gamma(S_0)$. This can be done by direct lengthy computation, using the expressions (II)₁ for $k(S_0)$ and (II)₂ for $D(S_0)$ in (6.4.7a) and (6.4.7b). A simpler procedure is to observe that (II)_{1,2} imply $k'(S_0) = (D(S_0) - 1)D(S_0)$ and $D'(S_0) = (2 - 4k(S_0))D(S_0)$ so that the expressions for $\gamma_1(S_0)$ and $\gamma_2(S_0)$ reduce to

$$\gamma_1(S_0) = -D(S_0)D'(S_0) = -\frac{1}{2}(D^2(S_0))', \quad (6.7.5a)$$

$$\gamma_2(S_0) = 4k'(S_0)(F - k(S_0)). \quad (6.7.5b)$$

We need to estimate

$$I = \frac{R}{2} \int_{\Omega} \gamma(S_0) \frac{dS_0}{dz} s^2 = \frac{R}{2} \int_{\Omega} (\gamma_1(S_0) + \gamma_2(S_0)) \frac{dS_0}{dz} s^2. \quad (6.7.6)$$

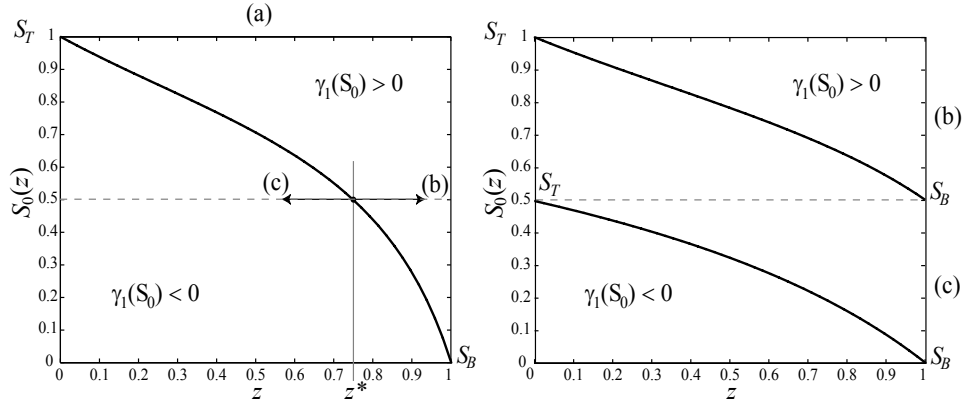


Figure 6.5. Definition of the point z^* for (a): $S_T = 1$ and $S_B = 0$, (b): $S_T = 1$, $S_B = \frac{1}{2}$, $z^* = 1$, and (c): $S_T = \frac{1}{2}$, $S_B = 0$, $z^* = 0$.

We first consider the downward flow case, i.e. $F > k(S_T) \geq k(S_0)$ for every $0 \leq S_B \leq S_0 < S_T \leq 1$. Since $\frac{dS_0}{dz}$ is negative, we want to show that $\gamma(S_0)$ is positive for all $R > 0$. From (6.7.5a) and (6.7.5b) it follows that $\gamma_2(S_0) > 0$ and

$$\gamma_1(S_0) = \begin{cases} < 0 & \text{for } 0 \leq S_B < S_0 < \frac{1}{2}, \\ > 0 & \text{for } \frac{1}{2} < S_0 < S_T \leq 1. \end{cases} \quad (6.7.7)$$

We distinguish the following cases:

- (i) $0 \leq S_B < \frac{1}{2} \leq S_T \leq 1$. Let z^* be such that $S_0(z^*) = \frac{1}{2}$. Then $S_B \leq S_0 < \frac{1}{2}$ for $z \in (z^*, 1]$, see also the construction in Figure 6.5(a). Hence, with (6.7.7) and inequality (6.3.9), we obtain

$$\begin{aligned} I &\leq \frac{R}{2} \int_{\Omega^*} \gamma_1(S_0) \frac{dS_0}{dz} s^2 = \frac{R}{4} \int_{\Omega^*} (D^2(S_0))' \left(-\frac{dS_0}{dz} \right) s^2 = \\ &= -\frac{R}{4} \int_{\Omega^*} \frac{d}{dz} (D^2(S_0)) s^2 \leq \left(-\frac{R}{4} \int_{z^*}^1 \frac{d}{dz} (D^2(S_0)) (1-z) dz \right) \int_{\Omega} |\nabla s|^2 =: \\ &=: \mu \int_{\Omega} |\nabla s|^2. \end{aligned}$$

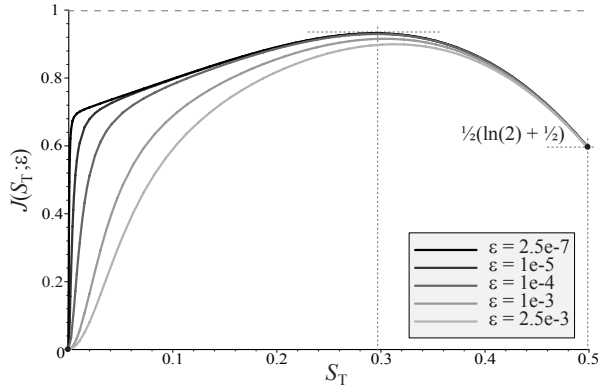


Figure 6.6. Plot of $J(S_T; \epsilon)$ for $0 \leq S_T \leq \frac{1}{2}$ and several values of ϵ . The maximum is located at $S_T \approx 0.2952$, and its value is given by 0.9296.

Integration by parts gives for μ

$$\begin{aligned} \mu &= \left[-\frac{R}{4} D^2(S_0(z))(1-z) \right]_{z^*}^1 - \frac{R}{4} \int_{z^*}^1 D^2(S_0(z)) dz = \\ &= \frac{R}{4} \int_{z^*}^1 \left[D^2\left(\frac{1}{2}\right) - D^2(S_0(z)) \right] dz = \\ &= \frac{1}{4} \int_{S_B}^{\frac{1}{2}} \frac{D^2\left(\frac{1}{2}\right) - D^2(S_0)}{F - k(S_0)} D(S_0) dS_0. \end{aligned} \quad (6.7.8)$$

The factor μ in (6.7.8) can be estimated by using $F > k(S_T) \geq k\left(\frac{1}{2}\right) = \frac{1}{2}$. This gives, using $D'(S) = 2(1-2S)D^2(S)$ and $(D\left(\frac{1}{2}\right) - D(S))/(k\left(\frac{1}{2}\right) - k(S)) = 2(1-2S)$,

$$\begin{aligned} \mu &< \frac{1}{4} \int_{S_B}^{\frac{1}{2}} \frac{D^2\left(\frac{1}{2}\right) - D^2(S_0)}{k\left(\frac{1}{2}\right) - k(S_0)} D(S_0) dS_0 \leq \\ &\leq \frac{1}{4} \int_0^{\frac{1}{2}} 2(1-2S_0)(2 + D(S_0)) D(S_0) dS_0 = \\ &\leq \frac{1}{2} \int_0^{\frac{1}{2}} \frac{D'(S_0)}{D(S_0)} dS_0 + \frac{1}{4} \int_0^{\frac{1}{2}} D'(S_0) dS_0 = \frac{1}{2}(\ln 2 + \frac{1}{2}) =: \mu_1, \end{aligned}$$

with $\mu_1 \approx 0.5966$.

(ii) $S_B < S_T < \frac{1}{2}$. For this case we have $z^* = 0$, see Figure 6.5(c). Again we obtain for μ an expression similar to (6.7.8):

$$\mu = \frac{1}{4} \int_{S_B}^{S_T} \frac{D^2(S_T) - D^2(S_0)}{F - k(S_0)} D(S_0) dS_0. \quad (6.7.9)$$

For a given S_T , S_B and $R > 0$, there exists a $\epsilon > 0$ such that $F = k(S_T) + \epsilon$. Hence

$$\mu = \frac{1}{4} \int_0^{S_T} \frac{D^2(S_T) - D^2(S_0)}{k(S_T) + \epsilon - k(S_0)} D(S_0) dS_0 =: J(S_T; \epsilon).$$

Since we could not find a closed form expression for $J(S_T; \epsilon)$, we evaluate it numerically. This is rather straight forward since the presence of $\epsilon > 0$ makes the integral nonsingular. Note that $J(S_T; \epsilon_1) < J(S_T; \epsilon_2)$ when $\epsilon_1 > \epsilon_2$ for every $0 < S_T < \frac{1}{2}$. Maximizing $J(S_T; \epsilon)$ for $0 < S_T < \frac{1}{2}$ and $\epsilon \downarrow 0$ gives $\mu < 0.9296 =: \mu_2$ (see Figure 6.6). For the derivation of this upperbound for μ , we have only used the soil properties $D(S_0)$ and $k(S_0)$. As a consequence, this upperbound is rather crude.

- (iii) $\frac{1}{2} \leq S_B < S_T \leq 1$. Now we have $z^* = 1$, see Figure 6.5(b). This case is trivial since $\gamma_1(S_0) > 0$ for every $\frac{1}{2} \leq S_B < S_0 \leq S_T \leq 1$.

Remark 6.7. The case $S_T \leq S_B$ is treated in a similar way. Now $\frac{dS_0}{dz} \geq 0$ and $F < k(S_T)$. Hence $\gamma_2(S_0) \frac{dS_0}{dz} < 0$. Further,

$$\gamma_1(S_0) = \begin{cases} < 0 & \text{for } 0 \leq S_T < S_0 < \frac{1}{2}, \\ > 0 & \text{for } \frac{1}{2} < S_0 < S_B \leq 1, \end{cases}$$

This implies a repetition of the derivation where now S_T is replaced by S_B and vice versa. It gives the same estimates for μ .

Finally, let $\bar{\mu} = \max\{\mu_1, \mu_2\} = 0.9296$. Using $\bar{\mu}$ and the fact that $\beta = 1$ in (6.4.9), we obtain

$$\int_{\Omega} s^2 \leq e^{-2(1-\bar{\mu})t} \int_{\Omega} s^2(0) \leq \int_{\Omega} s^2(0), \quad (6.7.10)$$

with $-2(1 - \bar{\mu}) \approx -0.1408$.

References

- Broadbridge, P. and I. White: 1988, 'Constant rate rainfall infiltration: A versatile nonlinear model i. Analytic solution'. *Water Resour. Res.* **24**, 145–154.
- Chuoke, R. L., P. van Meurs, and C. van der Poel: 1959, 'The instability of slow, immiscible, viscous liquid-liquid displacements in porous media'. *Petroleum Transactions of the American Institute of Mining Engineering* **216**, 188–194.
- Clothier, B. E., J. H. Knight, and I. White: 1981, 'Burgers' equation: Application to field constant-flux infiltration'. *Soil Sci.* **132**, 252–261.
- de Rooij, G. H.: 2000, 'Modeling fingered flow of water in soils owing to wetting front instability: A Review'. *J. Hydrol.* **231–232**, 277–294.

- Diment, G. A. and K. K. Watson: 1982, 'Stability analysis of water movement in unsaturated porous materials: 1. Theoretical considerations'. *Water Resources Res.* **18**(2), 1248–1254.
- Diment, G. E. and K. K. Watson: 1983, 'Stability analysis of water movement in unsaturated porous materials: 2. Numerical studies'. *Water Resour. Res.* **19**, 1002–1010.
- Diment, G. E. and K. K. Watson: 1985, 'Stability analysis of water movement in unsaturated porous materials: 3. Experimental studies'. *Water Resour. Res.* **21**(7), 979–984.
- Egorov, A. G., R. Z. Dautov, J. L. Nieber, and A. Y. Sheshukov: 2002, 'Stability analysis of traveling wave solution for gravity-driven flow'. In: S. M. Hassanizadeh, R. J. Schotting, W. G. Gray, and G. F. Pinder (eds.): *Computational Methods in Water Resources, Vol. 1*. Amsterdam, pp. 121–128, Elsevier.
- Egorov, A. G., R. Z. Dautov, J. L. Nieber, and A. Y. Sheshukov: 2003, 'Stability analysis of gravity-driven infiltrating flow'. *Water Resour. Res.* **39**(9), 1266, doi:10.1029/2002WR001886.
- Engelberts, W. F. and L. J. Klinkenberg: 1951, 'Laboratory experiments on the displacement of oil by water from packs of granular material'. In: *Proceedings 3rd World Petroleum Congress, The Hague*, Vol. 2. pp. 544–554.
- Farrell, B. F. and P. J. Ioannou: 1996, 'Generalized stability theory. Part I: Autonomous operators'. *J. Atmos. Sci.* **53**(14), 2025–2040.
- Gardner, W. R.: 1958, 'Some steady-state solutions of the unsaturated moisture flow equation with application to evaporation from a water table'. *Soil Sci.* **85**, 228–232.
- Gilbarg, D. and N. S. Trudinger: 1977, *Elliptic Partial Differential Equations of Second Order*. Berlin: Springer-Verlag.
- Hassanizadeh, S. M. and W. G. Gray: 1990, 'Mechanics and thermodynamics of multiphase flow in porous media including interphase boundaries'. *Adv. Water Resour.* **13**, 169–186.
- Hassanizadeh, S. M. and W. G. Gray: 1993, 'Thermodynamic basis of capillary pressure in porous media'. *Water Resources Res.* **29**, 3389–3405.
- Hendrickx, J. M. H. and M. Flury: 2001, 'Uniform and preferential flow mechanisms in the vadose zone'. In: E. Commission on Geosciences and R. (CGER) (eds.): *Conceptual Models of Flow and Transport in the Fractured Vadose Zone*. Washington, DC, pp. 149–188, National Academy Press.
- Hill, D. E. and J.-Y. Parlange: 1972, 'Wetting front instability in homogeneous soils'. *Soil Sci. Soc. Am. Proc.* **36**, 697–702.
- Hill, S.: 1952, 'Channelling in packed columns'. *Chemical Engineering Science* **1**, 247–253.
- Kapoor, V.: 1996, 'Criterion for instability of steady-state unsaturated flows'. *Transport in Porous Media* **25**, 335–350.
- Kirchhoff, G.: 1894, *Vorlesungen über Die Theorie der Wärme, Herausgegeben Von M. Planck*. Leipzig: Teubner.
- Miller, E. E. and R. D. Miller: 1956, 'Physical theory of capillary flow phenomena'. *J. Appl. Phys.* **27**, 324–332.
- Parlange, J.-Y. and D. E. Hill: 1976, 'Theoretical analysis of wetting front instability in soils'. *Soil Sci.* **122**, 236–239.
- Parlange, J.-Y., T. S. Steenhuis, L. Li, D. A. Barry, and F. Stagnitti: 2002, 'Column

- flow in stratified soils and fingers in Hele–Shaw cells: A review’. In: P. A. C. Raats, D. Smiles, and A. W. Warrick (eds.): *Environmental Mechanics. Water, Mass and Energy Transfer in the Biosphere*. Washington, DC and CSIRO, Australia: American Geophysical Union, pp. 79–85.
- Philip, J. R.: 1975a, ‘The growth of disturbances in unstable infiltration flows’. *Soil Sci. Soc. Am. Proc.* **39**, 1049–1053.
- Philip, J. R.: 1975b, ‘Stability analysis of infiltration’. *Soil Sci. Soc. Am. Proc.* **39**, 1042–1049.
- Raats, P. A. C.: 1973a, ‘Steady upward and downward flows in a class of unsaturated soils’. *Soil Sci.* **115**, 409–413.
- Raats, P. A. C.: 1973b, ‘Unstable wetting fronts in uniform and nonuniform soils’. *Soil Sci. Soc. Amer. Proc.* **37**, 681–685.
- Raats, P. A. C.: 1984, ‘Applications of the theory of mixtures in soil science’. In: C. Truesdell (ed.): *Rational Thermodynamics, with an Appendix by C. -C. Wang*. New York: Springer–Verlag, Chapt. Appendix 5D, pp. 326–343.
- Reddy, S. C. and D. S. Henningson: 1993, ‘Energy growth in viscous channel flows’. *J. Fluid Mech.* **252**, 209–238.
- Richards, L. A.: 1931, ‘Capillary conduction of liquids through porous mediums’. *Physics* **1**, 318–333.
- Saffman, P. G. and S. G. Taylor: 1958, ‘The penetration of a fluid into a porous medium or Hele–Shaw cell containing a more viscous liquid’. *Royal Society of London Proceedings A* **245**, 312–329.
- Straughan, B.: 2004, *The Energy Method, Stability and Nonlinear Convection*, Vol. 91 of *Applied Mathematical Sciences*. New York: Springer–Verlag, 2nd edition.
- Tabuchi, T.: 1961, ‘Infiltration and ensuing percolation in columns of layered glass particles packed in laboratory’. *Nogyo Dobuku Kenkyu, Bessatu (Transactions Agricultural Engineering Society, Japan)* **2**, 27–36.
- van Duijn, C. J., G. J. M. Pieters, and P. A. C. Raats: 2004, ‘Steady flows in unsaturated soils are stable’. *Transport in Porous Media* **57**, 215–244.
- Whitaker, S.: 1986, ‘Flow in porous media II: The governing equations for immiscible, two-phase flow’. *Transport in Porous Media* **1**, 105–125.
- Yortsos, Y.: 2004. Private communication.
- Zeidler, E.: 1995, *Applied Functional Analysis*, No. 108, 109 in *Applied Mathematical Sciences*. New York: Springer-Verlag.

Appendix A

A modified spectral Chebyshev–Galerkin method

In this appendix we discretize problem (3.1.8) by using a modified spectral Galerkin method. We use the method of lines, considering space and time discretisations separately. For the discretisation of operator L_α in (3.1.8) we apply a modified Chebyshev–Galerkin method. Essentially, there are two approaches to discretize this operator with emphasis on the semi-infinite domain:

- (i) the truncation of the semi-infinite domain $(0, \infty)$ to a finite interval (Mack, 1976; van Stijn and van de Vooren, 1980),
- (ii) the transformation of $(0, \infty)$ to a finite interval by virtue of an *algebraic mapping* (Grosch and Orszag, 1977) or an *exponential mapping* (Spalart, 1984).

Option (ii) result in a modified operator \tilde{L}_α in which the derivatives are multiplied by additional coefficients that depend on the mapping and vary in space. In particular, these transformations bring in singular coefficients in the operator and this strongly influences the efficiency of the method. Therefore we choose here for option (i). For the domain truncation we need an additional boundary condition at $z=h$. For initial conditions satisfying $g \in L^2(\mathbb{R}_+) \cap L^\infty(\mathbb{R}_+)$ we have $u \rightarrow 0$ as $z \rightarrow \infty$ (see also Chapter 2). Based on this observation, it is reasonable to impose a zero Dirichlet boundary condition at $z=h$.

The standard Chebyshev–Galerkin method uses the Chebyshev polynomials for both the shape and the test functions. This leads in general to full matrices, which is numerically inefficient. The modification of the standard Chebyshev–Galerkin method is basically a combination of ideas posed by Heinrichs (1989, 1991) and Shen (1995), see also (Pop, 1995). Key feature in Galerkin methods is the use of shape and test functions that satisfy *a priori* the boundary conditions. However, there are many ways to put the boundary conditions in the shape and test functions. In this appendix they are chosen in such a way that they lead to banded matrices having good condition numbers, which makes the numerical treatment more efficient. Further, the technique followed in this appendix also removes so-called spurious eigenvalues.

The discretization of (3.1.8) will be used to compute the eigenvalue problems (3.1.7) and (3.3.4), and to compute the transient growth behaviour of the system (Section 3.3). Further, the eigenfunctions of $L = L_0$ and the corresponding w and p eigensolutions, which all play an important role in the model reduction in Chapter 4, are determined as well.

A.1 Discretization of the initial value problem

We consider the initial value problem (3.1.8) in the truncated domain $Q_h := \{(z, t) : z \in (0, h), t > 0\}$, $0 < h < \infty$. Subsequently increasing the value of h until convergence is reached gives us the desired truncation depth. Thus we discretize the problem

$$\left\{ \begin{array}{l} \frac{\partial u}{\partial t} = D^2 u + (1 - \alpha) Du + \\ \quad + \left(\frac{1}{4}\alpha^2 - \frac{1}{2}\alpha - a^2\right)u - a^2 R e^{\frac{1}{2}\alpha z} \frac{\partial S_0}{\partial z}(z, t) w \quad \text{in } Q_h, \quad (\text{A.1.1a}) \\ -D^2 w + a^2 w = a^2 e^{-\frac{1}{2}\alpha z} u \quad \text{in } Q_h, \quad (\text{A.1.1b}) \\ u = w = 0 \quad \text{at } \{z = 0\} \cup \{z = h\}, t > 0, \quad (\text{A.1.1c}) \\ u = g \quad \text{in } (0, h), t = 0. \quad (\text{A.1.1d}) \end{array} \right.$$

To use the Chebyshev polynomials, we need to transform (A.1.1) to the finite interval $I := (-1, 1)$ for all $t > 0$. For this purpose we introduce the *linear* transformation $\zeta : (0, h) \mapsto (-1, 1)$ defined by

$$\zeta(z) = \frac{2z - h}{h}, \quad z(\zeta) = \frac{1}{2}h(\zeta + 1). \quad (\text{A.1.2})$$

Now let $u(z) = u(z(\zeta)) = \tilde{u}(\zeta)$, $w(z) = w(z(\zeta)) = \tilde{w}(\zeta)$ and $S_0(z, t) = S_0(z(\zeta), t) = \tilde{S}_0(\zeta, t)$. Then substitution in (A.1.1) yields

$$\left\{ \begin{array}{l} \frac{\partial \tilde{u}}{\partial t} = \frac{4}{h^2} \tilde{D}^2 \tilde{u} + \frac{2}{h} (1 - \alpha) \tilde{D} \tilde{u} + \left(\frac{1}{4}\alpha^2 - \frac{1}{2}\alpha - a^2\right) \tilde{u} - \\ \quad - \frac{2}{h} a^2 R e^{\frac{1}{2}\alpha z(\zeta)} \frac{\partial \tilde{S}_0}{\partial \zeta}(\zeta, t) \tilde{w} \quad \text{in } (-1, 1), t > 0, \quad (\text{A.1.3a}) \\ -\frac{4}{h^2} \tilde{D}^2 \tilde{w} + a^2 \tilde{w} = a^2 e^{-\frac{1}{2}\alpha z(\zeta)} \tilde{u} \quad \text{in } (-1, 1), t > 0, \quad (\text{A.1.3b}) \\ \tilde{u} = \tilde{w} = 0 \quad \text{at } \{\zeta = -1\} \cup \{\zeta = 1\}, t > 0, \quad (\text{A.1.3c}) \\ \tilde{u} = \tilde{g} \quad \text{in } (-1, 1), t = 0. \quad (\text{A.1.3d}) \end{array} \right.$$

From this point on we drop the tildes. The unknown functions $\{u, w\}$ in (A.1.3) are represented by the series expansion

$$\{u, w\}(\zeta, t) = \sum_{j=0}^{\infty} \{u_j, w_j\}(t) \mathcal{W}_j(\zeta), \quad (\text{A.1.4})$$

where $\{\mathcal{W}_j\}$ are the – yet unspecified – shape functions. We approximate the solutions u and w by truncating the series expansion in (A.1.4). The result is projected on a finite dimensional space in order to get a finite algebraic system.

Let $T_k(\zeta)$ denote the Chebyshev polynomial of degree k . We define the shape functions (Heinrichs, 1989, 1991)

$$\mathcal{W}_j(\zeta) = (1 - \zeta^2)T_j(\zeta), \quad j \geq 0,$$

and approximate $\{u, w\}$ by $\{u_K, w_K\} = \sum_{j=0}^K \{u_j, w_j\} \mathcal{W}_j$. Clearly,

$$\mathbb{X}_K = \text{span}\{\mathcal{W}_j, j = \overline{0, K}\} = \{p \in \mathbb{P}_{K+2} : p(\pm 1) = 0\},$$

where \mathbb{P}_k denotes the space of polynomials of order k , and therefore $\{u_K, w_K\}$ satisfy the boundary conditions *a priori*. For the definition of the test functions we use the functions (Gottlieb and Orszag, 1983; Shen, 1995)

$$\mathcal{V}_j(\zeta) = T_j(\zeta) - T_{j+2}(\zeta), \quad j \geq 0.$$

Obviously,

$$\mathbb{Y}_K = \text{span}\{\mathcal{V}_j, j = \overline{0, K}\} = \{p \in \mathbb{P}_{K+2} : p(\pm 1) = 0\}.$$

Substitution of (A.1.4) in (A.1.3a,b), multiplying by $\omega(\zeta)\mathcal{V}_k(\zeta)$ and integrating over I yields the semi-discretizations

$$\begin{aligned} \sum_{p=0}^K \frac{du_p}{dt} \int_I \mathcal{W}_p(\zeta)\mathcal{V}_k(\zeta)\omega(\zeta) d\zeta &= \sum_{p=0}^K u_p \int_I \frac{4}{h^2} D^2 \mathcal{W}_p(\zeta)\mathcal{V}_k(\zeta)\omega(\zeta) d\zeta + \\ &+ (1-\alpha) \sum_{p=0}^K u_p \int_I \frac{2}{h} D \mathcal{W}_p(\zeta)\mathcal{V}_k(\zeta)\omega(\zeta) d\zeta + \\ &+ (\frac{1}{4}\alpha^2 - \frac{1}{2}\alpha - a^2) \sum_{p=0}^K u_p \int_I \mathcal{W}_p(\zeta)\mathcal{V}_k(\zeta)\omega(\zeta) d\zeta - \\ &- a^2 R \sum_{p=0}^K w_p \int_I \frac{2}{h} e^{\frac{1}{2}\alpha z(\zeta)} \frac{\partial S_0}{\partial \zeta} \mathcal{W}_p(\zeta)\mathcal{V}_k(\zeta)\omega(\zeta) d\zeta \quad (\text{A.1.5}) \end{aligned}$$

and

$$\begin{aligned} - \sum_{p=0}^K w_p \int_I \frac{4}{h^2} D^2 \mathcal{W}_p(\zeta) \mathcal{V}_k(\zeta) \omega(\zeta) d\zeta + a^2 \sum_{p=0}^K w_p \int_I \mathcal{W}_p(\zeta) \mathcal{V}_k(\zeta) \omega(\zeta) d\zeta = \\ = a^2 \sum_{p=0}^K u_p \int_I e^{-\frac{1}{2}\alpha z(\zeta)} \mathcal{W}_p(\zeta) \mathcal{V}_k(\zeta) \omega(\zeta) d\zeta, \quad (\text{A.1.6}) \end{aligned}$$

where the prime denotes differentiation with respect to ζ and where $\omega(\zeta) = (1 - \zeta^2)^{-\frac{1}{2}}$.

Now let the matrices \mathbf{I} , \mathbf{D}_2 , \mathbf{D}_1 , \mathbf{E}_1 and \mathbf{E}_2 be defined as follows:

$$\begin{aligned} \mathbf{I}_{p,k} &= \langle \mathcal{W}_p, \mathcal{V}_k \rangle_\omega, \quad \mathbf{D}_{2,p,k} = \langle \frac{4}{h^2} D^2 \mathcal{W}_p, \mathcal{V}_k \rangle_\omega, \quad \mathbf{D}_{1,p,k} = \langle \frac{2}{h} D \mathcal{W}_p, \mathcal{V}_k \rangle_\omega, \\ \mathbf{E}_{1,p,k} &= \langle e^{-\frac{1}{2}\alpha z(\cdot)} \mathcal{W}_p, \mathcal{V}_k \rangle_\omega, \quad \mathbf{E}_{2,p,k}(t) = \left\langle \frac{2}{h} e^{\frac{1}{2}\alpha z(\cdot)} \frac{\partial \mathcal{S}_0}{\partial \zeta}(\cdot, t) \mathcal{W}_p, \mathcal{V}_k \right\rangle_\omega, \end{aligned}$$

where $\langle u, v \rangle_\omega = \int_{-1}^1 u v \omega d\zeta$. The matrices \mathbf{D}_2 , \mathbf{D}_1 and \mathbf{I} can be determined explicitly. Table A.1 shows the coefficients of these matrices. Matrices \mathbf{E}_1 and $\mathbf{E}_2(t)$ are determined by a Gauss–Lobatto integration method, i.e.

$$\mathbf{E}_{1,p,k} \cong \sum_{j=0}^{(p+2)(k+2)+1} \beta e^{-\frac{1}{2}\alpha z(\zeta_j)} \mathcal{W}_p(\zeta_j) \mathcal{V}_k(\zeta_j)$$

and

$$\mathbf{E}_{2,p,k}(t) \cong \frac{2}{h} \sum_{j=0}^{(p+2)(k+2)+1} \beta e^{\frac{1}{2}\alpha z(\zeta_j)} \frac{\partial \mathcal{S}_0}{\partial \zeta}(\zeta_j, t) \mathcal{W}_p(\zeta_j) \mathcal{V}_k(\zeta_j),$$

where

$$\zeta_j := -\cos \frac{(2j+1)\pi}{2((p+2)(k+2)+1)}, \quad \beta := \frac{\pi}{(p+2)(k+2)+1}$$

are respectively the Gauss nodes and the corresponding (constant) weighting coefficients (Quarteroni et al., 2000).

Using the notations $\mathbf{u} = (u_0, u_1, \dots, u_K)^\top$ and $\mathbf{w} = (w_0, w_1, \dots, w_K)^\top$, we obtain the semi-discretization

$$\begin{cases} \mathbf{I} \frac{d\mathbf{u}}{dt} = \mathbf{D}_2 \mathbf{u} + (1 - \alpha) \mathbf{D}_1 \mathbf{u} + (\frac{1}{4}\alpha^2 - \frac{1}{2}\alpha - a^2) \mathbf{I} \mathbf{u} - a^2 R \mathbf{E}_2(t) \mathbf{w} & (\text{A.1.7a}) \\ \mathbf{B} \mathbf{w} := -\mathbf{D}_2 \mathbf{w} + a^2 \mathbf{I} \mathbf{w} = a^2 \mathbf{E}_1 \mathbf{u}, & (\text{A.1.7b}) \\ \mathbf{u}(0) = \mathbf{u}^0. & (\text{A.1.7c}) \end{cases}$$

The initial condition \mathbf{u}^0 is defined as follows. Assume

$$g(\zeta) = \sum_{p=0}^K u_p^0 \mathcal{W}_p(\zeta), \quad (\text{A.1.8})$$

which implies that $g(-1) = g(1) = 0$. Multiplying (A.1.8) by $\mathcal{V}_k(\zeta)\omega(\zeta)$, and integrating over I yields

$$\mathbf{u}^0 = \mathbf{I}^{-1}\mathbf{U}^0 \quad \text{with } \mathbf{u}^0 = (u_0^0, \dots, u_K^0)^\top \text{ and } \mathbf{U}_k^0 = \langle g, \mathcal{V}_k \rangle_\omega.$$

The entries U_k^0 are again computed using the Gauss–Lobatto method.

For the equilibrium boundary layer the implicit θ -scheme (Wesseling, 2001) is used for time marching. The scheme is unconditionally von Neumann stable for $\frac{1}{2} \leq \theta \leq 1$. Furthermore, the local truncation error is maximal of order 2 for $\theta = \frac{1}{2}$. Our choice of $\theta = 0.55$ falls within the stability region and the local truncation error is nearly of second order. Let \mathbf{u}^n be the solution of (A.1.7) at time $t = n \cdot \Delta t$ and let $\mathbf{A} := \mathbf{D}_2 + (1 - \alpha)\mathbf{D}_1 + (\frac{1}{4}\alpha^2 - \frac{1}{2}\alpha - a^2)\mathbf{I}$. Discretization in time is given by

$$\begin{aligned} \mathbf{u}^0 &= \mathbf{u}^0, \\ \mathbf{B}\mathbf{w}^0 &= a^2\mathbf{E}_1\mathbf{u}^0 \\ (\mathbf{I} - \theta\Delta t\mathbf{A})\mathbf{u}^{n+1} &= (\mathbf{I} + (1 - \theta)\Delta t\mathbf{A})\mathbf{u}^n - \Delta t a^2 R \mathbf{E}_2(\infty)\mathbf{w}^n \\ \mathbf{B}\mathbf{w}^{n+1} &= \mathbf{E}_1\mathbf{u}^{n+1}. \end{aligned}$$

A.2 Solving the discrete eigenvalue problem

To obtain the eigenvalues and eigenfunctions of operator L_α as defined in (3.1.8a), we use the discretization (A.1.7). We consider the generalized eigenvalue problem

$$\mathbf{D}_2\mathbf{u} + (1 - \alpha)\mathbf{D}_1\mathbf{u} + (\frac{1}{4}\alpha^2 - \frac{1}{2}\alpha - a^2)\mathbf{I}\mathbf{u} - a^2 R \mathbf{E}_2(\infty)\mathbf{B}^{-1}\mathbf{u} = \sigma\mathbf{I}\mathbf{u}. \quad (\text{A.2.1})$$

The eigenvalues of the matrix eigenvalue problem (A.2.1) form a finite set of approximations of the spectrum of operator L_α . With respect to the Chebyshev–Galerkin method, a rule of thumb is that only one third of the lowest order eigenvalues of (A.2.1) are accurate approximations of the eigenvalues of L_α .

The eigenvector \mathbf{u}_j corresponding to eigenvalue σ_j of (A.2.1) is used to build the approximate eigenfunction, i.e.

$$\bar{u}_j(\zeta) = \sum_{p=0}^K u_{j,p} \mathcal{W}_p(\zeta) = \sum_{p=0}^K u_{j,p} \mathcal{W}_p(\zeta(z)) =: u_j(z). \quad (\text{A.2.2})$$

In the Galerkin projection method as discussed in Chapter 4, we need the eigenfunctions $s_j(z)$, $w_j(z)$, $p_j(z)$ and its derivatives to compute the coefficients in the amplitude expansion. The eigenfunctions s_j are found by setting $\alpha = 0$ in (A.2.1).

Table A.1. Discretization matrices. Here $c_p = 0$ for $p < 0$, $c_p = 2$ for $p = 0$ and $c_p = 1$ for $p > 0$. All coefficients have to be multiplied by $\frac{1}{2}\pi$.

$\mathbf{I}_{p,k} = \langle \mathcal{W}_p, \mathcal{V}_k \rangle_\omega$	$k = p - 4$ $\frac{1}{4}$	$k = p - 3$	$k = p - 2$ $-\frac{1}{2} - \frac{1}{4}c_{p-2}$
$\mathbf{D}_{2,p,k} = \langle D^2 \mathcal{W}_p, \mathcal{V}_k \rangle_\omega$			$p(p - 3) + 2c_p$
$\mathbf{D}_{1,p,k} = \langle D \mathcal{W}_p, \mathcal{V}_k \rangle_\omega$		$1 - \frac{1}{2}p$	
$\mathbf{W}_{p,k} = \langle \mathcal{W}_p, T_k \rangle_\omega$			$-\frac{1}{4}c_{p-2}$
	$k = p - 1$	$k = p$	$k = p + 1$ $k = p + 2$
$\langle \mathcal{W}_p, \mathcal{V}_k \rangle_\omega$		$\frac{1}{2} + \frac{1}{2}c_p - \frac{1}{4}c_{p-1}$	$-\frac{1}{4}c_p$
$\langle D^2 \mathcal{W}_p, \mathcal{V}_k \rangle_\omega$		$-p(p + 3) - 2c_p$	
$\langle D \mathcal{W}_p, \mathcal{V}_k \rangle_\omega$	$p + \frac{1}{2}(c_p - c_{p-1})$		$-c_p - \frac{1}{2}p$
$\langle \mathcal{W}_p, T_k \rangle_\omega$		$c_p - \frac{1}{4}c_p^2 - \frac{1}{4}c_{p-1}$	$-\frac{1}{4}c_p$
$\langle T_p, T_k \rangle_\omega$		c_p	

The eigenfunctions $w_j(\zeta)$ are computed from (A.1.7b): $\mathbf{w}_j = a^2 \mathbf{B}^{-1} \mathbf{E}_1 \mathbf{u}_j$ and

$$w_j(\zeta) = \sum_{p=0}^K w_{j_p} \mathcal{W}_p(\zeta) = \sum_{p=0}^K w_{j_p} \mathcal{W}_p(\zeta(z)) =: w_j(z) .$$

For the pressure eigenfunctions $p_j(z)$ we follow a different route. From the Darcy law (2.2.3c) we derive $Dp = s - w$, hence $\mathbf{p}'_j = \mathbf{s}_j - \mathbf{w}_j$. This also implies $Dp(0) = Dp(h) = 0$ and the solution can thus be represented by

$$Dp_j(z) = \sum_{p=0}^K p'_{j_p} \mathcal{W}_p(\zeta(z)) . \quad (\text{A.2.3})$$

The eigenfunction $p_j(z)$ is then found by integrating (A.2.3) with respect to z . The constant of integration is found from relations $D^2 p = Ds - Dw$ and $D^2 p - a^2 p = Ds$ (cf. equation (4.2.1c)). This gives the additional condition that $p(0) = -Dw(0)/a^2$, $a \neq 0$.

Since the derivatives of $u_j(z)$ and $w_j(z)$ are not expected to be zero in $z = 0, h$, we have to change the basis $\{\mathcal{W}_j\}$ by standard Chebyshev polynomials $\{T_j\}$, i.e.

$$\{u_j, w_j\}(\zeta) = \sum_{p=0}^K \{u_{j_p}, w_{j_p}\} \mathcal{W}_p(\zeta) \equiv \sum_{p=0}^{K+2} \{\tilde{u}_{j_p}, \tilde{w}_{j_p}\} T_p(\zeta) . \quad (\text{A.2.4})$$

In (A.2.4) we need Chebyshev polynomials $T_p(\zeta)$ up to order $K+2$ since \mathcal{W}_K is a polynomial of order $K+2$. Next we multiply (A.2.4) by $T_k(\zeta)\omega(\zeta)$ and integrate over I to obtain

$$\mathbf{W}\{\mathbf{u}_j, \mathbf{w}_j\} := \sum_{p=0}^K \{u_{j_p}, w_{j_p}\} \langle \mathcal{W}_p, T_k \rangle_\omega \equiv \sum_{p=0}^{K+2} \{\tilde{u}_{j_p}, \tilde{w}_{j_p}\} \langle T_p, T_k \rangle_\omega =: \mathbf{T}\{\tilde{\mathbf{u}}_j, \tilde{\mathbf{w}}_j\} ,$$

and this implies $\{\tilde{\mathbf{u}}_j, \tilde{\mathbf{w}}_j\} = \mathbf{T}^{-1} \mathbf{W}\{\mathbf{u}_j, \mathbf{w}_j\}$, where $\mathbf{W} \in \mathbb{R}^{(K+3) \times (K+1)}$ and $\mathbf{T} \in \mathbb{R}^{(K+3) \times (K+3)}$, see Table A.1. We are now in the position to take derivatives of $u_j(z)$ and $w_j(z)$:

$$D\{u_j, w_j\}(\zeta) = \sum_{p=0}^{K+2} \{\tilde{u}_{j_p}, \tilde{w}_{j_p}\} DT_p(\zeta) . \quad (\text{A.2.5})$$

Observe that the right-hand side of (A.2.5) is a polynomial of order $K+1$. To project this polynomial onto the Chebyshev basis, we only need $K+1$ basis functions:

$$\sum_{p=0}^{K+2} \{\tilde{u}_{j_p}, \tilde{w}_{j_p}\} DT_p(\zeta) \equiv \sum_{p=0}^{K+1} \{\tilde{u}'_{j_p}, \tilde{w}'_{j_p}\} T_p(\zeta) . \quad (\text{A.2.6})$$

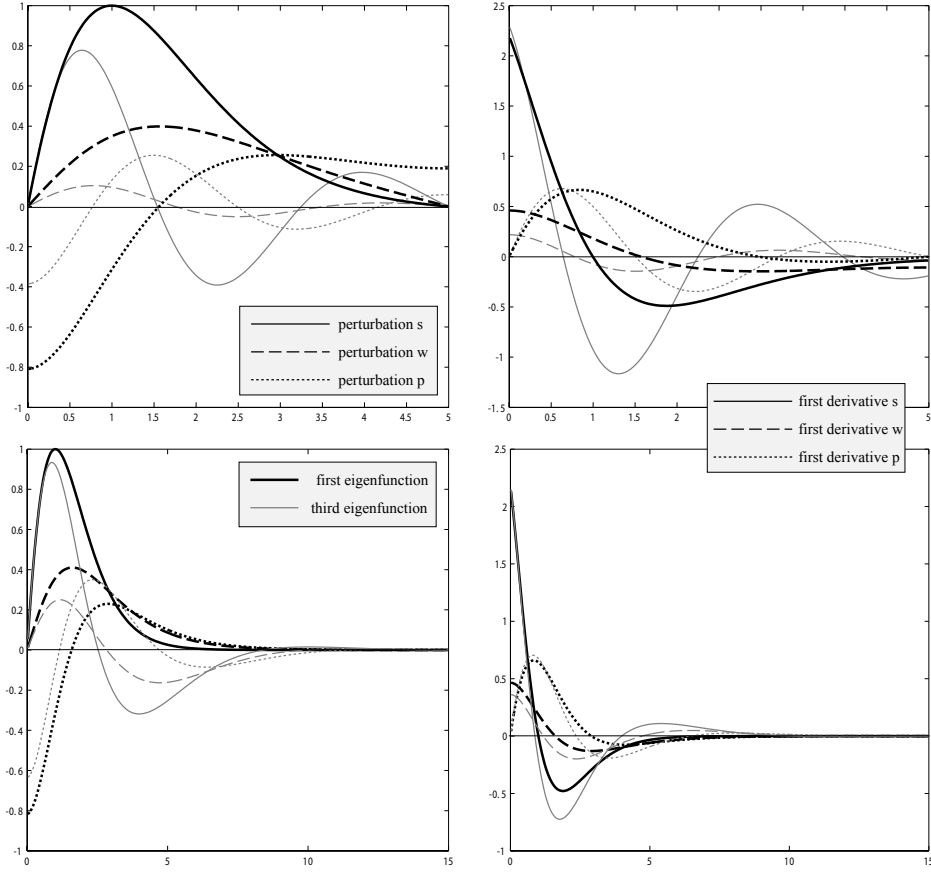


Figure A.1. Plots of $s_1(z)$, $Ds_1(z)$, $s_3(z)$, $Ds_3(z)$ and the corresponding $w_1(z)$, $Dw_1(z)$, $w_3(z)$, $Dw_3(z)$, $p_1(z)$, $Dp_1(z)$, $p_3(z)$ and $Dp_3(z)$ as function of z for $h = 5$ and $h = 15$. The parameters are $R = 14.5$ and $a = 12\pi/50$.

Again we multiply (A.2.6) by $T_k(\zeta)\omega(\zeta)$ and integrate over I to obtain

$$\mathbf{T}_1\{\tilde{\mathbf{u}}_j, \tilde{\mathbf{w}}_j\} := \sum_{p=0}^{K+2} \{\tilde{u}_{j_p}, \tilde{w}_{j_p}\} \langle DT_p, T_k \rangle_\omega = \sum_{p=0}^{K+1} \{\tilde{u}'_{j_p}, \tilde{w}'_{j_p}\} \langle T_p, T_k \rangle_\omega = \mathbf{T}\{\tilde{\mathbf{u}}'_j, \tilde{\mathbf{w}}'_j\}, \quad (\text{A.2.7})$$

where $\mathbf{T}_1 \in \mathbb{R}^{(K+2) \times (K+3)}$ and $\mathbf{T} \in \mathbb{R}^{(K+2) \times (K+2)}$. In this way we find $\{\tilde{\mathbf{u}}'_j, \tilde{\mathbf{w}}'_j\} = \mathbf{T}_0^{-1} \mathbf{T}_1\{\tilde{\mathbf{u}}_j, \tilde{\mathbf{w}}_j\}$. The matrices \mathbf{W} , \mathbf{T} , \mathbf{T}_1 and \mathbf{T}_2 can be determined explicitly, see Table A.1 and Gottlieb and Orszag (1983). Figure A.1 depicts the first and third eigenfunction $s_1(z)$ and $s_3(z)$ together with their first derivative.

References

- Gottlieb, D. and S. A. Orszag: 1983, *Numerical Analysis of Spectral Methods: Theory and Applications*. Philadelphia: SIAM.
- Grosch, C. E. and S. A. Orszag: 1977, 'Numerical solution of problems in unbounded regions: Coordinate transforms'. *J. Comp. Phys.* **25**, 273–296.
- Heinrichs, W.: 1989, 'Improved condition number for spectral methods'. *Math. Comput.* **53**, 103–119.
- Heinrichs, W.: 1991, 'Stabilization techniques for spectral methods'. *J. Sci. Comp.* **6**, 1–19.
- Mack, L. M.: 1976, 'A numerical study of the temporal eigenvalue spectrum of the Blasius boundary layer'. *J. Fluid Mech.* **73**, 497–520.
- Pop, I. S.: 1995, 'Numerical Approximation of Differential Equations by Spectral Methods'. Technical report, "Babes-Bolyai" University, Cluj-Napoca. (in romanian).
- Quarteroni, A., R. Sacco, and F. Saleri: 2000, *Numerical Mathematics*. New York: Springer-Verlag.
- Shen, J.: 1995, 'Efficient spectral-Galerkin method II. Direct solvers of second and fourth order equations by using Chebyshev polynomials'. *SIAM J. Sci. Comput.* **16**, 74–87.
- Spalart, P. R.: 1984, 'A spectral method for external viscous flows'. *Contemp. Math.* **28**, 315–335.
- van Stijn, T. L. and A. I. van de Vooren: 1980, 'An accurate method for solving the Orr–Sommerfeld equation'. *J. Eng. Math.* **14**, 17–26.
- Wesseling, P.: 2001, *Principles of Computational Fluid Dynamics*, Vol. 29 of *Computational Mathematics*. Berlin: Springer-Verlag.

Summary

In this thesis we analyse the stability of flows in porous media, where the action of gravity on the distribution of a fluid

1. with decreasing density due to spatial variations of solute concentration or temperature in a fully saturated porous medium, or
2. with constant density during infiltration into an (partly) unsaturated porous medium

may give rise to convective motion, mixing and pattern formation. The stability analyses give stability thresholds in terms of the physical parameters of the system. Based on these thresholds, we predict the evolution of these flows.

The analysis involves the method of linearised stability, the energy method with different constraints, and a nonlinear stability analysis by means of a reduced model. In addition, we investigated the small time behavior of the evolution of growing perturbations. These methods give a complete picture in the sense that a) we can predict for which parameters the system remains stable with respect to perturbations of specific classes; b) we can predict when the system becomes unstable to infinitesimally small perturbations; c) we have full insight in the small time behavior of the system; d) we can predict what kind of patterns may possibly appear when the system is unstable.

For the verification and validation of the (in)stability thresholds, we use both an advanced two-dimensional numerical method and results obtained from laboratory experiments. All experiments show excellent agreement with the theory.

The analysis also applies to gravity-driven flow problems arising in ecology and hydrology. One application is solute transport in fully saturated peat moss layers. We give criteria for which convection and mixing of dissolved solutes occurs when the surface of a fully saturated porous medium is cooled during the night. This is confirmed by laboratory experiments and two-dimensional numerical simulations. The second application deals with steady infiltration of water in an unsaturated porous medium. We show for several soil classes that this is always a stable process.

Samenvatting

In dit proefschrift onderzoeken we de stabiliteit van vloeistofstromingen in poreuze media waar de werking van de zwaartekracht op een vloeistof

1. met afnemende dichtheid als gevolg van ruimtelijke variaties in concentratie en temperatuur in een volledig verzadigd porous medium, of
2. met een constante dichtheid tijdens infiltratie in een onverzadigd of gedeeltelijk verzadigd poreus medium

aanleiding kan geven tot convectieve stromingen, menging en de vorming van ruimtelijke stromingspatronen. Stabiliteitsanalyses geven stabiliteitsgrenzen in termen van de fysische parameters van het onderliggende stromingsprobleem. Aan de hand van deze stabiliteitsgrenzen kunnen we voorspellingen doen over het gedrag van de stroming in de tijd.

De in dit proefschrift gebruikte stabiliteitsanalyses zijn de (klassieke) lineaire stabiliteitsanalyse, de energie-methode met verschillende beperkingen voor de verstoringen, en niet-lineaire stabiliteitsanalyse met behulp van een gereduceerd model. Bovendien onderzoeken we voor kleine tijden het gedrag van de verstoringen. Deze technieken geven een compleet beeld in de zin dat: a) we kunnen voorspellen voor welke parameters het systeem stabiel blijft met betrekking tot willekeurige verstoringen; b) we kunnen voorspellen wanneer het systeem instabiel wordt met betrekking tot willekeurig kleine verstoringen; c) we volledig inzicht hebben in het gedrag van de stroming voor kleine tijden; d) we kunnen voorspellen wat voor soort stromingspatronen er mogelijk kunnen ontstaan wanneer het systeem daadwerkelijk instabiel wordt.

Voor de verificatie en validatie van de gevonden stabiliteitsgrenzen gebruiken we zowel een geavanceerde numerieke methode als laboratoriumexperimenten. Beide experimenten vertonen uitstekende overeenkomsten met de theoretische drempelwaarden.

De stabiliteitsanalyses zijn ook toepasbaar op andere ecologische en hydrologische zwaartekrachts-geïnduceerde stromingen. Een toepassing betreft het transport van opgeloste (voedings)stoffen in volledig verzadigde veenlagen. We geven stabiliteitsgrenzen voor het ontstaan van convectie en menging in een veenlaag tijdens de afkoeling van deze laag gedurende de nacht. Deze menging is bevestigd door zowel numerieke als laboratorium experimenten. De tweede toepassing betreft de stationaire infiltratie in een onverzadigd poreus medium. We laten voor verschillende grondtypes met name zien dat dit altijd een stabiel proces is.

Curriculum Vitae

Gert-Jan Joseph Mathilde Pieters werd op 22 juni 1975 geboren te Hulst. Hij behaalde in 1995 het VWO diploma aan het Jansenius SG, thans het Reynaertcollege, in Hulst, en vervolgde zijn opleiding aan de Technische Universiteit Delft met de studie Technische Wiskunde. In 2000 studeerde hij cum laude af met het afstudeerwerk '*Stability Analysis for a Saline Boundary Layer Formed by Uniform Upflow Using Finite Elements*'.

Vanaf januari 2001 tot en met november 2004 was hij werkzaam bij de Technische Universiteit Eindhoven, waar hij onderzoek deed naar de stabiliteit van dichtheidsgeïnduceerde stromingen in poreuze media. Het onderzoek werd begeleid door prof. dr. ir. C.J. van Duijn en heeft geresulteerd in dit proefschrift.